Surface-Enhanced Raman Scattering (SERS) Studies of Pyrazine Adsorbed on Polycrystalline and Single Crystal Electrodes.

by

Alexandre Guimarães Brolo

A thesis
presented to the University of Waterloo
in fulfilment of the
thesis requirement for the degree of
Doctor of Philosophy in
Chemistry

Waterloo, Ontario, Canada, 1998

The University of Waterloo requires the signatures of all persons using or photocopying this thesis. Please sign below, and give address and date.

Abstract

Surface-Enhanced Raman Scattering (SERS) Studies of Pyrazine Adsorbed on Polycrystalline and Single Crystal Electrodes

The nature and the orientation of molecules adsorbed on certain rough metallic surfaces can be readily determined by surface-enhanced Raman scattering (SERS). This surface-enhancement phenomenon, allied to basic characteristics of Raman scattering, suggests that the SERS effect is potentially a powerful tool for the investigation of electrochemical problems. However, the magnitude of the enhancement depends on several factors, such as electrode potential, laser wavelength, surface coverage and morphology. The objective of this thesis was to extend the knowledge of the influence of these factors on the overall SERS. Pyrazine (pz) was chosen as the probe molecule. Pz has a molecular centre of inversion which makes this molecule a good model for molecular orientation studies.

A Raman study of pz and its protonated forms in solution was performed in order to better understand the pz vibrational spectrum. All bands for pz and its protonated forms were assigned using the correlation table technique and ab initio calculations. The pK_a values for both the first and the second protonation of pz were also estimated, and were in good agreement with previous measurements. SERS spectra of pyrazine adsorbed on a polycrystalline silver electrode were obtained. The SERS selection rules indicated that pz adsorbs end-on, using one of its nitrogen electron lone pairs. It was observed that pz is electrochemically reduced at potentials more negative than -900 mV. The reduction

process was investigated using SERS and electrochemical techniques. The observation of bands, arising from reduction products of pz, at positive potentials explained most of the controversial results for the SERS spectrum of pz, previously reported in the literature. The SERS spectra of pyrazinium (pzH^+) adsorbed on a polycrystalline silver electrode indicated that the orientation of the adsorbed cation depends on the applied potential.

SERS spectra of pyrazine adsorbed on "smooth" and rough polycrystalline gold electrodes were also obtained. The roughness factors of a number of gold surfaces, prepared by varying the number of applied oxidation-reduction cycles (ORCs), were monitored by atomic-force microscopy (AFM). The surface-enhancement was correlated to the surface morphology. The results indicated that an optimum SERS signal was generated from a surface containing features of approximately 100 nm-size. The SERS intensity was also correlated to surface concentration data, obtained independently by electrochemical methods. A novel procedure to determine the SERS intensity from a "smooth" surface was developed, and a linear relationship between SERS intensities and the surface concentration data was observed. Finally, the SERS spectra from pz adsorbed on a Au(210) single-crystal electrode was obtained; this is the first report of a SERS spectrum from this "unroughened" surface. The correlation between the SERS intensities and the surface coverage was also investigated for Au(210).

Acknowledgment

I would like to express my sincere gratitude to Professor D. E. Irish for his help, guidance, encouragement and patience throughout the course of this work.

I would like to thank Professor J. Lipkowski and his co-workers for the opportunity to work cooperatively with the University of Guelph, and for all insightful discussions and advice. I specially want to thank Dr. G. Szymanski for the help with the AFM/STM measurements and with the preparation of the single-crystal electrode. I wish to thanks Dr. Z. Morbi for the help in setting up the dye laser. I also wish to thank Dr. M. Melinda Gugelchuk for the help with the ab intio calculations.

I would also like to thank Dr. G. E. Toogood for helpful discussions and suggestions. I wish to thank B. Smith, R. Bartholomew, M. Odziemkowski, and all of my other co-workers in this group during the last few years. All of them made a significant contribution to make this work possible.

Finally, I wish to thank my family, especially my wife, Elaine, for all their encouragement and support.

List of Figures

List of Tables

1. Preface

The surface-enhanced Raman scattering (SERS) technique is widely used to probe *in situ* electrochemical processes [1, 2, 3, 4, 5, 6]; however, several basic aspects of SERS are still being debated [1 - 6]. One of these unclear aspects, most important for the investigation of electrochemical interfaces, is the relationship between SERS intensities and surface coverage. In order to understand this relationship, one has to compare surface concentration data, measured independently, with SERS intensities. Basic thermodynamic data, including surface concentrations, for the adsorption of organic molecules on noble metal electrodes can be obtained by chronocoulometry; such data are being acquired in our Centre [7]. These data can be correlated to the SERS results in order to gain understanding of the relationship between SERS intensities and surface coverage. An initial collaborative work, involving the adsorption of pyridine on gold electrodes, has been carried out [8,9]. The continuation of these collaborative works is described in this thesis; the probe molecule, pyrazine, adsorbed on polycrystalline and single-crystal electrodes, has been investigated.

Chapter 2 is the introductory chapter, where the basic aspects of Raman spectroscopy and SERS (the techniques most used in this thesis) are described. The results are presented in Chapters 3 through 8. Each chapter has its own introduction, experimental, results, discussion, and conclusion sections. Brief theoretical background for the techniques or concepts are presented in the pertinent chapter. The normal Raman spectra of pyrazine and its protonated forms are presented in Chapter 3. This

study was carried out to identify all vibrational bands due to pyrazine and protonated pyrazine before adsorbing the molecule onto the electrode surface. Ab initio calculations, presented in Chapter 4, were performed. These helped to confirm the assignments of some vibrational bands for pyrazine and its protonated forms, and give some insights about molecular properties of these compounds. The SERS studies were initiated by observing the behaviour of pyrazine adsorbed on silver electrodes. The orientation of the organic molecule and the spectral dependence on potential and wavelength were observed. The electrochemical reduction of pyrazine was also monitored. These results are presented in Chapter 5. The adsorption of pyrazinium cation on silver was also studied and the results are presented in Chapter 6.

After gaining a good understanding of the SERS spectrum of pyrazine adsorbed on silver, including the identification of all SERS bands, relative intensities, and the molecular orientation, the SERS study was extended to gold electrodes. The relationship between SERS intensities and both surface coverage and morphology are presented in Chapter 7 for pyrazine adsorbed on a polycrystalline gold electrode. Data for adsorption of pyrazine on a well characterized single-crystal surface, Au(210), are presented in Chapter 8. Chapter 9 is a general conclusion and summary section.

1.1. References

[1] B. Pettinger, in Adsorption of Molecules at Metal Electrodes, J. Lipkowski and P. N. Ross, eds., VCH, New York, 1992, Ch. 6, p. 285.

[2] R. K. Chang and B. L. Laube, *CRC Crit. Rev. Solid State Mater. Sci.*, **1984**, 12, 1.

[3] R. L. Birke and J. R. Lombardi, in *Spectroelectrochemistry - Theory and Practice*, R. J. Gale, ed., Plenum, NY, **1988**, Ch. 6, p. 263.

[4] J. E. Pemberton, in *Electrochemical Interfaces: Modern Techniques for in situ Interface Characterization*, H. D. Abruna, ed., VCH, NY, **1991**, Ch. 5, p. 193.

[5] T. M. Cotton, in *Spectroscopy of Surfaces - Advances in Spectroscopy*, R. J. H. Clark and R. E. Hester, eds., Wiley, NY, Vol. 16, **1988**, Ch. 3, p. 91.

[6] R. L. Garrell, *Anal. Chem.*, **1989**, 61, 401A.

[7] L. Stolberg and J. Lipkowski, in *Adsorption of Molecules at Metal Electrodes*, J. Lipkowski and P. N. Ross, eds., VCH, New York, **1992**, Ch. 4, p. 171.

[8] L. Stolberg, J. Lipkowski and D.E. Irish, *J. Electroanal. Chem.*, **1991**, 300, 563.

[9] J. Lipkowski, L. Stolberg, S. Morin, D. E. Irish, P. Zelenay, M. Gamboa and A. Wieckowski, *J. Electroanal. Chem.*, **1993**, 335, 147.

Chapter 2

Introduction to Raman Spectroscopy and Surface-Enhanced Raman Scattering

2. Introduction to Raman Spectroscopy and Surface-Enhanced Raman Scattering

2.1. Raman Spectroscopy

Vibrational Raman spectroscopy is the main experimental technique used in this thesis. Raman spectroscopy is a well known technique, and has become a standard tool in chemistry laboratories. Several books [1,2,3] and reviews [4] describe the theory of the technique and its applications. Detailed description of the Raman mechanism and theory can also be found in other thesis from our laboratory [5]. Therefore, in this Chapter we will only give a brief background; the reader may consult the references for a more comprehensive description.

The vibrational Raman effect arises from the inelastic scattering of photons from molecules. The scattering of photons occurs when monochromatic radiation, of energy $h\nu_L$, interacts with molecules. A schematic representation of the scattering of photons from molecules is given in Figure 2.1. Most of the photons are elastically scattered, i.e., they preserve their initial energy. This phenomenon is known as Rayleigh scattering. The inelastically scattered photons (Raman radiation), with energy distinct from the initial radiation, may either transfer vibrational energy to the molecule and emerge with less energy than the incident light (Stokes radiation) or acquire vibrational energy during the interaction with the molecule (anti-Stokes radiation). These scattering events can be quantitatively described classically [6]. When a molecule interacts with the electric field of

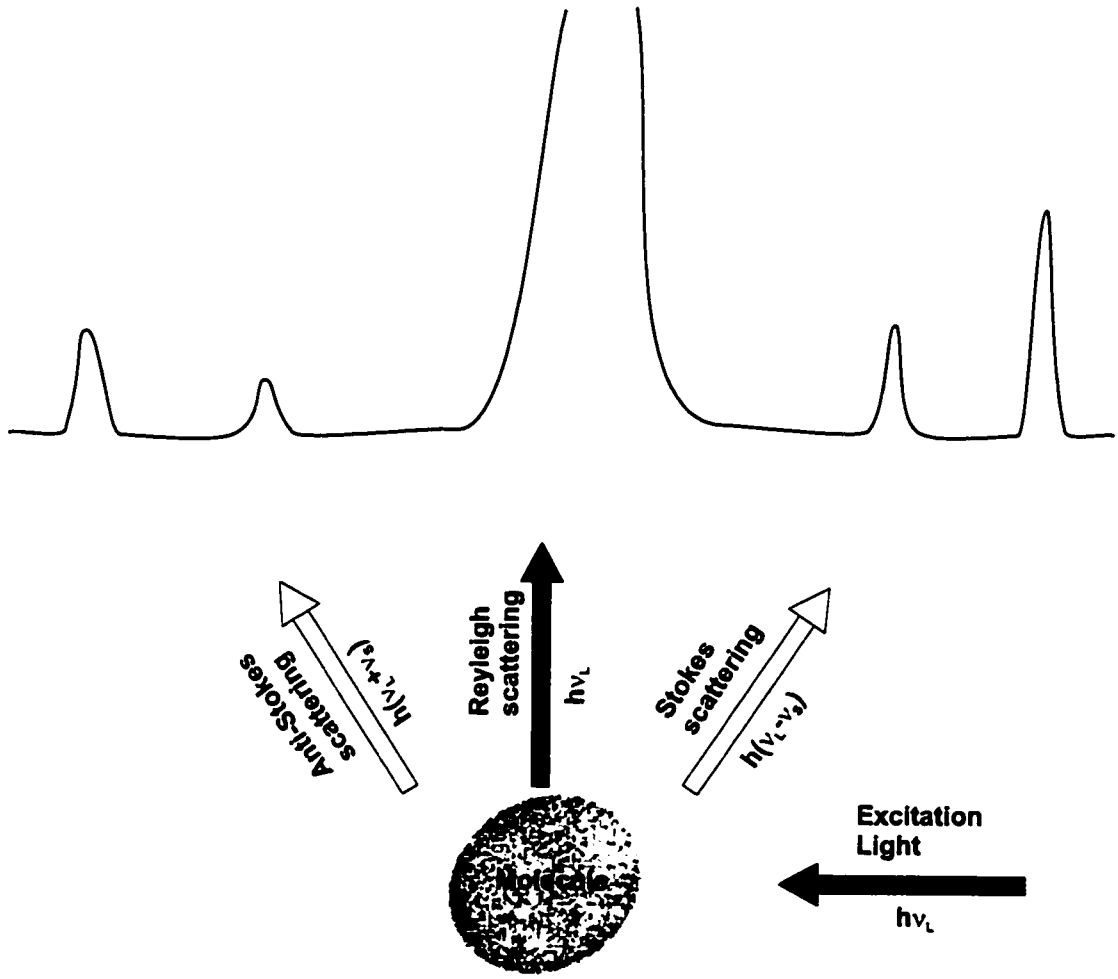

Figure 2.1: Schematic representation of a Raman experiment. The Rayleigh radiation corresponds to the elastic scattering. The anti-Stokes and the Stokes radiation are the blue and red-shifted, respectively, inelastic scattering. The Stokes and anti-Stokes branches contain the vibrational energy information and their relative intensities reflect the populations of the initial states.

the radiation, E, an electric dipole moment, μ, is induced in the particle. The amplitude of μ, to the first approximation, is given by:

$$\mu = \alpha E \qquad (1)$$

In a molecule whose atoms are vibrating with a frequency ω_K, a time (t) dependence is introduced in α, which is represented by:

$$\alpha = \alpha_0 + \alpha_1 \cos(\omega_K t) \qquad (2)$$

where α_0 is the molecular polarizability for the equilibrium geometry, and α_1 is the change of the polarizability around the equilibrium value of the normal coordinate. Likewise, the intensity of **E** changes with time through the frequency of the light source, ω_L.

$$E_{(\omega_L)} = E_0 \cos(\omega_L t) \qquad (3)$$

Therefore, substituting equations (2) and (3) into equation (1), expanding, and collecting the terms, one obtains equation (4), below:

$$\mu_{(\omega_L)} = \alpha_0 E_0 \cos(\omega_L t) + \left(\frac{1}{2}\right)\alpha_1 E_0 \cos(\omega_L - \omega_K)t + \left(\frac{1}{2}\right)\alpha_1 E_0 \cos(\omega_L + \omega_K)t \qquad (4)$$

The first term on the right hand side of equation (4) refers to the elastic scattered light (Rayleigh radiation). The second and the third terms, corresponding to the inelastic scattering (Raman radiation), are the Stokes and the anti-Stokes emissions, respectively. The classical theory predicts that the same information is contained in both Stokes and anti-Stokes branches of the Raman spectrum. The vector and tensor designations were omitted in all equations for simplification.

The fundamental aspects of the quantum mechanical treatment for Raman scattering are shown in Figure 2.2. For Stokes radiation (Fig. 2.2a), the molecule is promoted from a lower vibrational state in the electronic ground state (g) to an intermediate "virtual" state, when it is excited by the incident light ($h\nu_L$). Then, it returns to the electronic ground state, but in a vibronically excited level. A scattered photon is emitted during this process whose energy is the difference between the excitation energy, $h\nu_L$, and the vibrational energy gap ($E_{(v = 1)}$ minus $E_{(v = 0)}$, in Fig. 2.2a). Therefore, as shown in Fig. 2.2a, the net of the overall two-photon scattering process is energetically equivalent to the absorption of a single IR photon (But the Raman spectrum is not necessarily equivalent to the IR spectrum. The selection rules for the two spectroscopies differ [7]). The same mechanism as described above is operative for anti-Stokes emissions, but, in this case, the initial vibrational state is higher than the final one; therefore, the scattered photon is blue-shifted. Quantum mechanical theory also indicates that the population of each molecular state is given by the Boltzmann distribution [1,7].

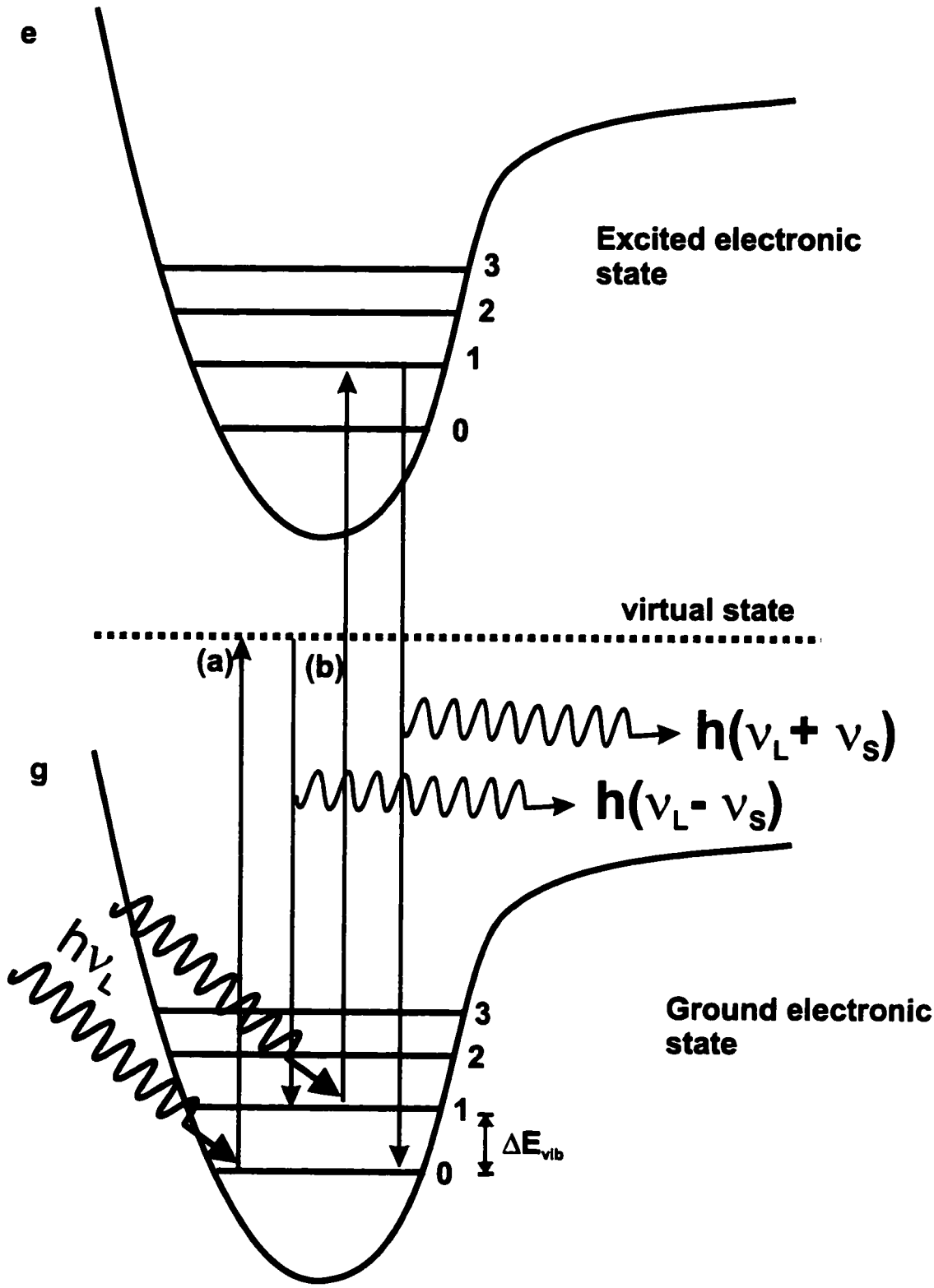

Figure 2.2: Energetics of Raman scattering. (a) Normal Raman; Stokes scattering. (b) This is a special case, where there is an energy match between the incident light energy and the difference in energy between the molecular electronic states. This phenomenon is called the Resonance Raman effect. An anti-Stokes scattering is illustrated in this example.

As the ground state population is much higher than the excited state population at room temperature, the Stokes emissions are more intense than the anti-Stokes (Fig. 2.1).

The Raman scattering may change the polarization state of the incident light [1]. Laser radiation, generally used as excitation sources in modern Raman experiments, is generally polarized in a single direction. The scattered light, at a 90° geometry from the sample, contains components polarized in two directions: perpendicular and parallel to the polarization direction of the incident light. The intensities of these two components of the scattered light are designated $I_{\perp}$ and $I_{||}$, respectively. The ratio of these quantities (ρ) is called the depolarization ratio. Depolarized bands have their ρ equal to 0.75. Polarized bands have their depolarization ratio values in the range: $0 \leq \rho \leq 0.75$. Polarized bands occur for vibrations which are totally symmetric. Therefore, it is possible to determine the totally symmetric vibrations through Raman polarization experiments, which is very helpful for the assignment of bands to normal modes of vibrations.

2.1.1. Raman Instrumentation

There are three generations of modern laser Raman instruments commercially available on the market. Figure 2.3 shows a schematic description of each of them. Scanning instruments, using a photomultiplier tube (PMT) as a detector, are the first generation. In the second generation, the monochromators are coupled to spectrographic systems and optical multichannel analyzer (OMA) detectors. In this situation, a wide range

of wavenumbers of the spectrum can be recorded in a very short time. The recent available third generation instruments show a dramatic increase in the sensitivity. The improvement is obtained by replacing the monochromators by holographic notch filters (in order to eliminate the elastic scattering) and a dispersing grating and the detector by charge-transfer devices (CCD). In this thesis, an instrument representative of each of these generations was used.

The instrument from the first generation (scanning instruments) was a Jarrell-Ash 25-100 1.0 meter Czerny-Turner double monochromator (Fig. 2.3a) equipped with a 129 cosecant stepping drive, an RCA 31034 photomultiplier tube (PMT), housed in a thermoelectrically cooled chamber, with a SSR model 1105/1120 photon counting system. The instrument from the second generation (multichannel instruments with monochromators) was a Dilor OMARS 89 spectrometer with microscope option. This instrument contains two 1800 groove/mm gratings coupled to a spectrograph stage (Fig. 2.3b) containing a 1800 groove/mm grating. The detector was an optical multichanel analyser (OMA) (a thermoelectric cooled 512 diode-array coupled to an image intensifier). The third generation of Raman instruments was a Renishaw 1000 Raman microscope (Fig. 2.3c) with a holographic notch filter, which selectively eliminates the intense Rayleigh light. The dispersion element was a holographic grating. The detector was a thermoelectrically cooled CCD.

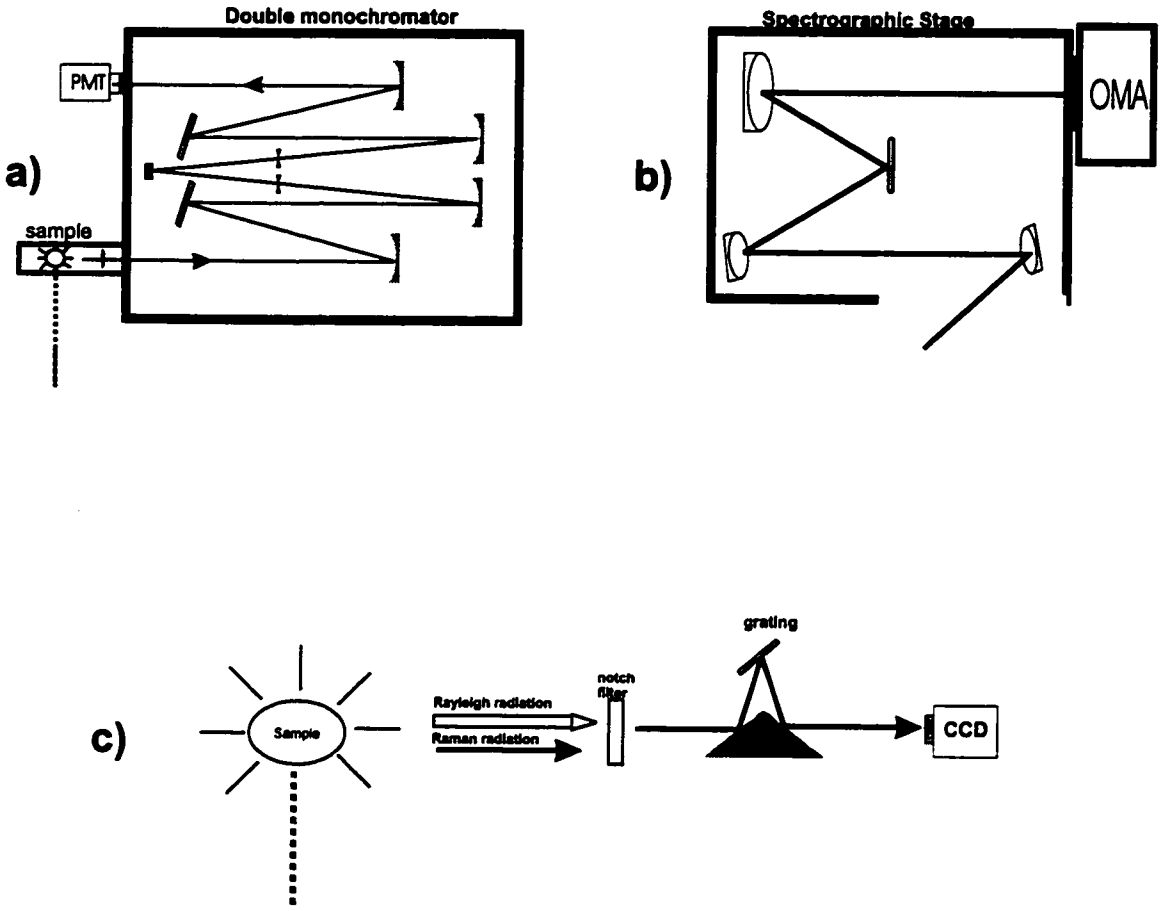

Figure 2.3: Schematic representation of Raman instruments. a) The double monochromator used in scanning experiments; b) The spectrographic stage of a Raman multichannel instrument; c) The new Raman instruments, with holographic notch filters to cut off the excitation radiation.

2.1.2. Raman Intensities

The intensity for a Raman transition between an initial (i) and final (f) state can be written as [8]:

$$I_{fi} = k\omega_L{}^4 I_0 \left| \sum_{\sigma\rho} \alpha_{fi}{}^{\sigma\rho} \right|^2 \qquad (5)$$

Here k is a term containing constants such as π and the speed of light, c. I_0 is the intensity of the incident light, and the term inside the brackets is the Raman polarizability tensor [9].

Equation (**5**) shows that the efficiency of the Raman scattering varies as the fourth power of the frequency of the exciting light. In theory, the scattering can be excited by any frequency, provided that an oscillating dipole can be induced in the particle due to the illumination. In this regard, the occupation of virtual states (as shown in Fig. 2.2a) seems to violate the quantum mechanical requirement for discrete excited states. However, the virtual state can be thought of as a time-dependent assemblage of molecular eingenstates. Therefore, its occupation by a molecule has, in quantum mechanical terms, a low probability of occurrence. In fact, only about 1 in 10^{10} incident photons result in Raman scattering. This natural inefficiency of the Raman process is a major limiting factor in its application. Nevertheless, there are enhancement mechanisms that, when operative, can increase the Raman cross-section by several orders of magnitude. The most common of

these mechanisms are the resonance Raman scattering and the surface-enhanced Raman scattering (SERS).

2.1.3. Resonance Raman Scattering

The quantum mechanical treatment of the Raman polarizability tensor involves second-order perturbation theory through the Kramers-Heisenberg expression [10].

$$\alpha^{\sigma\rho} = \sum_{v} \left| \frac{\langle \psi_f | \mu_\sigma | \psi_v \rangle \langle \psi_v | \mu_\rho | \psi_i \rangle}{E_v - E_i - h\nu_L + i\Gamma_v} + \frac{\langle \psi_f | \mu_\sigma | \psi_v \rangle \langle \psi_v | \mu_\rho | \psi_i \rangle}{E_v - E_f + h\nu_L + i\Gamma_v} \right| \qquad (6)$$

Here μ_σ and μ_ρ are the electronic dipole moment operators, and E_i, E_f and E_v are the energies of the initial, final, and virtual eigenstates, respectively.

The energy of the excitation photon in a Raman experiment can be selected in such a way that the intermediate (or virtual) state in the two photon process is a real molecular electronic excited state (E_e, instead of E_v in equation (**6**)). This situation is illustrated in Figure 2.2b. In this case, the difference in energy between two molecular electronic states (E_e - E_i) is in resonance with the incident photon energy ($h\nu_L$). Consequently, the denominator in the first term of equation (**6**) becomes very small (for $h\nu_L=(E_e-E_i)$). Therefore, the Raman scattering from the molecule increases dramatically as $\alpha^{\sigma\rho}$ becomes large. The Lorentzian line width term, $i\Gamma_v$, is a damping factor, used here to avoid a

division by zero in equation (**6**) when resonance occurs. In practice, resonance Raman (RR) signals can be 10^2 to 10^6 times larger than normal Raman scattering (NRS). The enhancement is specific to chromophore groups, responsible for the electronic transition. This feature makes RR an important tool to obtain specific molecular information on large and complex molecules, such as biological systems [11].

2.1.4. Surface-Enhanced Raman Scattering

Surface-enhanced Raman scattering (SERS) is a powerful technique for characterizing adsorbed species and processes at metallic surfaces. The giant signal enhancement (10^4 - 10^6 larger compared to normal Raman scattering) makes this technique sensitive to even sub-monolayer amounts of adsorbate on the surface. Consequently, the application of SERS to the *in situ* study of electrochemical processes provides useful mechanistic and structural information.

Surface-enhanced Raman scattering (SERS) was first recognized ca. 20 years ago [12,13]. The Raman scattering enhancement occurs for species excited with visible light (mainly green and red light) adsorbed on the rough surface of a free electron metal, such as Au, Ag, and Cu [14]. The electrochemical SERS technique has been widely used for the study of metal-adsorbate interactions. Its applications range from "classical" electrochemical studies such as corrosion processes [15], film growth [16], and self-assembled monolayers [17] to medical applications [18,19] and trace analysis [20,21]. Several reviews [22,23,24,25,26,27] have helped to disseminate the basic principles of the

technique and broaden the range of its applications. Some of these reviews are very comprehensive [28,29], and others emphasize specific applications, for instance to biological [30] and to analytical problems [31]. A review from our laboratory, with emphasis on the application of SERS to electrochemistry, has also been published [32].

2.1.5. The SERS experiment

A schematic drawing of the three electrode spectroelectrochemical cell, used in SERS experiments in this thesis, is shown in Figure 2.4. A more detailed description of the cell design can be found elsewhere [32]. The counter electrode is isolated from the main solution by a porous frit and the reference electrode is connected via a Luggin capillary tube. The working electrode and Teflon holder are machined so that the electrode can be slid snugly in and out of the Teflon. A brass rod is screwed into the back of the working electrode, in order to provide electrical contact. The potential on the working electrode is controlled with a potentiostat. The surface of the working electrode must be activated (i.e., roughened) in order to support the enhancement. The working electrode is polished, and cleaned before being roughened. The rough electrode is prepared by the application of one or more Oxidation-Reduction Cycles (ORCs), which are designed to remove metal from the electrode surface and redeposit it onto the surface. The ORC can be accomplished by either a potential step or a potential sweep. The specific ORC conditions, such as the anodic and cathodic limits, the potential step hold time, or the potential sweep speed, varies from system to system.

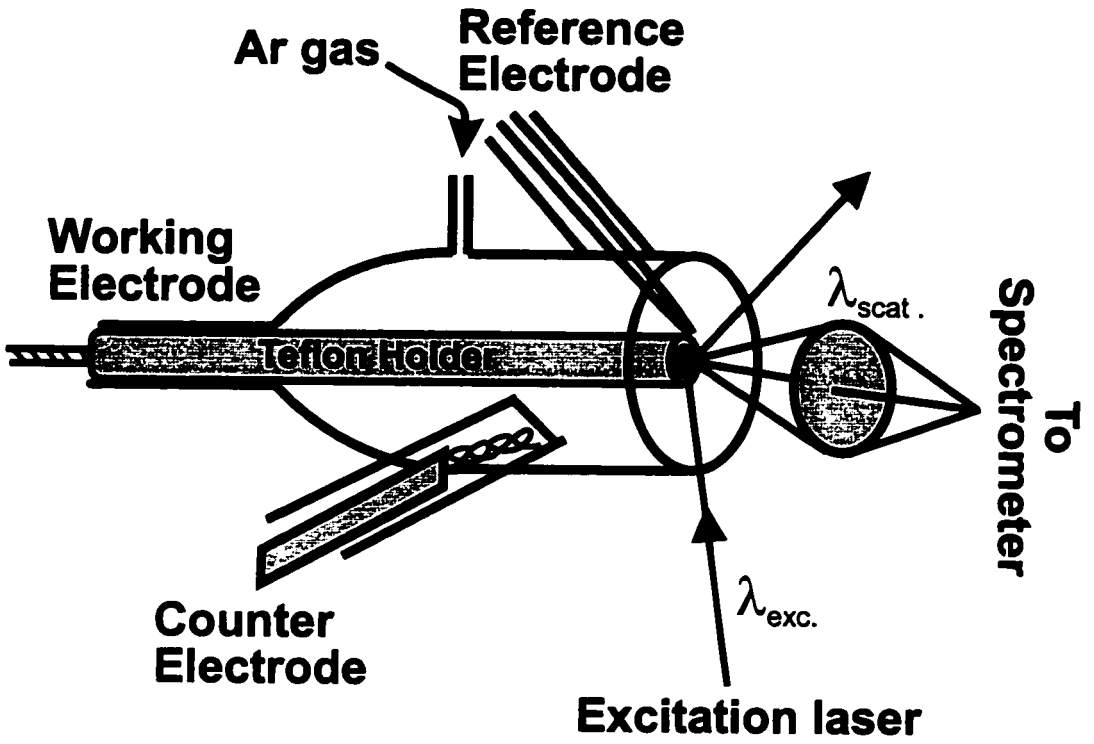

Figure 2.4: The spectroelectrochemical cell.

2.1.6. Why does the enhancement occur ?

The intensities of the inelastic scattered light in a normal Raman spectroscopic (NRS) experiment are proportional to the square of the induced dipole moment (μ). For a molecule adsorbed on a metallic electrode surface, and therefore subjected to an additional electric field from that surface, the induced dipole moment is given by the expression in Figure 2.5. An additional field gradient term is included due to the inhomogeneous electric field enveloping the molecule [33]. The two most important mechanisms that contribute to the overall enhancement are related to an exceptional increase of both the molecular polarizability (α) of the adsorbed species and the local electric field (E_{local}) near the metallic surface. The former accounts for the "chemical" or "CT" mechanism and the latter for the "electromagnetic (EM)" mechanism. There has been a dispute as to which of these mechanisms is dominant. Most authors now agree that both mechanisms contribute to the overall effect; however, either of them can be dominant for certain systems. Some of the important aspects of both mechanisms will be presented in the next sections; a detailed description of the CT [34, 35] and the EM mechanisms [36] can be found elsewhere, and a general discussion involving quantum mechanical aspects of the enhancement appeared in a review by Pettinger [29].

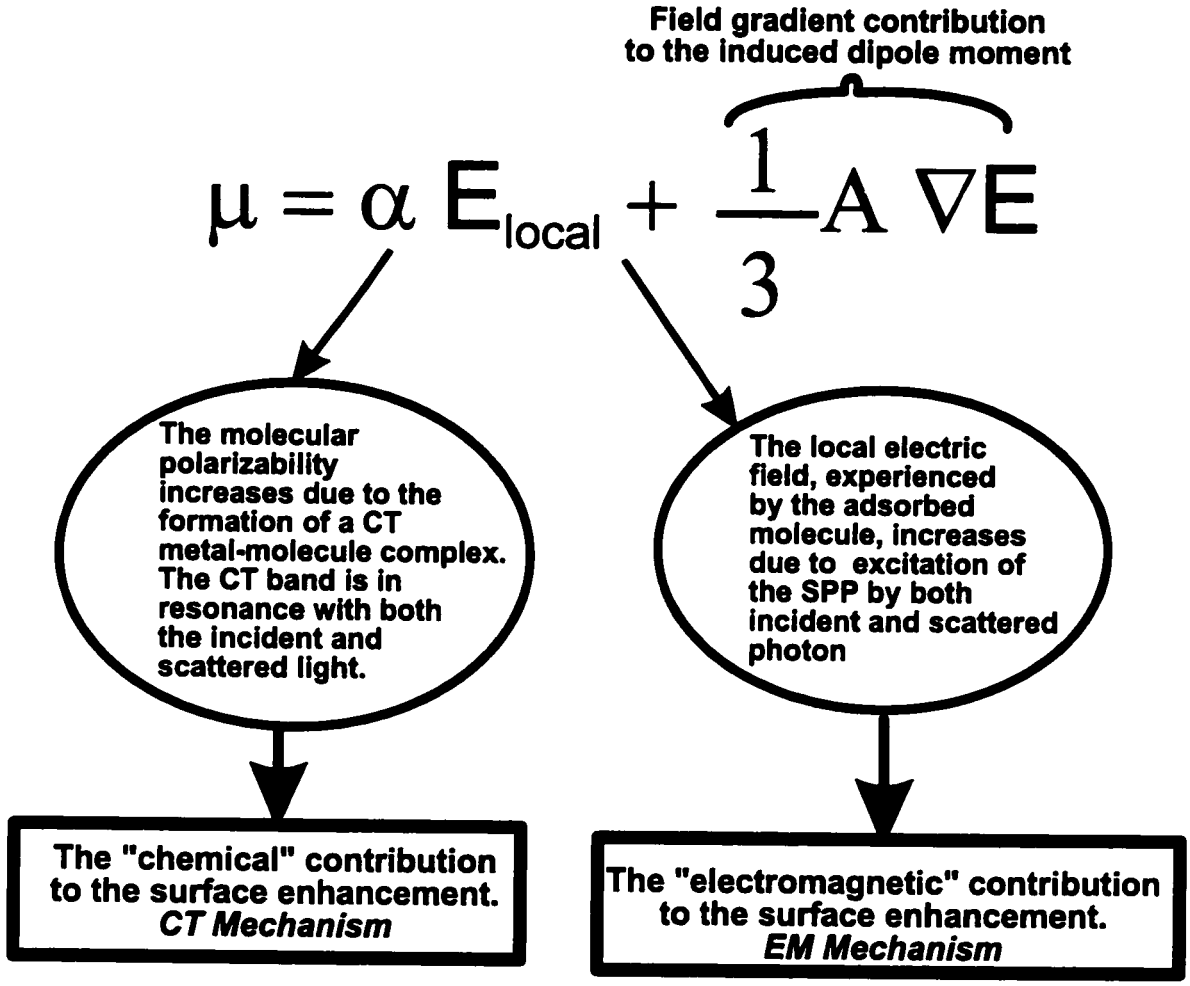

Figure 2.5: The induced molecular dipole (μ) for a molecule adsorbed onto a metallic surface. α is the molecular polarizability, E_{local} is the electric field experienced by the molecule, A is the quadrupole polarizability and ∇E is the electric field gradient. The vector and tensor representations were omitted for simplification.

2.1.7. The Electromagnetic Contribution to SERS - The EM Mechanism

In the EM mechanism, the enhancement of the Raman signal occurs due to a coupling between the incident light and the electron oscillations at the metallic surface, known as surface plasmons (SP). The SP are confined in a smooth surface, their amplitude decays exponentially with the distance away from the surface, and they cannot be excited by the incident photon due to a momentum mismatch [29]. The bumps in a rough surface (which contain curves) provide an additional momentum for the photon, and the SP can now be excited. The simplest case to be treated quantitatively is for molecules adsorbed on a small metallic sphere, as shown in Figure 2.6a. When the radius of this metallic sphere is much smaller than the wavelength of the excitation photon, the electric field from the light polarizes the sphere. The polarized sphere presents a dipolar response. The surface plasmons' (SP) normal modes of oscillation can be resonant with both the excitation and the scattered photon for surface features smaller than the optical wavelength. In this case, the calculated local electric field is found to be proportional to the term [37]:

$$g = \frac{(\varepsilon_{1(\omega)} - \varepsilon_2)}{(\varepsilon_{1(\omega)} + 2\varepsilon_2)} \qquad (7)$$

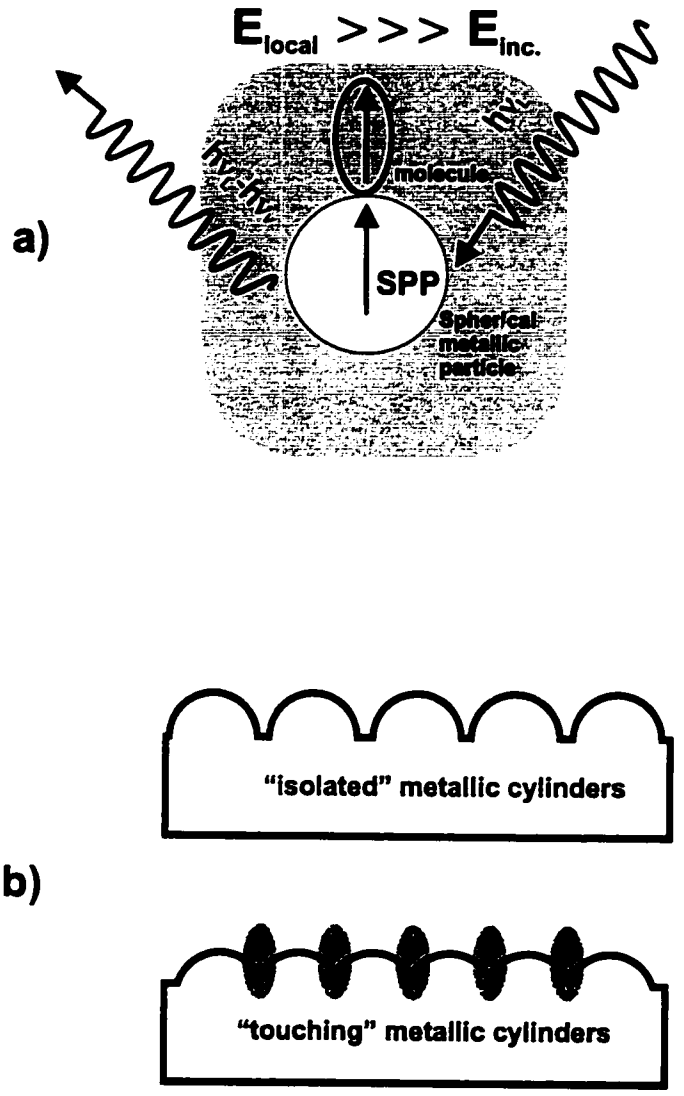

Figure 2.6: Models for electromagnetic calculation of the surface enhancement. a) A small metallic sphere presents a dipole response due to the coupling of the surface plasmon (SP) with the excitation line. The shadowed area indicates the enhanced local electric field enveloping the system. b) A "rough" surface, modeled as an array of metallic half cylinders embedded in a flat surface. The calculated electric field is very localized. The calculated enhancement from isolated particles is smaller than from touching metallic cylinders. The shadowed areas indicate the position where the electric field is maximum.

where ε_2 is the optical dielectric constant of the surrounding medium and $\varepsilon_{1(\omega)}$ is the complex dielectric function of the metal, given by:

$$\varepsilon_{1(\omega)} = \mathrm{Re}\left[\varepsilon_{1(\omega)}\right] + i\,\mathrm{Im}\left[\varepsilon_{1(\omega)}\right] \qquad (8)$$

It is clear from equations (**7**) and (**8**) that the local electric field becomes large when the real part of the complex dielectric constant is equal to $-2\varepsilon_2$ and the imaginary part is small. Hence, the frequency of the SP oscillations depends on the dielectric constant of the metal. This severe condition accounts for the observation of SERS from only a few metals (Cu, Ag, Au, alkali metals) using visible excitation [38, 29]. The calculation for spheres also shows a dependence of the SERS enhancement factor on the radius of the metallic spheres [37]. The enhancement profile (SERS enhancement factor versus wavelength plots) broadens with increase of the radius, due to multipolar response from the polarized sphere [39].

Further calculations for isolated particles coated by molecules indicate a strong dependence on the enhancement factor and the metallic particle morphology. Studies of oblate and prolate spheroids [40, 41] show that the coupling between the incident photon and the surface plasmons' resonances concentrates the electromagnetic field in certain regions of the surface, and a very high field gradient is observed when the molecule is positioned at the tip of the spheroid (lightning rod or antenna effect).

The calculations for isolated particles can predict some important properties of the enhancement, but their application is obviously very limited for electrochemically-roughened surfaces. Advancement in the theory consisted in modeling a group of metal particles [42,43,44]. The interactions between these metal particles are an important contribution to the overall enhancement [42-44]. A new formalism to investigate the interaction of light with metal surfaces has been developed recently [45]. The technique allows handling of complex surfaces, containing particles close enough to interact strongly. In this case, a rough metallic surface is modeled as an array of half cylinders embedded in a silver surface (Figure 2.6b). It is observed that very localized surface plasmon modes, created by strong electromagnetic coupling between touching particles, dominate the SERS response [45]. For instance, the overall enhancement factor increases from 10^3 for an "isolated" (non-touching) cylinder to 10^6 when the cylinders are touching each other [45].

The EM enhancement depends only on the metal's characteristics; hence vibrational modes with the same symmetry species should have the same enhancement factor for the same surface morphology.

2.1.8. The "Chemical" contribution to SERS - The CT mechanism

Some experimental results suggest that another mechanism also plays a role in the overall enhancement. For instance, the fact that different molecules with similar polarizability, adsorbed on the same metallic substrate, exhibit distinctly different enhancement factors cannot be explained by EM arguments only [34, 35]. The different excitation profiles (SERS intensities vs excitation wavelength plots) obtained for different bands in the same molecule, and the dependence of the potential profiles (SERS intensities vs electrochemical applied potential plots) on the energy of the excitation radiation are also indicative that another mechanism, besides EM, is operative in SERS.

In this additional "chemical" mechanism, the enhancement is because of a CT complex, formed between the atomic scale roughness on the metal (adatoms) and the adsorbed molecule, as shown in Figure 2.7. The energy of the frontier molecular orbitals of the adsorbed molecule are close to the metal's Fermi level because of the complex formation. The difference in energy between the Fermi level and the frontier orbital of the adsorbed species is close in frequency to the incident light, and an enhancement mechanism occurs, which is analogous to the Resonance Raman process [46].

A CT process can also occur via an increase in the metal's electron-photon coupling in the atomic scale roughness, which leads to a large production of electron-hole pairs [34, 35]. This process is described in Figure 2.8, and is known as a photon-driven charge transfer (PDCT) mechanism.

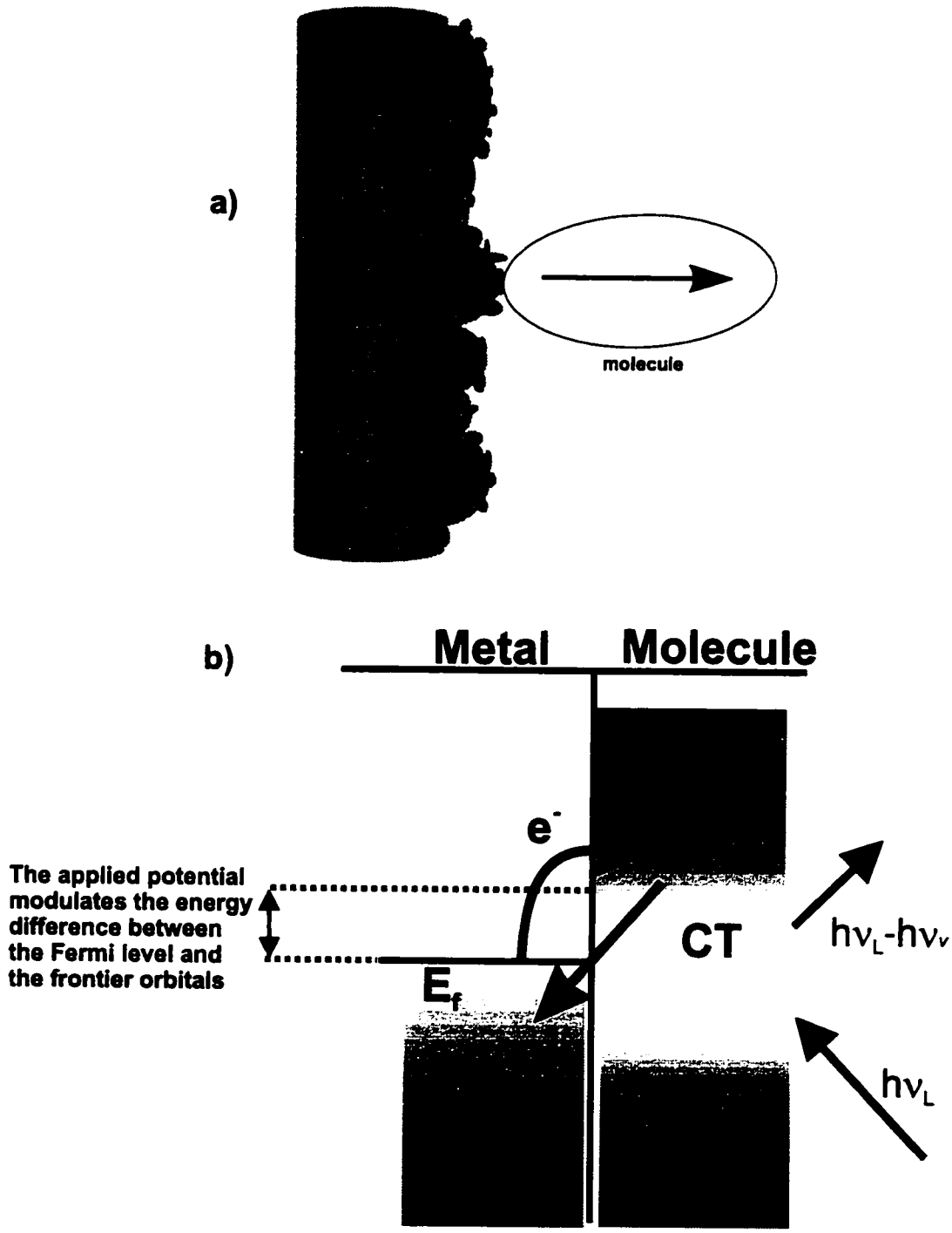

Figure 2.7: a) The CT complex between the molecule and the atomic active sites, present on a rough surface. b) For adsorbed molecules containing low energy π^* orbitals, an electron is transferred from the metal's Fermi level to the LUMO. This process is in resonance with the energy of the incident photon ($h\nu_L$). The energy of the Fermi level can be modulated by the applied potential; the energy of the Fermi level increases or decreases as a negative or positive potential, respectivelly, is applied.

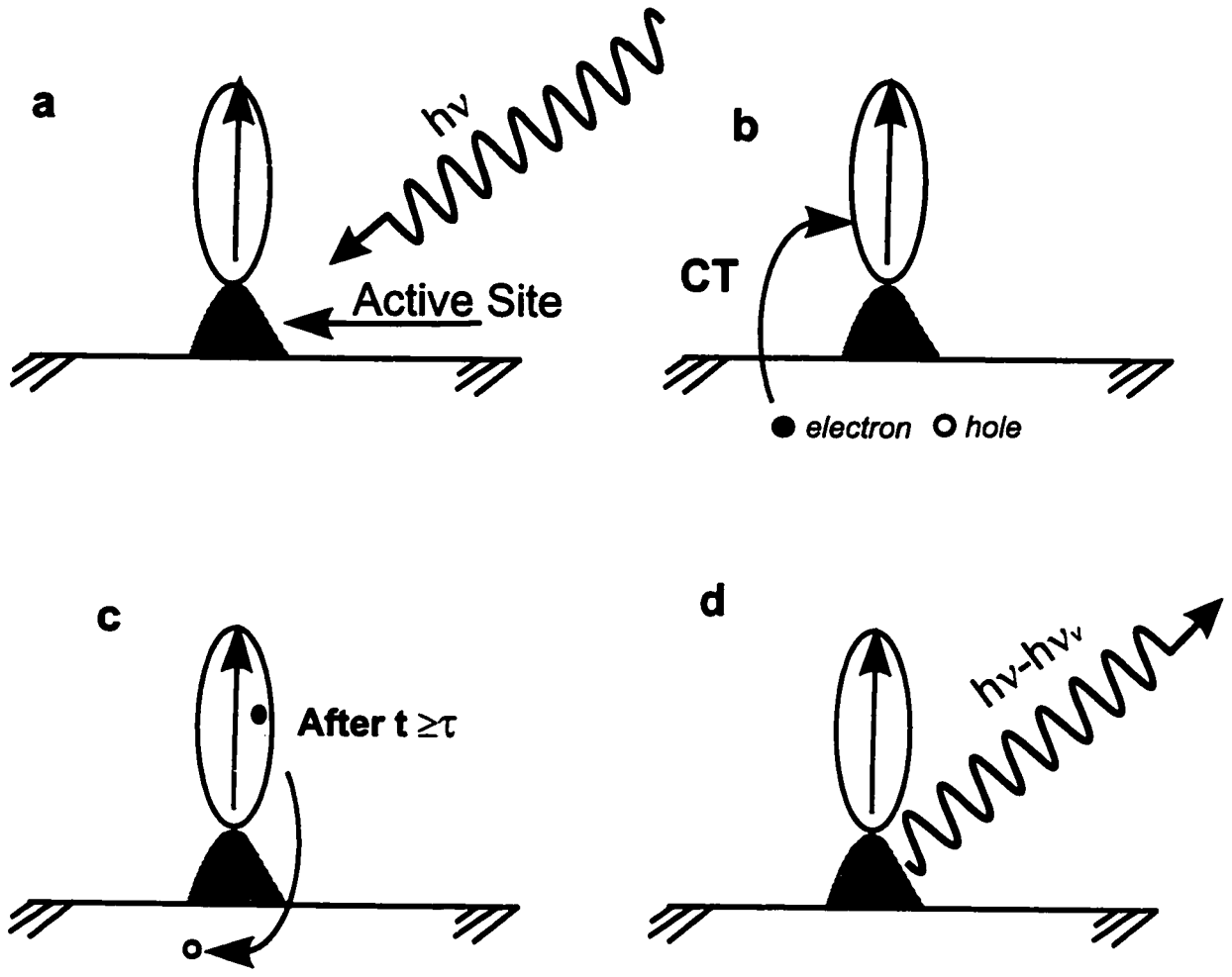

Figure 2.8: The photon-driven charge transfer mechanism (PDCT). a) The radiation bathes a molecule adsorbed onto an atomic scale active site. The interaction leads to the formation of an electron-hole pair. This process occurs at an enhanced rate on these adatom sites. b) The electron tunnels from the metal to the molecule. c) If the electron resides in the molecule long enough for a vibrational change, it will carry this information when it tunnels back to the metal. d) The annihilation of the electron occurs by recombination with the hole, and a Raman photon is created.

2.1.9. EM vs. CT

In this section, we will compare some of the features due to each of the most contributing SERS mechanisms (EM and CT). A full comparison between these mechanisms for electrochemistry SERS is presented in Table 2.1.

The SERS intensities versus applied potential plots, known as potential profiles, are readily obtained from electrochemical SERS experiments. Generally, the potential profiles are bell shaped curves for neutral molecules, and a decrease in the SERS intensity as the potential becomes either negative or positive is observed for adsorbed anions and cations, respectively [47, 48]. The enhancement of the local electric field depends only on the metal characteristics; hence, under the EM model, the change in the SERS intensity with potential largely reflects a change in the surface coverage. In fact, the surface coverage of a neutral molecule rises to a maximum near the point-of-zero-charge (pzc) and then falls off as the electrode potential is swept through a suitable range [49].

The potential profile plots obtained using various excitation lines can give an indication of the role played by the *chemical* mechanism in the overall effect. Under the CT model, the maximum could result when the potential change moves the Fermi level in and out of the resonance condition [50,51]. This situation is illustrated in Figure 2.7.

Table 2.1: Comparison of the salient features of the two most accepted surface enhancement contributions.

		EM mechanism	CT Mechanism
1.	Origin	Enhancement of the local electric field due to the coupling of the incident photon with the metal's surface plasmons	Resonance process involving the incident light and the CT band of the metal-molecule complex. (Resonance Raman like process)
2.	Roughness	Large scale roughness (ca. 10 - 600 nm)	Atomic scale roughness (active sites)
3.	Distance dependence	Long range. Important even for species several nm away from the surface, but decays with the distance	Short range. Important only for species adsorbed directly on the surface
4.	Potential dependence	The changes in the dielectric constant of the bulk metal with the applied potential is expected to be small. Hence, the enhancement factor does not depend on the applied potential; intensity changes in the potential profile are due to the variation of the surface coverage with potential	The CT band can be tuned by the applied potential; therefore, the enhancement factor is potential dependent
5.	Excitation wavelength dependence	The enhancement factor depends on the metal's dielectric constant, which is wavelength dependent. The E_{max} does not shift for different incident photon energies	The resonance condition depends on the excitation wavelength. The potential where the SER intensity maximizes (E_{max}) is different for different incident photon energies

The EM contribution to the enhancement depends on the dielectric constant of the metal, and the dielectric constant is dependent on the incident light. Therefore, different relative enhancements are expected for different metals at different excitation wavelengths. For instance, the relative enhancements for a 20 nm silver sphere in water peaks at ~ 400 nm. The same gold sphere in water peaks at 530 nm. [52]. The enhancement expected from the EM model depends only on metallic properties; hence vibrational modes of similar symmetry species should be enhanced by the same amount at a given potential (respecting the selection rules). Therefore the potential where the SERS intensities are at maximum (E_{max}) is expected to be the same for similar modes of vibration, and is not expected to change for different incident wavelengths.

Figure 2.9 shows the dependence of E_{max} on excitation energy for the ν_4 band of DABCO adsorbed on silver electrodes in the presence of different electrolytes [53]. One can notice that the E_{max} shifts to more negative potentials as the photon excitation energy increases. This behaviour can be interpreted in terms of the CT argument illustrated in Figure 2.7. The potentials where resonance is satisfied are different for different excitation energies. The linear relationship of the E_{max} vs. photon energy plots is expected from the CT model [54]. In fact, the sign of the slope of these plots reveals the direction of the CT process. A positive slope indicates a CT process from the Fermi level of the metal to the LUMO orbital of the molecule. This kind of result is expected for molecules containing a low-lying π^* orbital, such as pyridine and pyrazine. A negative slope indicates a CT

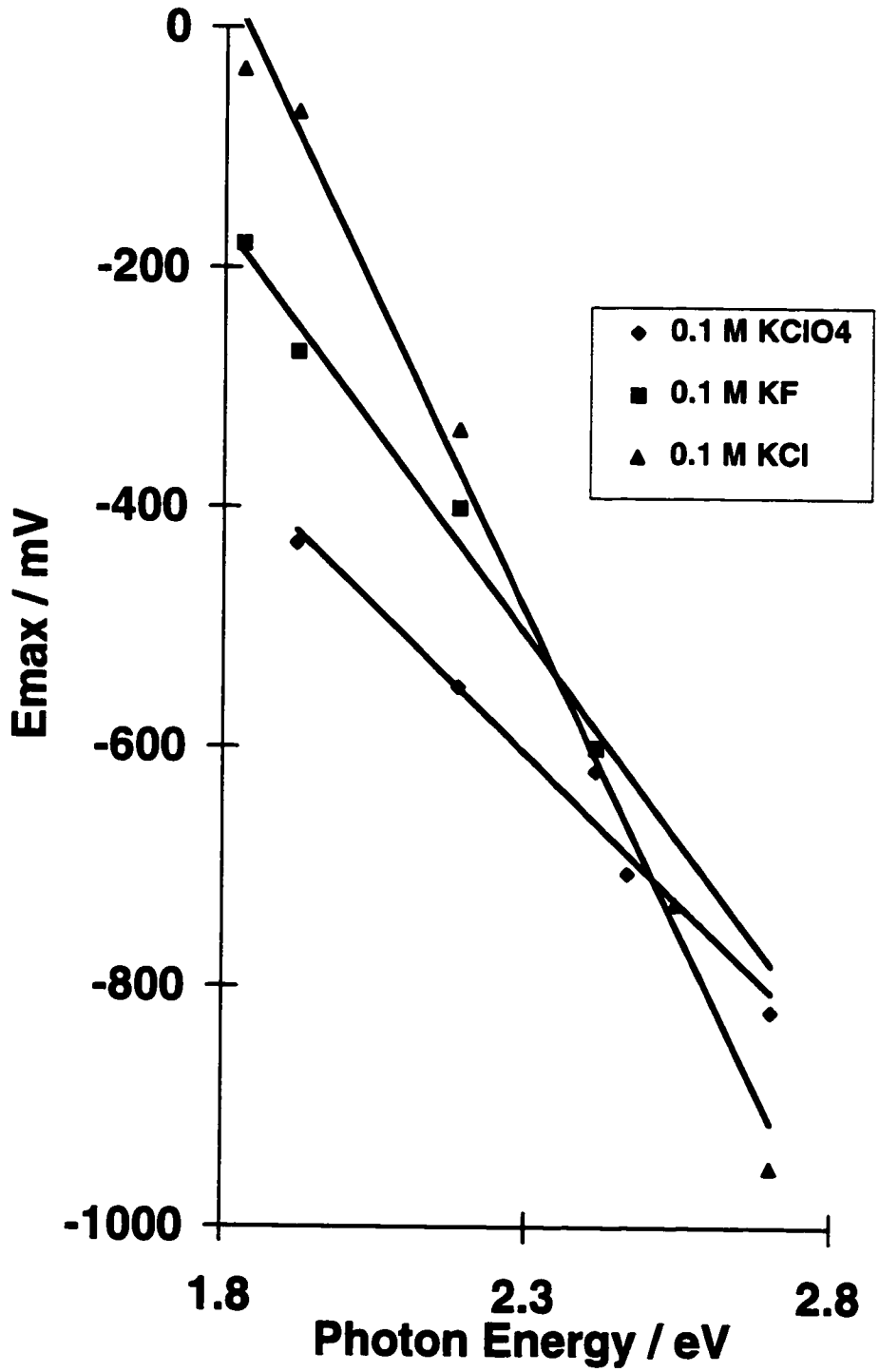

Figure 2.9: Plot of the maximum intensity of the potential profile of the ν_4 DABCO band vs the excitation photon energy (ref. 53).

process from the HOMO molecular orbital to the Fermi level [23]. Situations can arise where several CT processes occur for the same species adsorbed on an electrode [55]. The dependence of E_{max} on excitation wavelength has been used to indicate a quantitative contribution of the CT mechanism to the overall effect [56]. However, one must be careful because the shift in E_{max} also depends on the concentration of the specifically adsorbed halide.

2.2. References

[1] D. A. Long, *Raman Spectroscopy*, McGraw Hill, New York, **1977**.

[2] J. R. Ferraro and K. Nakamoto, *Introductory Raman Spectroscopy*, Academic Press, Toronto, **1994**.

[3] J. G. Grasselli and B. J. Balkin, eds., *Analytical Raman Spectroscopy*, Wiley - Interscience, Toronto, **1991**.

[4] D. A. Long, *Chemistry in Britain*, **1989**, 6, 592 (and other papers in this issue).

[5] R. J. Bartholomew, Ph.D. thesis, University of Waterloo, **1996**.

[6] M. Kerker, *The Scattering of Light and Other Electromagnetic Radiation*, Academic, NY, **1969**.

[7] E. B. Wilson, Jr., J. C. Decius and P. C. Cross, *Molecular Vibrations, The Theory of Infrared and Raman Spectroscopy*, McGraw Hill, NY, **1955**.

[8] R. M. Hexter and A. C. Albrecht, *Spectrochim. Acta*, **1979**, 35A, 233.

[9] P. M. Champion and A. C. Albrecht, *Ann. Rev. Phys. Chem.*, **1982**, 33, 353.

[10] D. Lee and A. C. Albrecht, in *Advances in Infrared and Raman Spectroscopy*, R.J. H. Clark and R. E. Hester, eds., Vol. 12, Wiley, NY, **1985**, p.193.

[11] T. G. Spiro and T. M. Loehr, in *Advances in Infrared and Raman Spectroscopy*, R.J. H. Clark and R. E. Hester, eds., vol. 1, Wiley, NY, **1975**, p.98.

[12] D. L. Jeanmaire and R. P. Van Duyne, *J. Electroanal. Chem.*, **1977**, 84, 1.

[13] M. G. Albrecht and J. A. Craighton, *J. Am. Chem. Soc.*, **1977**, 99, 5215.

[14] H. Seki, *J. Electron Spect. Relat. Phenom.*, **1986**, 39, 289.

[15] L. J. Oblonsky, S. Virtanen, V. Schroeder and T. M. Devine, *J. Electrochem. Soc.*, **1997**, 144, 1604.

[16] Y. Misono, M. Nagase and K. Itoh, *Spectrochim. Acta*, **1994**, 50A, 1539.

[17] N. Matsuda, T. Sawaguchi, M. Osawa and I. Uchida, *Chem. Letters*, **1995**, 145.

[18] I. Nabiev, I. Chourpa and M. Manfait, *J. Raman Spect.*, **1994**, 25, 13.

[19] X. Dou, T. Takama, Y. Yamaguchi and H. Yamamoto, *Anal. Chem.*, **1997**, 69, 1492.

[20] V. J. P. Gouveia, I. G. Gutz and J. C. Rubin, *J. Electroanal. Chem.*, **1994**, 371, 37.

[21] C. Rodger, W. E. Smith, G. Dent and M. Edmondson, *J. Chem. Soc., Dalton Trans.*, **1996**, 791.

[22] R. K. Chang and B. L. Laube, in *CRC Critical Reviews in Solid State and Material Sciences*, **1984**, 12, 1.

[23] R. L. Birke and J. R. Lombardi, in *Spectroelectrochemistry - Theory and Practice*, R. J. Gale, ed., Plenum, New York, **1988**, Ch. 6, p. 263.

[24] R. K. Chang, in *Spectroscopic and Diffraction Techniques in Interfacial Electrochemistry - NATO ASI Series. Serie C, no. 320, C.*, Gutierrez and C. Melendres eds., Kluwer, Boston, **1990**, p.155.

[25] R. L. Birke, T. Lu and J. R. Lombardi, in *Techniques for Characterization of Electrodes and Electrochemical Processes*, R. Varma and J. R. Selman, eds., Wiley, New York, **1991**, Ch. 5, p. 211.

[26] E. S. Brandt and T. M. Cotton, in *Physical Methods of Chemistry Volume IXB - Investigations of Surfaces and Interfaces - Part B*, B. W. Rossiter and R. C. Baetzold, eds., 2nd. edition, Wiley, New York, **1993**, Ch. 8, p. 633.

[27] W. Suetaka, *Methods of Surface Characterization - Surface Infrared and Raman Spectroscopy: Methods and Applications*, Plenum, New York, **1995**.

[28] J. E. Pemberton, in *Electrochemical Interfaces: Modern Techniques for in situ interface Characterization*, H.D. Abruna ed., VCH, New York, **1991**, Ch. 5, p. 193.

[29] B. Pettinger, in *Adsorption of Molecules at Metal Electrodes*, J. Lipkowski and P. N. Ross, eds., VCH, New York, **1992**, Ch. 6, p. 285.

[30] T. M. Cotton, in *Spectroscopy of Surfaces - Advances in Infrared and Raman Spectroscopy*, , R. J. Clark and R. E. Hester, eds., vol. 16, Wiley, New York, **1988**, p.91.

[31] R. L. Garrell, *Anal. Chem.*, **1989**, 61,401A.

[32] A. G. Brolo, B. D. Smith and D. E. Irish, *J. Mol. Struct.*, **1997**, 405, 29.

[33] A. D. Buckingham, *Adv. Chem. Phys.*, **1967**, 12, 107.

[34] A. Otto, I. Mrozek, H. Grabhorn and W. Akemann, *J. Phys. Condes. Matter*, **1992**, 4,1143.

[35] A. Otto, *J. Raman Spect.*, **1991**, 22, 743.

[36] M. Moskovits, *Rev. Mod. Phys.*, **1985**, 57, 783.

[37] M. Kerker, *Acc. Chem. Res.*, **1984**, 17, 271.

[38] E. J. Zeman and G. C. Schatz, *J. Phys. Chem.*, **1987**, 91, 634.

[39] M. Kerker, D.-S. Wang and H. Chew, *Appl. Opt.*, **1980**, 19, 4159.

[40] D.-S. Wang and M. Kerker, *Phys. Rev. B*, **1981**, 24, 1777.

[41] R. K. Chang and B. L. Laube, *CRC Crit. Rev. Solid State Mater. Sci.* **1984**, 12, 1.

[42] M. Xu and M. J. Dignam, *J. Chem. Phys.*, **1992**, 96, 7758.

[43] M. Xu and M. J. Dignam, *J. Chem. Phys.*, **1993**, 99, 2307.

[44] M. Xu and M. J. Dignam, *J. Chem. Phys.*, **1994**, 100, 197.

[45] F. J.Garcia-Vidal and J. B. Pendry, *Phys. Rev. Letters*, **1996**, 77, 1163.

[46] R. H. Clark and T. J. Dines, *Angew. Chem. Int. Ed. Engl.*, **1986**, 25, 131.

[47] A. G. Brolo and D. E. Irish, *J. Chem. Soc, Faraday Trans.*, **1997**, 93, 419.

[48] A. G. Brolo and D. E. Irish, *J. Electroanal. Chem.*, **1996**, 414, 183.

[49] R. Guidelli, in *Adsorption of Molecules at Metal Electrodes*, J. Lipkowski and P. N. Ross, eds., VCH, New York, Ch. 1, **1992**, p.1.

[50] J. R. Lombardi, R. L. Birke, T. Lu and J. Xu, *J. Chem. Phys.*, **1986**, 84, 4174.

[51] J. C. Rubin, P. Corio, M. C. C. Ribeiro and M. Matz, *J. Phys. Chem.*, **1995**, 99, 15765.

[52] R. Aroca and G. J. Kovacs, in *Vibrational Spectra and Structure*, J. R. Durig, ed., Elsevier, **1991**, 19, 55.

[53] D. A. Guzonas, D. E. Irish and G. F. Atkinson, *Langmuir*, **1990**, 6, 1102.

[54] J. Thietke, J. Billmann and A. Otto, in *Dynamics on Surfaces*, B. Pullman, J. Jortner, A. Nitzan and B. Gerber, eds., Reidel, Boston, **1984**, p. 345.

[55] J. C. Rubin, M. L. A. Temperini, P. Corio, O. Sala, A. H. Jubert, M. E. Chacon-Villalba and P. J. Aymonino, *J. Phys. Chem.*, **1995**, 99, 345.

[56] A. Kudelski and J. Bukowska, *Chem. Phys. Letters*, **1994**, 222, 555.

Chapter 3

Raman Spectral Studies of Aqueous Pyrazine and its Protonated Forms

3. Raman Studies of Pyrazine and its Protonated Forms

3.1. Introduction

This study of the vibrational spectra of pyrazine and its protonated forms has been motivated by our interest in the surface enhanced Raman scattering (SERS) of pyrazine adsorbed on gold electrodes [1]. Some thermodynamic properties of this system, such as the Gibbs free energy of adsorption, the Gibbs surface excess, and the electrosorption valence, have been measured in our Centre [2] using electrochemical techniques. A goal of this work is to extend the understanding of the relationship between the SERS intensity and surface coverage and orientation at a given potential. An extensive study of this matter, involving the adsorption of pyridine on a gold electrode was conducted in our laboratory [3, 4]. In that work it was demonstrated that SERS intensity is directly proportional to surface coverage to about 60% of a monolayer for "unroughened" electrodes. In preliminary studies of pyrazine, no spectra were obtained from "unroughened" electrodes; following one oxidation reduction cycle, enhanced intensity from pyrazine was observed [1]. A band at ~ 1220 cm^{-1} was significantly enhanced, as reported by Erdheim et al.. [5], but this band was **not** assigned by them ! Progress in understanding SERS is dependent on knowledge of the origin of all pyrazine bands.

Pyrazine is a non-polar, planar molecule with D_{2h} symmetry. Dornhaus et al. [6]. suggested that the selection rules for symmetry D_{2h} break down at the electrode surface; C_{2v} symmetry would result from the removal of the inversion operation. Such symmetry lowering, if true, makes this system very attractive for the study of selection rules at surfaces [7, 8].

On the other hand, this simplistic interpretation (symmetry lowering) has been contested by Moskovits et al. [9]. They suggested that the observed small shifts of bands of adsorbed pyrazine, compared to the spectrum of liquid pyrazine, are not compatible with a pyrazine-surface complex strong enough to justify the symmetry lowering. They showed that the presence of forbidden bands can be explained based on electromagnetic considerations. Face-on, end-on, or edge-on orientations are possible for pyrazine adsorbed to a metal surface. For cold deposited silver films, it was suggested that the molecules lie flat at low coverage and stand up as the surface concentration increases [9]. From the calculated bond polarizabilities an end-on configuration [10] is predictable on a silver electrode. The same result (pyrazine molecules perpendicular to the electrode surface) was observed in our Centre by A. Ianneli at high coverage on positively charged gold electrodes [2].

The assignment of the new bands that appear in the spectrum of pyrazine at the electrode surface is a very important step. One can attempt to lower the symmetry of pyrazine in solution and compare the new bands to those from adsorbed pyrazine. In order to break down the symmetry of pyrazine in aqueous solution the molecule can be protonated. However, pyrazine is a very weak base [11] (pK_{a1} = 0.65 and pK_{a2} = -5.8) and protonation can be accomplished only in a very acidic medium.

Therefore, to place the interpretation of SERS on a firm basis, there is a need to understand the vibrational spectrum of pyrazine and its protonated forms in solution. Raman and IR spectra of pyrazinium halides were reported by Foglizzo and Novak [12]. The diprotonated pyrazine spectrum has not been reported before. The new features from the protonated pyrazine will be related to the spectrum from the surface adsorbed species. It is evident that the SERS from pyrazine adsorbed on Ag and Au electrodes deserves further investigation in order to clarify fundamental questions, such as orientation,

coverage, and predominant enhancement mechanisms. Furthermore, it is surprising to note that, when compared to pyridine, little work has been done so far on the SERS from pyrazine on gold electrodes.

Preliminary results of this spectral study of pyrazine and its protonated form were presented at the XIVth ICORS conference [13], and the data and discussion presented in this chapter have been published [14]. A brief background about the pyrazine acidity and its vibrational spectrum will be presented in the next sections. This information will help the reader to understand the data treatment presented in the Results and Discussion section.

3.1.1. Acidity of Pyrazine

The effect of the introduction of another nitrogen atom in the pyridine ring is a considerable decrease in the basicity from its original value (pK_a = 5.2). The major contribution for this decrease is from an inductive effect (*-I*). The inductive effect is invoked to explain the effect of substituents on the acidity of an organic compound. The substituents can be either acid-weakening (*+I*) or acid-strengthening (*-I*). The second nitrogen in the heteroaromatic is roughly equivalent, in terms of inductive effect, to a nitro group attached in the same site in the benzene ring. The *-I* effect, however, cannot fully explain the increase of the pK_a (and consequently increase in the basicity) on the series: pyrazine (nitrogens in 1,4 positions) < pyrimidine (nitrogens in 1,3 positions) < pyridazine (nitrogen in 1,2 positions) [15].

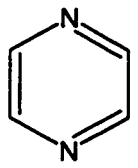

pyrazine

nitrogens in 1,4 positions

$pK_{a1} = 0.65$

<

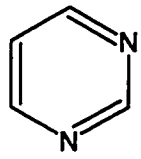

pyrimidine

nitrogens in 1,3 positions

$pK_{a1} = 1.23$

<

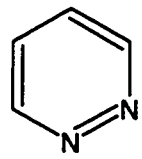

pyridazine

nitrogens in 1,2 positions

$pK_{a1} = 5.25$

It is also clear that the inductive effect alone cannot explain the unusually high basicity exhibited by pyridazine. This is an indication that a mesomeric effect (*-m*) also plays some role in the low basicity of mononuclear diazoaromatic compounds. The mesomeric effect ($\pm$ *m*) arises from the π electron delocalization (resonance).

Therefore, pyrazine is the weakest base in this diazoaromatic series, and to study the protonation of pyrazine one has to work in a medium for which the acidity cannot be expressed by a simple scale.

The acidity of dilute solutions is generally expressed in the pH scale. The pH is defined as the negative common logarithm of the hydrogen ion activity [16]. For low concentration solutions, the activity of hydrogen ions is roughly equal to the molar concentration. Hence, a $1x10^{-4}$ M solution of HCl has a pH equals to 4. However, a 10 M solution of HCl is much more acidic than expected from the pH scale (the expected pH for this solution would be -1) [17]. Concentrated acidic solutions are non-ideal, and the activity of hydrogen ions (the tendency of these solutions to protonate an organic base) is higher than expected from the simple concentration values. New scales must be used to express the acidity of aqueous concentrated acid solutions. The most common of these

acidity functions is the one introduced by Hammett and Deyrup [18] and called the *Hammett acidity function.*

Consider the deprotonation equilibrium of a weak base, given below:

$$HB^+ \overset{K_a}{\rightleftharpoons} H^+ + B \qquad (1)$$

The equilibrium constant K_a, considering ideal (diluted) solutions, is given by:

$$K_a = \frac{[H^+][B]}{[HB^+]} \qquad (2)$$

Taking the negative of the logarithm of both sides of equation (2) above yields:

$$pK_a = pH - \log\left(\frac{[B]}{[HB^+]}\right) \qquad (3)$$

However, for a base in concentrated acid (non-ideal solution), the concentrations have to be replaced by activities, and equation (3) becomes:

$$pK_a = -\log(a_{H^+}) - \log\left(\frac{a_B}{a_{HB^+}}\right) \qquad (4)$$

The activity of a substance X is related to the concentration by:

$$a_x = \gamma_x [X] \tag{5}$$

where γ_X is the activity coefficient of the species X. Therefore, equation (**5**) can be substituted into equation (**4**) yielding:

$$pK_a = -\log[H^+] - \log\left(\frac{\gamma_{H^+}\gamma_B}{\gamma_{HB^+}}\right) - \log\left(\frac{[B]}{[HB^+]}\right) \tag{6}$$

The difficulty of determining the activity coefficients is the major experimental limitation. However, the Hammett acidity function can be defined as [19]:

$$H_0 = -\log[H^+] - \log\left(\frac{\gamma_{H^+}\gamma_B}{\gamma_{HB^+}}\right) = pK_a + \log\left(\frac{[B]}{[HB^+]}\right) \tag{7}$$

Therefore, if the ratio of the amount of non-protonated to protonated "standard" base (indicator or "anchor" compound), with known equilibrium constant value, can be determined by spectroscopy, the value of H_0 can be calculated for different amounts of acid in the solution. Figure 3.1 shows the plot of the Hammett acidity function for several concentrations of HCl [20] and H_2SO_4 [21]. The H_0 is the simplest acidity function and it has several limitations. For instance, this scale is only accurate for nitro-substituted primary amines [22]. Other acidity functions are available [23]. These are derived either using different classes of "anchor" compounds or using different techniques

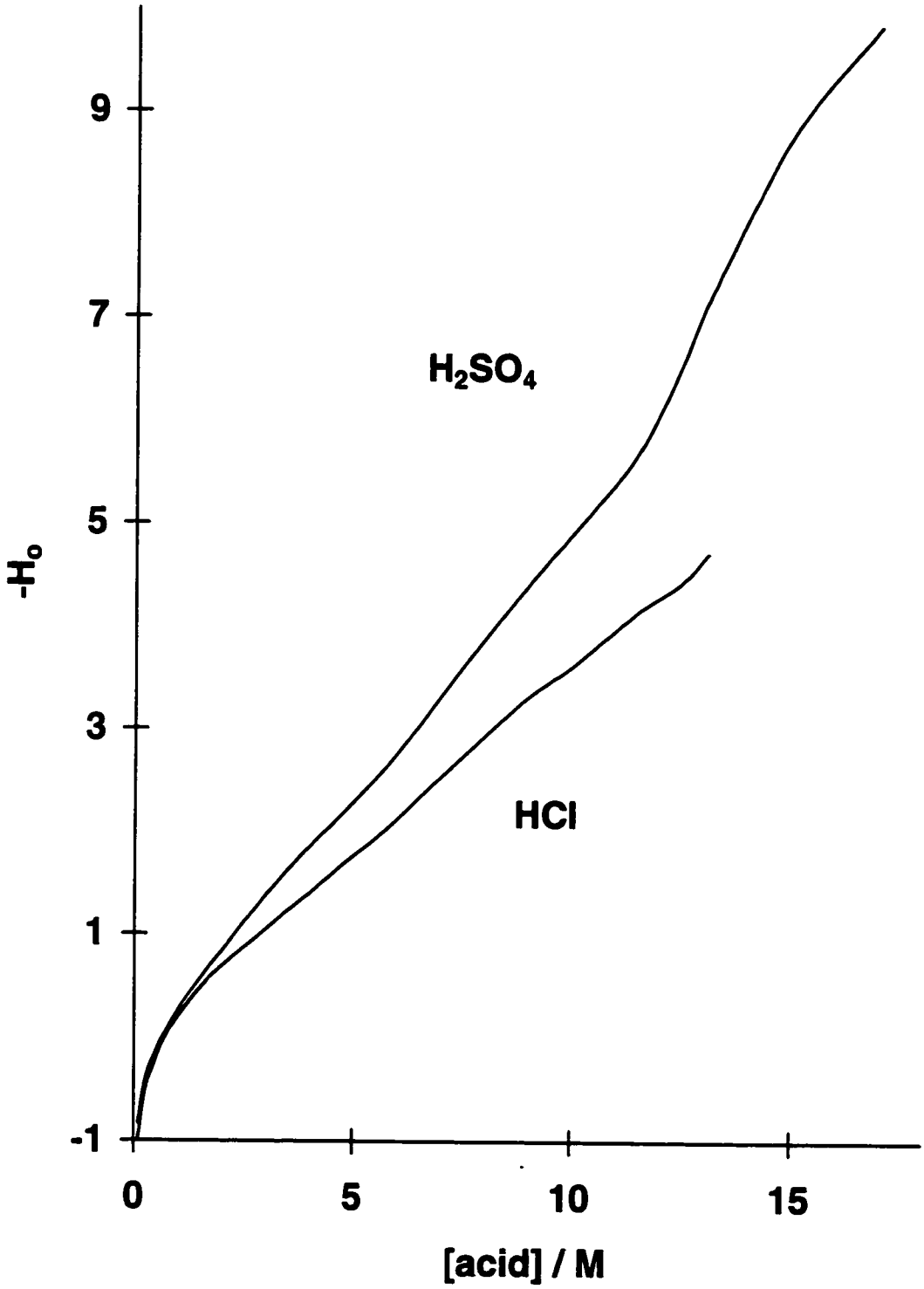

Figure 3.1: Hammett acidity function H_0 for aqueous H_2SO_4 and HCl.

to determine the concentration ratio between the non-protonated and protonated base [24].

Figure 3.2 shows the calculated fractional composition of the pyrazine species using the pK_a values given above [11]. The acidity function [24] (H_0) was used to replace the simple pH function for high acidic concentrations.

3.1.2. Vibrational Analysis

Symmetry analysis leads to the following vibrational representation for free pyrazine with D_{2h} symmetry (with the molecule lying in the xz plane; and the z axis containing both nitrogens - Figure 3.3a):

$$\Gamma^{vib} = 5A_g + 1B_{1g} + 4B_{2g} + 2B_{3g} + 2A_u + 4B_{1u} + 2B_{2u} + 4B_{3u} \quad (8)$$

The Raman selection rules for a centrosymmetric molecule establish that only the normal modes symmetrical to the molecular center of inversion have allowed transitions. Therefore, only the "g" species are Raman active. Moreover, the character table for D_{2h} symmetry indicates that all "g" modes transform as one or more components of the polarizability. On the other hand, the A_u modes do not contain any dipole moment component; hence, these modes are expected to be silent in the IR spectrum.

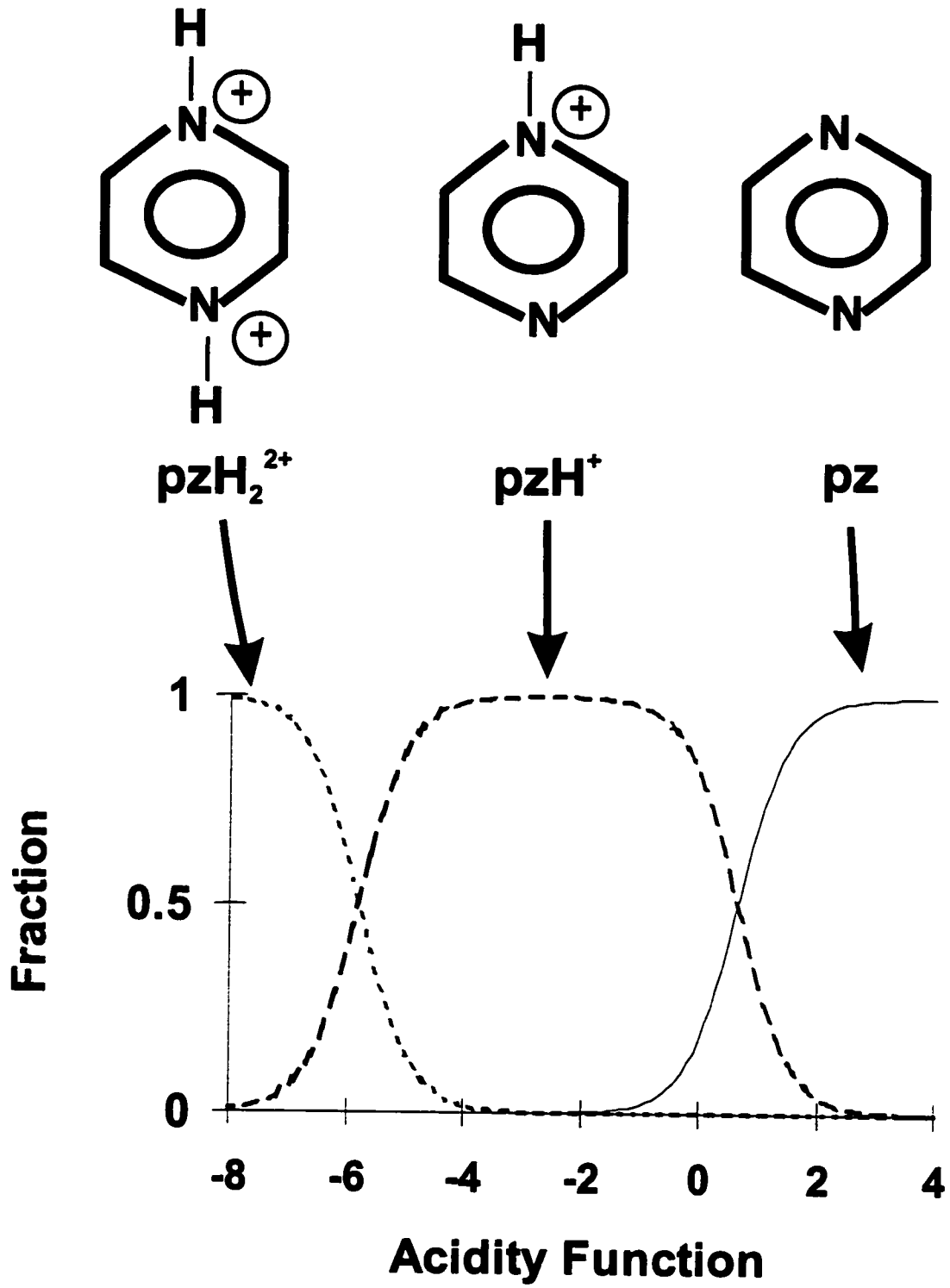

Figure 3.2: Calculated fractional distribution of 1 M pyrazine (pz) species in solutions of varying acidity.

For monoprotonated pyrazine (C_{2v} symmetry), the vibrational modes span:

$$\Gamma^{vib} = 10A_1 + 3A_2 + 9B_1 + 5B_2 \qquad (9)$$

In this case, all modes are Raman allowed. Therefore, the number of bands in the Raman spectrum should change from 12 to 27 with protonation. The A_2 modes are not allowed in the IR for this symmetry.

For a diprotonated pyrazine (D_{2h}), we have:

$$\Gamma^{vib} = 6A_g + 1B_{1g} + 5B_{2g} + 3B_{3g} + 2A_u + 5B_{1u} + 3B_{2u} + 5B_{3u} \qquad (10)$$

The centre of symmetry is regenerated and the exclusion rule for active modes in Raman and IR is valid again. Hence, 15 bands are expected in the Raman spectrum. The correlation table between D_{2h} and C_{2v} symmetries is given in Figure 3.3b. The symmetries of modes generated by protonation are also given.

a)

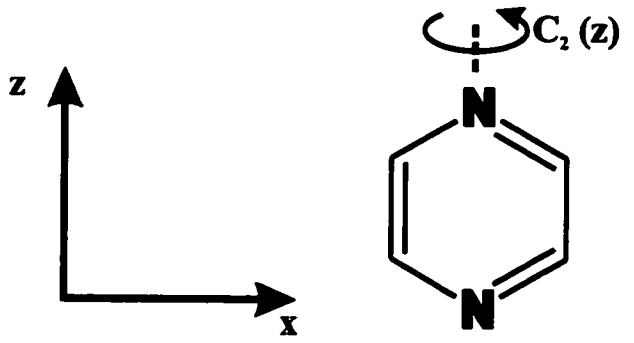

b)

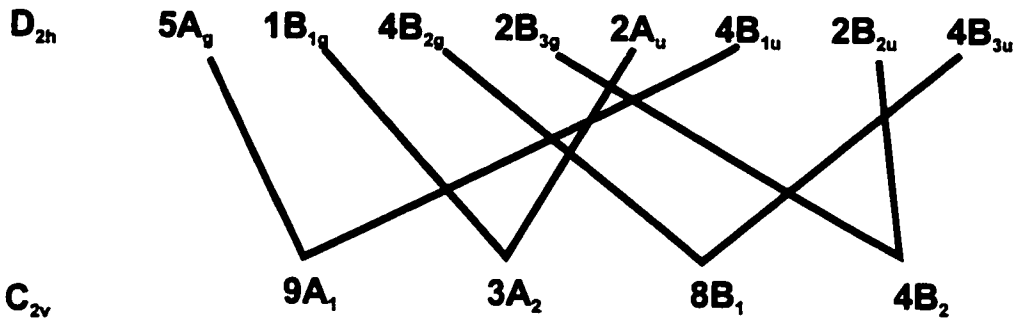

PzH^+ additional modes = $1A_1 + 1B_1 + 1B_2$

PzH_2^{2+} additional modes = $1A_g + 1B_{2g} + 1B_{3g} + 1B_{1u} + 1B_{2u} + 1B_{3u}$

Figure 3.3: a) Definition of the Cartesian frame for pyrazine, used in the calculation of the vibrational representations. b) Correlation Table Between D_{2h} and C_{2v} symmetries, with reference to pz and its protonated forms.

3.2. Experimental

Raman spectra were measured with a Jarrell-Ash 25-100 spectrometer (1-m double Czerny-Turner monochromator) with an RCA 31034 photomultiplier tube and an SSR Model 1105/1120 photon counting system. Spectra were excited by the 514.5 nm (1.5 W at the head) line of a Coherent Innova 300 argon ion laser. For data acquisition the spectrometer is interfaced to an IBM PC-AT 286 computer. The acquisition time was 1 second, and two accumulations were performed for each experimental point. The spectra were treated with an IBM PC-AT 486 computer on which baseline correction, band-fitting, and plotting programs were available. Pyrazine 99+% from Aldrich, H_2SO_4 96% (d=1.84 g/mL) from BDH, HCl 37% (d=1.19 g/mL) from BDH and $HClO_4$ 71% (d=1.76 g/mL) from Baker were used. All solutions were prepared with Milli-Q water. The solutions were injected into capillary tubes and sealed. All spectra were recorded with the samples held at a controlled temperature of 25 ^oC.

3.3. Results and Discussion

3.3.1. Studies of Pyrazine in solution with several solvents

In order to obtain information about possible interactions between pyrazine and the solvent, spectra of aqueous solutions of pyrazine at several concentrations were measured. Some small shifts were observed, mainly in the 1500 cm^{-1} region (ν - ring modes), as shown in Figure 3.4. These shifts are surely related to a pz - water interaction. As the water concentration increases from liquid pz to 0.3M aqueous solution the B_{2g} and A_g

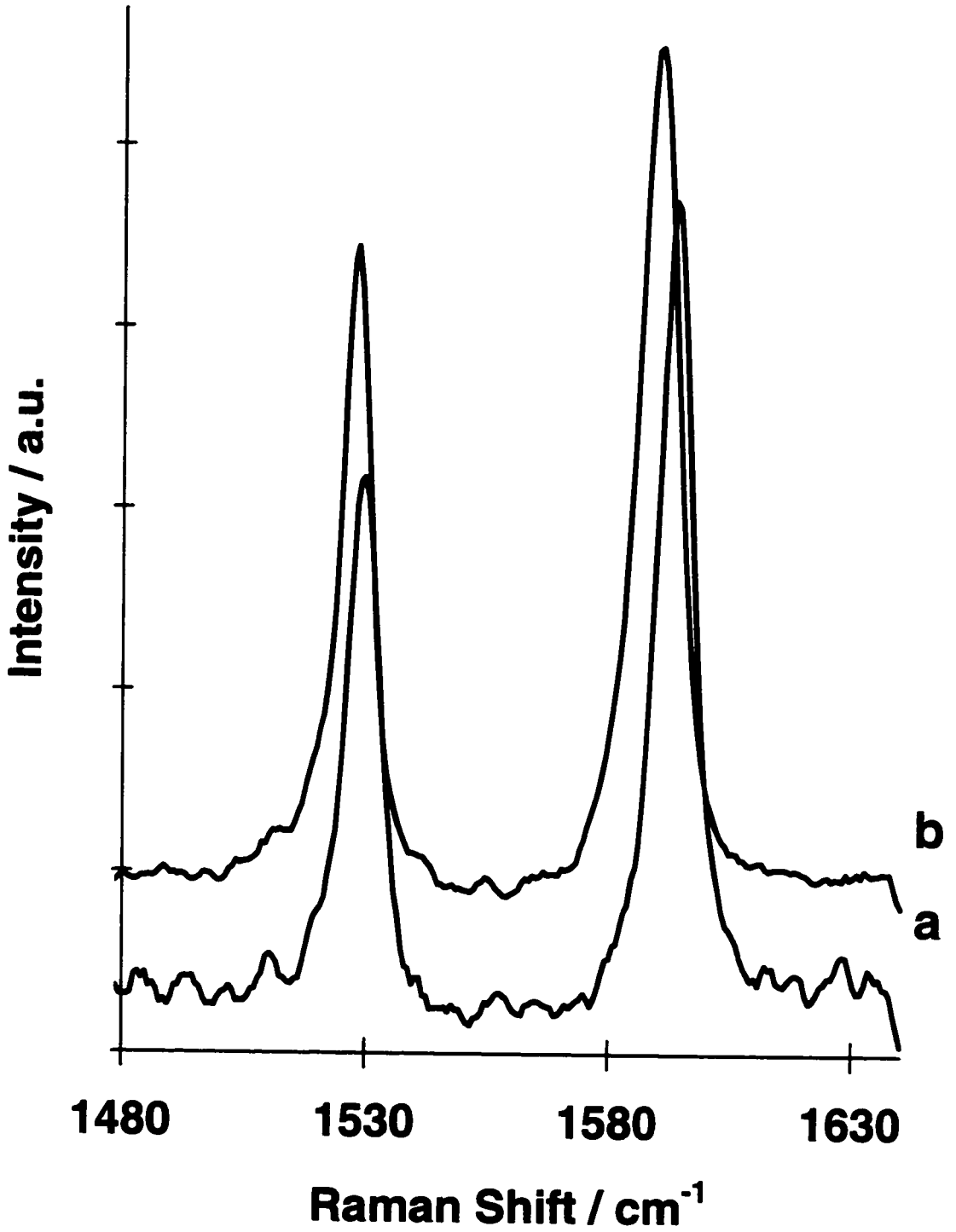

Figure 3.4: Raman spectra of two aqueous pz solutions in the 1480 - 1640 cm^{-1} region. a) [pz] = 0.3 M; b) [pz] = 5 M

Table 3.1: Vibrational wavenumbers (cm^{-1}) of liquid pyrazine, aqueous pyrazine at several concentrations, and 1M pyrazine in CCl_4.

pz liquid (from ref.25)	[pz] = 1M in CCl_4	[pz] = 5M in H_2O	[pz] = 0.3M in H_2O
602 (w)[a]	610 (w)	617 (w)	620 (w)
704 (s)	704 (m)	702 (m)	703 (m)
927 (w)	918 (w)	921 (w)	923 (w)
	1006 (sh)	1010 (sh)	1010 (sh)
1016(vs)	1014 (vs)	1018 (vs)	1020 (vs)
1208(m)	1201 (w)	1217 (sh)	1220 (sh)
1233(s)	1232 (m)	1237 (m)	1238 (m)
1346(w)	1345 (w)	1346 (w)	1349 (w)
1525(m)	1527 (m)	1528 (m)	1530 (m)
1580 (s)	1579 (m)	1591 (m)	1594 (m)
2820 (w)	2820 (w)		
2865 (w)	2865 (w)		
2883 (w)	2883 (w)		
2959 (w)	2960 (w)	2969 (w)	2972 (w)
3040 (sh)	3045 (sh)	3057 (sh)	3063 (sh)
3055 (s)	3058 (s)	3071 (s)	3077 (s)
3152 (vw)	3152 (w)		

[a] w - weak; m - medium; s - strong; v - very; sh - shoulder

ring vibrations rise in frequency (1525 and 1580 to 1530 and 1594 cm^{-1}, respectively). A summary for the most sensitive bands of these systems is given in Table 3.1.

Figures 3.5a and 3.5b, regions 1 to 2B, shows the spectra of pyrazine in water (H_2O), in heavy water (D_2O) and in carbon tetrachloride (CCl_4). Almost no peak shifts are observed when the spectra of pyrazine in water and in heavy water are compared. On the other hand, both are different from the spectrum of pz in CCl_4. The wavenumbers are in good agreement with the literature [25, 26, 27, 28, 29, 30, 31]. Some of these bands are summarized in Table 3.1, and compared to the liquid pyrazine spectrum reported previously [26]. The Wilson numbering scheme [32] is used to facilitate the identification of the main contributions to each vibrational mode. It is interesting to note, from Table 3.1 and Figures 3.5, that the shoulders in the aqueous pyrazine spectrum at around 1010, 1220, and 3060 cm^{-1} appear as very well resolved bands in the spectrum of pyrazine in CCl_4 at ~ 1006, 1202, and 3045 cm^{-1}, respectively. In addition, significant shifts occur for the bands of pyrazine in H_2O, compared to the bands of pyrazine in CCl_4. For instance, the bands of aqueous pyrazine at ~ 620, 921, 1019, 1237, 1590, 2970, and 3076 cm^{-1} shift to 610, 918, 1014, 1232, 1579, 2960, and 3058 cm^{-1} for pyrazine in CCl_4. Also, it is clear from Table 3.1, that the peak positions in the spectrum of pz in CCl_4 have more similarity to the spectrum of liquid pz.

Close examination of the spectra in Figure 3.5b, region 2B, reveals differences between the spectra of aqueous pyrazine and pyrazine in heavy water in the 1220 cm^{-1} region. The bandfitting program indicated two bands from the aqueous pz, coincident with two bands of pz in heavy water, at 1220 (sh) and 1237 cm^{-1}; however, in the spectrum of pz in heavy water, an additional band at 1200 cm^{-1} was found. This band arises from the

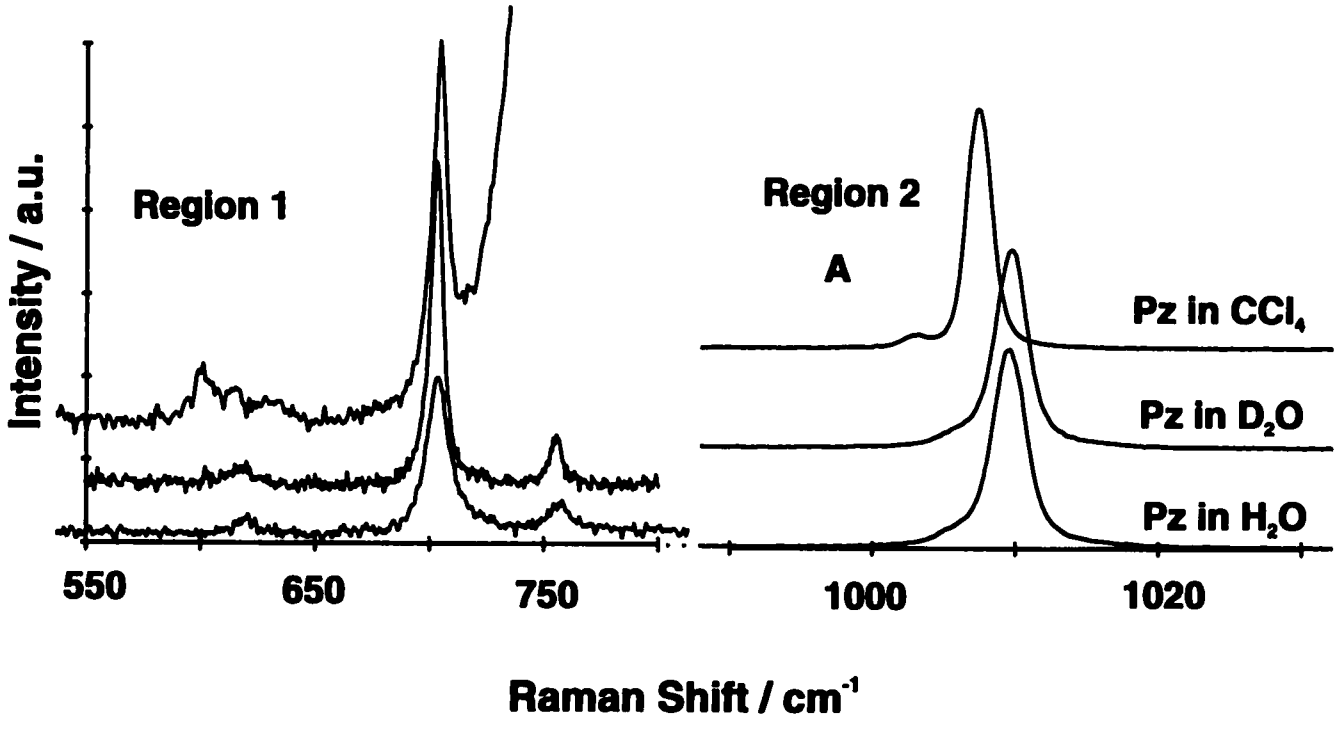

Figure 3.5a: Spectra of solutions of 1 M pz in three different solvents. Region 1: from 550 to 800 cm^{-1}; Region 2: from 990 to 1030 cm^{-1}.

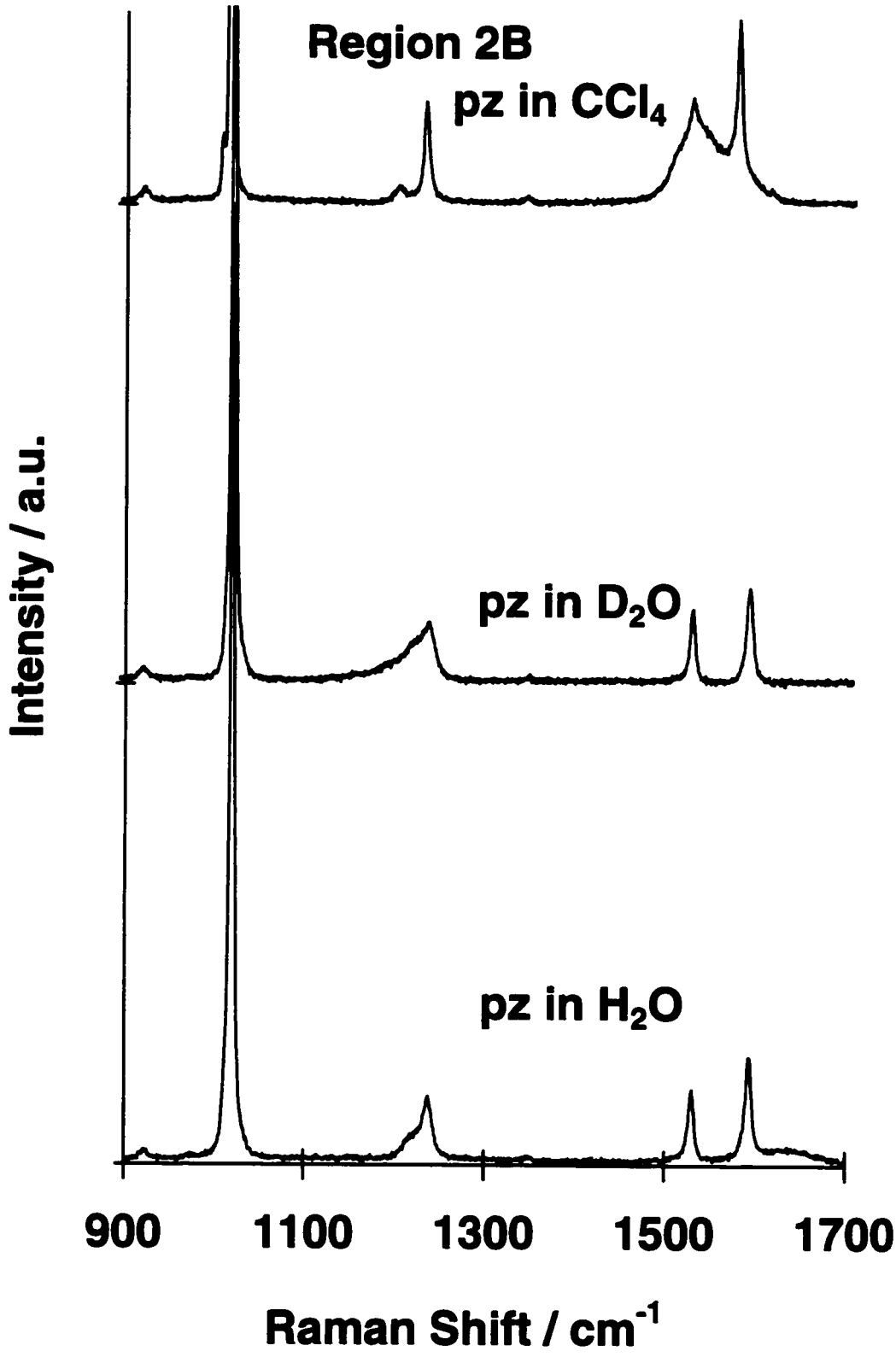

Figure 3.5b: Spectra of solutions of 1 M pz in three different solvents. Region 2B: from 900 to 1700 cm^{-1}.

bending mode of heavy water [33]. A curious background shows up under the 1527 cm^{-1} band in the spectrum of pz in CCl_4; it arises from a combination band of the solvent.

Pyrazine can interact with water by hydrogen bonding, either via the lone pairs of electrons of nitrogen or by the π cloud of the aromatic ring. The intermolecular pz interaction (present in liquid pz) and the interaction between pyrazine and CCl_4 have the same nature, and mainly can be attributed to London forces. The hydrogen bond interaction between pz and water is stronger than London forces causing broadening and band shifts that result in overlap. This can explain the better resolution in the spectrum of pyrazine in CCl_4. The absence of pz-water complexes in the pz/CCl_4 solutions leaves the pyrazine molecules more isolated, leading to sharper bands and, consequently, to better resolution. The band positions of pz in CCl_4 are similar to those of liquid pyrazine, due to the weaker intermolecular interactions, compared to aqueous pz solutions.

One can notice that the majority of the shifts in the spectrum of pyrazine in CCl_4 are to lower frequency, when compared to the spectrum of aqueous pyrazine. This can also be evidence of the presence of a pyrazine - solvent complex. The shift in the wavenumbers of the intramolecular vibrations induced by intermolecular forces have been reported for pyrazine crystal [34]. An overall broadening in the vibrational bands and a positive shift in the vibrational wavenumbers has been observed as the pressure (intermolecular forces) experienced by a pyrazine crystal was increased [34]. For an aqueous pyrazine complex the nature of the hydrogen bonding is similar for both water and heavy water, and thus small or no shifts are expected in their vibrational spectrum. However, when water is replaced by the inert solvent, CCl_4, significant shifts occur, mainly to lower wavenumbers. This trend is consistent with the stronger intermolecular interactions on the hydrogen bonded pyrazine molecules.

Another interesting point is the nature of the shoulder at 1225 cm^{-1} in the spectrum of aqueous pyrazine. As observed by Erdheim et al. [5], this band suffers a very significant enhancement when pz is on the electrode surface and its intensity becomes greater than that of the 1235 cm^{-1} band. Erdheim et al. [5] did not assign this band. We will delay the explanation for these two bands (1225 and 1235 cm^{-1}) which appear in the pz spectrum from the electrode surface until the next section. A survey of the pyrazine SERS studies [1, 5, 6, 9], shows that the bands at 615, 1020, 1220, 1235, 1590, and 3074 cm^{-1} are the predominant features. These same bands suffer the major shifts when the solvent is changed from CCl_4 to water. These coincidences suggest that the interaction of pyrazine with water and with the electrode surface occur via the same molecular site (e.g., the nitrogen lone pair of electrons).

3.3.2. Studies of pyrazine in aqueous HCl solutions

In Figure 3.6a-3.6c (regions 1 to 4) spectra of 1M pyrazine in several concentrations of aqueous HCl are presented. One can notice that practically all bands shift and new features show up in the spectrum as the HCl concentration increases.

At pH values higher than 1.5 the predominant species in solution are the aquated pyrazine molecules (accurately, a pyrazine - water complex, as shown in the section above). When the pH is around 0.5 the spectrum includes bands due to both pz and pzH^+. At HCl concentrations greater than 5.4 M, the aquated pzH^+ is the only species present in the solution. Therefore, it is possible to identify and assign specific bands related to each species. These new bands can be related to bands that appear on the electrode surface.

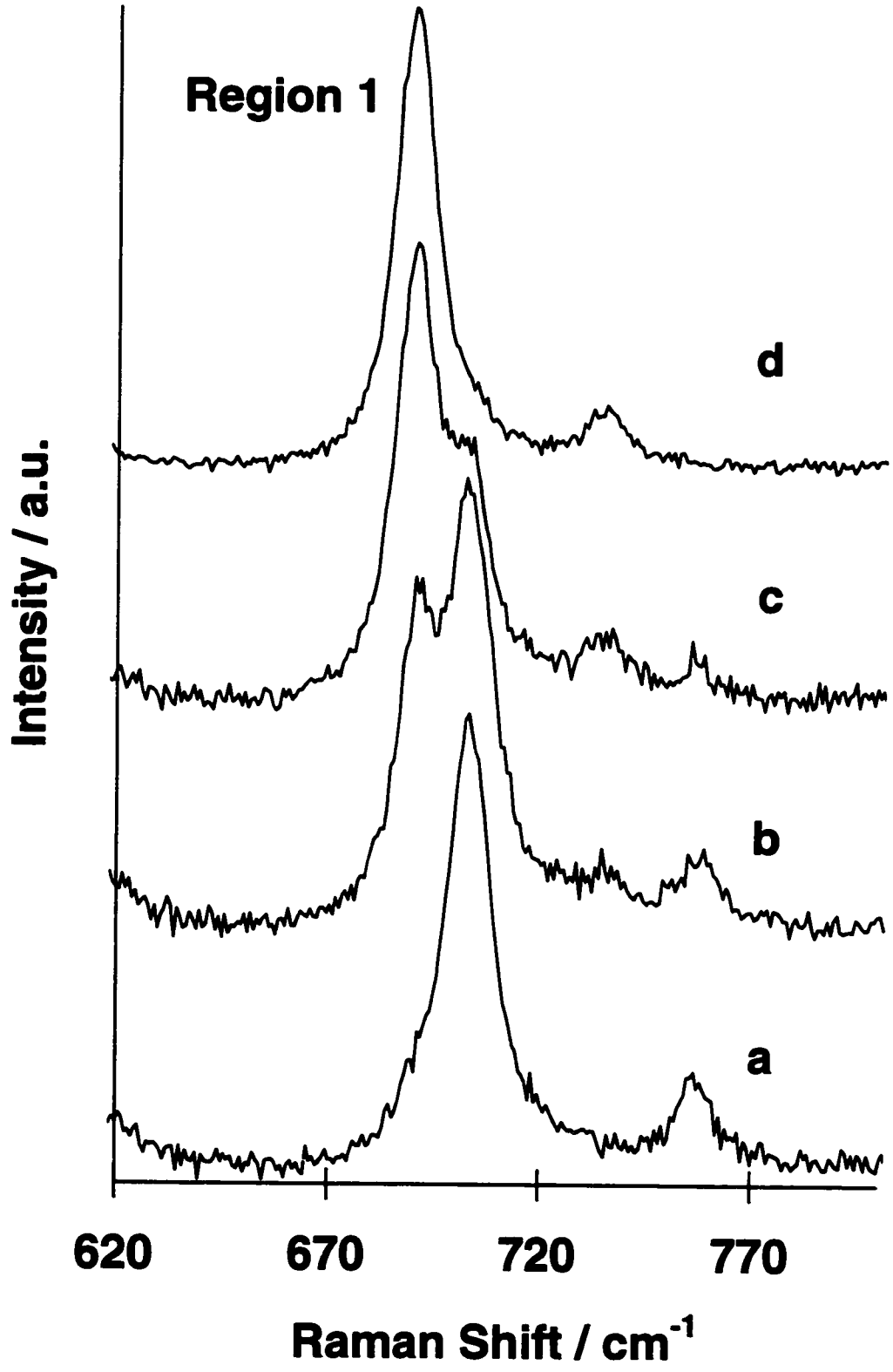

Figure 3.6a: Spectra of solutions of 1 M pz in HCl. Region 1: from 620 to 800 cm^{-1}. a) pH = 1.5; b) pH = 1.0; c) pH = 0.5; d) [HCl] = 2.7 M.

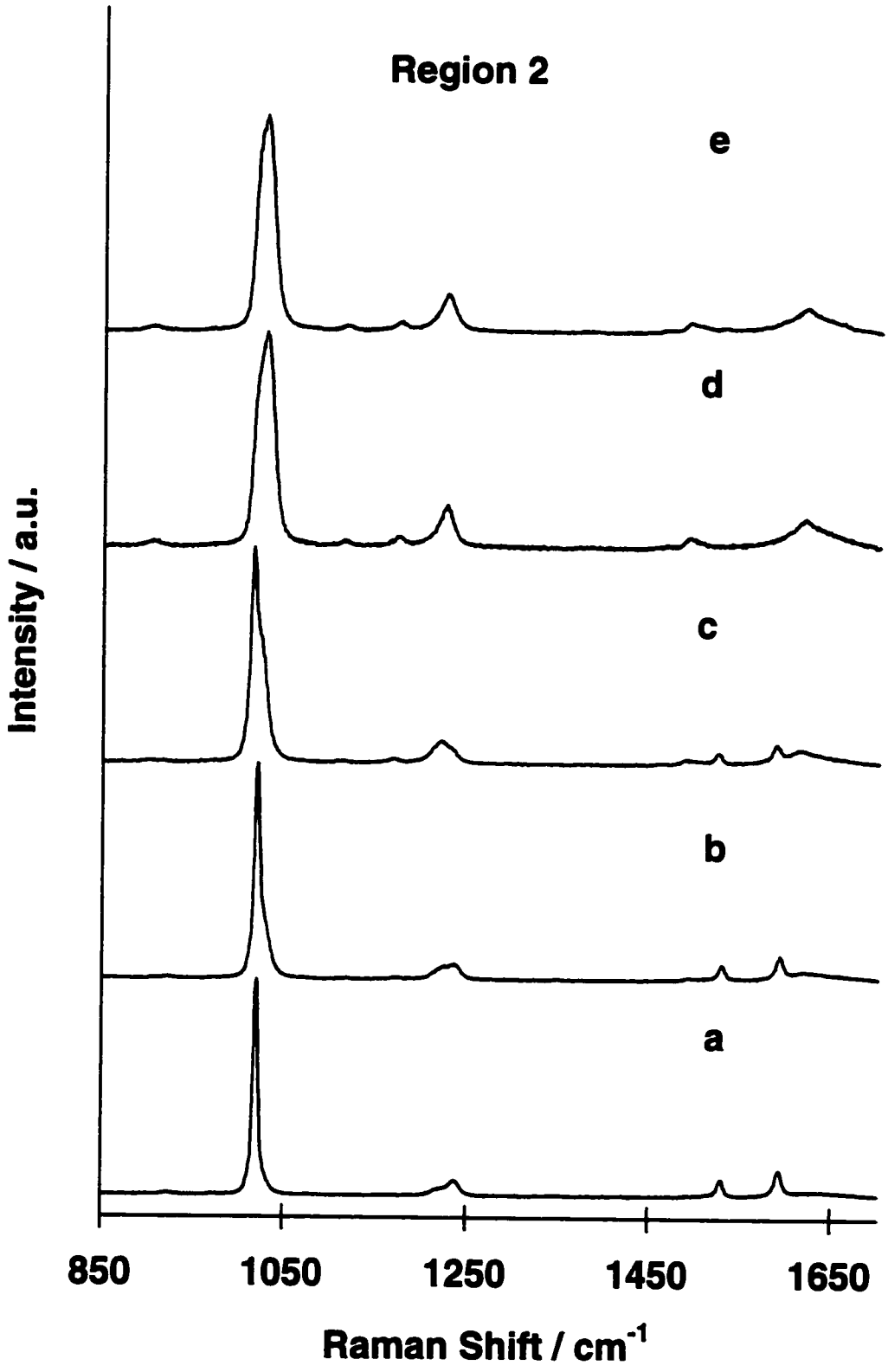

Figure 3.6b: Spectra of solutions of 1 M pz in HCl. Region 2: from 850 to 1700 cm^{-1}. a) pH = 1.5; b) pH = 1.0; c) pH = 0.5; d) [HCl] = 1.3 M; e) [HCl] = 2.7 M.

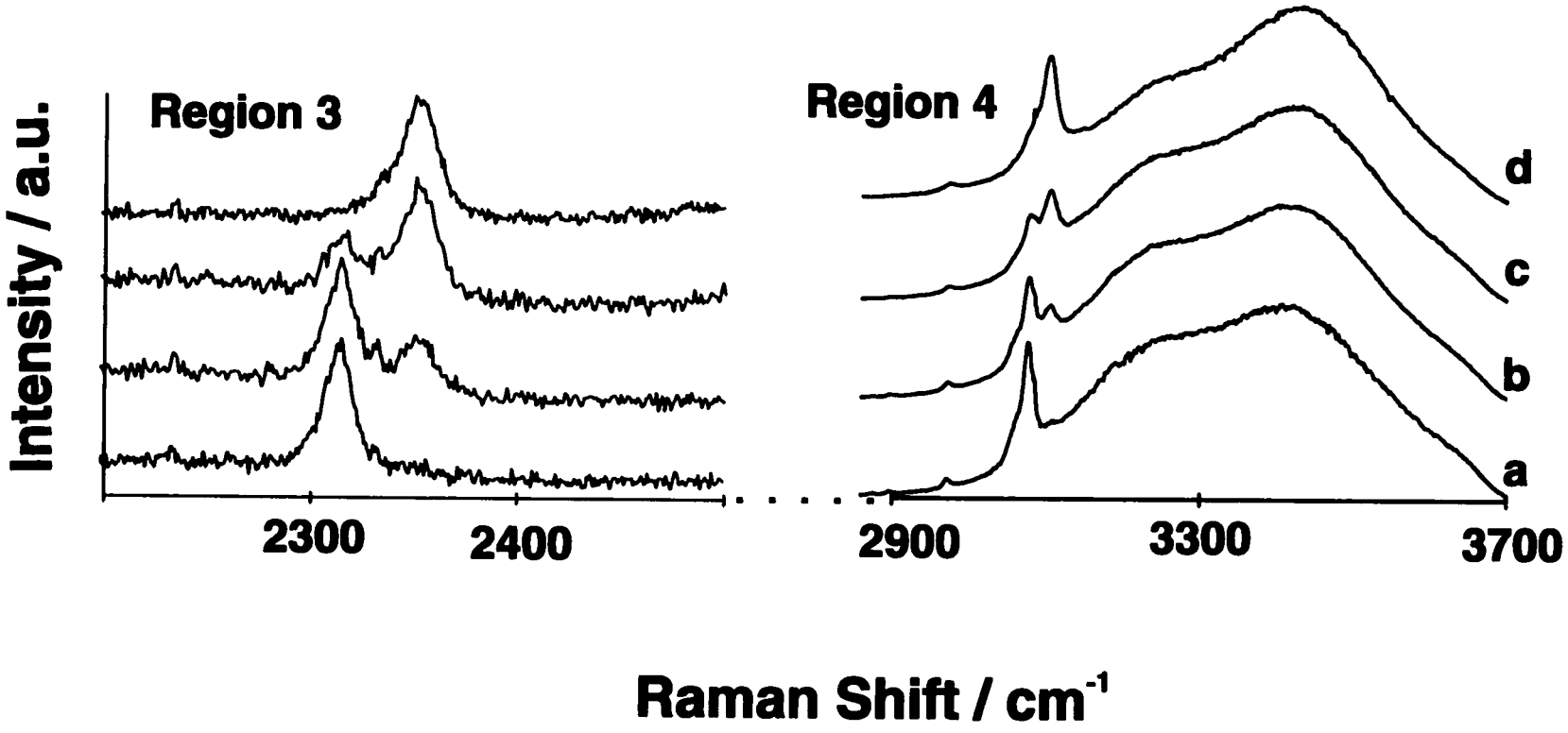

Figure 3.6c: Spectra of solutions of 1 M pz in several HCl concentrations (different acidity). Region 3: from 2200 to 2500 cm^{-1}. Region 4: from 2900 to 3700 cm^{-1}. a) pH=1.5; b) pH=1.0; c) pH=0.5; d) [HCl]=2.7 M.

Table 3.2: Vibrational wavenumbers (cm^{-1}) for 1M pyrazine in aqueous HCl solutions[a]: Comparision to the literature and assignments[b].

This work [14]						Literature[c]				
Assign. for pz	pH=4	pH=1.1	pH=0.5	[HCl]=8.1M	Assign. for pzH^+	solution [9]	SERS [9]	liquid [29]	solution [26]	solution [25]
		606 w	605 w	606 w (p)	A1 (6a) δ ring	600 vw	615 m	596	602	602
A_g (6a) δ ring	620 w (p)	617 w						641		
		691 m	690 m	688 m (dp)	B1 (6b) δ ring					
B_{2g} (6b) δ ring	702 m (dp)	702 m	702 sh			699 m	700 w	703	704	704
		735 w	735 w	732 w (dp)	B2 (4) γ ring					
B_{3g} (4) γ ring	758 w (dp)	757 w	754 vw			756 w	753 w	757	756	754
B_{2u} (11) γ CH						(785)	792 m	(804)	(785)	(784)
		906 vw	911 w	898 w (dp)	A2 (10a) γ CH					
B_{1g} (10a) γ CH	922 w (dp)	921 w				(927)	922 w	919	927	
	973 vw	973 vw		970 vw	B2 (5) γ CH	(960)	972 w			975
B_{3g} (5) γ CH						(983)			983	997
A_g (1) ν ring	1019 vs (p)	1019 vs	1020 vs	1020 sh (p)	A1 (1) ν ring	1015 s	1015 s	1015	1016	1014
B_{1u} (12) δ ring			1031 sh	1031 vs (p)	A1 (12) δ ring	(1018)	1031 w	(1021)	(1018)	(1018)
B_{3u} (15) δ CH						(1063)	1088 m	(1063)	(1063)	(1061)
		1119 w	1117 w	1112 w (p)	A1 (18a) δ CH			1118		
B_{1u} (18a) δ CH						(1130)		(1135)	(1130)	(1130)
B_{3u} (14) ν ring		1172 w	1175 w	1173 w (dp)	B1(14) ν ring				(1149)	(1150)
A_g (11+16b)	1218 sh (p)									
		1225 m	1226 m	1223 m (p)	A1 (9a) δ CH					
A_g (9a) δ CH	1238 m (p)	1235 m	1235 sh			1239	1233 m	1230	1233	1248
B_{2g} (3) δ CH	1348 vw	1347 vw				(1347)	1347 w	(1346)	1346	
				1372 vw	B1(3) δ CH	(1360)	1360 w			1358
B_{3u} (19b) ν ring						(1411)	1410 m	(1418)	(1411)	(1411)
				1464 vw	B1 (19b) ν ring					
B_{1u} (19a) ν ring		1498 vw	1495 w	1488 w (dp)	A1 (19a) ν ring	(1483)	1484 m	(1484)	(1483)	(1482)
B_{2g} (8b) ν ring	1530m (dp)	1530 m	1528 w			1524	1522 m	1524	1525	1521
A_g (8a) ν ring	1593 m (p)	1594 m	1594 m	1594 m	B1 (8b) ν ring	1583	1578 s	1578	1580	1581
A_g (1+6a)		1618 w	1619 m	1618 m (p)	A1 (8a) ν ring				1615	
	2312 m (p)	2314 m	2317 w						2304	
A_g (2x14)		2350 w	2350 m	2346 m (p)	A1					
A_g (2x19a)	2970 w (p)	2970 w	2970 w	2962 w	A1				2955	
B_{1u} (13) ν CH						(3012)			(3012)	(3011)
						(3013)				
B_{2g} (7a) ν CH	3061 sh					(3040)		3041	3040	3030
A_g (2) ν CH	3077 s (p)	3077s	3079 m	3080 sh	B1 (7a) ν CH	3055 s	3055 w	3054	3055	3046
		3105 m	3103 s	3092 s (p)	A1 (2) ν CH			(3066)	3063	(3061)

[a] Intensities - see Table 1; p - polarized; dp - depolarized.
[b] Assignments are made with consideration of references [9], [12] and [25-31]; the Wilson numbering scheme [32] is presented in parenthesis following the species symbol.
[c] Values in parenthesis are calculated or IR.

These results are summarized in Table 3.2; the modes are numbered according to the Wilson scheme [32].

Using computer bandfitting techniques two bands were isolated under the envelope around 1025 cm^{-1} in the pzH^+ spectrum. One band is at 1020 cm^{-1} and is due to the symmetrical ring breathing mode. The other one is located at 1030 cm^{-1} and is assigned to a ring deformation mode; both are A_1 modes. Although this 1030 cm^{-1} band is strong for aqueous solutions, it is a very weak band from the electrode surface [1, 5-10].

The shoulder in the aquated pz spectrum at 1220 cm^{-1} disappears and the band at 1235 shifts to the 1225 cm^{-1} position as the solution becomes more acidic. The new 1225 cm^{-1} band can be assigned to a symmetrical CH bending (A_1-9a).

A relatively intense band was always observed in the SERS spectrum of pyrazine due to this 9a mode [1, 5, 6, 9]. This band was detected by both Moskovits et al. [9], at 1233 cm^{-1} in the pz spectrum from silver in UHV, and Dornhaus et al. [6], at 1242 cm^{-1} in the pz spectrum from a silver electrode in KCl aqueous solution. However, Erdeheim et al. [5] reported two bands in the SERS spectrum of pz from a silver electrode in that region, one at 1220 and another at 1237 cm^{-1}. The same two bands were also observed in our laboratory in a preliminary study of the pz spectrum from gold electrodes [1], one at 1213 and another at 1233 cm^{-1}. In both cases, the former band was stronger than the latter. Assuming that the SERS spectrum of pz should be similar to the spectrum of monoprotonated pz (considering the simplistic argument that both monoprotonated pzH^+ and pz adsorbed at the electrode surface have the same symmetry - C_{2v}), one would expect just one band in the SERS spectrum in that region at ~ 1225 cm^{-1} (small shifts are expected when a species in solution is adsorbed at a surface). In order to explain these two bands in the spectrum from the electrode surface, one must look back and analyze this

region in the spectrum of aquated pz. In the latter case, two bands were observed: a shoulder at ~ 1220 cm^{-1} and a medium intensity band at ~ 1230 cm^{-1}. All authors [26-30] agree that the assignment of the ~ 1230 cm^{-1} band is to the fundamental 9a mode. Sbrana et al. [29] assigned the 1201 cm^{-1} band of pz in CCl_4 (recall that the 1220 cm^{-1} aquated pz band shifts when the solvent is changed to CCl_4 - see Table 3.1) to an overtone of the 6a ring deformation mode at 600 cm^{-1}(δ ring). Despite the fact that this assignment is suitable to explain the 1208 cm^{-1} band of liquid pz, Zarembowitch et al. [25] chose an alternative possibility; they assigned that band to the combination B_{2u} (11 γ CH 785 cm^{-1}) $\otimes$ B_{2u} (16b ring 418 cm^{-1}) = A_g 1203 cm^{-1}. This latter assignment was supported by Arenas et al. [26] from the study of the spectrum of d_4-pz.

However, from Tables 3.1 and 3.2, it should be noted that the A_g 6a (δ ring) mode of pyrazine in aqueous solution occurs at ~ 618 cm^{-1}. This band would give an overtone of A_g symmetry at 1236 cm^{-1}, which is very close to the fundamental A_g at 1235 cm^{-1} (9a - δ CH). These coincidences suggest a Fermi resonance involving the 9a fundamental mode and a combination with A_g symmetry. Fermi resonance occurs when two modes of the same symmetry are accidentally degenerate. The result is usually a doublet, in which the bands share their energy and intensity [35]. Both modes 11 and 16b were observed in the pzH^+ spectra as weak bands [12] at 780 and 418 cm^{-1}, respectively. The fundamental 6a shifts down to 605 cm^{-1} in the aquated monoprotonated pz spectrum. These shifts of the fundamentals bands could be enough to take the combination out of the resonance condition. This could explain only one band at 1225 cm^{-1} in the aquated pyrazinium spectrum. This hypothesis is supported by the higher intensity of the 1225 cm^{-1} pzH^+ band when compared to the 1235 cm^{-1} band from "free" aqueous pyrazine (see Figure 3.6, region 2). At the electrode, the surface perturbation might be enough to provoke shifts in the wavenumbers of the fundamental modes that put these in Fermi resonance again. Changes in Fermi resonance conditions due to shifts induced by the surface have been

invoked previously [36]. The 6a vibrational mode was reported at 636 cm^{-1} by both Erdheim et al. [5] and us [1] when pz is adsorbed on a metallic surface. It would give an overtone at ~ 1272 cm^{-1}. On the other hand, for pz at the electrode surface, the 11 and 16b modes show up at 800 and 440 cm^{-1}, which would give an overtone at 1240 cm^{-1}. Hence, we suggest that the band of pz at the electrode surface at ~ of 1235 cm^{-1} can be assigned as the combination 11+16b.

The 2312 cm^{-1} band in the pz spectra shifts to 2350 cm^{-1} for pzH^+. While no fundamental vibrations of pz are expected in this region, we follow Arenas et al. [26] and assign these bands as an overtone from the ν_{14} (B_{3u}) mode which appears at ~ 1148 cm^{-1} in the liquid pz and at ~ 1175 cm^{-1} in the aquated pyrazinium spectrum.

The 702 cm^{-1} band in the pz spectrum (symmetrical ring deformation) shifts to 690 cm^{-1} in the pzH^+ spectrum. Using a band fitting program, it was possible to isolate each band for a mixture of both species. Figure 3.7 shows an example of this procedure. The 702 cm^{-1} band intensity (I_{702}) is proportional to the amount of pz in solution and the 690 cm^{-1} band intensity (I_{690}) is proportional to the amount of pzH^+ in solution. Therefore, the fractional amount of both pz and pzH^+ is given by the expressions:

$$I_{702} \propto [pz] \tag{11}$$

$$I_{690} \propto [pzH^+] \tag{12}$$

so,

$$X_{pz} \propto \frac{I_{702}}{I_{702} + I_{690}} \tag{13}$$

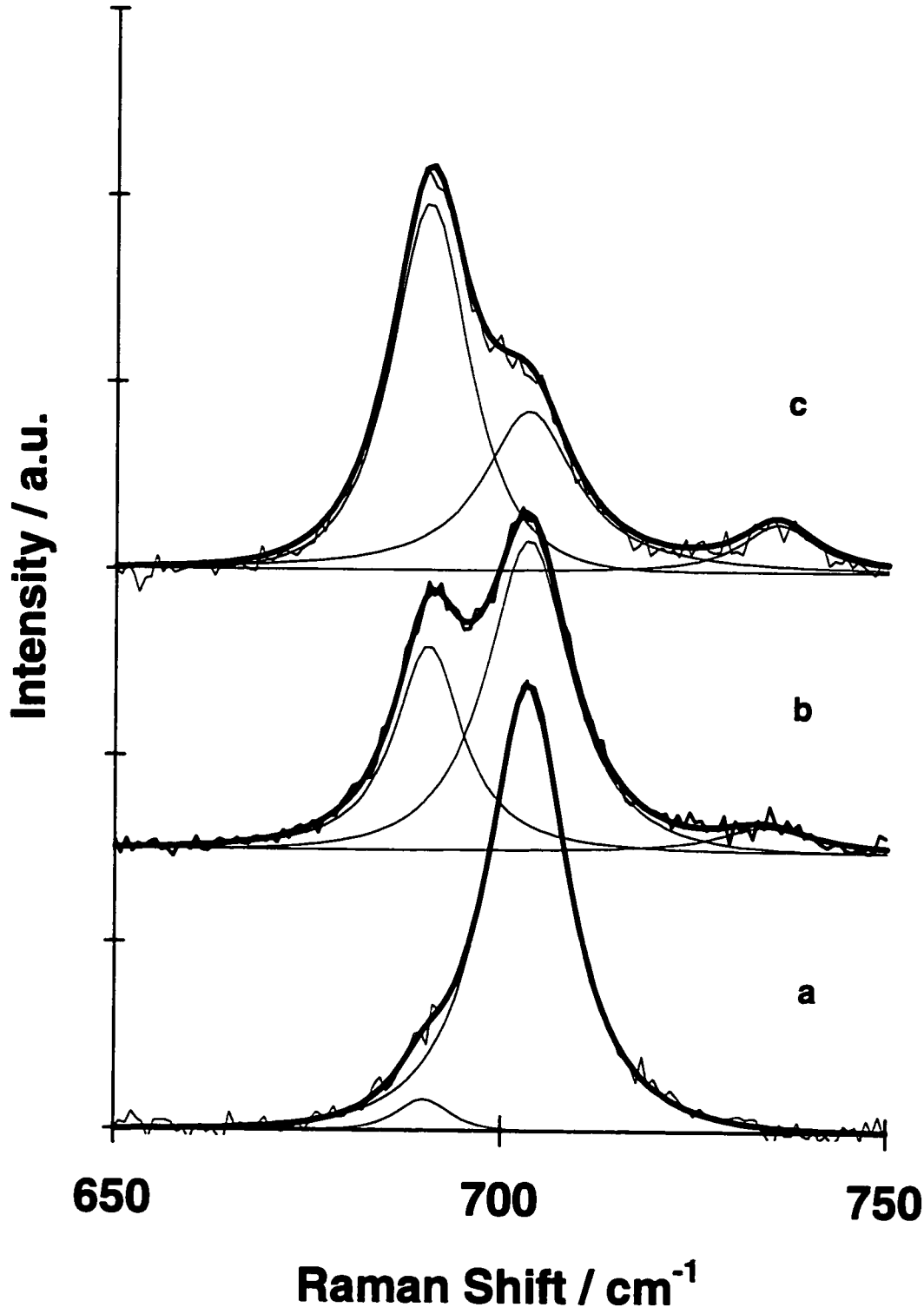

Figure 3.7: Sample of the bandfitting procedure. Solutions are 1 M pz in HCl. The component bands, their sum and the original spectra are shown. a) pH = 1.5; b) pH = 1.0; c) pH = 0.5.

and

$$X_{pzH^+} = (1 - X_{pz}) \tag{14}$$

The fractional distribution calculated in this way is presented in Figure 3.8. The pK_{a1} value obtained from the intersection is 0.70. This is in surprisingly good agreement with the literature value 0.65 [11]. We did not expect such good agreement, because the Raman intensity does not depend only on the concentration, but also on the Raman polarizability which can differ considerably for the two species. A 5% error is not unreasonable from the bandfitting procedure.

It was not possible to observe the spectrum of the diprotonated pyrazine, even in the most concentrated HCl solution (37%). The spectrum of diprotonated pyrazine can be useful in order to identify bands which arise from protonation of the "free" N of an eventually end-on adsorbed pyrazine molecule at very acidic interfacial conditions. Therefore, we measured some spectra of more acidic media and these results are presented in the next section.

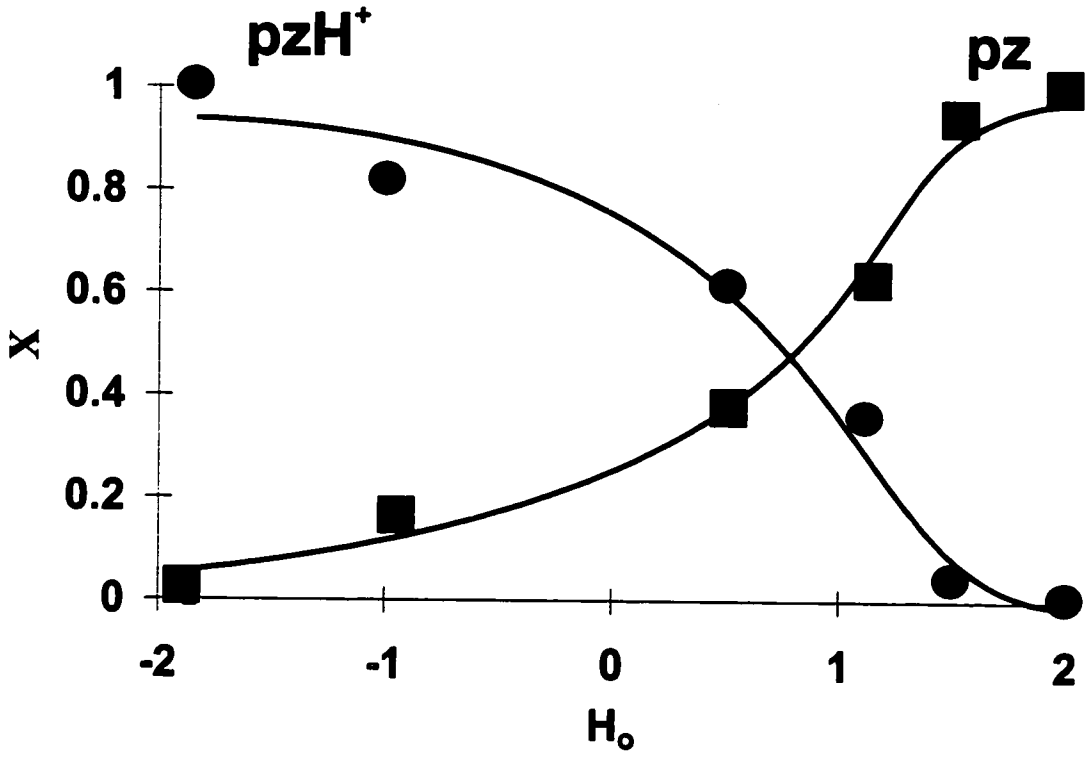

Figure 3.8: Experimental fractional distribution of 1 M pyrazine and its monoprotonated form in HCl. The fraction of pyrazine species has been calculated as explained in the text.

3.3.3. Studies of pyrazine in $HClO_4$ and H_2SO_4 solutions

In order to achieve the protonation of both nitrogen atoms in pyrazine, acidic compounds stronger than HCl have to be used. The diprotonated pyrazinium cation has been produced in sulfuric acid solutions, and studied by NMR [37]. The biggest problem for a vibrational study in these acids is the overlap between bands due to the acids and those due to the protonated pyrazine. In spite of these problems, some bands due to the diprotonated pyrazine are apparent. Figure 3.9 shows spectra in the 980 - 1100 cm^{-1} spectral region, of pyrazine in $HClO_4$ at different concentrations. Bands due to pz, pzH^+ and pzH_2^{2+} can be identified. At a concentration of $HClO_4$ equal 0.3M the aquated pz is the predominant species, and just one sharp band is observed at 1019 cm^{-1}. As the $HClO_4$ concentration increases to 4M a broad envelope containing two intense bands at ~ 1020 and 1030 cm^{-1} appears which is characteristic of aquated pyrazinium ion. The broad feature completely disappears at an $HClO_4$ concentration equal to 12M, and in this condition just one band is observed at 1034 cm^{-1}; it is attributed to the aquated diprotonated pzH_2^{2+} species.

The fractional distribution of pyrazine in H_2SO_4 was obtained in a manner similar to that described for HCl. Spectra shown in Figure 3.10 were used and the curve, with the H_o values from Tickle et al. [21], is presented in Figure 3.11. The pK values, obtained from the points of intersection are pK_{a1}= 0.5 and pK_{a2}= -7. These results differ from the literature values (0.65 and -5.8) [11]. The difference can be attributed to the change in polarizability of the protonated species, to the overlap of the 700 cm^{-1} band of pyrazine and a broad sulfuric acid band at 570 cm^{-1} (mainly at elevated acid concentrations) and to the ambiguity in the precise definition of various acidity scales. Bands due to all pyrazine species in these acidic media are presented and assigned in Table 3.3.

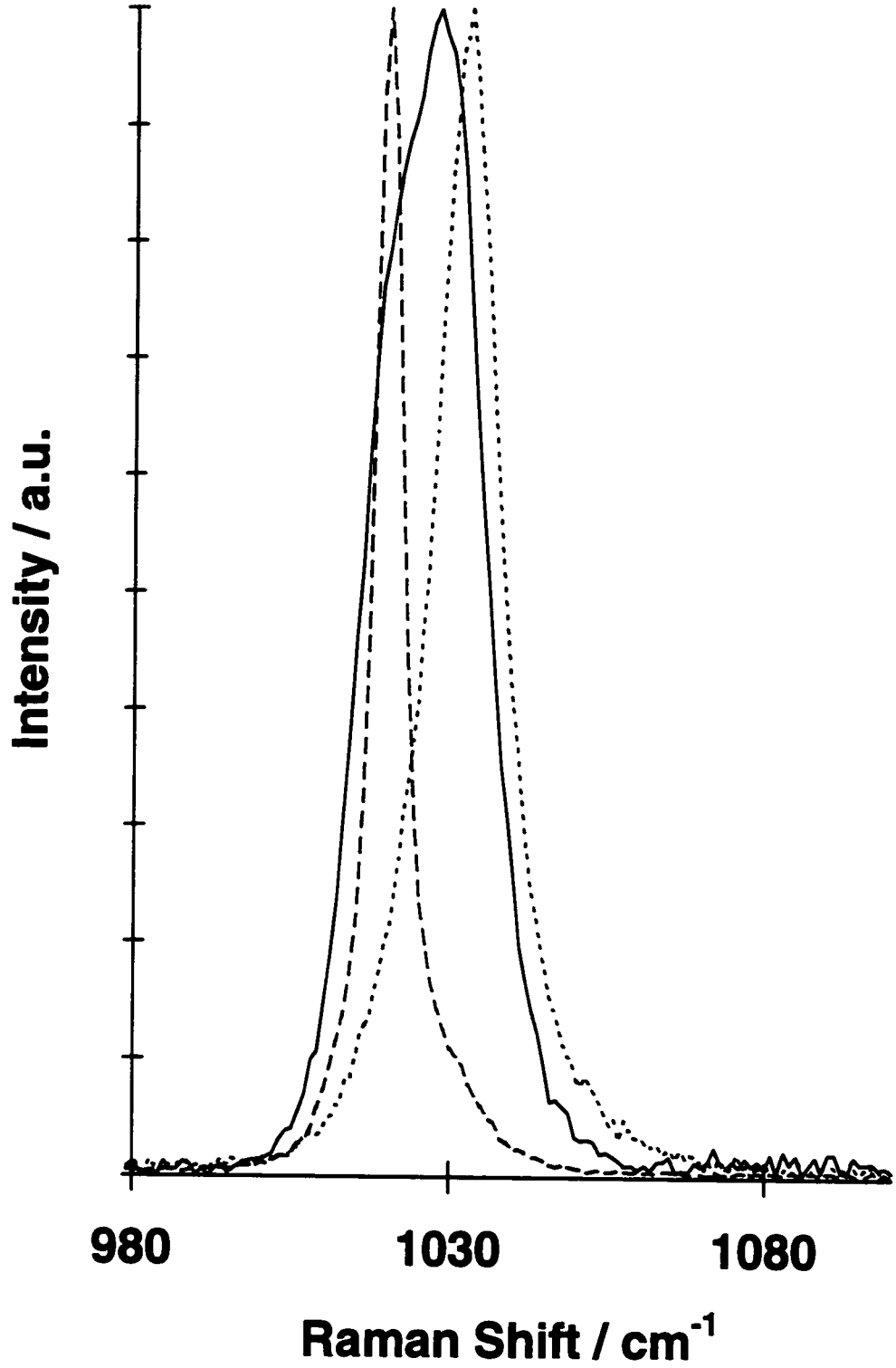

Figure 3.9: Spectra of solutions of 1 M pz in $HClO_4$.
Dashed line, $[HClO_4] = 0.3$ M; solid line, $[HClO_4] = 4$ M; dotted line, $[HClO_4] = 12$ M.

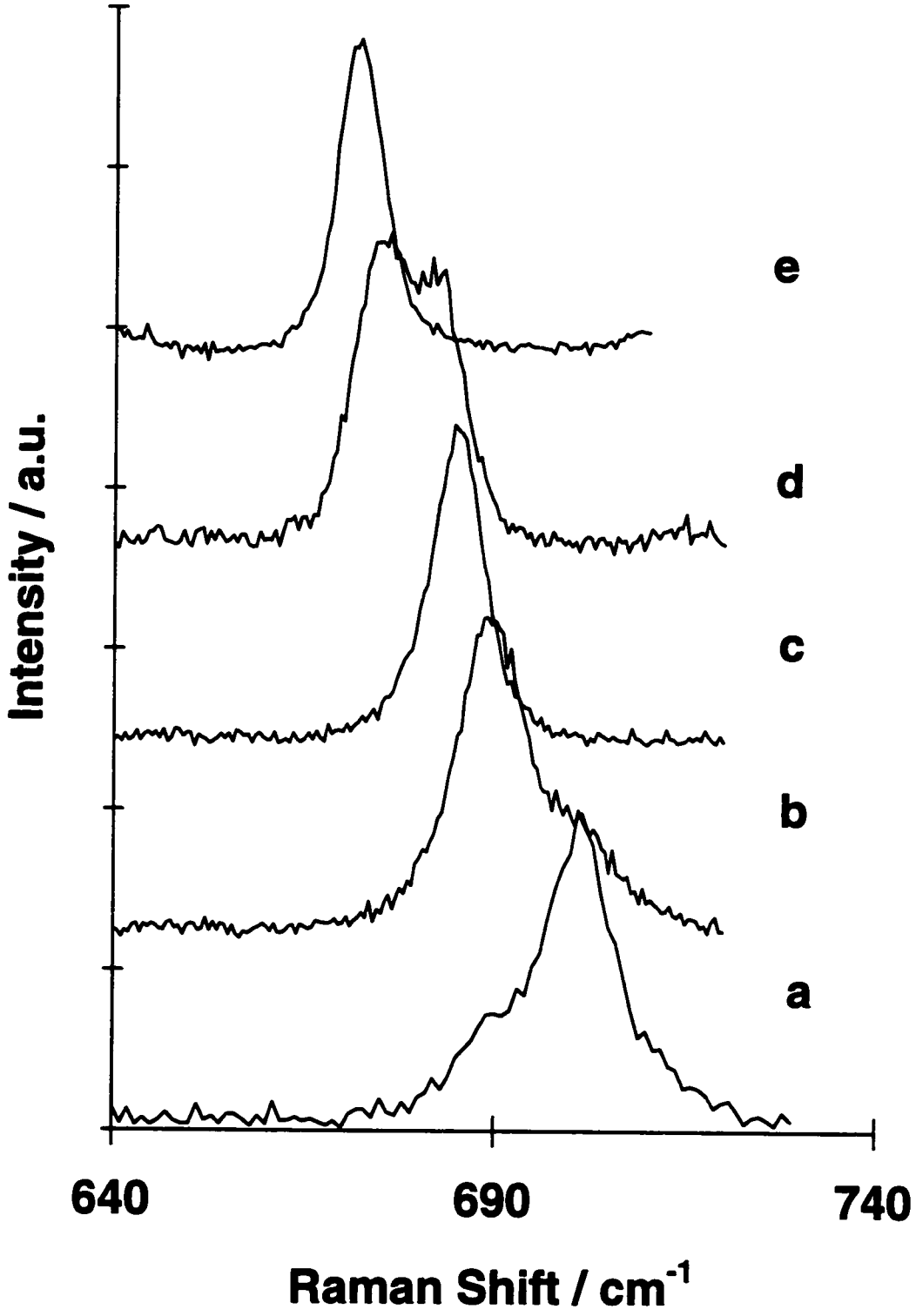

Figure 3.10: Spectra of solutions of 1 M pz in H_2SO_4.
a) 0.1 M; b) 0.8 M; c) 10 M; d) 12 M; e) 17 M.

Table 3.3: Wavenumbers (cm^{-1}) of vibrational modes for all three pyrazine species in aqueous sulfuric, perchloric and hydrochloric acid media.

pyrazine - pz				monoprotonated pyrazine				diprotonated pyrazine		
H_2SO_4	$HClO_4$	HCl	assign.	H_2SO_4	$HClO_4$	HCl	assign.	H_2SO_4	$HClO_4$	assign.
		620	A_g (6a)		609	606	A_1 (6a)	614		A_g (6a)
702	701	702	B_{2g} (6b)	689	689	688	B_1 (6b)	671	675	B_{2g} (6b)
756	755	758	B_{3g}(4)	734	734	732	B_2 (4)			
921	922	922	B_{1g} (10a)							
1019	1019	1019	A_g (1)	1015	1015	1020	A_1 (1)			
				1030	1030	1031	A_1 (12)	1034	1032	A_g (1)
				1114		1117	A_1(18a)			
					1173	1173	B_1 (15)			
								1208	1214	A_g (9a)
1222	1217	1218	A_g (11+16b)	1224	1225	1223	A_1 (9a)			
1237	1237	1238	A_g (9a)							
1348	1347	1348	B_{2g} (3)					1376		B_{2g} (3)
				1491	1491	1495	A_1 (19a)			
1529	1529	1530	B_{2g} (8b)			1594	A_1 (8b)			
1593	1593	1593	A_g (8a)	1621	1619	1618	A_1 (8a)	1612	1609	A_g (8a)
								1661	1660	B_{2g} (8b)
2312	2312	2312	A_g (2x14)	2350	2350	2350	A_1 (2x14)	2345	2364	A_g (2x14)
2972	2967	2970	A_g (2x19a)	2969	2971	2970	A_1 (2x19a)		2982	A_g (2x19a)
3075	3074	3077	A_g (2)	3105	3104	3103	A_1 (2)	3125	3110	A_g (2)

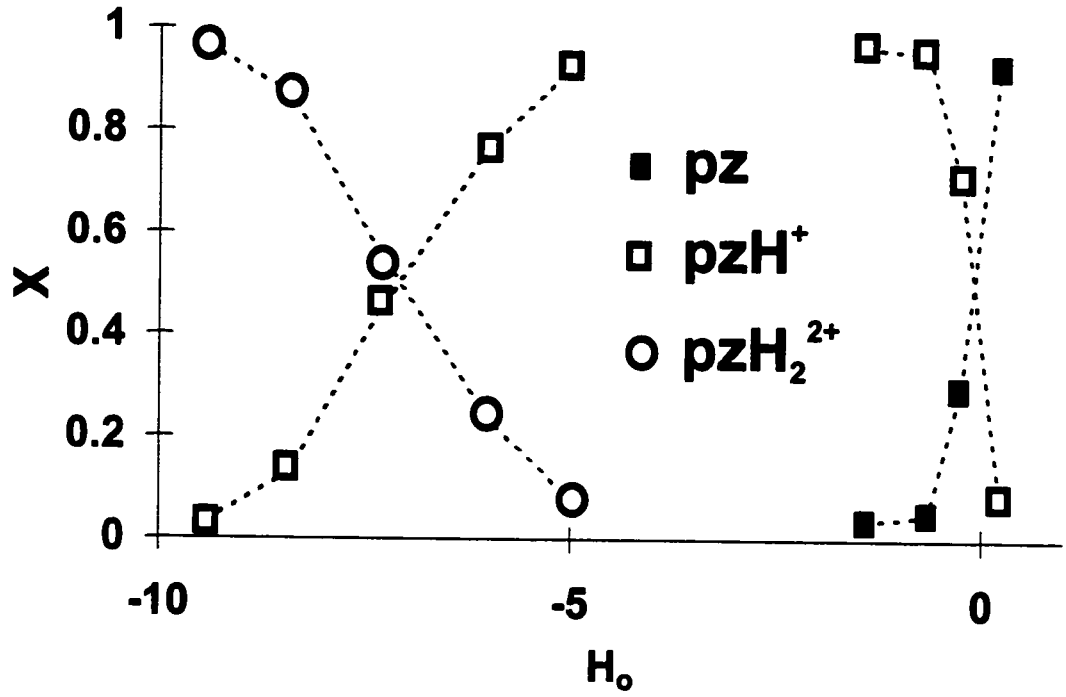

Figure 3.11: Experimental fractional distribution of 1 M pyrazine and its mono and diprotonated forms in sulfuric acid.

3.4. Conclusions

Raman spectra of pyrazine solutions are presented for various acidic media. From these spectra, bands due to 3 different pyrazine species, pz, pzH^+ and pzH_2^{2+} have been identified. The spectra also suggest an interaction between pyrazine and water; the specific geometry and stoichiometry of this interaction cannot be deduced from the spectral changes alone. An unassigned band at 1235 cm^{-1} (electrode surface) has been assigned as the 11 + 16b combination.

An approximate fractional distribution of these pyrazine species was obtained through the relation between band intensity and species concentration. The estimated pyrazine pK_a values were reasonably consistent with the literature.

The new bands can be related to those observed when pyrazine adsorbs to an electrode surface. Therefore, these results should prove useful when interpreting the SERS spectrum of adsorbed pyrazine - to follow. Insight may thus be gleaned into the nature of surface acidity.

3.5. References

[1] D. E. Irish and G. Szymanski, *Proceedings of the XIII International Conference on Raman Spectroscopy,* Wurzburg, Germany, Wiley, Chichester, UK, **1992**, p.690.

[2] A. Ianneli, J. Richer and J. Lipkowski, *Langmuir* **1989**, 5, 466.

[3] L. Stolberg, J. Lipkowski and D. E. Irish, *J. Electroanal. Chem.*, **1991**, 300, 563.

[4] J. Lipkowski, L. Stolberg, S. Morin, D. E. Irish, P. Zelenay, M. Gamboa and W. Wieckowski, *J. Electroanal. Chem.* **1993**, 355, 147.

[5] G. R. Erdheim, R. L. Birke and J. R. Lombardi, *Chem. Phys. Letters*, **1980**, 69, 495.

[6] R. Dornhaus, M. B. Long, R. E. Benner and R. K. Chang, *Surf. Sci.*, **1980**, 93, 240.

[7] V. M. Hallmark and A. Campion, *J. Chem. Phys.*, **1986**, 84, 2933.

[8] R. Bhattacharjee, *J. Raman Spect.*, **1990**, 21, 301.

[9] M. Moskovits, D. P. DiLella and K. J. Maynard, *Langmuir*, **1988**, 4, 67.

[10] Y. Huang and G. Wu, *Spectrochim. Acta*, **1990**, 46A, 377.

[11] A. S-C. Chia and R. F. Trimble, Jr, *J. Phys. Chem.*, **1961**, 65, 863.

[12] R. Foglizzo and A. Novak, *Appl. Spectr.*, **1970**, 24, 601.

[13] A. G. Brolo and D. E. Irish, *Proceedings of the XIV International Conference on Raman Spectroscopy*, Hong Kong, Wiley, Chinchester, UK, **1994**, p. 592.

[14] A. G. Brolo and D. E. Irish, *Z. Naturforsch.*, **1995**, 50A, 274.

[15] D. D. Perrin, B. Dempsey and E. P. Serjeant, *pK_a Prediction for Organic Acids and Bases*, Chapman and Hall, NY, **1981**.

[16] L. Pauling, *General Chemisty*, Dover, New York, **1988** (republication of the 3rd edition, published originally by Freeman, San Francisco, in 1970).

[17] J. E. Leffler and E. Grunwald, *Rates and Equilibria of Organic Reactions*, Dover, New York, **1989** (republication of the 1st edition, published by Wiley, New York, in 1963)

[18] L. P. Hammett and A. J. Deyrup, *J. Am. Chem. Soc.*, **1932**, 54, 2721.

[19] J. N. Murrell and A. D. Jenkins, *Properties of Liquids and Solutions*, 2nd edition, Wiley, New York, **1994**.

[20] R. A. Cox and K. Yates, *Can. J. Chem.*, **1981**, 59, 2116.

[21] P. Tickle, A. G. Briggs and J. M. Wilson, *J. Chem. Soc. (B)*, **1970**, 65.

[22] M. J. Jorgenson and D. R. Harter, *J. Am. Chem. Soc.*, **1963**, 85, 878.

[23] C. H. Rochester, *Acidity Functions - Organic Chemistry A Series Monographs*, Vol. 17, Academic Press, **1970**.

[24] R. A. Cox and K. Yates, *Can. J. Chem.*, **1983**, 61, 2225.

[25] J. Zarembowitch and L. Bokobza-Sebagh, *Spectrochim. Acta*, **1976**, 32A, 605.

[26] J. F. Arenas, J. T. Lopez-Navarrete, J. C. Otero, J. I. Marcos and A. Cardenete, *J. Chem. Soc. Faraday Trans.*, **1985**, 81, 405.

[27] R. C. Lord, A. L. Marston and F. A. Miller, *Spectrochim. Acta*, **1957**, 9, 113.

[28] J. D. Simmons and K. K. Innes, *J. Mol. Spect.*, **1964**, 14, 190.

[29] G. Sbrana, V. Schettino and R. Righini, *J. Chem. Phys.*, **1973**, 59, 2441.

[30] M. Muniz-Miranda, N. Neto and G. Sbrana, *J. Phys. Chem.*, **1988**, 92, 954.

[31] D. B. Scully, *Spectrochim. Acta*, **1961**, 17, 233.

[32] E. B. Wilson, Jr., J. C. Decius and P.C. Cross, *Molecular Vibrations: The Theory of Infrared and Raman Vibrational Spectra*, McGraw Hill, New York, **1955**.

[33] C. I. Ratcliffe and D. E. Irish, *J. Phys. Chem.*, **1982**, 86, 4897.

[34] M. Maehara, H. Kawano, Y. Nibu, H. Shimada and R. Shimada, *Bull. Chem. Soc. Jpn.*, **1995**, 68, 506.

[35] G. Herzberg, *Molecular Spectra and Molecular Structures: II Infrared and Raman Spectra of Polyatomics Molecules*, Van Nostrand, New York, **1945**, p.215.

[36] K. C. McGee, A. T. Capitano and V. H. Grassian, Langmuir, **1994**, 10, 632.

[37] H. Kamei, J. Phys. Chem., **1965**, 69, 2791.

Chapter 4

Ab Initio Calculation for Pyrazine and its Protonated Forms

4. Ab initio Calculations for Pyrazine and Its Protonated Forms

4.1. Theoretical Background

In this section, some basic quantum mechanical concepts will be briefly described, in order to help the reader follow the presentation of the ab initio results. All discussion in this introductory section is based on references [1] and [2].

According to quantum mechanics, the energy and many properties of a stationary state of a molecule can be obtained by solving the Schrodinger equation.

$$\mathbf{H}\Psi = E\Psi \qquad (1)$$

Here, **H** is the Hamiltonian operator, representing the sum of the potential and kinetic energy of the system (total energy). E is the numerical value of the total energy and Ψ is the wavefunction, which depends on both the Cartesian coordinates of all particles and on the spin coordinates. The square of the wavefunction, $|\Psi|^2$, gives the probability distribution of the particle within the molecule. The Schrodinger equation can be solved analytically for only a very small number of cases. Other theoretical models are used to calculate molecular properties by solving the Schrodinger equation numerically. The calculations which do not contain any empirical data or approximations (apart from approximations inherent in the theoretical scheme) are called *ab initio calculations*.

In the molecular orbital model the individual electronic wavefunctions are linearly combined (linear combination of atomic orbitals - LCAO - approximation) to form a many-electron wavefunction.

$$\psi_i = \sum_{\mu=1}^{N} c_{\mu i} \phi_\mu \qquad (2)$$

The functions ϕ_i are one electron atomic basis functions, and they constitute a basis set. The coefficients $c_{\mu i}$ are calculated so that the total energy of the many-electron wavefunction, ψ_i, is minimized, and it is as close as possible to the energy corresponding to the exact solution of the Schrodinger equation (variational theorem).

The Hartree-Fock (HF) models are the simplest to use for chemical applications and they have been widely applied for several systems. This self-consistent field (SCF) method consists of using a set of "guessed" orbitals, selecting one electron, and calculating the potential in which it moves while the other distributions of electrons are frozen. All electrons, but the selected one, contribute to the overall potential. The Schrodinger equation for the electron is solved for this potential, and a new wavefunction for this electron is obtained. This procedure is repeated for all electrons in the system, generating a new set of orbitals which differs from the initial set. The cycle is then repeated using the new set of orbitals. The field is self consistent when a set of orbitals through the cycle does not provoke any further change.

The choice of the initial basis set is a very important step in the procedure. The solution of the Schrodinger equation for hydrogen-like atoms suggests that Slater atomic orbitals are a very good choice for an initial calculation. These Slater type orbitals (STO) are of the form:

$$X_{nlm} = r^{n-1}e^{-\xi r}Y_{lm}(\theta,\phi) \tag{3}$$

The radial variation consists of a power of r multiplied by an exponential function. The angular part in θ and ϕ is a spherical harmonic ($Y_{lm}(\theta,\phi)$). The exponent ξ is an adjustable parameter. Thus, it is possible to construct a basis set for a many-electron atom using one or more STOs of the correct symmetry for each occupied orbital. A minimal basis set is obtained if one exponential for each occupied orbital is used. However, often two atomic orbitals, with different exponents, are used for each occupied orbital (double zeta, DZ, basis set).

A simpler extension of the minimal basis set is to double only the number of basis functions in the valence region (split-valence basis set). The 3-21g is an example of a simple split valence basis set, defined through the fourth row of the periodic table. Larger split-valence representations can also be used, such as the 4-31g and the 6-31g basis sets. The former is defined for the first row of the periodic table and for some second row elements, and it utilizes an inner shell expansion of four gaussian functions and two

valence shells comprising three and one gaussian, respectively. The 6-31g basis set, defined for all first and second rows of the periodic table, contains a combination of six gaussians as inner shell functions and two valence shells, represented by three and one gaussian, respectively. The addition of polarization functions (which allow a non-uniform distribution of charges around the nucleus) and diffuse functions may also improve the calculated result for some particular systems. The polarization functions are represented in a basis set by an asterisk, 6-31g*, for instance. STOs yield accurate calculations for atoms and small molecules. However, the calculations using these orbitals are difficult and time consuming. This is a severe limitation for large molecules and different types of basis functions have to be used for these large systems. The evaluation of the molecular integrals can be simplified by using gaussian-type orbitals (GTO), but more of these have to be used. These may be chosen as single (uncontracted or primitive) gaussian functions or as fixed, predefined linear combinations of such functions (contracted). The use of contracted GTOs minimizes the discrepancies between a single GTO and a real atomic orbital wavefunction.

The molecular orbital energies are obtained from ab initio calculations. The energy values for the occupied orbitals are approximately equal to the ionization potential (Koopmans' theorem). The fractional distribution of the electronic charges among various parts of the molecule (atoms and bonds) can also be obtained. It may be useful to define a total electronic charge on a particular atom in a molecule in order that quantitative meaning may be given to concepts like electron withdrawing or donating ability. This distribution is called the Mulliken population analysis.

The main deficiency of the HF method is its incomplete description of the correlation between motions of the electrons. The full solution of the Schrodinger equation cannot be obtained by considering a single assignment of electrons to an orbital. There are several theoretical methods that can be used to calculate the correlation effect. The most economical general correlation methods are based on the perturbation theory of Møller and Plesset (MP). These methods treat the complete Hamiltonian as a sum of two parts, the non-HF part (V) being treated as a perturbation of the HF hamiltonian (H_0).

$$H_\lambda = H_0 + \lambda V \tag{4}$$

The "perturbation" λV is defined by:

$$\lambda V = \lambda(H - H_0) \tag{5}$$

where H is the corrected Hamiltonian and λ is a dimensionless parameter. According to the Rayleigh-Schrodinger perturbation theory, the energy E_λ can be expanded in powers of λ.

$$E_\lambda = E^{(0)} + \lambda E^{(1)} + \lambda^2 E^{(2)} + \ldots \tag{6}$$

Practical correlation methods may now be formulated by setting the parameter λ equal to unity, and by truncations of the series in equation (**6**) to various orders. We refer to the methods by the highest order of the energy term allowed, that is, truncation after second order as MP2, after the third order as MP3 and so on.

The harmonic vibrational wavenumbers of a molecule can also be calculated by ab initio methods. The total energy of a molecule, containing N atoms, near its equilibrium geometry can be given by:

$$E = \frac{1}{2}\sum_{i=1}^{3N} \dot{q}_i^2 + V_{eq} + \frac{1}{2}\sum_{i=1}^{3N}\sum_{j=1}^{3N}\left(\frac{\partial^2 V}{\partial q_i \partial q_j}\right)_{eq} q_i q_j \qquad (7)$$

where the mass-weighted Cartesian displacements, q_i *and* q_j, are defined in terms of their locations (x_i *and* x_j) of the nuclei relative to their equilibrium positions and their masses (M),

$$q_i = \sqrt{M_i}(x_i - x_{eq}) \qquad (8)$$

V_{eq} is the potential energy at the equilibrium nuclear configuration, and the expansion of the vibrational energy in terms of a power series is truncated at second order. The classical equations of motion for this system are of the form (for j = 1, 2,... 3N):

$$\ddot{q}_j = -\sum_{i=1}^{3N} f_{ij} q_i \qquad (9)$$

The quadratic force constants, f_{ij}, are the second derivatives of the potential energy with respect to the Cartesian displacements, evaluated at the equilibrium geometry, that is:

$$f_{ij} = \left(\frac{\partial^2 V}{\partial q_i \partial q_j} \right)_{eq} \qquad (10)$$

The f_{ij} values can be evaluated numerically and equation (**9**) may be solved to yield a set of 3N normal mode vibrational wavenumbers. Six of these (or five, for linear molecules) correspond to the rotational and translational degrees of freedom, and their vibrational wavenumbers will be zero. The calculated vibrational wavenumbers are, generally, 10 to 15 % higher than the experimentally determined ones. The errors in the calculated wavenumbers arise both from the inherent inaccuracies of the differentiation techniques required to calculate the force constants and from uncertainties in the selection of the equilibrium geometry. The calculated wavenumbers and the corresponding theoretical equilibrium geometry may also be employed to obtain thermodynamic properties, such as entropy.

4.2. Introduction

The advent of fast computers with large data storage capacity, at a reasonable price, makes ab initio calculations a routine procedure in a spectroscopic laboratory. This technique can be very accurate in the description of the electronic and vibrational energies, if one uses the appropriate method and basis set. However, even modern computers have problems in handling the large number of functions, at a fair theoretical level, when dealing with a polyatomic system. Consequently, it is not unusual to find reports of calculated vibrational wavenumbers ~ 10 % higher than their experimental values for polyatomic molecules. It is usual to scale down the calculated wavenumbers, forcing them to match to experimental values [3]. A more realistic force field is obtained from this procedure.

The substitution of two CH groups of benzene by two N atoms causes a new kind of electronic transition ($n \rightarrow \pi^*$) to be available. This new situation results in pyrazine, one of the most attractive systems for spectroscopists and theoreticians [4,5,6,7]. A theoretical study of the π-electron delocalization of pyrazine showed that its delocalization energy is essentially the same as for benzene [8]. Recent ab initio calculations of the electronic spectra of pyrazine reported excitation energies with an accuracy as good as 0.25 eV when compared to the experimental data [9]. Potential energy surfaces of the three lowest singlet states of pyrazine have been computed [10. 11]. These calculations confirm the existence of a conical intersection between the S_1 ($n\pi^*$) and S_2 ($\pi\pi^*$) surfaces [12]. The absorption, resonance - Raman [13], fluorescence, and femtosecond, time-resolved, pump-

probe spectra were calculated, using a vibronic coupling model that considered the conical intersection, with good experimental agreement [10,11]. Ab initio calculations were also performed in a series of studies regarding the protonation of pyrazine, proton affinities, and hydrogen bond interactions [14,15,16]. A correlation between the increase of the n orbital energy with the increase of proton affinity was found in a series of nitrogen bases [16]. On the other hand, the hydrogen bonding interaction depends on the p character of the nitrogen lone pair [14]. Therefore, pyrazine showed the lowest proton affinity and hydrogen bonding tendency when compared to ammonia, pyridine, and the other aromatic diazines [14-16].

We have reported a Raman spectral study of pyrazine and its protonated forms (Chapter 3 and [17]). In that Chapter, we investigated the Raman spectra of aqueous pyrazine in HCl, H_2SO_4, and $HClO_4$ solutions at several acid concentrations. Vibrational bands due to unprotonated, monoprotonated, and diprotonated pyrazine were identified. The diprotonated pyrazine band positions were reported for the first time. All bands were assigned, based on pyrazine [18,19,20,21,22] and monoprotonated pyrazine [23] vibrational studies and the correlation table technique. Theoretical calculations of the vibrational wavenumbers, presented in this chapter, are a useful complement to that work. These calculations provide basic information about physical-chemical properties of pyrazine and its protonated forms. The calculated vibrational wavenumbers can be compared to our previous assignments, and the positions the undetected peaks can be estimated. The wavenumbers for the out-of-plane modes of pyrazine have been calculated

[24, 25]; however, no reports involving a complete theoretical analysis of the vibrational modes of pyrazine and its protonated forms have appeared.

4.3. Results and Discussion

Table 4.1 shows the equilibrium geometry of pyrazine and its protonated forms obtained with different basis sets at RHF and MP2 levels. The molecular orientation for all calculations is shown below.

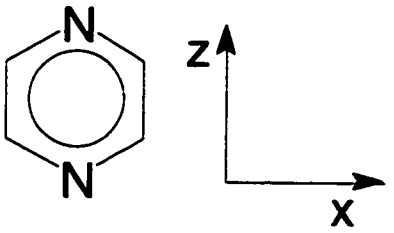

The calculated bond distances and angles for pyrazine are in good agreement with both experimental data [26] and previous calculations [9-16]. The usual value for a normal covalent NH bond length is about 102 pm [1]. Our calculated results for the NH distance for both mono and diprotonated pyrazine range from 100 to 104 pm. Other calculated atomic distances, CC, CN and CH, do not suffer any significant change with protonation. The calculated NCC angles decrease and the CNC angles increase when protons are added to the N in the aromatic ring. The structural changes seem to be necessary for the pyrazine aromatic ring to accommodate the new proton with a positive charge.

Table 4.1: Optimized geometry for pyrazine and its protonated forms at RHF and MP2 levels, with several basis sets.

A. Pyrazine

	3-21g	4-31g	6-31g	6-31**	6-311g**	MP2/6-21g*	Expt.[a]
CC / pm	138	138	139	139	139	139	140.3
CN / pm	133	133	133	132	132	134	133.9
CH / pm	107	107	107	108	108	109	111.5
NCC / °	120.98	120.87	120.95	121.11	121.71	122.60	122.2
CNC / °	118.02	118.25	118.10	116.58	116.57	115.14	115.6
NCH / °	117.69	117.44	117.34	117.45	117.41	116.57	113.9

a Experimental data from reference [26].

B. Monoprotonated pyrazine cation

	3-21g	4-31g	6-31g	6-31g*	6-31**	6-311g**	MP2/3-21g*
CC / pm	138	138	138	138	138	138	140
CN / pm	134	134	134	132	132	132	137
CH / pm	107	107	107	107	107	107	108
NH / pm	101	101	100	100	100	100	103
NCC / °	119.32	119.18	119.20	119.44	119.44	119.47	119.93
CNC / °	121.35	121.46	121.59	121.11	121.10	121.05	120.15
NCH / °	118.35	118.18	118.09	118.05	118.11	118.11	117.87

C. Diprotonated pyrazine cation

	3-21g	4-31g	6-31g	6-31g*	6-31g**	6-311g**	MP2/3-21g*
CC / pm	138	139	139	139	139	139	140
CN / pm	134	134	134	133	133	133	137
CH / pm	107	107	107	107	108	108	109
NH / pm	102	102	101	101	101	101	104
NCC / °	118.09	118.00	117.88	117.83	117.84	117.88	118.41
CNC / °	123.82	124.00	124.25	124.35	124.33	124.24	123.19
NCH / °	119.31	119.17	119.12	118.95	119.01	119.03	118.99

Table 4.2: Calculated properties for pyrazine and its protonated forms at RHF and MP2 levels

4.2A. Pyrazine

	3-21g	4-31g	6-31g	6-31**	6-311g**	MP2/6-21g*	
Electronic Energy(RHF) / a.u.	-261.20	-262.28	-262.56	-262.69	-262.74	-262.51	
Nuclear Repulsion Energy / a.u.	210.14	210.40	209.85	211.01	211.15	207.95	
Energy total (thermal) / $Jmol^{-1}$	228623.60	229736.70	229539.00	227252.14	225789.63	214611.30	
Zero Point Energy /$Jmol^{-1}$	218610.40	219714.00	219465.70	217032.50	215541.50	203659.80	
C_v / $Jmol^{-1}K^{-1}$	55.947	55.881	56.306	57.503	57.85	63.237	
Entropy / $Jmol^{-1}K^{-1}$	269.481	269.511	269.823	270.395	270.504	274.48	
Rotational Constants							**Expt[a]**
A(GHz)	6.36	6.37	6.35	6.54	6.55	6.39	6.41
B(GHz)	6.15	6.17	6.12	6.08	6.09	5.88	5.90
C(GHz)	3.13	3.13	3.12	3.15	3.16	3.06	3.06

[a] from ref. 28.

4.2B. Monoprotonated pyrazine cation

	3-21g	4-31g	6-31g	6-31g*	6-31g**	6-311g**	MP2/3-21g*
Electronic Energy (RHF) / a.u.	-261.56	-262.46	-262.92	-263.03	-263.04	-263.09	-261.55
Energy total (thermal) / $Jmol^{-1}$	267376.92	266935.86	269110.88	266341.89	265570.71	263852.91	248701.49
Nuclear Repulsion Energy / a.u.	220.37	220.24	220.16	221.19	221.21	221.38	215.88
Zero Point Energy /$Jmol^{-1}$	257171.50	256687.80	258847.30	255845.30	255067.90	253303.70	237594.70
C_v / $Jmol^{-1}K^{-1}$	58.23	58.60	58.53	60.61	60.68	61.19	66.22
Entropy / $Jmol^{-1}K^{-1}$	276.70	276.92	277.03	278.02	278.05	278.24	281.62
Rotational Constants							
A(GHz)	6.14	6.13	6.13	6.24	6.25	6.26	5.94
B(GHz)	5.94	5.94	5.93	6.93	5.93	5.94	5.65
C(GHz)	3.02	3.02	3.01	3.04	3.04	3.05	2.90
Dipole moment / Debye	4.79	4.77	4.91	4.57	4.57	4.55	4.80

4.2C. Diprotonated Pyrazine cation

	3-21g	4-31g	6-31g	6-31g*	6-31g**	6-311g**	MP2/3-21g*
Electronic Energy (RHF) / a.u.	-261.73	-262.63	-263.09	-263.20	-263.21	-263.26	-261.72
Nuclear Repulsion Energy / a.u.	230.35	230.24	230.26	231.02	231.08	231.25	225.65
Energy total (thermal) / $Jmol^{-1}$	303682.60	303358.12	307142.17	302935.70	302084.54	300037.71	283150.42
Zero Point Energy / J/mol	293366.10	293006.40	296810.10	292311.20	291455.10	289341.20	272020.70
C_v / $Jmol^{-1}K^{-1}$	59.875	60.170	59.746	62.643	62.708	63.450	67.606
Entropy / $Jmol^{-1}K^{-1}$	272.026	272.21	272.147	273.414	273.430	273.712	276.406
Rotational Constants							
A / GHz	6.00	5.99	5.98	6.04	6.04	6.06	5.75
B / GHz	5.65	5.65	5.65	5.68	5.68	5.69	5.43
C /GHz	2.91	2.91	2.91	2.93	2.93	2.93	2.79

Tables 4.2a to 4.2c summarize other calculated properties for unprotonated, monoprotonated, and diprotonated pyrazine. The calculated pyrazine properties can be compared to previous calculations and experimental data found in the literature [27]. The rotational constants for pyrazine in its ground and excited states have recently been determined by high resolution IR in a molecular beam [28] and they are in fair agreement with our calculated results.

The calculated energies, presented in Tables 4.2, can be used to estimate the proton affinities for pyrazine and its derivative. The proton affinity of a base B, can be defined as the negative of the energy for the following process [29]:

$$B + H^+ \rightarrow BH^+$$

Therefore, the energy for the protonation of pyrazine and pyrazinium can be estimated from the values presented in Tables 4.2. The total energy for each compound (pyrazine, pyrazinium, and diprotonated pyrazinium) must be corrected, taking into account the zero point energy. The quantum mechanical calculated properties (energies) are expected to correlated with the strength of the base (pK_a values) [30]. Recently, a linear relationship has been found between the ab initio calculated energy of the localized frontier orbitals and the pK_a for heterocyclic bases and substituted benzoic acids [31]. However, for a description of acid-base strength, it is easier to present the calculated

results relative to another base. The ammonia molecule is usually used as a standard; the energy for the process:

$$NH_3 + H^+ \rightarrow NH_4^+$$

is set to zero.

Table 4.3 shows the relative proton affinities (relative energy, $\delta\Delta E$) for some nitrogen bases. The energy values for pyrazine, pyrazinium, and diprotonated pyrazine were obtained using the data presented in Tables 4.2. The values for the other bases were obtained from [29]. A correlation between the relative energies and the pK_a is observed. The relative energies increase as the pK_a of the nitrogen bases increases.

The calculated charge over each atom is presented in Figure 4.1. The resonance structures for pyrazine, monoprotonated pyrazine, and diprotonated pyrazine are illustrated in Figures 4.2, 4.3, and 4.4, respectively. These resonance structures are useful to understand the calculated charge distribution due to protonation presented in Figure 4.1. For instance, the most important contributions to the pyrazine structure are represented in Figs. 4.2a and 4.2b. The separation of charges observed in Fig. 4.2c, minimizes its importance. An overall increase in the positive charge over all atoms occurs when pyrazine is protonated, as expected. However, a closer analysis of Figs. 4.1a and 4.1b suggests that the nitrogen in position 4 (non-protonated) and the carbon in position 2 are the atoms which became more positives due to the protonation. The charge

Table 4.3: Calculated (RHF - 6-31g*) relative proton affinities of some nitrogen bases.

Nitrogen Base (B)	pK_a	$\delta\Delta E$ / kJmol^{-1}
pyrazinium (pzH^+)	-5.8	-509.9
pyrazine (pz)	0.65	-39.9
ammonia (NH_3) [a]	9.25	0
aniline (ϕ-NH_2) [a]	4.63	+33.6
pyridine (py) [a]	5.22	+75.6

[a] from ref. 29.

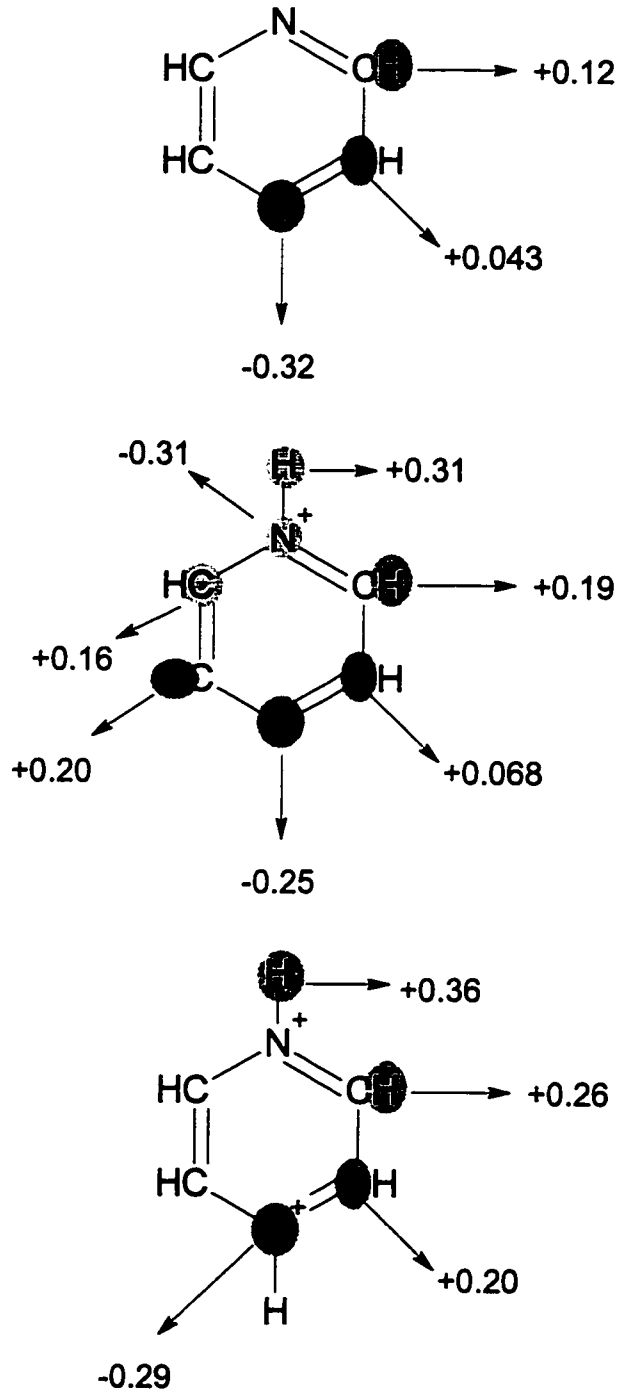

Figure 4.1: Calculated (RHF - 6-311g**) total atomic charge (Mulliken population analysis) for pyrazine and its protonated forms.

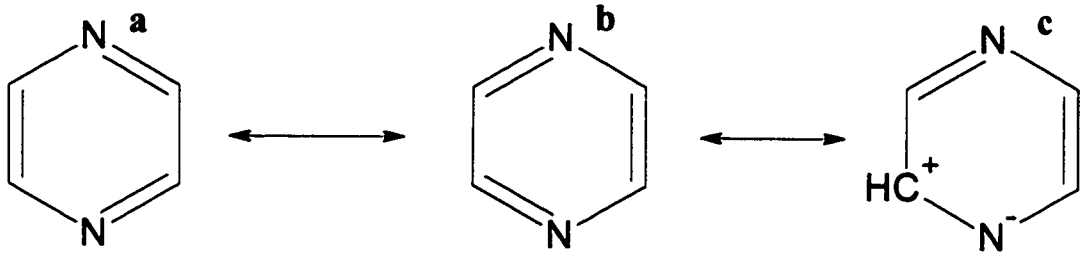

Figure 4.2: Possible resonance structures for pyrazine.

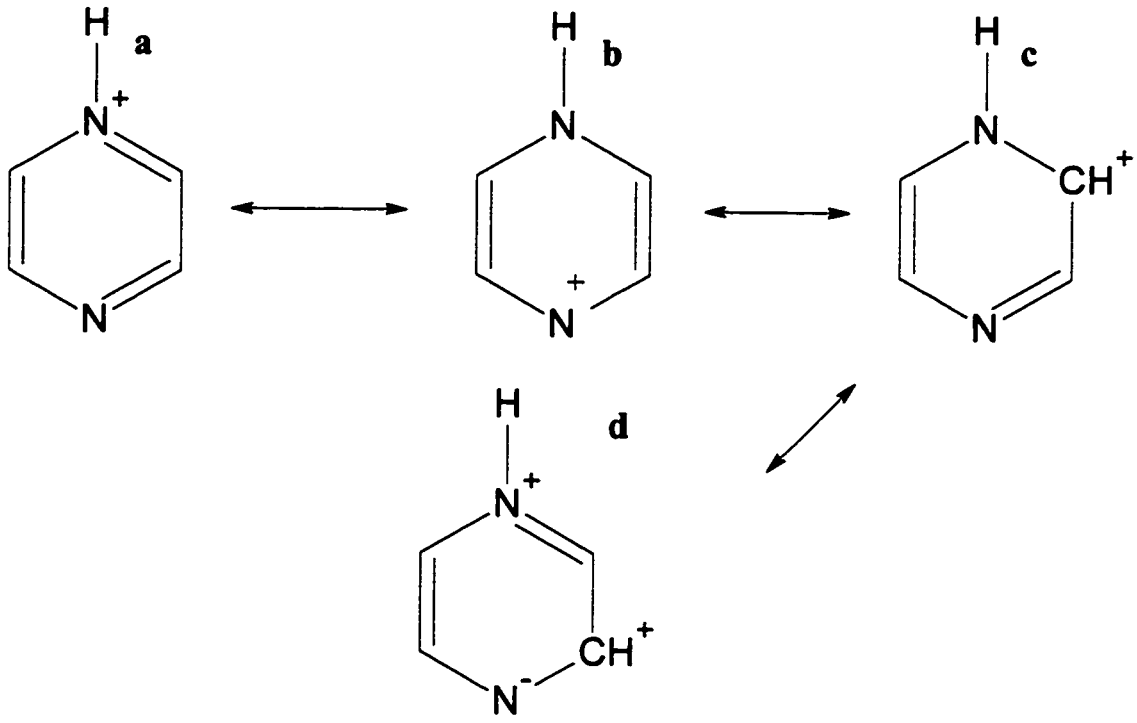

Figure 4.3: Resonance structures for monoprotonated pyrazine.

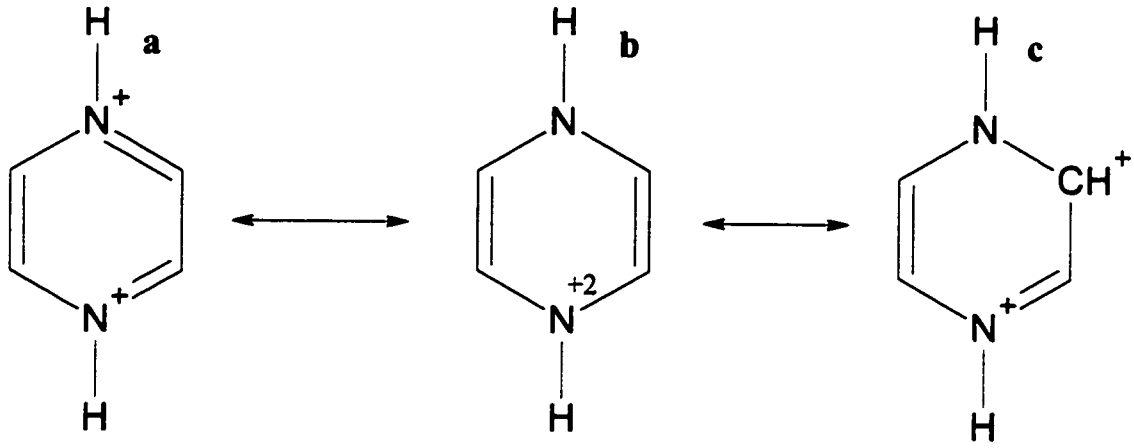

Figure 4.4: Possible resonance structures for diprotonated pyrazine.

on the nitrogen 1 (protonated) changed from -0.32 on pyrazine to -0.31 on pyrazinium. On the other hand, the charge on nitrogen 4 changed to -0.25 (Figs. 4.1a and 4.1b). The charge for carbon 2 changed from +0.04 on pyrazine to +0.16 on pyrazinium. The carbon 3 only changed to +0.06 (Figs. 4.1a and 4.1b). This charge redistribution due to protonation indicates that the positive charge from the hydrogen is delocalized into the aromatic ring. Therefore, Figs. 4.3b and 4.3c show important contributions to the structure of the monoprotonated pyrazine. The same argument is valid in the comparison of the charge distribution between the monoprotonated pyrazine and the diprotonated pyrazine. The charges over the nitrogen and the carbon are more positive in the diprotonated pyrazine, suggesting that resonance structures presented on Figs. 4.4b and 4.4c may contribute to the overall structure of the bivalent cation.

Table 4.4 shows the calculated energies for the frontier molecular orbitals of pyrazine and its protonated forms. The lowest experimental observed transition in the electronic spectra of pyrazine, assigned to a $n \rightarrow \pi^*$ transition, lies around 3.8 eV [32]. A value of 4.35 eV is obtained for this transition from the values on Table 4.4. The results presented on Tables 4.1, 4.2, and 4.4 agree with previous calculation at this level [32]. Experimental data for pyrazine show that the energies of n-type orbitals (a_g and b_{1u}) are misplaced [33]. These observations were confirmed in more sophisticated multi-reference configuration interaction calculations [33].

Table 4.4: Calculated energies in atomic units for orbitals from pyrazine and its protonated forms at RHF level with a 6-311g** base set.

Occupied Orbitals

pz		pzH^+		pzH_2^{2+}	
b_{3g}	-0.56	b_1	-0.83	b_{3u}	-1.05
b_{1u}	-0.50	b_2	-0.78	b_{3g}	-1.01
b_{2g}	-0.44	b_1	-0.68	a_g	-1.00
a_g	-0.41	a_1	-0.63	b_{2g}	-0.94
b_{1g}	-0.36	a_2	-0.58	b_{1g}	-0.78

Unoccupied Orbitals

pz		pzH^+		pzH_2^{2+}	
b_{3u}	0.09	b_1	-0.15	b_{3u}	-0.38
a_u	0.12	a_2	-0.09	a_u	-0.30
a_g	0.16	a_1	-0.05	a_g	-0.21
b_{2u}	0.17	b_2	0.01	b_{1u}	-0.18
b_{1u}	0.21	a_1	0.02	b_{2u}	-0.14

Therefore, the ordering for the highest energy occupied molecular orbitals is $a_g(n)>b_{1g}(\pi)>b_{1u}(n)>b_{2g}(\pi)$.

The calculated energies for the unoccupied orbitals (LUMOs) are related to the electronic affinity. Positive values for electronic affinities, as observed in Table 4.4, indicate non-bonding states. However, the experimental result for the first electronic affinity energy of pyrazine is around -0.40 eV (-0.015 a.u.) [34]. In spite of these limitations, the calculated molecular orbital energies (Table 4.4) can be qualitatively useful in a comparative analysis between pyrazine and its protonated forms. For instance, one can observe from Table 4.4 that the first ionization potential increases with protonation (The ionization potential is the negative of the energy of the orbital, according to Koopmans' theorem. Therefore, the first ionization potential is related to the energy of the HOMO). The pyrazine cation cannot be generated electrochemically due to its high ionization potential [35]. The results presented in Table 4.4 suggest that the oxidation (withdrawal of electrons) of pyrazine becomes even more difficult after protonation. On the other hand, from the calculated first electronic affinities (related to the energy of the LUMOs), one can conclude that protonation facilitates the electron acceptance of pyrazine, because the energies of the unoccupied orbitals decrease with the addition of the hydrogen ion (see Table 4.4). This hypothesis is supported from electrochemical data [36]. It has been demonstrated that the half-wave reduction potential correlates with the theoretical electronic affinities for nitrogen containing molecules [37]; therefore, the results presented in Table 4.4 indicate that the protonated pyrazine radical is more stable than the pyrazine

radical. In fact, the pyrazine radical does not form in aqueous (or protic) media. Electron spin resonance studies of the pyrazine radical (formed *in-situ* by pulse radiolysis), in aqueous solutions at several pH values, have shown that the diprotonated pyrazinium radical is the most stable species [38,39]. The 1-hydropyrazine cation has also been produced and investigated [40]. The non-protonated pyrazine ion radical has been observed in non-protic media from ESR studies [41]. The relative decrease in energy for the n-type orbital with protonation is a consequence of the proton addition to the nitrogen lone electron pair.

Tables 4.5a to 4.5c show the calculated vibrational wavenumbers for pyrazine and its protonated species with different basis sets. The calculated values are generally higher than the experimental ones, within a ~10% error. It is also important to point out that the calculated values do not take into account any intermolecular interaction. Hence, the calculated vibrational wavenumbers should resemble the gas phase spectrum rather than the aqueous solution.

The calculated pyrazine wavenumbers shown in Tables 4.5a - 4.5c indicate that the A_u 16a vibrational mode is at lower frequency than the B_{3u} 16b. This contradicts Arenas et al. [21], who assigned the A_u 16a mode at 422 cm^{-1} and the 16b B_{3u} mode at 418 cm^{-1}. Moreover, Zarembowitch [19] estimated its value at 350 cm^{-1}. This mode is silent in both Raman and IR. From our calculated results, the wavenumbers for these modes

Table 4.5: Calculated vibrational wavenumbers (cm^{-1}) from pyrazine species. The calculated Raman activities are given, in parentheses, after the calculated wavenumber. The experimental data are also presented.

4.5A. Unprotonated Pyrazine

Modes	description	3-21g	4-31g	6-31g	6-31g**	6-311g**	MP2/6-21g*	Experimental
A_g	δ ring (6a)	677.8 (2.64)	674.7 (3.17)	668.9 (3.4)	653.6 (2.49)	654.3 (2.74)	608.4	620
	ν ring (1)	1110.9 (38.59)	1127.1 (40.77)	1123.2 (43.31)	1130.3 (41.73)	1120.7 (45.82)	1036.0	1019
	δ CH (9a)	1361.5 (14.65)	1366.1 (14.70)	1363.2 (14.27)	1355.2 (15.85)	1347.2 (13.55)	1280.5	1238
	ν ring (8a)	1731.5 (16.48)	1770.5 (15.52)	1774.9 (15.90)	1807.1 (13.33)	1794.1 (13.25)	1625.0	1593
	ν CH (2)	3417.5 (276.00)	3423.9 (297.66)	3434.9 (300.2)	3378.7 (301.8)	3353.7 (310.4)	3232.3	3077
B_{1g}	γ CH (10a)	1086.9 (4.79)	1071.9 (3.26)	1063.5 (2.61)	1045.5 (2.56)	1041.7 (0.022)	960.8	922
B_{2g}	δ ring (6b)	794.1 (6.84)	787.0 (7.03)	787.0 (7.52)	778.4 (7.37)	775.5 (7.77)	721.0	702
	δ CH (3)	1508.9 (0.22)	1510.3 (0.63)	1503.6 (0.65)	1490.2 (0.86)	1482.0 (0.38)	1397.5	1348
	δ ring (8b)	1679.3 (11.56)	1729.8 (10.52)	1734.0 (10.88)	1767.5 (13.68)	1748.9 (15.24)	1565.8	1530
	ν CH (7b)	3387.1 (127.50)	3396.0 (133.05)	3407.0 (130.1)	3353.3 (127.4)	3328.6 (125.1)	3210.5	3061
B_{3g}	γ ring (4)	881.1 (1.92)	868.7 (0.77)	857.5 (0.57)	837.5 (0.86)	837.7 (0.44)	780.5	758
	γ CH (5)	1177.9 (0.43)	1151.5 (0.74)	1135.5 (0.83)	1099.1 (0.49)	1096.2 (0.017)	977.3	973
A_u	γ ring (16a)	442.8	438.9	435.2	425.6	424.7	348.1	[350]
	γ CH (17a)	1193.1	1172.0	1158.4	1122.9	1119.8	989.7	(1001) *
B_{1u}	δ ring (12)	1113.9	1124.1	1121.1	1120.5	1120.0	1037.4	(1019)
	δ CH (18a)	1248.9	1256.1	1251.0	1258.8	1252.3	1174.2	(1130)
	ν ring (19a)	1643.6	1658.3	1654.5	1666.9	1654.0	1531.9	(1482)
	ν CH (13)	3391.1	3399.5	3410.6	3354.7	3330.0	3211.4	(3011)
B_{2u}	γ ring (16b)	514.05	514.1	508.4	487.4	485.4	429.7	(422) *
	γ CH (11)	930.7	919.0	912.1	896.3	891.6	812.3	(784)
B_{3u}	δ CH (15)	1110.7	1184.0	1192.5	1113.2	1086.6	1107.7	(1061)
	ν ring (14)	1178.9	1197.0	1201.8	1201.7	1186.2	1316.9	(1150)
	ν ring (19b)	1557.9	1570.7	1566.5	1568.0	1556.6	1467.6	(1411)
	ν CH (20b)	3404.8	3415.0	3426.2	3372.2	3347.6	3226.4	(3061)

IR experimental values for pz solution from ref. [21] in parentheses; estimated value from ref.[20] in square bracket.
Raman experimental values from ref. [17] are presented without parentheses. * IR in solid state from ref.[21].
The Wilson numbering scheme is presented in parentheses following the species symbol.

Table 4.5B. *Monoprotonated pyrazine*

Modes	description	3-21g	4-31g	6-31g	6-31g*	6-31g**	6-311g**	MP2/3-21g*	Experimental
A_1	δ ring (6a)	678.0 (2.05)	675.6 (2.01)	670.4 (2.49)	649.7 (2.02)	649.6 (1.96)	649.0 (2.14)	627.3	606
	ν ring (1)	1101.0 (42.50)	1097.8 (42.04)	1117.5 (51.15)	1117.3 (50.17)	1116.7 (51.07)	1115.2 (54.98)	979.2	1020
	δ ring (12)	1128.6 (3.06)	1123.8 (3.69)	1131.5 (0.78)	1126.1 (0.35)	1125.6 (0.17)	1117.3 (1.26)	1027.3	1031
	δ CH (18a)	1225.4 (2.03)	1223.5 (2.11)	1227.3 (2.21)	1230.3 (2.10)	1228.3 (2.09)	1222.5 (2.05)	1135.5	1119
	δ CH (9a)	1345.6 (6.61)	1345.0 (6.68)	1349.3 (6.64)	1334.9 (8.15)	1330.2 (8.45)	1324.0 (7.07)	1268.9	1223
	ν ring (19a)	1623.6 (6.79)	1622.2 (6.71)	1638.5 (5.49)	1645.3 (5.68)	1641.6 (5.65)	1631.5 (5.56)	1485.8	1488
	ν ring (8a)	1765.9 (14.69)	1765.6 (14.94)	1803.1 (16.78)	1818.4 (12.51)	1816.6 (12.87)	1806.7 (13.39)	1599.2	1618
	ν CH (13)	3430.9 (4.67)	3431.0 (3.87)	3448.9 (0.35)	3435.4 (1.94)	3410.4 (0.08)	3384.4 (0.78)	3255.0	(3080)
	ν CH (2)	3447.8 (205.0)	3448.1 (207.8)	3464.6 (228.6)	3449.0 (229.0)	3424.6 (231.5)	3399.0 (221.9)	3270.6	3103
	ν NH	3677.9 (57.08)	3678.8 (57.77)	3750.9 (51.98)	3782.5 (55.00)	3788.6 (54.18)	3767.8 (52.87)	3443.1	(2800)
A_2	γ ring (16a)	444.0 (0.050)	439.8 (0.050)	436.4 (0.050)	421.0 (0.060)	420.4 (0.058)	418.5 (0.034)	370.4	(367)
	γ CH (10a)	1066.5 (1.06)	1060.2 (1.12)	1044.2 (0.26)	1016.6 (0.27)	1016.3 (0.28)	1008.8 (0.23)	936.3	911
	γ CH (17a)	1205.8 (0.85)	1192.5 (0.85)	1172.0 (0.77)	1129.2 (0.61)	1129.4 (0.34)	1116.3 (0.30)	1030.9	[1000]
B_1	δ ring (6b)	767.1 (6.53)	764.6 (6.58)	760.9 (7.12)	744.3 (6.69)	744.3 (6.68)	741.7 (6.99)	703.8	690
	δ CH (15)	1120.2 (1.77)	1118.1 (1.78)	1190.2 (0.006)	1125.8 (4.48)	1125.5 (4.39)	1099.8 (4.87)	1061.8	(1067)
	ν ring (14)	1177.2 (0.54)	1177.8 (0.49)	1211.0 (3.88)	1193.3 (0.14)	1191.0 (0.17)	1180.0 (0.038)	1211.0	1173
	δ NH + δ ring	1432.7 (0.49)	1433.8 (0.47)	1445.7 (0.62)	1421.8 (0.46)	1415.6 (0..44)	1409.6 (0.27)	1329.6	(1253)
	δ CH (3)	1520.7 (0.14)	1519.8 (0.12)	1516.6 (0.43)	1504.2 (0.42)	1499.1 (0.46)	1492.1 (0.31)	1409.9	1372
	ν ring (19b)	1642.2 (4.46)	1641.8 (4.55)	1680.5 (2.42)	1678.9 (0.84)	1674.6 (0.80)	1665.6 (1.01)	1474.7	1464
	ν ring (8b)	1774.9 (10.84)	1775.2 (10.78)	1811.4 (11.43)	1822.4 (14.80)	1821.0 (14.95)	1810.4 (16.03)	1607.4	1594
	ν CH (7b)	3428.2 (87.20)	3428.5 (89.18)	3446.9 (90.68)	3434.8 (92.16)	3409.7 (91.09)	3383.6 (83.08)	3251.5	3080
	ν CH (20b)	3443.4 (1.53)	3443.8 (1.26)	3460.4 (0.31)	3446.7 (1.02)	3421.8 (0.009)	3396.2 (0.20)	3266.5	(3128)
B_2	γ ring (16b)	484.7 (0.040)	480.5 (0.040)	478.9 (0.0006)	460.9 (0.0005)	460.3 (0.001)	457.8 (0.0006)	420.7	(417)
	γ ring (4)	851.6 (1.83)	842.8 (1.90)	825.3 (0.94)	789.9 (1.13)	790.6 (1.16)	785.9 (0.69)	760.2	735
	γ CH (11)	883.5 (0.22)	879.2 (0.17)	874.4 (0.05)	840.6 (0.001)	839.6 (0.0003)	834.3 (0.008)	786.3	(783)
	γ CH (5)	1101.3 (0.69)	1093.8 (0.73)	1087.5 (0.34)	1023.8 (0.30)	1022.7 (0.32)	1013.1 (0.045)	978.1	970
	γ NH +γ CH	1226.1 (0.36)	1210.8 (0.35)	1196.3 (0.14)	1130.1 (0.029)	1129.7 (0.59)	1117.3 (0.27)	1031.1	(974)

Experimental values from ref.[17] without parentheses; experimental values from ref. [23] in parentheses; the square bracket indicate a estimated value. The Wilson numbering scheme is presented in parentheses following the species symbol.

Table 4.5C. *Diprotonated pyrazine*

Modes	description	3-21g	4-31g	6-31g	6-31g*	6-31g**	6-311g**	MP2/3-21g*	Experimental
A_g	δ ring (6a)	697.39 (1.99)	696.01 (1.98)	694.52 (2.33)	669.84 (2.01)	669.56 (1.95)	669.19 (2.07)	640.58	614
	ν (1)	1090.24 (66.96)	1088.50 (67.21)	1107.45 (76.34)	1110.45 (72.84)	1110.18 (73.76)	1103.22 (80.60)	979.53	1034
	δ ring (9a)	1352.64 (10.49)	1342.46 (10.52)	1356.97 (10.93)	1332.59 (13.13)	1328.57 (13.58)	1323.44 (12.77)	1266.27	1214
	ν ring (8a)	1807.55 (6.76)	1807.01 (7.04)	1850.43 (7.28)	1854.39 (5.57)	1853.40 (5.57)	1845.99 (6.47)	1625.87	1660
	ν CH (2)	3408.74 (169.4)	3409.32 (170.6)	3432.86 (190.2)	3429.92 (188.4)	3403.06 (188.0)	3378.17 (178.3)	3236.34	3110
	νNH+νCH(7a)	3535.82 (105.1)	3536.65 (106.3)	3662.08 (93.2)	3663.10 (99.64)	3665.51 (97.89)	3645.21 (95.60)	3319.85	
B_{1g}	γ CH (10a)	1064.82 (0.0014)	1058.81 (0.001)	1045.99 (0.21)	1006.10 (0.072)	1006.54 (0.067)	993.80 (0.76)	939.10	
B_{2g}	δ ring (6b)	750.21 (6.88)	748.09 (6.91)	744.30 (7.31)	723.98 (7.42)	724.28 (7.40)	721.68 (7.58)	689.00	675
	δ CH (3)	1439.09 (0.084)	1439.30 (0.064)	1452.62 (0.55)	1425.96 (0.39)	1420.16 (0.41)	1413.96 (0.26)	1317.42	1376
	δNH+δCH(9b)	1581.80 (3.65)	1581.75 (3.63)	1605.63 (2.62)	1577.16 (1.13)	1571.49 (1.11)	1566.79 (1.21)	1446.93	
	δ ring (8b)	1776.43 (24.60)	1777.46 (24.64)	1820.25 (23.67)	1828.37 (25.79)	1828.15 (25.85)	1819.32 (26.78)	1598.26	1609
	ν CH (7b)	3394.42 (58.89)	3395.00 (59.91)	3419.34 (61.14)	3419.16 (65.27)	3391.89 (62.37)	3366.36 (55.84)	3222.50	
B_{3g}	γ ring (4)	822.51 (1.12)	814.87 (1.17)	804.37 (0.74)	772.24 (0.80)	773.49 (0.79)	768.29 (0.52)	740.31	
	γNH+γCH (10b)	1093.69 (0.73)	1090.39 (0.69)	1091.27 (0.093)	1028.96 (0.24)	1027.01 (0.27)	1014.58 (0.045)	963.87	
	γ CH (5)	1259.09 (2.12)	1246.14 (2.17)	1244.25 (1.14)	1161.15 (0.72)	1159.40 (0.74)	1136.40 (0.78)	1062.56	
A_u	γ ring (16a)	447.97	444.29	443.02	430.12	429.60	427.63	403.65	
	γ CH (17a)	1206.18	1193.95	1181.72	1132.56	1132.47	1112.60	1022.37	
B_{1u}	δ ring (12)	1155.64	1151.99	1160.20	1131.38	1130.17	1126.62	1052.75	
	δ CH (18a)	1215.57	1214.04	1217.94	1207.76	1206.69	1200.48	1117.31	
	ν ring (19a)	1653.66	1652.84	1668.50	1666.80	1663.80	1655.45	1510.75	
	ν CH (13)	3395.43	3395.74	3419.69	3419.10	3391.66	3366.12	3224.47	
	νNH+νCH(20b)	3526.01	3526.89	3654.12	3655.01	3657.03	3636.70	3313.15	
B_{2u}	γ ring (16b)	471.82	468.44	467.78	449.65	449.47	446.77	414.72	
	γ CH (11)	879.70	876.33	871.12	826.07	825.33	815.35	783.95	
	γNH+γCH (17b)	1234.55	1230.80	1239.07	1156.03	1153.81	1136.91	1073.37	
B_{3u}	δ CH (15)	1017.30	1015.09	1103.84	992.44	993.08	962.61	1050.77	
	ν ring (14)	1145.59	1147.43	1175.94	1174.11	1171.79	1164.47	1242.03	
	ν ring (19b)	1450.05	1452.28	1460.58	1432.14	1427.37	1421.29	1364.09	
	δNH+δCH(18b)	1768.58	1759.71	1798.16	1766.83	1762.62	1759.84	1623.56	
	ν CH 20b	3404.46	3405.23	3428.77	3427.12	3399.90	3374.81	3233.00	

Experimental values from ref.[17] The Wilson numbering scheme is presented in parentheses following the species symbol.

can be predicted at around 380 cm^{-1} and 430 cm^{-1} for the 16a and 16b, respectively (after scaling the calculated frenquencies down 10 %).

Another controversial point in the pyrazine spectrum is the assignment of the 14 B_{3u} ν-ring mode. Some authors [22] report this band at ~1350 cm^{-1}, and others assign the mode to a ~1150 cm^{-1} band [17]. The assignment of this fundamental to the band at ~1350 cm^{-1} seems unlikely for several reasons: First of all, the ~ 1150 cm^{-1} band is too intense in the IR spectrum [19] to be considered a combination. Moreover, the combination band of A_g symmetry in the Raman spectrum at ~ 2310 cm^{-1} can only be explained as an overtone of this ~ 1150 cm^{-1} fundamental mode [17]. The combination shifts to ~ 2346 cm^{-1} upon protonation, as the 1150 cm^{-1} band shifts to ~ 1174 cm^{-1} [17]. Finally, from the calculated wavenumbers from pyrazine and its protonated forms, we conclude that 1150 cm^{-1} is a reasonable expected position for this mode.

It is interesting to notice that, for the pyrazinium cation, the calculated NH stretch mode frequency is the highest one. This mode is reported by Foglizzio [23] as a strong IR band in the solid at 2800 cm^{-1}. We did not observe this band either in the 2800 cm^{-1} region or in the 3200 cm^{-1} region in the Raman of the pyrazinium solutions [17]. In spite of this band being predicted by the calculation as having medium intensity, it could be masked by the OH stretch envelope in aqueous solution. For pyridinium ion, this band intensity is also known to be very dependent of the counter ion [42].

The ab initio method seems to fail to predict the large Raman intensity presented by the mode number 12 (~ 1035 cm^{-1}) in the pyrazinium spectrum. This mode is inactive in the pyrazine spectrum (B_{1u}) , but becomes active due to the protonation (A_1). Two strong bands were observed as an envelope in the ~ 1020 cm^{-1} region in the aqueous pzH^+ spectrum [Chapter 3, 17]. One, at ~ 1020 cm^{-1}, was assigned to the ring breathing of pyrazinium, and the other, at ~ 1030 cm^{-1}, was assigned to this ring mode number 12. The calculated Raman activity, presented in Tables 4.5, forecasts that the number 12 mode should be, at least, 40 times weaker than the ring breathing mode, which was not observed [17]. It is possible that the proximity between the wavenumbers of these two bands allows some intensity to be transferred from the ring breathing mode to this number 12 mode, in a resonance-like mechanism. This would occur because, under protonation, the number 12 mode becomes A_1, the same symmetry as the ring breathing mode.

For the diprotonated cation, a good agreement exists between the previous assignment and the calculated wavenumbers. Few bands could be identified experimentally from the pzH_2^{2+} spectrum, due to the overlap between the pyrazine and the sulfuric and perchloric acids bands. The calculation shows the expected position for the A_g (7a), B_{2g} (9b), B_{3g} (10b), B_{1u} (20b), B_{2u} (17b) and B_{3u} (18b) modes, all absent in the unprotonated pyrazine spectrum.

4.4. Conclusions

The ab initio calculated properties for pyrazine, presented in this chapter, are in good agreement with previous theoretical works. The calculation for pyrazinium and diprotonated pyrazine are reported for the first time.

The theoretical results show that the first ionization potential increases as pyrazine is protonated. Hence, the oxidation of protonated pyrazine is even more difficult than is unprotonated pyrazine. Therefore, the protonated radical cations should not be formed by electrochemical means.

The calculated electronic affinity decreases as pyrazine is protonated. Therefore, the protonated forms of pyrazine are easier to reduce electrochemically when compared to unprotonated pyrazine.

The charge distribution over the atoms for pyrazine and its derivatives are rationalized by using the possible contributions from their resonance structures. The calculated ab initio energies correlate with the strength of the bases.

The calculated vibrational wavenumbers are in good agreement with the experimental values, taking into account the ~ 10% error expected in the calculation at

this level. Based on this calculation, the assignments for pyrazine and its protonated forms are reviewed. This work also include a theoretical prediction for the position of all diprotonated pyrazine bands observed for the first time and reported on Chapter 3.

4.5. References

[1] W. J. Hehre, L. Radom, P.V.R.Schleyer and J. A. Pope, *Ab initio Molecular Orbital Theory*, Wiley, New York, **1985**.

[2] W. G. Richards and D. L. Cooper, *Ab initio Molecular Orbital Calculations for Chemists*, 2nd edition, Clarendon, Oxford, **1983**.

[3] F. Negri, G. Orlandi, F. Zerbeto, P. Palmieri and R. Tarroni, *Chem. Phys.*, **1993**, 178, 133

[4] S. Canuto, O. Goscinski and M. Zerner, *Chem. Phys. Letters*, **1979**, 68, 232.

[5] W. R. Wadt and W. A. Goddard III, *J. Am. Chem. Soc.*, **1975**, 97, 2034.

[6] D. A. Kleier, R. L. Martin, W. R. Wadt and W. R. Moomaw, *J. Am. Chem. Soc.*, **1982**, 104, 60.

[7] P. Bischof, R. Gleiter and P. Hofmann, *J. Chem. Soc. Chem. Comm.*, **1974**, 767.

[8] K. B. Wiberg, D. Nakaji and C. M. Breneman, *J. Am. Chem. Soc.*, **1989**, 111, 4178.

[9] M. P. Fulscher, K. Andersson and B. O. Roos, *J. Phys. Chem.*, **1992**, 96, 9205

[10] L. Seidner, G. Stock, L. Sobolewski and W. Domcke, *J. Chem. Phys.*, **1992**, 96, 5298

[11] C. Woywod, W. Domcke, A. L. Sobolewski and H.-J. Werner, *J. Chem. Phys.*, **1994**, 100, 1400

[12] W. Domcke, A. L. Sobolewski and C. Woywod, *Chem. Phys. Letters*, **1993**, 203, 220.

[13] G. Stock, C. Woywod, W. Domcke, T. Swinney and B. S. Hudson, *J. Chem. Phys.*, **1995**, 103, 6851.

[14] J. E. Del Bene, *J. Am. Chem. Soc.*, **1975**, 97, 5330.

[15] J. E. Del Bene, *Chem. Phys.* **1976**, 15, 463.

[16] J. E. Del Bene, *J. Am. Chem. Soc.*, **1977**, 99, 3617.

[17] A. G. Brolo and D. E. Irish, *Z. Naturforsh. part A*,**1995**, 50A, 274.

[18] G. Sbrana, V. Schettino and R. Righini, *J. Chem. Phys.*, **1973**, 59, 2441.

[19] N. Nishi, M. Kinoshita, T. Nakashima, R. Shimada and Y. Kanda, *Mol. Phys.*, **1977**, 33, 31.

[20] J. Zarembowitch and L. Bokobza-Sebagh, *Spectrochim. Acta*, **1976**, 32A, 605.

[21] J. F. Arenas, J. T. Lopez-Navarrete, J. C. Otero and J. I. Marcos, *J. Chem. Soc. Faraday Trans. 2*, **1985**, 81, 405.

[22] M. Moskovits, D. P. Dilella and K. J. Maynard, *Langmuir*, **1988**, 4, 67.

[23] R. Foglizzo and A. Novak, *Appl. Spect.*, **1970**, 24, 601.

[24] P. J. Chappell and I. G. Ross, *J. Mol. Spectrosc.*, **1977**, 66, 192.

[25] J. F. Arenas, J. I. Marcos, J. T. Lopez-Navarrete and J. C. Otero, *Collection Czechoslovak Chem. Commun.*, **1986**, 51, 2656.

[26] B. J. Bormans, G. DeWith and F. C. Mijlhoff, *J. Mol. Struct.*, **1977**, 42, 121.

[27] K. K. Innes, I. G. Ross and W. R. Moomaw, *J. Mol. Spect.*, **1988**, 132, 492.

[28] K. B. Hewett, M. Shen, C. L. Brummel and L. A. Philips, *J. Chem. Phys.*, **1994**, 100, 4077.

[29] W. J. Hehre, L. Radom, P. V. R Schleyer and J. A. Pope, *Ab initio Molecular Orbital Theory*, Wiley, New York, Ch. 6, **1985**.

[30] P. Van De Weijer, *Acid-Base Properties of Aza-Aromatics: NMR Investigations and Semi-Empirical Calculations*, **1977**.

[31] Y. Kurita and C. Takayama, *J. Phys. Chem. A*, **1997**, 101, 5593.

[32] M. Hackmeyer and J. L. Whitten, *J. Chem. Phys.*, **1971**, 54, 3739.

[33] I. C. Walker and M. H. Palmer, *Chem. Phys.*, **1991**, 153, 169.

[34] I. Nenner and G. J. Schulz, *J. Chem. Phys.*, **1975**, 62, 1747.

[35] W. Kaim, *Angew. Chem. Int. Ed. Engl*, **1983**, 22, 171.

[36] J. Swartz and F. C .Anson, *J. Electroanal. Chem.*, **1980**, 114, 117.

[37] B. J. Tabner and J. R. Yandler, *J. Chem. Soc (A)*, **1968**, 381.

[38] R. W. Fessenden and P. Neta, *Chem. Phys. Letters*, **1973**, 18, 14.

[39] D. V. Bent, E. Hayon and P. N. Moorthy, *J. Am. Chem. Soc.*, **1975**, 97, 5065.

[40] H. Zeldes and R. Livingston, *Mol. Phys.*, **1974**, 27, 261.

[41] T. Kato and T. Shida, *J. Am. Chem. Soc.*, **1979**, 101, 6869.

[42] V. P.Glazunov and S. E. Odinokov, *Spectrochim. Acta*, **1982**, 38A, 409.

Chapter 5

SERS Studies on the Adsorption of Pyrazine onto Polycrystalline Silver Electrodes

5. SERS Studies on the Adsorption of Pyrazine onto Polycrystalline Silver Electrodes

5.1. Introduction

Surface-enhanced Raman spectroscopy (SERS) is a very powerful technique for the study of adsorption of molecules on metallic surfaces. Earlier controversies about the enhancement mechanism have diminished. There is general consensus that both the electromagnetic and chemical enhancement mechanisms contribute to the overall effect; the predominant mechanism will depend on the nature of the system and on the experimental conditions. However, some fundamental aspects of SERS, including the relation between SERS intensity and both surface coverage and molecular orientation, require further investigation.

An extensive study concerning the relationship between SERS intensity and surface coverage involving the adsorption of pyridine on gold electrodes has been conducted [1,2]. A linear relationship was found between the SERS intensity and the surface coverage to about 60 % of a monolayer for a "unroughened" electrode. Extension of this work requires the SERS study of other molecules, such as pyrazine, on the electrode surface. Preliminary results of the SERS spectra of pyrazine on a gold electrode have been obtained [3]. Progress in understanding the relationship between the SERS intensity of pyrazine and surface coverage is dependent on knowledge of the molecular orientation, and consequently, of the origin of all bands. We have recently identified and assigned all Raman bands of pyrazine and its protonated forms (Chapter 3 and [4]).

The relationship between the vibrational mode activity and band intensity with molecular orientation can be inferred from the application of the SERS selection rules. These can be derived from both the charge transfer (CT) and electromagnetic model (EM) enhancement mechanisms [5]. Pyrazine (pz) adsorption on a metallic surface is a good system to test the application of SERS selection rules derived from these two models.

Several studies of the adsorption and/or application of the SERS selection rules have involved pz on metals [6-13]. However, the literature has revealed several controversial aspects. Differences in the spectral features reported by different workers need to be resolved.

Erdheim et al. [6] reported the SERS spectrum of pz from KCl aqueous solutions adsorbed on silver electrodes. The electrodes were electrochemically activated by potential steps in the presence of pyrazine. The spectrum was dominated by the 1020 and 1597 cm^{-1} bands. Other intense totally symmetrical modes appeared at 636, 1220, and 3066 cm^{-1}. Some forbidden bands in the normal Raman spectrum (NRS) of aqueous pz became active with fair intensity at 440, 800, 1317, and 1488 cm^{-1}. The presence of forbidden bands was explained as resulting from a symmetry lowering of the pz molecule due to the adsorption. Several other unassigned bands were also reported at 670, 1088 and 1560 cm^{-1}. Their potential profiles showed an identical voltage dependence, and all lines reached their maxima between -0.4 and -0.5 V vs. SCE.

The most unusual SERS spectra of pz adsorbed on a silver electrode in 0.1 M KCl aqueous solution were presented by Dornhaus et al. [7]. The electrode was activated by ORCs in the presence of pz. The SERS spectrum was potential dependent, and showed a maximum intensity for all bands at -0.4V vs. SCE. The spectrum was dominated by the 1420 and 1480 cm^{-1} bands. These two modes are forbidden in the NRS of aqueous pz.

Moreover, all A_g modes also emerged as strong bands. Dornhaus et al. claimed to observe practically all bands of pyrazine, including forbidden modes. The spectra were recorded on a time scale of 25 ms, and proved to be time dependent at constant potential, with some relative intensity changes observed during a time period of 4 to 5 hours. The time dependence suggested an orientation rearrangement for the pyrazine molecules on the surface.

The SERS of pyrazine on silver in 0.1M KCl and 0.1 M Na_2SO_4 aqueous solutions was also studied by Otto et al. [8]. The electrode was activated by potential steps in the presence of pyrazine. The excitation profile was obtained, and the relative intensity change with the incident light energy agreed with a photon-driven charge transfer (PDCT) resonance Raman model. New bands due to electrochemical pyrazine reduction showed up at potentials as negative as -1 V vs SCE. They observed that the A_g modes were the most intense. The only other "g" mode observed was the 8b B_{2g} mode at 1518 cm^{-1}. The observed bands at 1081, 1333, and 1412 were assigned as B_{3u} modes numbers 15, 14, and 19b, respectively. A band at 1492 cm^{-1} was assigned as the B_{1u} 19a mode.

Moskovits et al. [9] studied the SERS spectra of both low coverage and multi-layer pyrazine films adsorbed on cold-deposited silver. Again the A_g modes were the most intense. Some band shifts were observed when the low coverage spectra were compared to the multi-layer spectra. The multi layer spectrum was more intense and presented more bands. In this condition, the intensity of the 1020 cm^{-1} band was almost the same as the 1595 cm^{-1} band. However, the 1020 cm^{-1} band was more intense than the 1595 cm^{-1}-band in the monolayer spectrum. The 6a and 9a modes were more intense in the high coverage than in the monolayer spectrum. The differences between the spectra in the two conditions were interpreted as due to a change in the molecule orientation. The pyrazine molecule was thought to adsorb flat at low surface concentrations and edge-on in the multi layer

situation. Nevertheless, it was not possible to confirm that just one orientation was present in each situation, and it was more likely that one was dominant in the presence of the other.

The spectrum of pyrazine on silver colloids was studied by Muniz-Miranda et al. [10]. The 1020 cm^{-1} band was the strongest, followed by the 1220 and the 1597 cm^{-1} bands. The spectrum is similar in terms of relative intensities to pyrazine in aqueous solution. For instance the band at 700 cm^{-1} was stronger than the one at 636 cm^{-1}. The forbidden bands occur at 1362, 800, and 426 cm^{-1}, respectively. The excess of reducing agent used in the colloid preparation decomposed the pyrazine and new bands appeared due to these decomposition products [11]. Some of these bands were assigned to di-hydro pyrazine or its dimer. The possibility of a ring opening process was not ruled out.

Recently, Wu et al. have presented some results of SERS of pyrazine both on silver [12] and on gold [13] electrodes in KCl aqueous solution. The variation of the bond polarizabilities of the adsorbed pyrazine molecules with the applied voltage was calculated from the SERS spectra. This kind of calculation can be used to draw conclusions about the molecular orientation and predominant SERS mechanism. The A_g modes, mainly at 1020 and 1597 cm^{-1}, were most intense. Moreover, the presence of the 1040 cm^{-1} B_{1u} band for silver was also reported. This band was not active in the SERS of pyrazine on the gold electrode. Two more bands at high wavenumbers, 3067 and 3070 cm^{-1}, were observed and assigned as the A_g and B_{1u} modes, respectively. From the polarizability change with potential, they concluded that pz adsorbs end-on. They state that the presence of the 1040 cm^{-1} band is evidence that the molecule adsorbed with this orientation and, as this band does not appear for gold, one must be careful when inferring conclusions about molecular orientation on the electrode surface from the SERS results. They also imply that the SERS of pyrazine on silver has a large contribution from the CT enhancement mechanism, but

the electromagnetic mechanism is the most important for accounting for the SERS of pyrazine on gold electrodes.

The objective of this work was to rationalize these SERS results of pz adsorbed on silver electrodes. Some of the unusual bands and controversial conclusions obtained in the previous works will be discussed. Assignments for the surface-enhanced pz bands will also be reviewed. Most of the results presented in this chapter has been published elsewhere [14, 15].

5.2. Experimental

5.2.1. Reagents

The following chemicals were used without further purification: pyrazine 99+% from Aldrich, KBr and KCl AnalR grade from BDH. All solutions were prepared with Milli-Q-water.

5.2.2. Electrochemistry

The three electrode spectroelectrochemical cell has been described elsewhere [16]. A potentiostat PAR model 273 was used to control the applied potential of the working electrode. The counter electrode was a 0.3 mm platinum wire (99.9%). A saturated calomel electrode (SCE) was used as reference. The working electrode was made from 99.9 % polycrystalline silver rod. A silver disk of ca 2 mm radius was mounted in a Teflon holder. The working electrode was first polished with emery-paper and then, with progressively finer grades of alumina powder down to 0.3 μm. The electrode was rinsed

with an abundant amount of Milli-Q-water, sonicated, rinsed again, and transferred to the spectroelectrochemical cell. The solution was degassed with Ar for half an hour prior to the experiment, and a gentle stream of Ar was maintained during data acquisition.

5.2.3. Activation Procedures

The process of roughening the metal surface electrochemically, in order to create the necessary SERS active sites, is called the activation procedure. In this work, two distinct activation procedures were used.

The first activation procedure consisted of applying several oxidation-reduction cycles (ORCs) to the silver electrode in an aqueous solution containing 1.0 M halide. The scan rate was 5 mV/s and the laser light was illuminating the surface during the cycles. Typical cyclic voltammograms for silver in both bromide and chloride are presented in Figure 5.1. Then, the potential immediately after the silver ion reduction was held, and pz was added to the system using a syringe. This procedure yields weaker SERS signals; however, it avoids the activation of bands due to trapped pyrazine or from pyrazine decomposition products, and the SERS spectrum is also time independent. This procedure will be referred to in the text as "activation in the absence of pyrazine ".

In the second activation procedure, oxidation-reduction cycles were performed on the silver electrode immersed in an aqueous solution containing 1.0 M halide and the desired pz concentration, the other conditions being the same as above. The presence of pz does not provoke significant changes in the voltammograms presented in

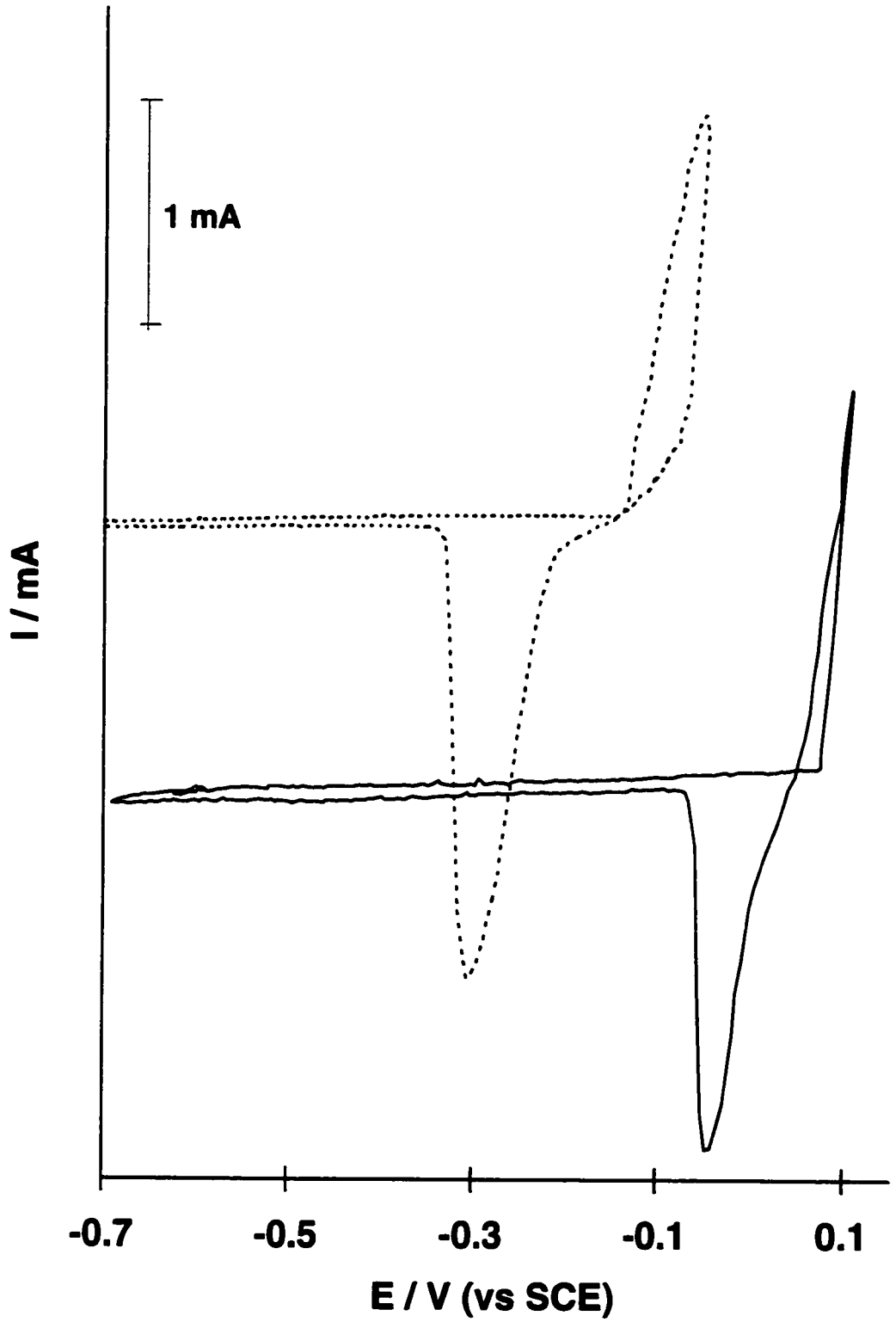

Figure 5.1: Activation ORCs. Solid line: Ag/KCl 1.0 M; from -700 to +150 mV, 5 mV/s. Dotted line: Ag/KBr 1.0 M; from -700 mV to -50 mV, 5 mV/s.

Fig. 5.1. The well known time dependence of the SERS spectrum when the electrode is activated this way was avoided by performing an ORC and stopping at the desired potential before each acquisition. This procedure gives reproducible and time-independent spectra [1]. This method will be referred to in the text as "activation in the presence of pyrazine".

5.2.4. Raman Spectra

Raman spectra were measured with a Dilor OMARS 89 spectrometer with an optical multichannel analyzer. The intensified diode array (512 diodes) detector was thermoelectrically cooled to ca -10 ^{o}C. The spectrometer was interfaced to an IBM PC-AT computer. Data were transferred to an IBM 486 computer on which baseline correction, band-fitting, and plotting programs were available. Spectra were excited by the 514.5 nmline (100 mW at the head) from a Coherent Innova 70 argon ion laser, chopped at a 1-s cycle, as required by the Dilor spectrometer. The acquisition time was 1 second, and 10 accumulations were performed for each spectrum.

5.3. Results and Discussion

This section will be divided into five parts. In *part I*, the general features of the SERS spectrum and its potential dependence will be discussed. *Part II* gives some general background on the SERS selection rules, which will be used in the discussion of the molecular orientation of pz presented in *part III*. The electrochemical reduction of pz in halide medium will be discussed in *part IV* and the comparison of the present data to previous results presented in the literature will be given in *part V*.

5.3.1. Part I: SERS of pyrazine and its dependence on the applied potential

In Figure 5.2, regions 1 to 3, the normal Raman spectra (NRS) of pz and pzH^+ cation in aqueous solution are compared to the SERS spectrum of pz on the silver electrode. For the pzH^+ cation, the binding of a hydrogen to one of the nitrogen atoms leads to a symmetry lowering which may be similar to an end-on adsorption of the pz molecule on an electrode surface. Spectra of aqueous pyrazine and its protonated forms have been described elsewhere [4]. The Raman intensities presented in Figure 5.2 are arbitrary, and conveniently chosen for a better comparison. Examining those spectra, one can notice that the peak positions do not shift very much on adsorption from the values for the aqueous pz species. Regarding peak positions, it seems that the spectrum of adsorbed pyrazine resembles that of aqueous pz rather than aqueous pzH^+. Adsorption to the electrode surface relaxes the selection rules for Raman, and some NRS forbidden bands of aqueous pz becomes active. The appearance of forbidden bands is anticipated by both the electromagnetic and the chemical enhancement mechanisms [5]. In order to facilitate the following discussion, schematic representations of some pyrazine vibrational modes, in analogy to the benzene modes presented by Lord et al. [17], are also displayed in Fig. 5.2.

Spectra of the low frequency region, Figure 5.2 - Region 1, for aqueous pz species solutions are not shown, because no bands were observed in that region. On the other hand, two ring deformation modes are observed from the electrode surface: the A_u ring puckering at ~ 360 cm^{-1}, which is only observed when the electrode is activated in the presence of pyrazine, and the B_{2u} ring deformation at ~ 430 cm^{-1}. It is important to point out that the ~ 360 cm^{-1} band is a silent mode even in the IR spectrum, and several

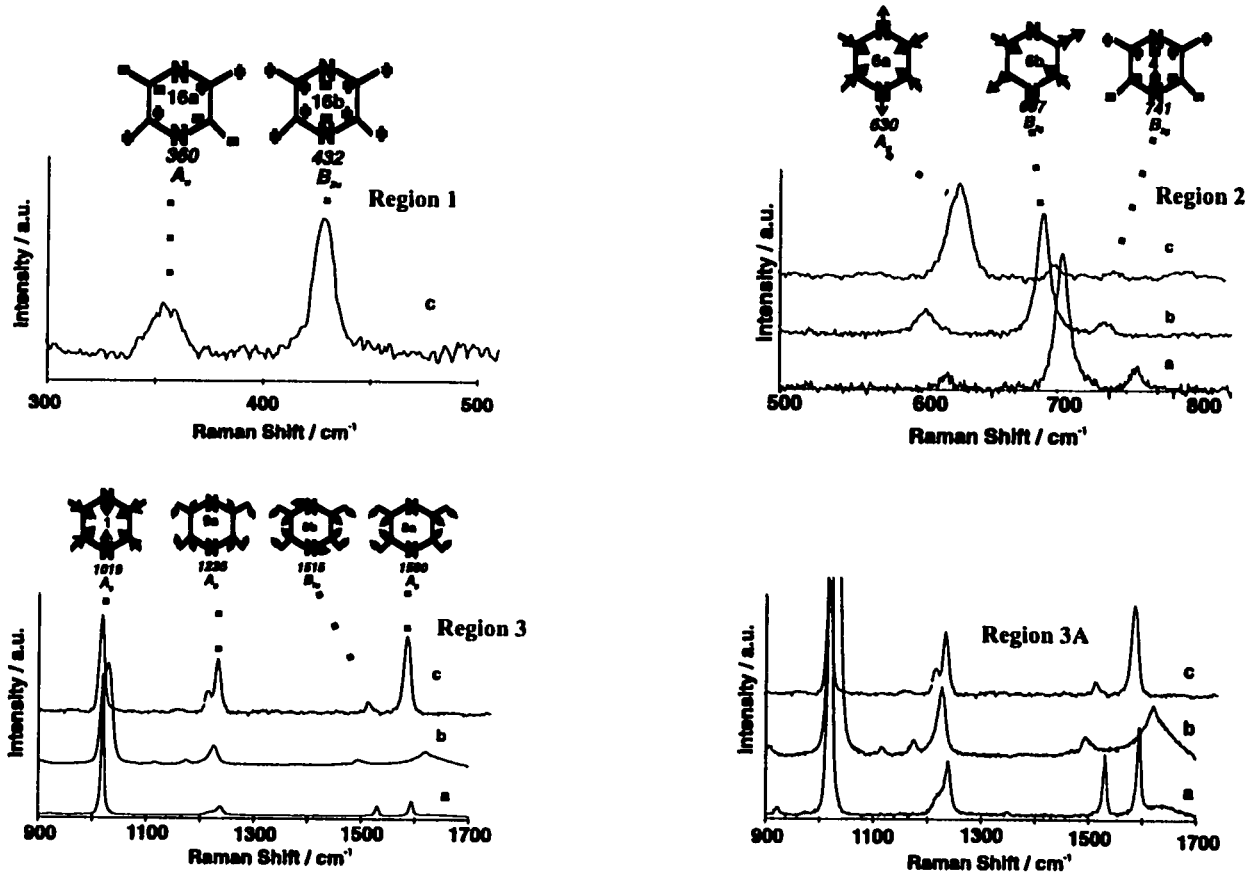

Figure 5.2: Spectra of aqueous pz solutions and SERS from the silver electrode, for three spectral regions, designated 1, 2, 3 and 3A. a) 1 M aqueous pz solution; b) 1 M aqueous pz in 3 M HCl solution. The spectral features are due to the monoprotonated pz cation; c) SERS spectrum of pz on a silver electrode from 1 M KBr + 0.1 M pz solution. E = -600 mV, region 3A is an enlarged version of region 3. The schematic representations of pz's vibrational modes are also presented. The Wilson numbering scheme is given within each representation. The number underneath each representation is the SERS vibrational frequency in wavenumbers.

works only report its estimated or calculated value [18]. Hence, the relative enhancement of these two modes is very significant.

In Figure 5.2 - Region 2 the most intense peak of the SERS spectrum is due to the A_g (6a) ring mode at 630 cm^{-1}. This band is weak for both the aqueous pz (at 620 cm^{-1}) and aqueous pzH^+ solutions (at 606 cm^{-1}). The dominant band from aqueous solutions in this region is the B_{2g} (6b) ring mode, which shows up at 702 cm^{-1} for the aqueous pz and 690 cm^{-1} for the aqueous pzH^+, respectively. This mode gives a weak feature at ~ 700 cm^{-1} from the electrode surface.

From the spectra in Figure 5.2 - Region 3 and Region 3A, one can conclude that the relative intensity of the ring breathing mode decreases substantially on the electrode surface at -600 mV when compared to aqueous pz. For instance, from the aqueous pyrazine solution the A_g (1) ring breathing mode at 1019 cm^{-1} is about 6 times greater than the A_g (8a) symmetrical in-plane CH bending mode at 1593 cm^{-1}, and from the aqueous pyrazinium solution the ring breathing mode at 1020 cm^{-1} is 5 times greater than the in-plane CH bending mode, 1634 cm^{-1}. From the electrode surface, however, both modes have approximately the same intensity at the given potential. Nevertheless, it is also important to point out that the relative intensity of bands in the SERS spectrum is highly potential sensitive. For instance, the ~ 1590 cm^{-1}- band is stronger than the 1020 cm^{-1} - band at -750 mV in bromide medium. It is also important to note that the free pz B_{1u} (12) mode, which is Raman forbidden but shows up in the aqueous pzH^+ at 1030 cm^{-1} as a very strong band, does not appear strongly from the electrode surface; its presence is observed in certain conditions as a weak band at 1040 cm^{-1}.

Two bands are observed, Figure 5.2 - Region 3A, in the electrode surface spectrum at 1215 cm^{-1} and 1235 cm^{-1}. The former band was assigned as a combination (11+16b), and the latter to the fundamental 9a δCH [4]. These two bands are similar in frequency to those observed in the aqueous pz spectrum, but they are better resolved in the spectrum of pz adsorbed on the electrode surface. The large intensity presented by this combination band can be attribute to a Fermi resonance phenomenon, because both the fundamental and the combination mode have the same symmetry (A_g) and similar wavenumbers. All the wavenumbers of the bands observed from the electrode surface are summarized in Table 5.1.

Figure 5.3, Regions 1 and 2, show spectra of pyrazine adsorbed from 1.0 M KCl solutions to the silver electrode at several potentials. The spectra presented in Figure 5.3 were obtained after an activation procedure in the absence of pyrazine; however, the overall features of these spectra do not change for the different surface preparations (activation procedures), although the bands obtained after ORCs in the presence of pyrazine are more intense than the ones obtained by electrode activation in the supporting electrolyte and subsequent addition of pz. The only band which shows up in the former treatment and not in the latter is the weak 360 cm^{-1}-band.

For a given excitation energy, the potential where the spectral intensities maximize (E_{max}) is dependent on the activation procedure, on the halide nature, and on the halide concentration. Generally, E_{max} is 50 mV more negative when the electrode is activated in the presence of pz. Figure 5.4 shows potential profiles (SERS intensity vs potential plots) for the ring breathing mode of pz (ca. 1020 cm^{-1}) adsorbed on silver from bromide and chloride medium. It can be observed that the SERS intensities maximize at more negative potentials for pz adsorbed from bromide medium than for pz adsorbed from chloride medium.

Table 5.1: Vibrational wavenumbers (cm^{-1}) for the SERS spectrum of pyrazine on silver electrodes: Assignments and comparison to the literature values.

Assignment	This work [14] [a]	ref. [6] [a, +]	ref. [7] [a]	ref. [10] [b, +]	ref. [8] [a]	ref. [9] [c]	ref. [43] [d]
A_u (16a)	360 vw		362 (w)			352 (m)	
B_{2u} (16b)	432 w	440 (2)	436 (m)	426 (1)		417 (m)	
A_g (6a)	630 m	636 (16)	635 (s)	636 Ag (1)	629 (w)	615 (m)	
		670 (4) *	662 (s) *				
			682 (s)				
B_{2g} (6b)	697 w	698 (2)	700 (m)	700 (5)		700 (w)	
B_{3g} (4)	741 w	743 (3)	744 (m)			753 (w)	
			764 (w) *				
B_{2u} (11)	797 w	800 (1)	797 (w)	800 (0.5)		792 (m)	785 (?)
B_{1g} (10a)	916 vw	897 (1)	916 (m-s)	916 (4)		922 (w)	927
						972 (w)	
			966 (vw) *				
A_g (1)	1019 s	1020 (55)	1018 (vs)	1022 (100)	1019 (vs)	1015 (s)	1015
B_{1u} (12)	1040 vw		1038 (vw)			1031 (w)	1018 (?)
		1088 (4) *	1069 (w) *		1081 (m) *	1088 (m)	
B_{1u} (18a)	1116 vw	1123 (4)	1121 (w)	1124 (3)			
			1164 (vw) *				
A_g (11 + 16b)	1215 m	1220 (15)		1222 (25)			
A_g (9a)	1235 s	1237 (10)	1242 (s)	1240 (8)	1229 (m)	1233 (m)	1240
B_{2g} (3)	1324 vw	1317 (4)	1340 (vw)		1333 (w)	1347 (w)	
				1362 (1)		1360 (w)	
			1420 (vs)		1412 (vw)	1410 (m)	
		1488 (9) *	1485 (s) *		1492 (m) *	1484 (m)	
B_{2g} (8b)	1514 w	1519 (5)	1520 (w)	1516 (10)	1519 (m)	1522 (m)	1524
		1560 (2)					
A_g (8a)	1587 s	1597 (59)	1590 (vs)	1594 (13)	1597 (vs)	1578 (s)	1583
B_{2g} (7b)	3020 m		3031 (vw)				3012 (?)
A_g (2)	3030 s		3050 (m)			3055 (w)	
		3066 (14)	3060	3072 (7)			
			3181 *				

Intensities: v - very; w - weak; s - strong and m - medium. + relative intensity in parenthesis.

[a] SERS of pyrazine on silver electrode from halide medium.
[b] SERS of pyrazine on silver colloid
[c] SERS of pyrazine on coldly deposited silver
[d] Normal Raman Spectrum of pyrazine on silver
* Possible bands due to trapped pyrazine or decomposed pyrazine species (see text).

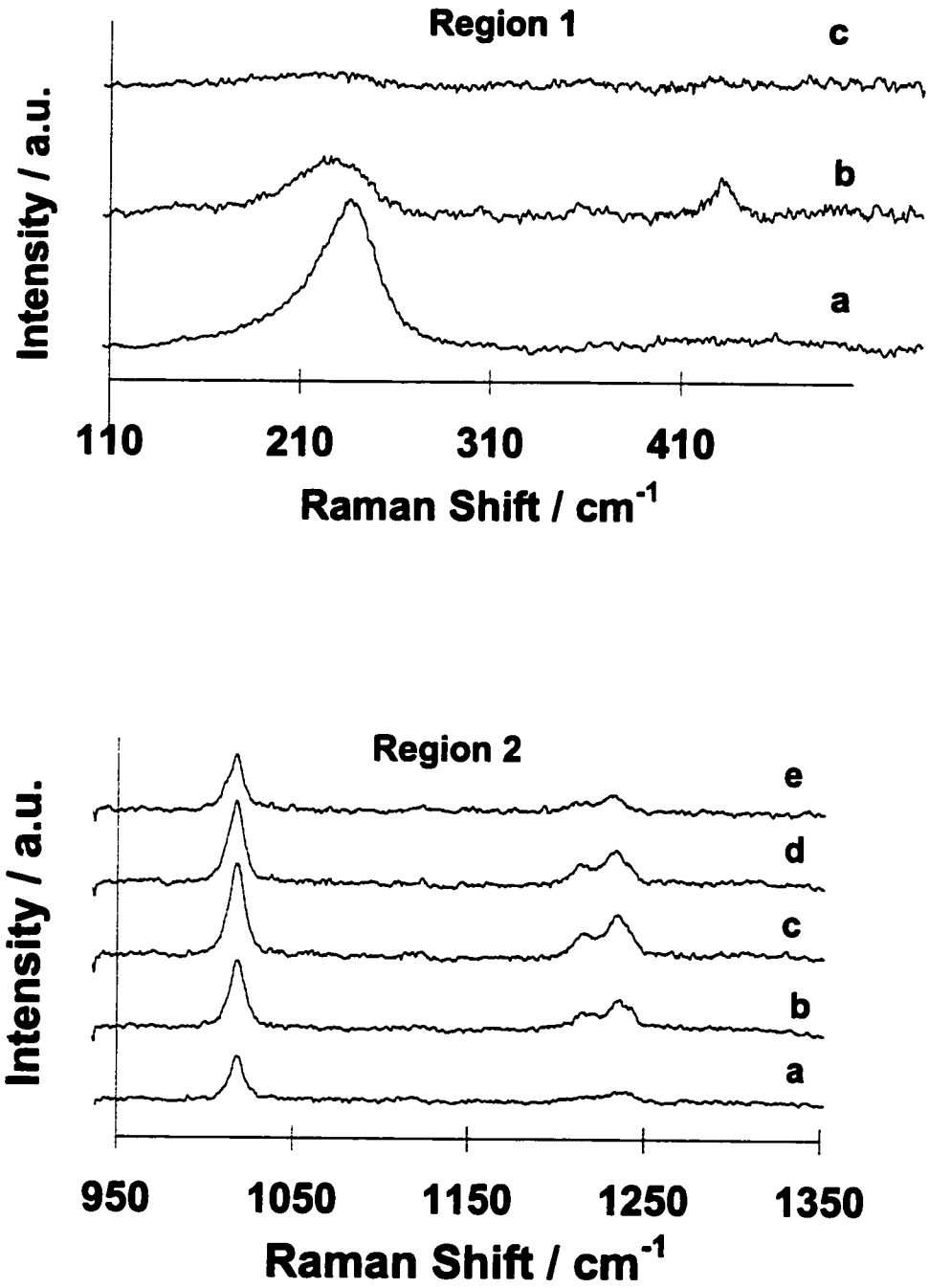

Figure 5.3: Spectra of pz adsorbed on a silver electrode at designated potentials. 1 M KCl + 0.1 M pz solution. Activation procedure in the absence of pz. The spectra at low frequencies (region 1) are presented after subtraction of the Rayleigh wing. Region 1: a) -200 mV; b) -600 mV; c) -800 mV. Region 2: a) -200 mV; b) -400 mV; c) -500 mV; d) -600 mV; e) -700 mV.

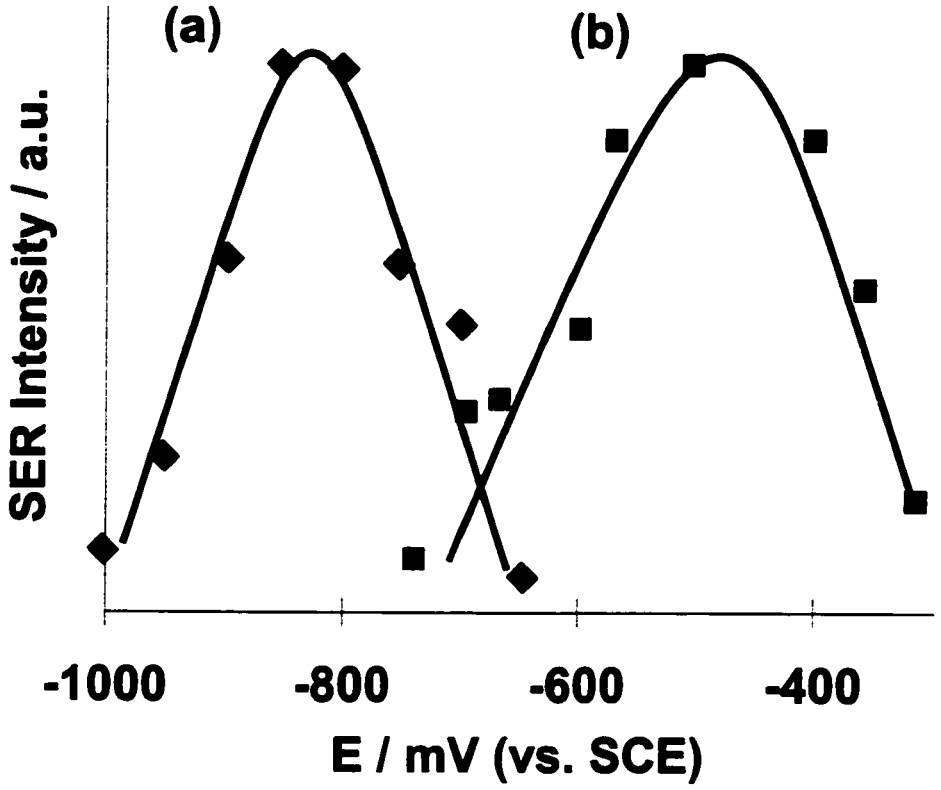

Figure 5.4: Potential profiles of the ring breathing mode of pz. Pz adsorbed on a Ag electrode. (a) 1.0 M KCl + 10 mM pz; (b) 1.0 M KBr + 10 mM pz.

The E_{max} values obtained when the electrode is activated in the presence of pz range between ca. -750 and -800 mV for 1.0 M KBr and from ca. -450 to -500 mV for 1.0 M KCl.

Broad envelopes, containing at least two bands, are observed at ~ 240 cm^{-1} in chloride medium (Figure 5.3 - Region 1) and at ~ 150 cm^{-1} in bromide medium. These bands are assigned as metal-halide stretch vibrations and they are also potential dependent. The presence of multiple bands in the metal-halide region were reported before [19]. These bands suggest different "types" of silver-halide vibrations, and were interpreted as an indication of distinct "active sites" or silver-halide clusters at the rough surface [20]. The intensities of these Ag-halide bands decrease as the potential becomes negative and they are rather weak at the potential where pz bands maximize. In the potential range where SERS bands can be observed for both the pz and the halide, it is quite clear that the two species are coadsorbed on the electrode surface.

The dependence of the ~ 1020 cm^{-1} pyrazine band intensity from the ring breathing mode on the potential for three pz concentrations in 1.0 M bromide medium is presented in Figure 5.5. From the analysis of this Figure, one can claim that the E_{max} slightly moves to more positive values as the pz concentration increases; however, the shift in the E_{max} presented there is within the experimental uncertainty. The pz concentration also affects the half width of the potential profiles. For instance, the half width values range from ca. 40 mV for 0.0125 M pz to ca. 300 mV for 0.075 M pz in 1.0 M KBr medium. The dependence of band intensities on applied potential for some important bands in the same spectrum is compared in Figure 5.6. It can be noticed that all bands of adsorbed pyrazine maximize at the same potential, close to the potential of zero charge (pzc). Figure 5.7 presents potential profiles for pz in bromide medium at two distinct excitation wavelengths. The profiles are wavelength independent.

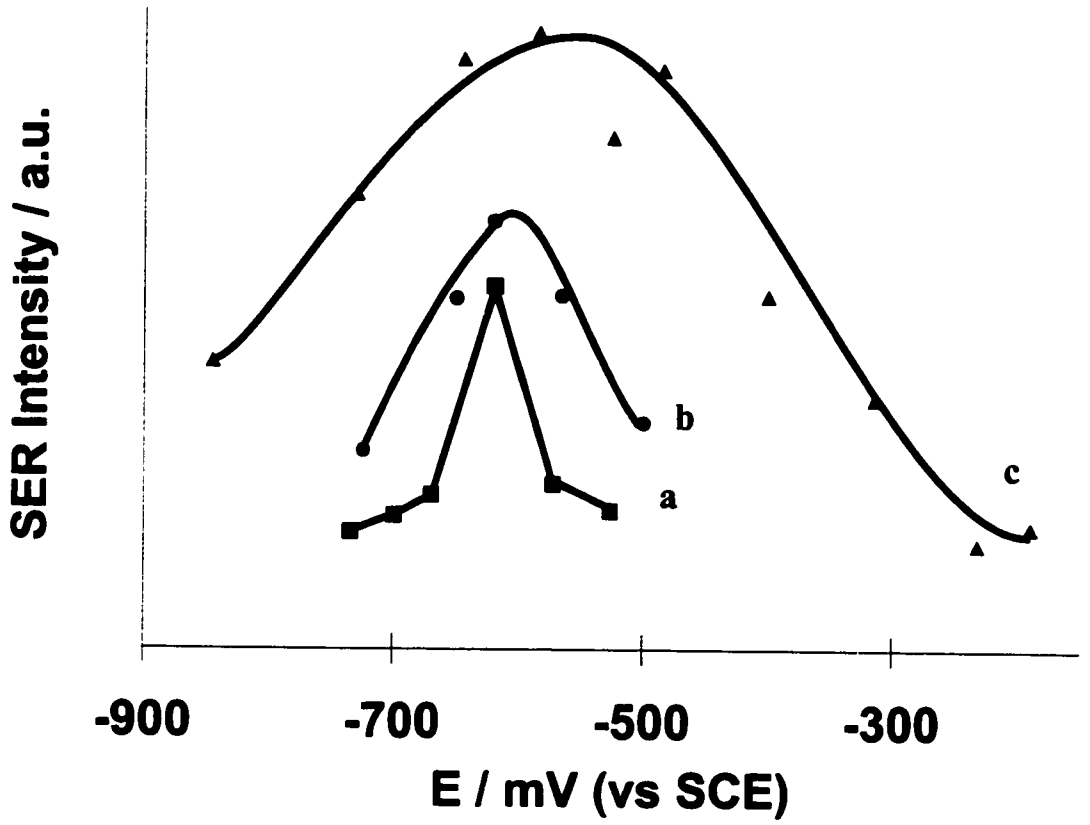

Figure 5.5: Potential profiles for the ca. 1020 cm^{-1} band intensity for three pz concentrations. (a) 12.5 mM; (b) 37.5 mM; (c) 75 mM. Activation in the absence of pz, using 1.0 M KBr.

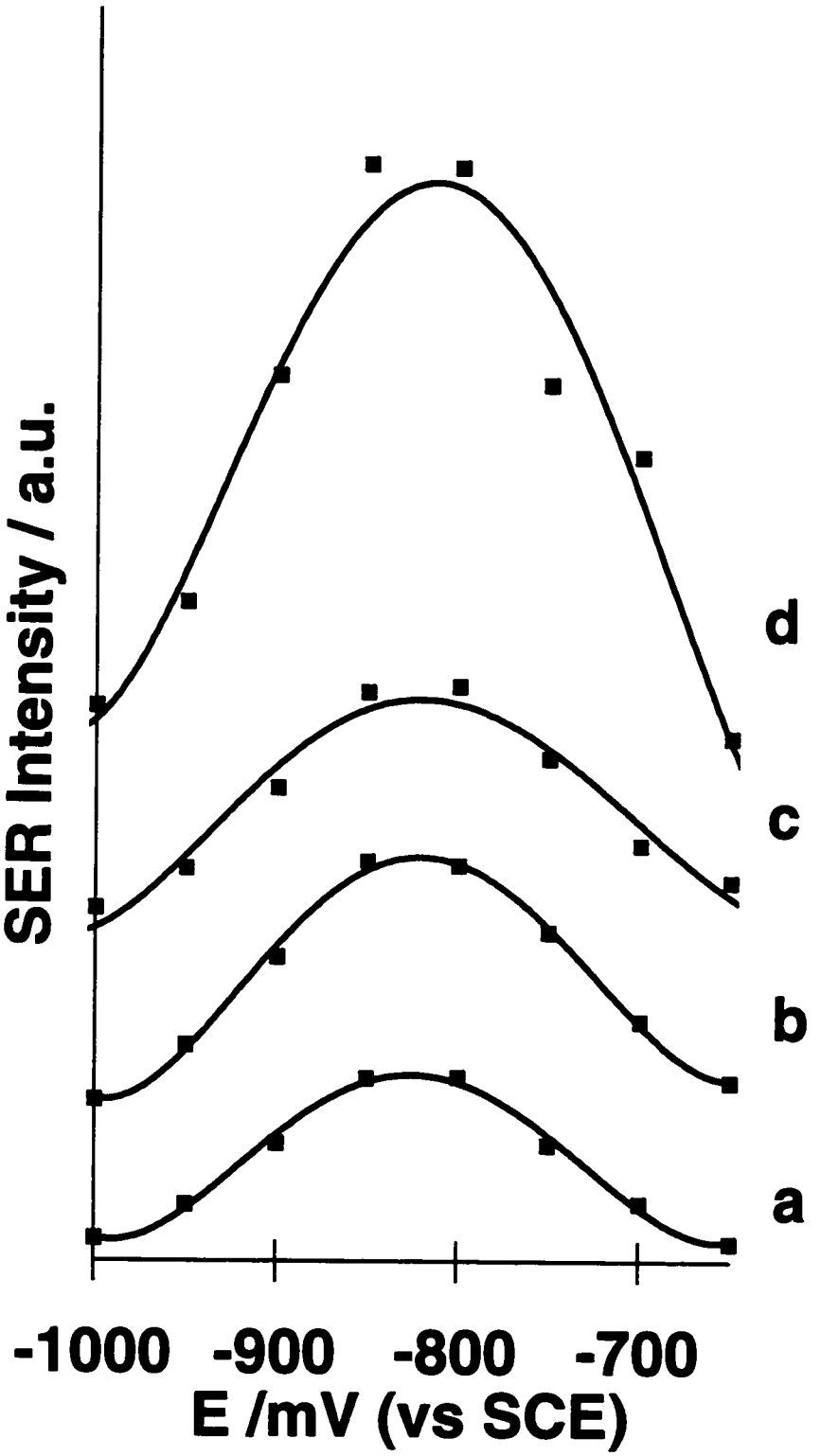

Figure 5.6: Potential profiles of adsorbed pz SERS bands.
a) 630 cm^{-1}; b) 1235 cm^{-1}; c) 1020 cm^{-1}; d) 1590 cm^{-1}.

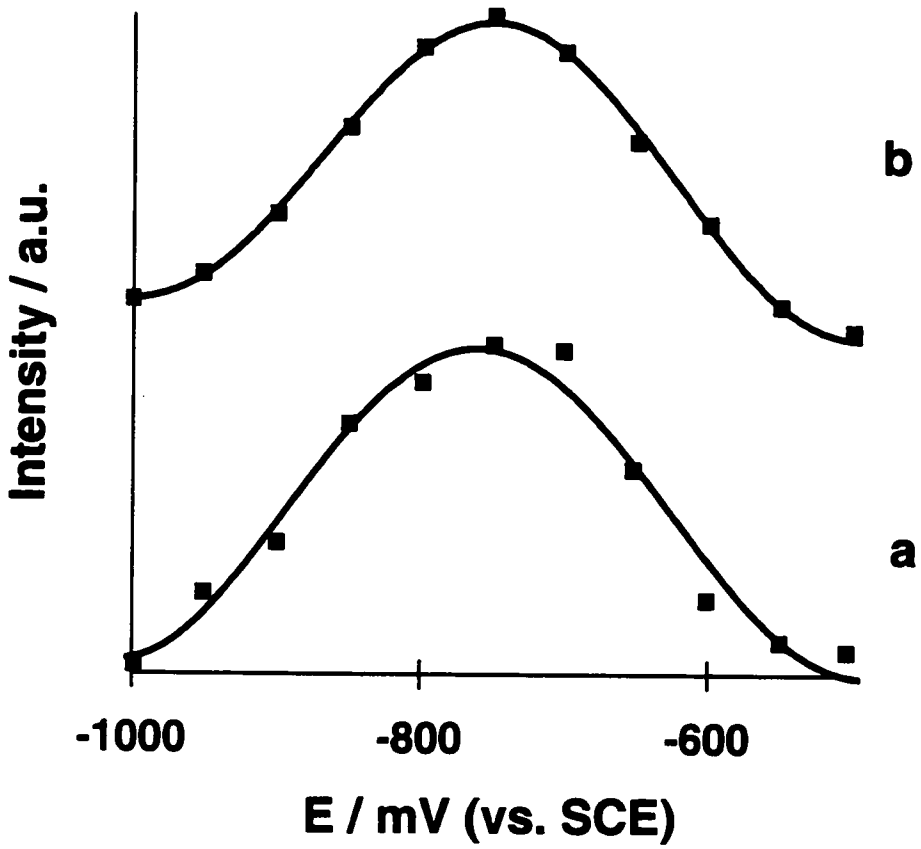

Figure 5.7: SERS potential profiles of pz obtained with different excitation energies. 1590 cm^{-1} - band. a) 613. 5 nm; b) 651.55 nm. Activation in the presence of pz

The SERS results have been interpreted in the literature in terms of the two most accepted theories for the enhancement - the charge transfer mechanism (CT) and the electromagnetic model (EM). In the CT model, the Raman signal enhancement occurs due to a resonance involving the incident radiation and a CT transition between the Fermi level of the metal and the frontier orbitals from the adsorbed molecule. The EM mechanism takes into account the enhancement of the local electromagnetic field induced by the coupling of the incident light with the local resonances present on the metallic surface known as the surface plasmons (SP). A recent and comprehensive discussion of the general features from these models can be found elsewhere [16, 21]. Both mechanisms contribute to the overall enhancement, which makes it difficult to quantify the individual contributions from each model, unless one deals with a situation where one of them is predominant. Hence, considerations from both mechanisms will be taken into account in the following discussion about the SERS results presented in this work.

A common feature which can be observed on the potential profiles presented in Figures 5.4 to 5.7 is the "bell shaped" SERS intensities versus potential curves. The EM model predicts that the enhancement should be potential independent (the potential-induced changes in the metallic surface does not significantly affect the dielectric constant of the bulk metal), and thus the intensity changes with potential would be due to the variation of surface coverage. In fact, the surface coverage versus electrode potential plot for a neutral organic molecule is expected to be "bell shaped", with a maximum around the pzc [22]; moreover, the half widths of these plots are expected to increase and their maxima shift slightly to positive potentials with the increase of the adsorbate concentration [22]. All these predictions agree with Figure 5.5. However, one must be reminded that a linear relationship between SERS intensity and the amount adsorbed does not hold for higher surface coverage values [1, 2]. The differences in the E_{max} obtained for distinct halide media can also be understood under the EM arguments. Supposing that in the

absence of specific adsorption the electrode charge is $\sigma_m{}^o$. In the presence of specifically adsorbed halide, the negative charges at the surface induce a positive counter charge in the polarizable electrode and the electrode charge shifts to a more positive value, $\sigma_{m'}$. In other words, the point of zero charge (pzc) of the electrode shifts to more negative potentials. This can explain the reason for the shift of the maximum in the potential profiles (E_{max}) to negative values with the replacement of Cl^- by Br^-, as observed in Fig. 5.4; thus, bromide ions adsorb more strongly to the surface than chloride ions. The CT mechanism also predicts a symmetric "bell shaped" curve for the potential profile [23]. In this case, the potential changes would tune the CT process into and off the resonance situation. The resonance condition for a CT transition is given by the equation [24]:

$$\Delta E_{CT} = h\nu_{exc} \qquad (1)$$

Here ΔE_{CT} is the energy gap between the Fermi level of the metal and the LUMO (or HOMO) orbital from the adsorbed molecule, and $h\nu_{exc}$ is the energy of the incident photon. The shift in the pzc for different anions also changes the potential where the resonance condition is satisfied; therefore a more negative value for E_{max} is expected in bromide than in chloride (Fig. 5.4).

The half-width of the potential profiles is frequently used to determine the contribution of the CT mechanism in SERS [25, 26]. The energy width of the CT resonance ($\Delta h\nu_{exc.}$) is given by equation (2) below [26]:

$$\Delta(h\nu_{exc.}) = \left(\frac{d(\Delta E_{CT})}{dE_{max.}}\right)\Delta E \qquad (2)$$

Hence, the CT energy width is proportional to the slope of the excitation energy ($h\nu_{exc.}$) vs. maximum potential (E_{max}) (excitation profile) multiplied by the half-width of the potential profile (ΔE). The half width of the potential profiles and the surface coverage do not change with the excitation energy [27]; therefore, based on the CT mechanism, our results presented in Figure 5.5 reflect a systematic change in the width of the CT energy band with the pyrazine concentration. The surface concentration of pz depends on the amount of pz in solution. When the surface concentration of pz is small, the CT process occurs from more localized states; as the surface concentration of pz increases, the surface becomes more ordered. In the latter situation, more mixing of the molecular electronic states is allowed. This would promote the appearance of electronic bands rather than defined states. This would explain the broadening of the potential profiles with the increase in the pz concentration by the CT model.

The EM enhancement depends only on the local electromagnetic field, and therefore, all vibrational modes of the same symmetry species should be uniformly enhanced (consistent, of course, with the SERS selection rules) with respect to the applied potential. This prediction is also confirmed in Fig. 5.6, which shows that the SERS bands of pyrazine maximize at the same potential. A different enhancement for different modes at different potentials may be evidence for the CT mechanism, following the CT relaxation through different normal coordinates. This would lead to different E_{max} values for different vibrational bands. However, this was not observed in this work.

The independence of the E_{max} with the energy of the excitation light, presented in Fig. 5.7, is expected from the SERS electromagnetic model. However, this issue may also be addressed invoking the CT theory. In this case, the E_{max} should depend on the energy of the incident light; however, the slopes from the $h\nu_{exc.}$ vs. E_{max} lines presented by Thietke

et al. [8] for the SERS spectrum of pyridine seem to be dependent on the nature of the anion. The slopes $(d(h\nu)/dE_{max})$ observed by Thietke et al. [8] increase in the order: SO_4^{-2} < Cl^- < Br^-. Furtak and Macomber [27] also found an increase in the slope $(d(h\nu)/dE_{max})$ for pyridine with increase of the Cl^- concentration. These results suggest that the dependence of E_{max} on excitation energy is a function of the amount of specifically adsorbed anions on the metallic surface. The explanation for that, given by Furtak and Macomber [27], is that anion adsorption induces a positive charge on the electrode, which leads to an increase in the ΔE_{CT}. Hence, a small dependence of the E_{max} on the excitation energy is expected for the SERS spectrum in 1.0 M halide solutions as presented in Figure 5.7. Therefore, the SERS results observed in this work are consistent with both enhancement mechanisms. Despite the indication that the EM arguments seem to be more reasonable and straightforward, it is not possible to determine how much it contributes to the overall intensity based on these experimental data.

5.3.2. *Part II: SERS Selection Rules*

The presence of the surface can modify both the activity and the intensity of a given vibrational mode. The vibrational spectral features can be very useful for determining molecular orientation on a surface. The most straightforward surface selection rule states that only vibrational modes with dipole components perpendicular to the surface will be active. This selection rule, completely true for IR and EELS spectroscopies, is illustrated in Figure 5.8. However, the metals' electrical conductivities are not as high in the visible spectral region as in the IR, and consequently the parallel components molecules do not vanish completely in the visible region. Therefore, this selection rule does not apply exactly to surface Raman spectroscopy. Moreover, in Raman spectroscopy one must consider the polarizability tensor, α, rather than the dipole moment and, in the specific case of SERS, one is working with a very roughened surface rather

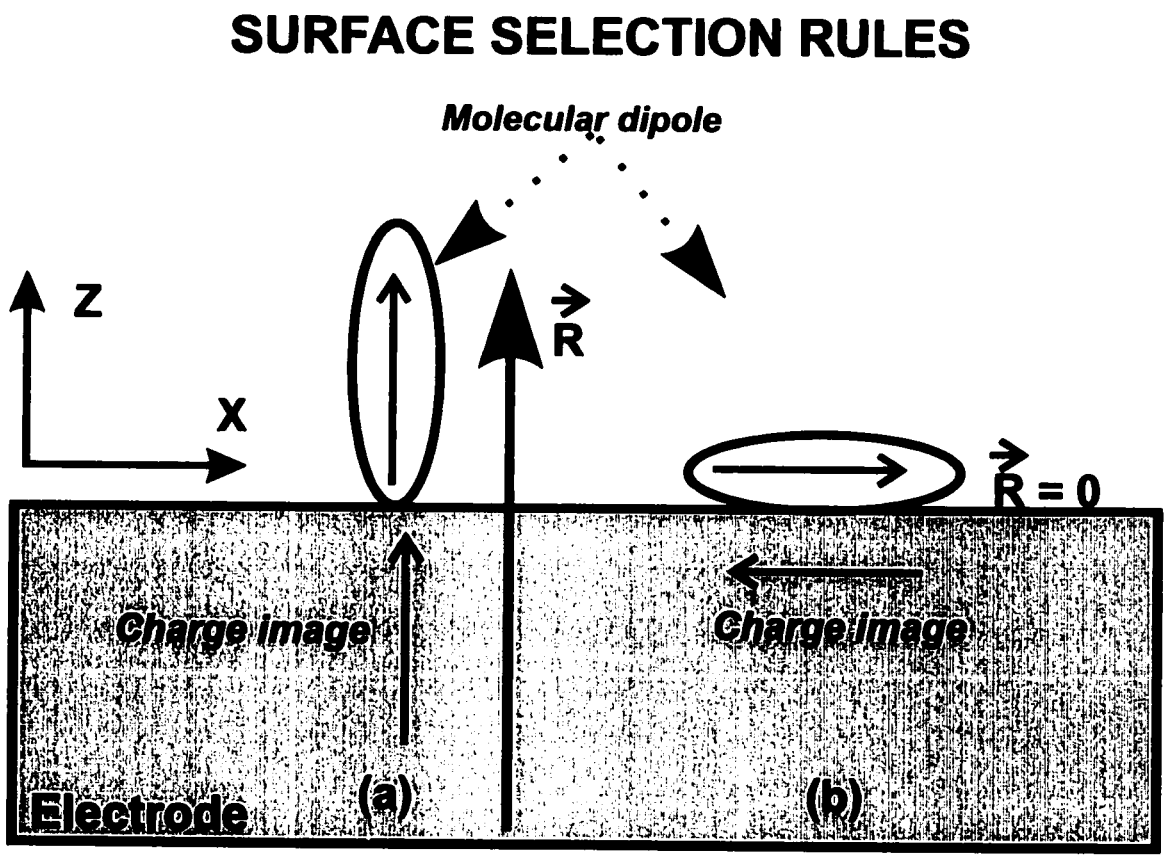

Figure 5.8: Surface selection rules for IR from the image-charge theory. In this model, the electrons inside high conductivity metals will suffer a rearrangement in order to screen the external charges. (a) The molecular dipole is perpendicular to the surface. This leads to a resultant dipole perpendicular to the surface (in the Z direction). (b) The molecular dipole is parallel to the surface. The dipole image in the metal cancels the molecule's dipole, and the resultant is null. Hence, only vibrational modes with a molecular dipole (or dipole changes) component perpendicular to the surface will have some activity.

than a smooth, mirror-like one. These characteristics of enhanced Raman spectroscopy make the surface selection rules more complicated than for IR. A very comprehensive description of the SERS selection rules can be found in a review by Creighton and the references therein [5]. The objective of this section is to outline the salient parts of the SERS selection rules which are important to the understanding of the following part of this work.

For a situation where only the electromagnetic mechanism (EM) is important, a SERS selection rule can be exactly derived [5]. Using the Cartesian coordinates given in Figure 5.9, an expression for the effective polarizability (equation (3), below) was derived by Creighton[5]:

$$\alpha_{eff} = \frac{9}{(\varepsilon_i + 2)(\varepsilon_s + 2)} \begin{pmatrix} \alpha_{XX} & \alpha_{XY} & \varepsilon_s \alpha_{XZ} \\ \alpha_{YX} & \alpha_{YY} & \varepsilon_s \alpha_{YZ} \\ \varepsilon_i \alpha_{ZX} & \varepsilon_i \alpha_{ZY} & \varepsilon_i \varepsilon_s \alpha_{ZZ} \end{pmatrix} \quad (3)$$

Here X, Y, and Z correspond to the coordinates referenced to the electrode surface, α is the Raman polarizability change, ε is the dielectric constant, and the subscript i and s stands for incident and scattered light, respectively. It is clear from the expression above that the enhancement factor can be different for each vibrational mode, depending on the values of the coefficients ε_i and ε_s. Usually the incident and the scattered light have similar wavenumbers, and hence, as a good approximation, one can consider: $\varepsilon_i \approx \varepsilon_s \approx \varepsilon$. Assuming that the direction of the vibration determines the contribution from the polarizability tensor one can find a set of SERS propensity selection rules with some similarity to the IR. For instance, it may be seen from equation (3) that modes transforming as α_{YX}, α_{YZ} and α_{ZZ} are enhanced by the relation $1: |\varepsilon|^2: |\varepsilon|^4$ for excitation

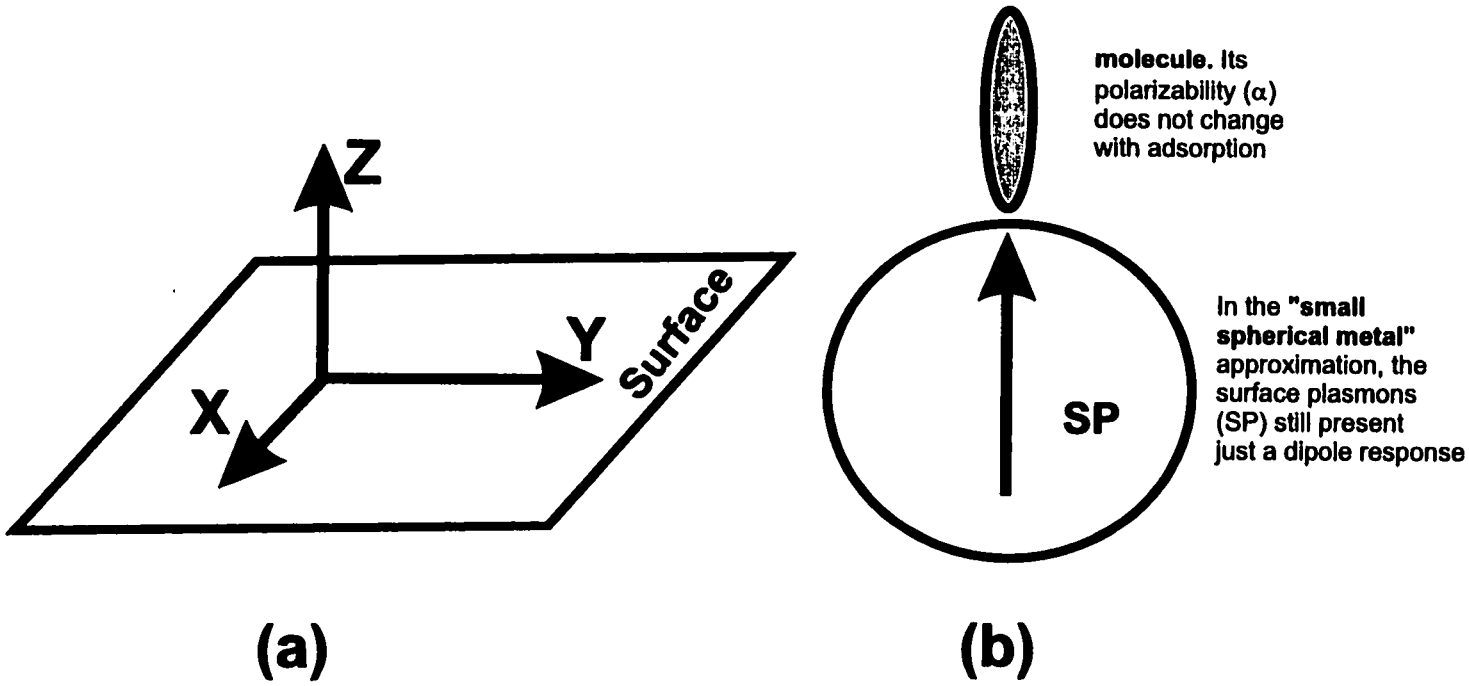

Figure 5.9: (a) The Cartesian coordinates with reference to the electrode surface (X, Y, Z). (b) The molecule adsorbed to a small metal sphere model for derivation of the SERS selection rules.

wavelengths where $|\varepsilon|^2 > 1$. In other words, the vibrational modes perpendicular to the surface must dominate the SERS spectrum. The generalization for any rough surface is straightforward and is demonstrated elsewhere [5].

The appearance of normally Raman forbidden bands in the SERS spectrum can also be explained by purely EM arguments [28]. When an inhomogeneous electromagnetic field bathes the molecule adsorbed on the metallic surface, the induced dipole moment (μ) is given by the expression [29]:

$$\mu = \alpha E + \frac{1}{3} A \nabla E \qquad (4)$$

Here A is a third rank tensor, called the quadrupole polarizability, operating over the field gradient. This tensor transforms as the hyperpolarizability, but it has a completely different physical meaning. α is the polarizability, E is the electric field and ∇E is the field gradient. The vector and tensor representations of the Cartesian components are omitted for simplification. The second term in the induced dipole expression is very important for rough surfaces and its contribution decreases with the distance from the electrode surface. The tensor A transforms as a product of three translations. Considering an image-charge approach, the translations in the X and Y direction should yield a $-X$ and $-Y$ image inside the metal (see Fig. 5.8b). The Z direction translation vector, however, would have an image with the same sign and intensity yielding a positive resultant (Fig. 5.8a). As the quadrupole polarizability can be thought of as a product of three translations, the products that do not change sign on the image-charge transformation would be active [28]. For instance, the A_{ZZZ}, A_{ZXY}, A_{YYZ}, and A_{XXZ} should be surface active and the A_{XXX}, A_{YYY}, A_{YZZ} A_{XYY}, A_{YXX}, and A_{XZZ} produce surface inactive vibrations. It is also

important to point out that the assumption that *X* and *Y* components are completely screened by the surface is not fully valid when one is working in the visible range of the electromagnetic spectrum [28] .

Due to the expectation of a preferential enhancement of components in the *Z* direction, the EM selection rules are widely applied in SERS studies for the determination of the molecular orientation on the surface.

The CT enhancement mechanism contribution occurs via a Resonance Raman (RR) process, involving a charge transfer between the Fermi level of the metal and either the HOMO or LUMO orbitals of the adsorbed organic molecule [5]. The RR theory [30] predicts that the symmetric modes, enhanced by a so called A-term mechanism (Franck-Condon), should dominate the spectrum. A *B*-term contribution (Herzberg-Teller) is non-zero if the irreducible representation of the normal coordinate is contained in the direct product of the irreducible representation between the resonance and the mixed excited states [30]. It is clear that the *B*-term can account for the eventual observation of the normal Raman-forbidden bands that arise in the RR or in the SERS spectrum.

The presence of normally Raman-forbidden bands in the SERS spectrum can also be explained by the CT mechanism as a consequence of the molecular symmetry perturbation due to the surface. For instance, a free pyrazine molecule with D_{2h} symmetry could lose its centre of symmetry due to adsorption and become a C_{2v} complex. The two most probable orientations for pz adsorbed on a metallic surface are presented in Figure 5.10. An edge-on orientation is also possible, but not probable from the chemical point of view. All modes are Raman allowed under C_{2v} symmetry.

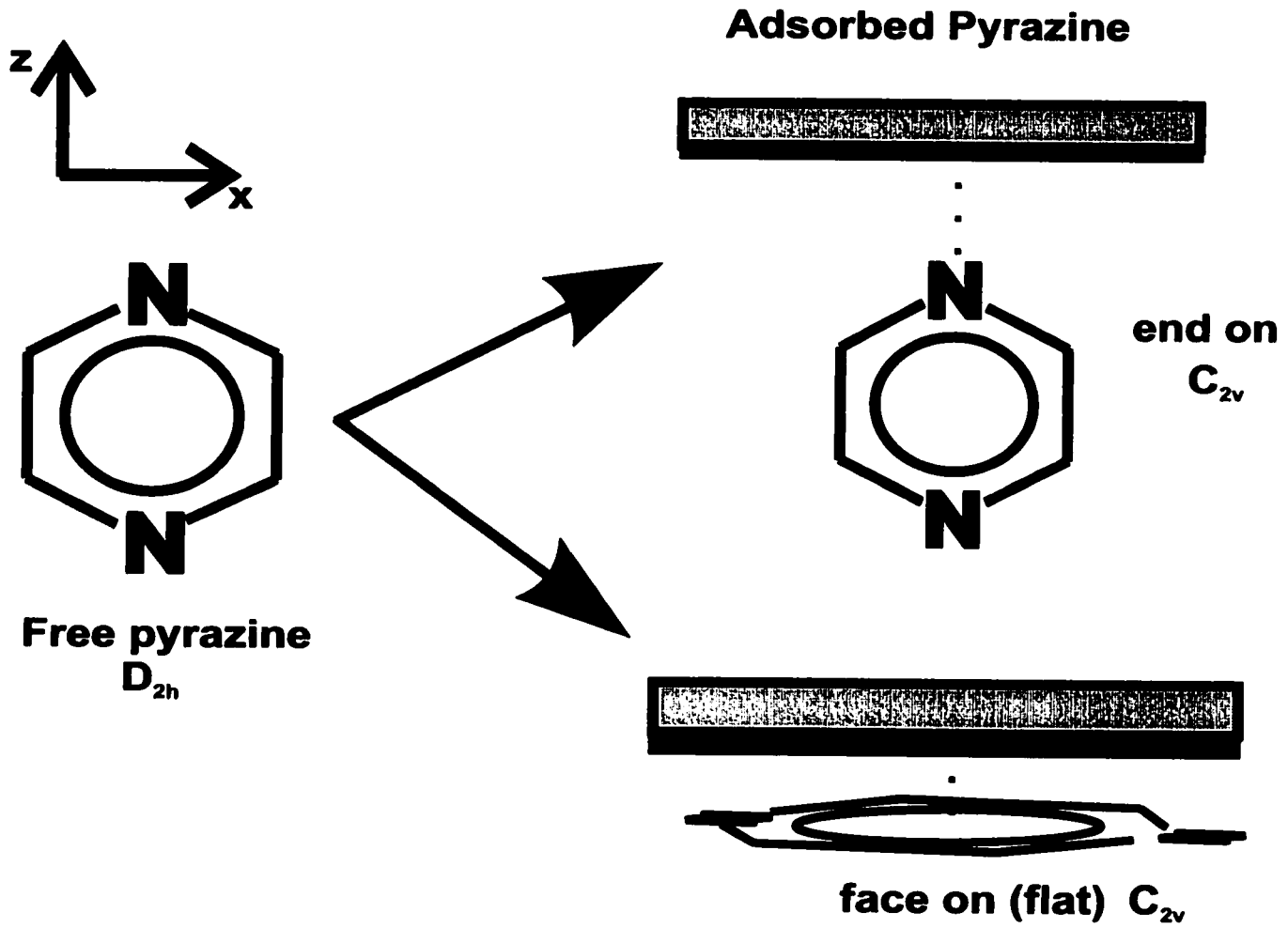

Figure 5.10: Two possible orientations for pz adsorbed on a metallic surface. In both cases the pz centre of symmetry is lost, and the pz symmetry is reduced from D_{2h} to C_{2v}. The molecular Cartesian reference (x, y, z) is also shown.

Table 5.2: SERS bands of pyrazine arranged in categories according to their intensity and species type:

Species	Frequency / cm^{-1}	Number	components
A_g	3030 (s)	2	α_{xx}, α_{yy}, α_{zz}
	1590 (vs)	8a	
	1215 (m)	11+16b	
	1235 (s)	9a	
	1020 (vs)	1	
	630 (m)	6a	
B_{1g}	916 (vw)	10a	α_{xy}
B_{2g}	3020 (m)	7b	α_{xz}
	1514 (m)	8b	
	1324 (w)	3	
	700 (m)	6b	
B_{3g}	741 (w)	4	α_{yz}
A_u	360 (w)	16a	A_{xyz}
B_{1u}	1118 (vw)	18a	A_{zzz}, A_{yyz}, A_{zzx}
	1040 (vw)	12	
B_{2u}	797 (w)	11	A_{yyy}, A_{xxy}, A_{yzz}
	430 (w)	16b	

5.3.3. Part III: The molecular orientation of pyrazine on silver electrodes

In order to facilitate the following discussion, the SERS-active Raman bands of pz, sorted according to intensity and symmetry species, are collected in Table 5.2.

Considering the metallic and the molecular axis, defined in Figs. 5.9 and 5.10 respectively, it is clear that for an end-on adsorption the molecular xz plane coincides with the surface XZ. The electromagnetic mechanism (EM) predicts that the vibrational modes containing the α_{zz} will be the most intense, followed by the α_{xz} , the α_{yz} , and finally, the modes containing the α_{xy}. In the D_{2h} point group, α_{zz} , α_{xz} , $\alpha_{yz,}$ and α_{xy} are contained in the A_g, B_{2g}, B_{3g}, and B_{1g} representations, respectively. In fact, the A_g modes dominate the SERS spectrum of pz adsorbed on silver. The 1590 cm^{-1} (8a) ring mode is the most intense band for the potential of maximum intensity. The 8a mode's polarizability change is mainly in the molecular *z* direction (see Fig. 5.2 - Region 3). The B_{2g} modes show up with medium intensity except for the ~ 1324 cm^{-1}-band (B_{2g} - number 3) which is weak. Only one B_{3g} mode is observed as a weak feature at 741 cm^{-1}. However, the other B_{3g} mode is expected at ~ 973 cm^{-1} [4], and it may be concealed by the strong ring breathing mode. The single B_{1g} mode is observed at ~ 916 cm^{-1} as a very weak band. Therefore, this analysis, involving all Raman allowed bands of pyrazine, is consistent with an end-on adsorption.

Considering that a CT complex is formed and its electronic energy is in resonance with the excitation radiation, one can also expect the totally symmetric modes to be enhanced by an *A*-term mechanism.

Thietke and co-workers [8] endorse the photon-driven charge transfer (PDCT) model, and suggest that the SERS spectrum should have some analogy to the inelastic scattering of the electron via a negative ion resonance known as shape resonance. According to the selection rules in shape resonance only totally symmetric modes are excited when the π^* orbitals corresponding to the affinity levels are non-degenerate as in the pz molecule. The shape resonance of pyrazine presents a vibronic progression entirely dominated by the 1020 cm^{-1} ring breathing (1) mode [31]. This vibrational mode is strong in the SERS spectrum and its polarizability also changes along the N-N axis (Figure 5.2 - Region 3).

The low frequency region of the SERS spectrum of pz is, in contrast to aqueous pz, dominated by the 630 cm^{-1} band (6a) rather than the ca 700 cm^{-1} band (6b). The former mode changes its polarizability along the molecular N-N axis, but less so for the latter (see Figure 5.2 for the vibrational mode descriptions). The 6a along with the 9a modes dominate the RR spectrum involving the first electronically excited state of pz ($B_{2u} \leftarrow A_g$) [32], and the ring breathing mode together with the 6a mode dominate the RR spectrum involving the second excited state of pz ($B_{3u} \leftarrow A_g$) [33]. Therefore, an additional contribution to these modes from a CT cannot be discarded. Moreover, the RR spectrum of pz contains the 10a out-of-plane mode of B_{1g} symmetry at ~ 916 cm^{-1} with fair intensity. This band is activated in the RR spectrum due to the vibronic coupling between the electronic excited states ($B_{2u} \otimes B_{3u}$). However, this band is very weak in the SERS (Table 5.1).

The chemical enhancement mechanism explains the presence of forbidden bands as a result of symmetry lowering due to adsorption (Fig. 5.10). For the C_{2v} surface complex the new Raman-allowed bands are $2\ A_u + 4\ B_{1u} + 2\ B_{2u} + 4\ B_{3u}$. However, Moskovits et al. [9] argue that the frequency shifts for the pz bands from the electrode surface

compared to the peak positions from pz in aqueous solutions are not sufficient to justify complex formation.

The 360 cm^{-1} band is an A_u out of plane band. It is practically impossible to detect this band in the IR of pz [16] because the A_u mode does not contain any component from the dipole moment. However, this mode contains the A_{xyz} component of the quadrupole polarizability, and hence it is expected to be surface active by the field gradient model [28], and it is observed (Figure 5.2).

Moreover, following the field gradient mechanism [28], the bands that contain the A_{zzz} components should also be enhanced. For pz under D_{2h} symmetry, A_{zzz} is contained in the B_{1u} modes. In fact, the B_{1u} mode bands are observed with a very weak intensity at 1118 and 1040 cm^{-1}.

Some B_{2u} out of plane bands also have weak intensity, but are undoubtedly present at 430 and 797 cm^{-1}. The B_{2u} modes contain the A_{yyy} , A_{xxy}, and A_{yzz} terms of the quadrupole polarizability; hence, these bands are expected to be surface inactive for a pz molecule adsorbed perpendicular to the surface by the field gradient model. There are several possibilities that would explain the presence of these out of plane modes. First of all, one can argue that these modes provide evidence that pz lies flat on the electrode surface. However, the large enhancement for the in-plane CC band at 1590 cm^{-1}, together with the large intensity of all modes with polarizability change in the N-N axis direction, argues against this hypothesis.

A second explanation is illustrated in Figure 5.11. As the potential becomes negative, some halide anion, which stabilizes pz in the end-on position, leaves the electrode surface. In this case, the pz molecules may laterally interact with each other, and

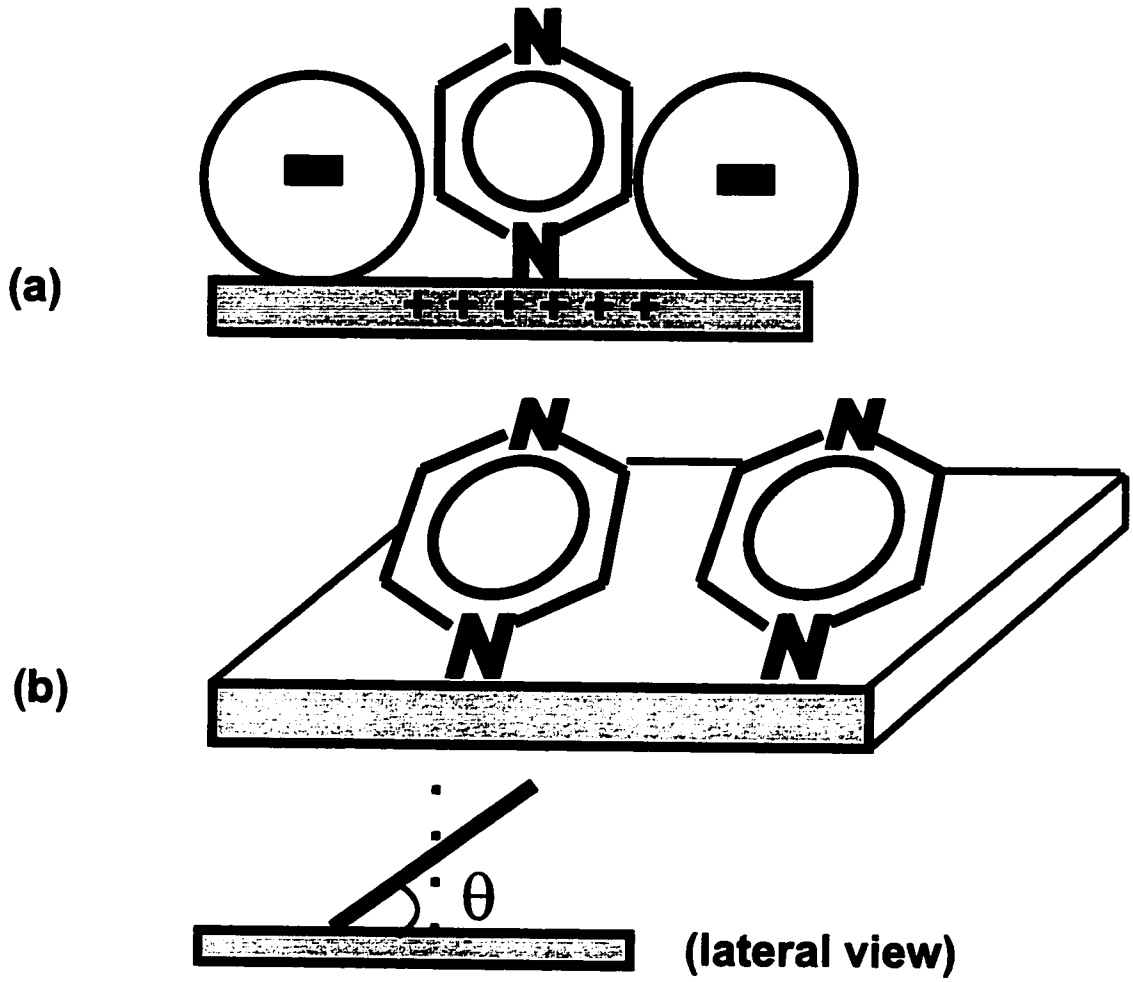

Figure 5.11: (a) In a positively charged electrode, pz is coadsorbed with bromide ions. This situation can stabilize the pz molecules in an end-on configuration. (b) As the electrode charge becomes negative, the bromide ions leave the metallic surface. This situation permits lateral interaction between pz molecules, and the molecules may tilt on the metallic surface.

they could tilt a little towards the electrode surface. This tilted configuration could account for the activity of both the in-plane and out-of-plane modes. A third, and most probable possibility is that the presence of unexpected "surface inactive" bands for the end on adsorption just reflects the limitation of the field gradient model. In order to derive the activity of "u" modes in the SERS spectrum, Sass et al. [28] considered an image-charge approach, but it is well known that the molecular dipole screening from the electrons in the metal in the *X* and *Y* direction is not as effective in the visible region as in the IR. Hence, for Raman spectroscopy, the *X* and *Y* contributions to the polarizability change may become important.

5.3.4. Part IV: The electrochemical reduction of pyrazine

Figure 5.12, A and B, shows the cyclic voltammogram obtained for the Ag electrode in 1.0 M KBr medium in the absence and in the presence of pz. Fig. 5.12A indicates that the presence of pz has some small influence on the silver anodic dissolution in this medium. In fact, the oxidation process was less effective for the solution containing the organic molecule, and it can be observed that the presence of pz adsorbed on the silver surface inhibited part of the metallic dissolution process. The electrochemical reduction of pz is shown in Fig. 5.12B. Pz decomposition occurs simultaneously with hydrogen evolution, and a reduction peak is observed at ca. -1250 mV (vs. SCE). After the electrochemical reduction of pz the potential sweep was switched to the positive direction, and a very weak oxidation peak was observed at ca. -1125 mV (Fig. 5.12B). This oxidation wave is due to the re-oxidation of the $DHPz^+$ cation to pz. Analysis of the cyclic voltammogram presented in Fig. 5.12B suggests that the electrochemical behaviour of pz is not reversible; Thietke et al. [8] reported a reversible electrochemical process for pyrazine reduction in a sulfate medium.

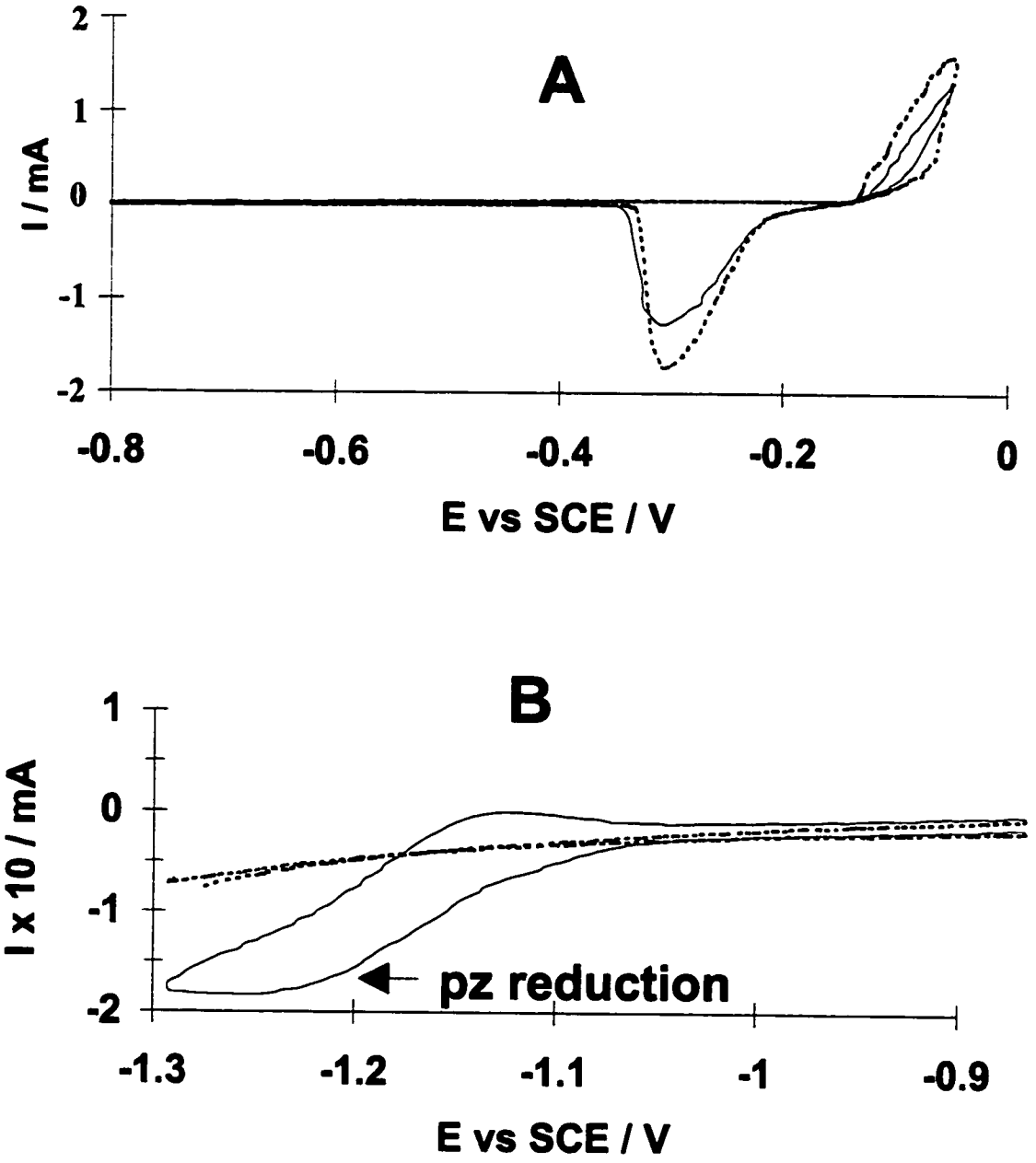

Figure 5.12: Cyclic voltammogram of the system Ag/KBr 1 M in the presence (solid line) and in the absence (dotted line) of pyrazine. Scan rate 5 mVs^{-1}. A) 0 to -0.8 V; B) -0.9 to -1.3 V.

Figure 5.13 - Regions 1 to 4, shows the spectral changes observed as pz was being reduced at potentials more negative than -900 mV. These spectra were obtained after an ORC from -1300 mV to -50 mV to -1300 mV at 5 mVs^{-1}; hence, some reduced pz was formed prior to the sweep. All pz characteristic bands either vanished or shifted as the potential was swept in the negative direction, and new bands attributed to pz reduction products were observed. For instance, the SERS intensity of the δ ring - 6a mode at 620 cm^{-1}, due to pyrazine, decreased as the potential became more negative (Fig. 5.13 - Region 1), and two new broad bands appeared at ~ 520 and 750 cm^{-1}, respectively. Fig. 5.13 - Regions 2 and 3 show the vanishing of the pz bands at 1019 cm^{-1} (ring breathing mode - number 1), 1220 cm^{-1} (combination 11+16b), and 1235 cm^{-1} (9a). New bands appeared in those regions at ~ 930 cm^{-1} and 1175 cm^{-1}. Finally, in Fig. 5.13-Region 4, one can notice the decrease of the 8a-ν ring pyrazine mode at 1590 cm^{-1} and the presence of a new band at ca 1630 cm^{-1}. These new bands are listed in Table 5.3.

It is not possible to infer the identity of the reduction product from only the Raman wavenumbers presented in Table 5.3. However, previous electrochemical work has shown that the main product in the reduction of pyrazine in aqueous medium is the 1,4-dihydropyrazine cation ($DHPz^+$) [34, 35] (Figure 5.14). Some dihydropyrazine SERS bands on silver colloid were reported by Muniz-Miranda et al. [11]. They also confirmed the presence of dihydropyrazine in monomeric and dimeric forms by mass spectroscopy. These compounds were formed from an excess of reducing agent during the formation of the silver colloid [10, 11]. It has also been predicted that $DHPz^+$ can undergo a homogenous chemical reaction leading either to ring opening or to ring condensation [34, 35]. A schematic summary of such processes is presented in Figure 5.14. These processes are catalyzed by hydronium cations, and therefore they are more likely to occur in a very acidic medium (pH < 2). This is not the medium used in this work; rather the pH was close to 7. Moreover, the spectral features, presented in Figure 5.13 and listed in Table 5.3, are

Table 5.3: Vibrational wavenumbers (cm^{-1}) and assignments for pyrazine and vibrational wavenumbers for the product.

Wavenumbers / cm^{-1} for pz adsorbed on Ag electrode [14].	**Assignment**	**Wavenumbers / cm^{-1} for electrochemically reduced pz.**
360 vw	A_u (16a)	295 (vw)
432 w	B_{2u} (16b)	520 (w)
630 m	A_g (6a)	620 (w)
697 w	B_{2g} (6b)	725 (w)
741 w	B_{3g} (4)	751 (w)
797 w	B_{2u} (11)	
916 vw	B_{1g} (10a)	906 (w)
1019 s	A_g (1)	1030 (m)
1040 vw	B_{1u} (12)	
1116 vw	B_{1u} (18a)	
1215 m	A_g (11 + 16b)	
1235 s	A_g (9a)	1175 (m)
1324 vw	B_{2g} (3)	
1514 w	B_{2g} (8b)	
1587 s	A_g (8a)	1630 (s)
3020 m	B_{2g} (7b)	
3030 s	A_g (2)	3060 (m)

Intensities: v - very; w - weak; s - strong and m - medium.

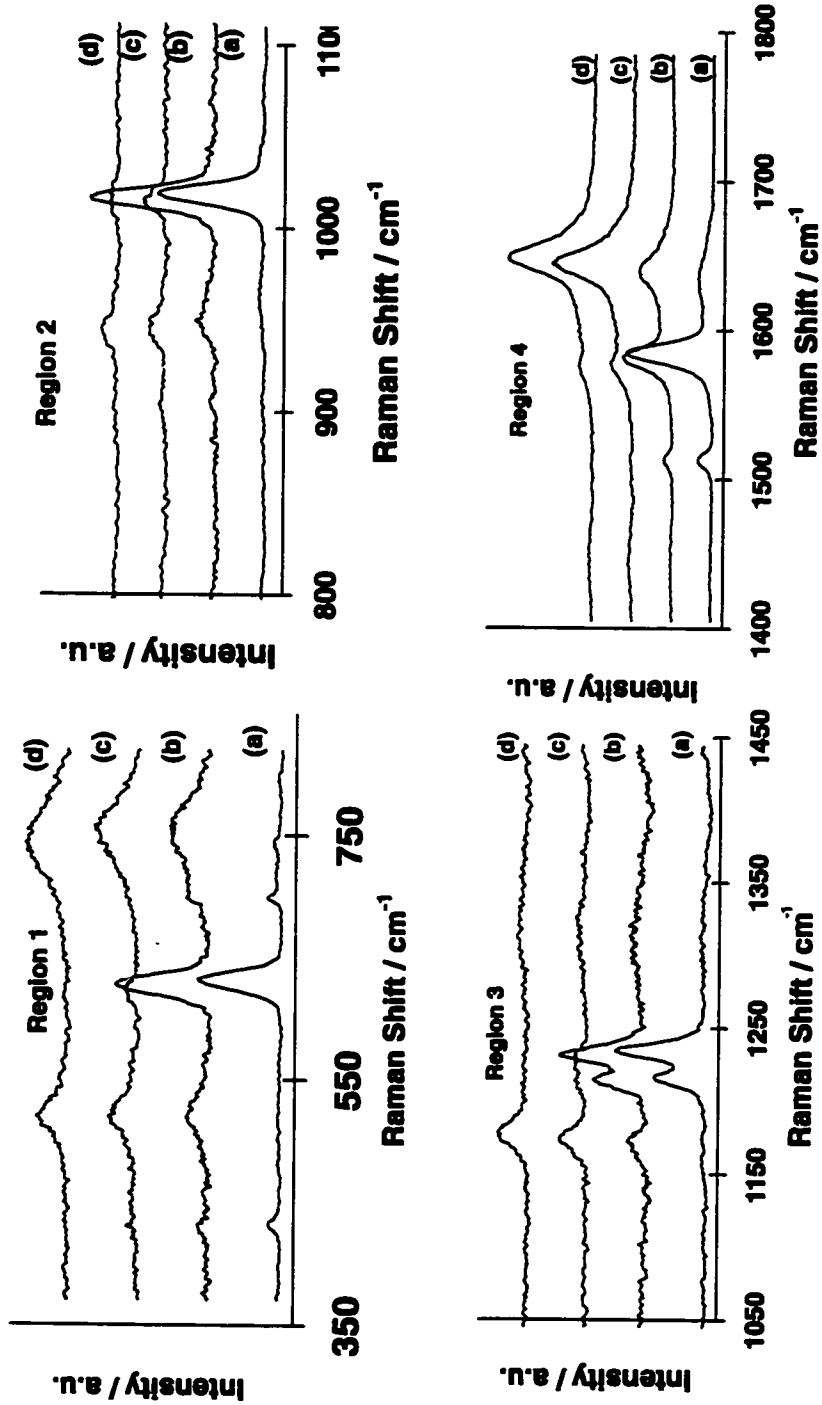

Figure 5.13: SERS spectra of pz adsorbed on a silver electrode at several potentials. System: Ag/1 M KBr/0.1 M pz. The DHPz' bands can be observed as the potentials become more negative. a) -900 mV; b) -1000 mV; c) -1100 mV; d) -1200 mV.

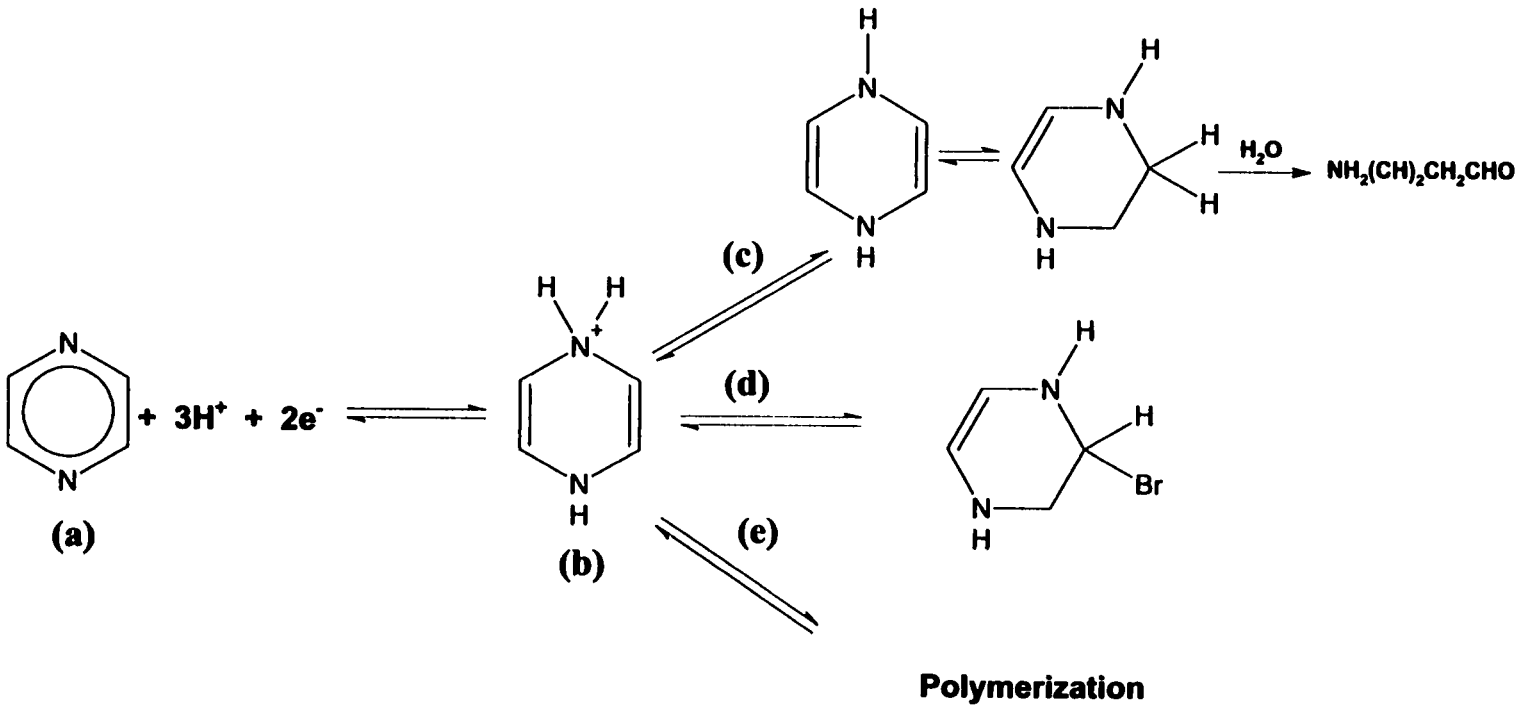

Figure 5.14: Pyrazine (compound (a)) reduction in protic medium leads directly to the formation of the 1,4-dihydropyrazinium cation (compound (b)). The cation can be reversibly re-oxidized to pz. However, the 1,4-dihydropyrazine cation can also undergo a different chemical process, which can lead to ring opening (process (c)), ring substitution (process (d)) and polymerization (process (e)). Some of these chemical products can be further re-oxidized or may became trapped in the electrode surface.

not compatible with the formation of either an aliphatic or a ring-condensed structure. Another homogeneous chemical process which may also be considered is the halogenation of the $DHPz^+$, because we work in a concentrated bromide medium. In fact, the band at ca 520 cm^{-1} can be assigned either to a C-Br stretch [36] or a ring deformation. However, as demonstrated later, our SERS results indicate that the species adsorbed on the electrode surface is a cation, and halogenation would probably yield a neutral species.

Figure 5.15 shows the SERS spectra of pyrazine in the ~ 1600 cm^{-1} region at several more positive potentials. Only one band at ~ 1590 cm^{-1} was observed in this region in the pz SERS spectrum [14]. However, two bands are observed in Fig. 5.15: 1590 cm^{-1} and 1610 cm^{-1}. The appearance of these two bands can be explained by the presence of trapped $DHPz^+$ cation (or structurally similar species), coadsorbed with pz molecules. In order to obtain the spectra presented in Fig. 5.15, the electrode potential was swept to values more negative than -1000 mV, and the negative potential was applied for sufficient time for the pz reduction to take place. The electrode was then swept to positive potentials; a very weak oxidation wave was observed (voltammogram presented in Fig. 5.12B), but the presence of a new peak at ~ 1610 cm^{-1} suggests that some of the reduced pz, which had not been re-oxidized to pz, was either trapped on the electrode surface or in the solution diffusion layer. This is consistent with an irreversible redox process. The electrode potential was again swept in the negative direction commencing from -350 mV and spectra were measured. The integrated intensities from the two bands at 1610 and 1590 cm^{-1}, shown in Fig. 5.15, were evaluated using bandfitting procedures, and are plotted against the applied potential in Fig. 5.16. It is clear that the 1610 cm^{-1}- band intensity from $DHPz^+$ decreases and the 1590 cm^{-1} - band intensity from pz increases as the applied potential becomes more negative. The 1610 cm^{-1}-band vanishes at potentials more negative than ca -700 mV.

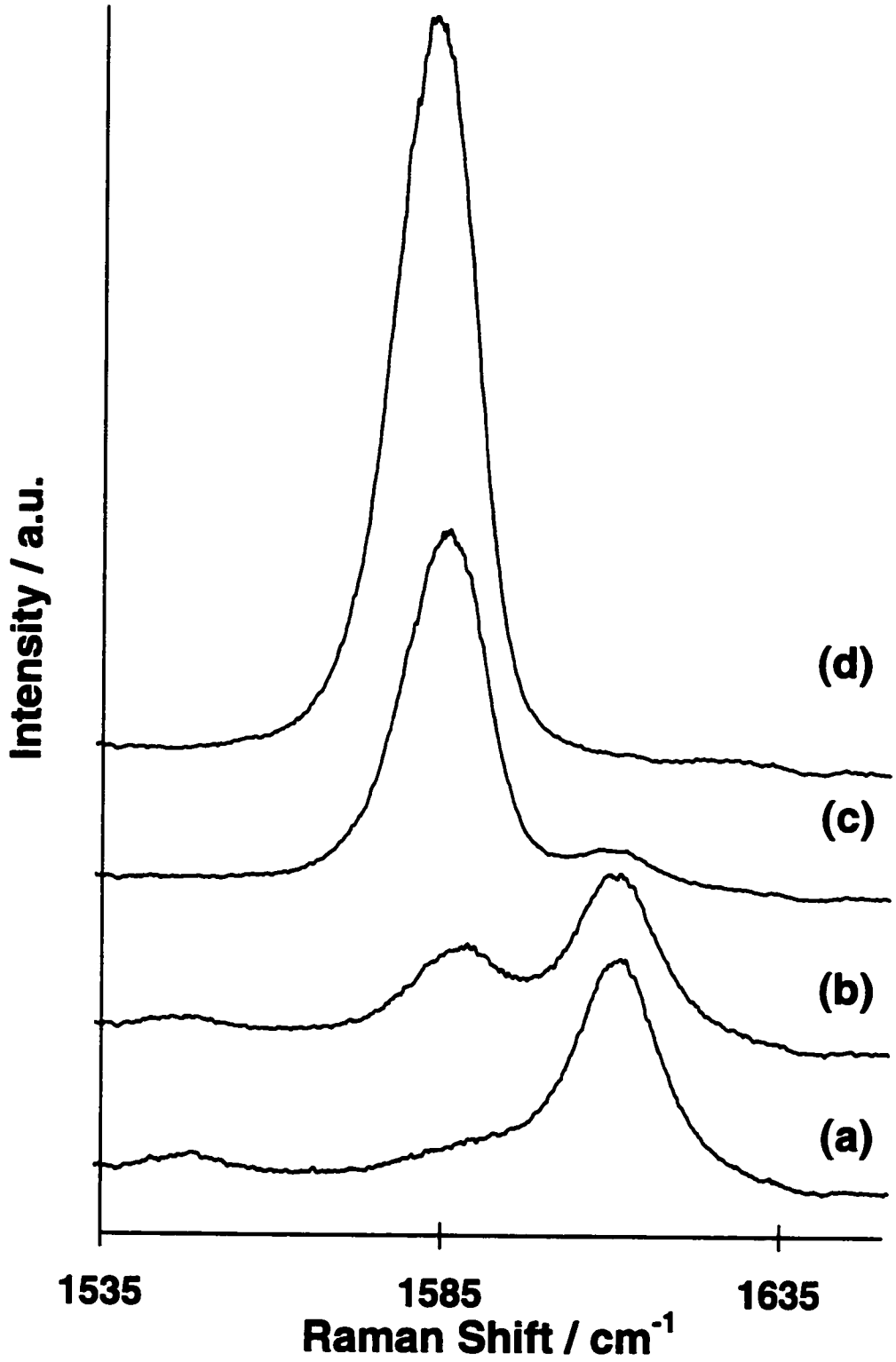

Figure 5.15: SERS spectra of pz and $DHPz^+$ (formed from the reduction of pz) at more positive potentials. a) -450 mV; b) -550 mV; c) -650 mV; d) -750 mV.

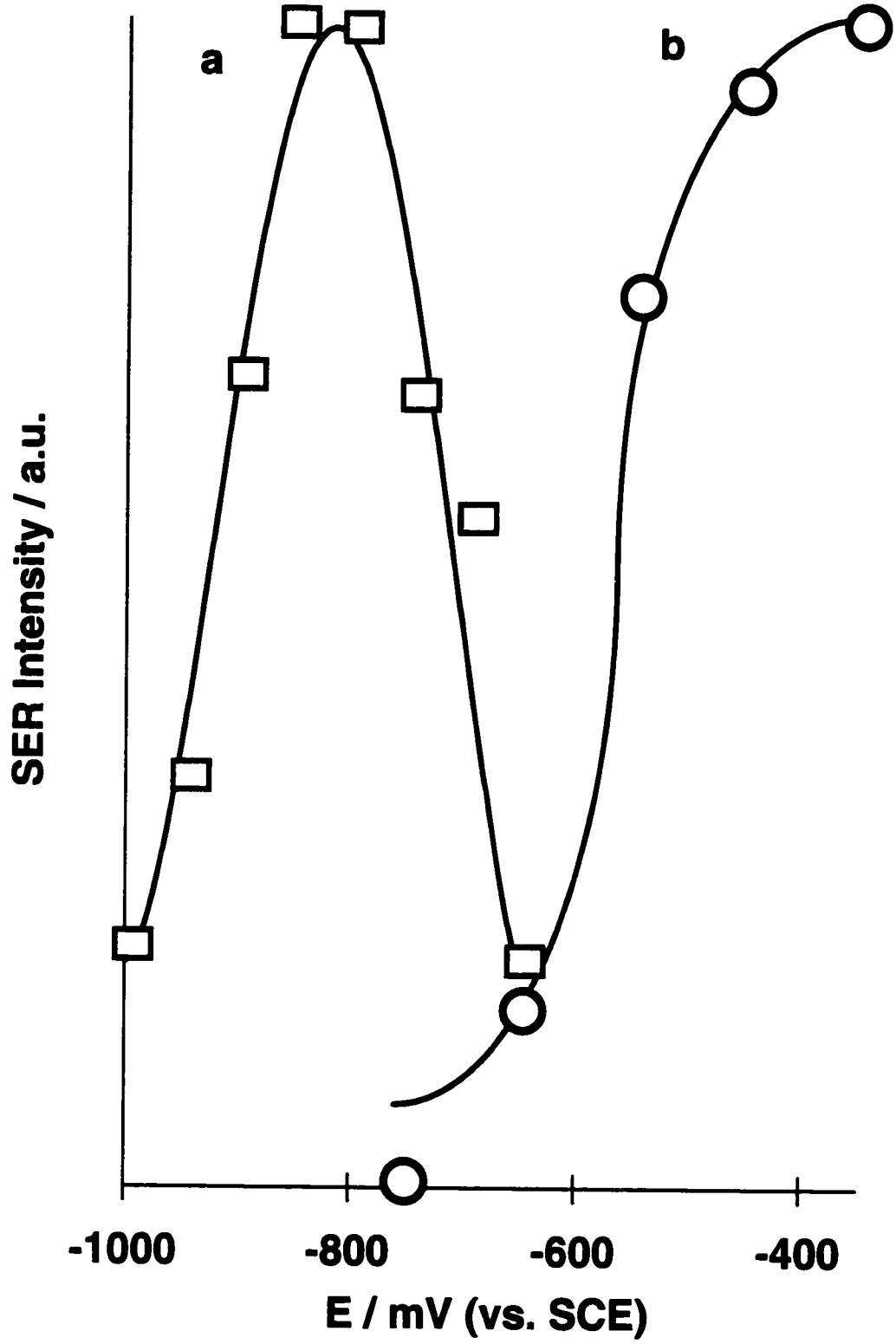

Figure 5.16: Potential profiles (a) for the 1590 cm^{-1}-band of pz; (b) for the 1610 cm^{-1}-band of $DHPz^{+}$.

The $DHPz^+$ band shows up again at ~ 1630 cm^{-1} when the electrode potential is more negative than -900 mV, as observed in Fig. 5.13 - Region 4.

The presence of bands due to reduced pz in the potential range between -450 mV to -650 mV can lead to misinterpretation of the SERS spectrum of pz. For instance, the bands due to reduced pz, shown in Table 5.3, do not show up, either in the activation procedure in the absence of pyrazine or before an electrode potential more negative than -900 mV. Comparing the vibrational wavenumbers in Table 5.3 to some band wavenumbers reported in the literature of SERS of pz (Table 5.1) we conclude that some authors have incorrectly assigned bands due to trapped pz reduction products to pz. This raises again the question about what is the best activation procedure for SERS [37]. The activation procedure in the presence of an organic molecule yields a better signal, but the spectrum obtained in that way must always be compared to the spectrum after an activation procedure in the absence of the organic molecule. Any eventual differences in the spectra obtained from these two activation procedures may be interpreted as arising from an electrochemical reaction and subsequent trapping of decomposition products.

The 1590 cm^{-1} band intensity (Figs. 5.15 and 5.16) increases as the potential becomes negative, reaches a maximum at -750 mV, and then decreases as the potential becomes more negative. This behaviour is common in SERS experiments, and is in accordance with other results for pz in the literature [6-13]. The symmetric profile of the intensity vs potential plot of the 1590 cm^{-1} -band is typical for neutral molecules, and largely reflects the changes in the surface coverage with potential. However, an additional intensity contribution from a resonance process involving the incident light and a charge-transfer between the Fermi level of the metal and the LUMO orbital of pz cannot be discounted [19]. The decrease of the 1610 cm^{-1} band intensity as the potential becomes negative is also consistent with the desorption of a positive ion (possibly as the $DHPz^+.Br^-$

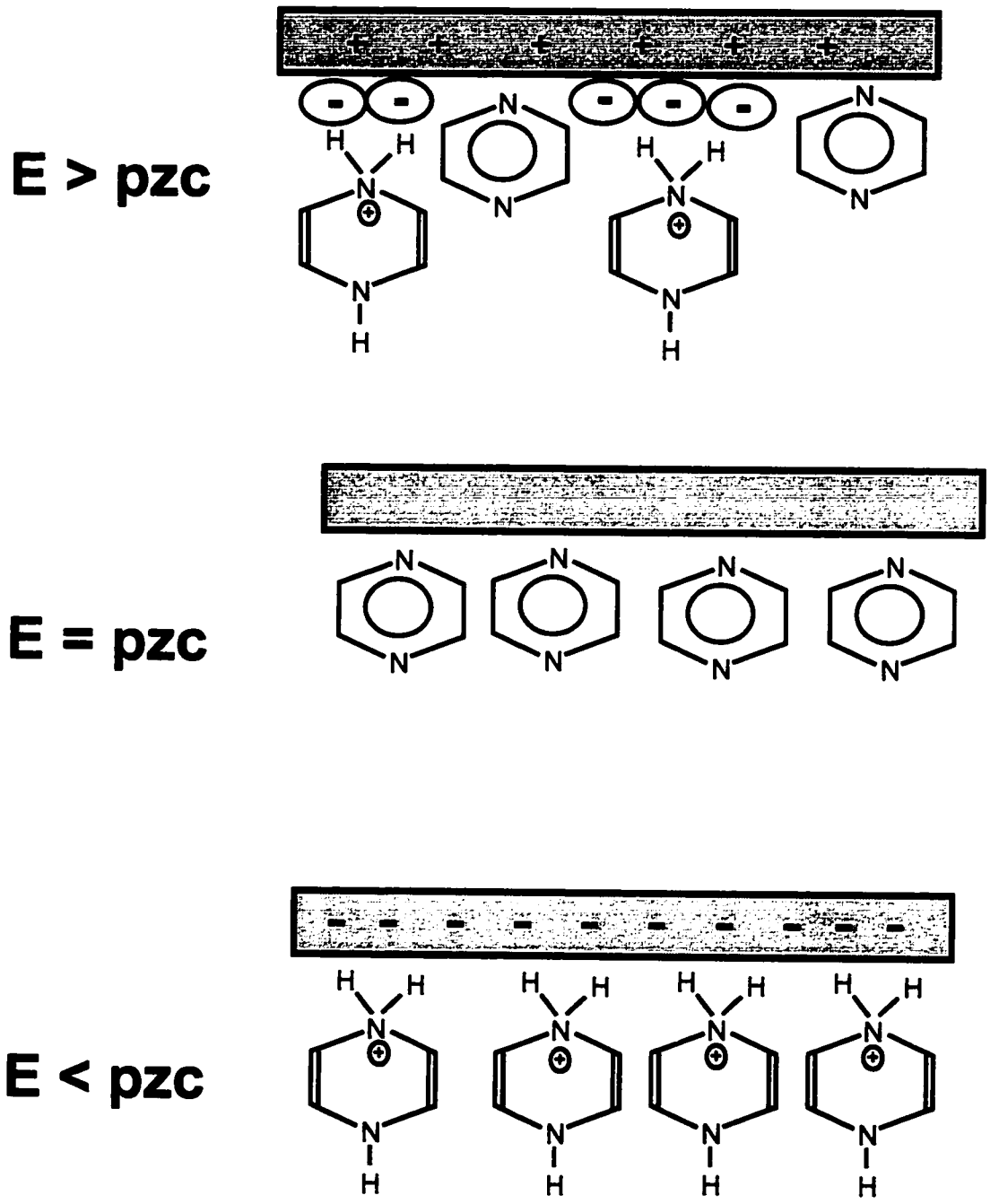

Figure 5.17: Models of the electrode surface at several potentials. Bromide ions are directly in contact with the electrode at potentials more positive than the pzc; the $DHPz^{+}$ can adsorb to the halide layer. As the potential becomes more negative, the amount of specifically adsorbed bromide decreases and the $DHPz^{+}$ Raman signal also decreases. At potentials near the pzc, the pz signal maximizes. At potentials more negative than the pzc, the $DHPz^{+}$ cations can interact directly with the electrode surface.

ion-pair from the bromide surface layer [24, 38]) from the electrode as shown in Figure 5.17. The fact that the band at 1610 cm^{-1} only appears after pz reduction at negative potentials is an indication that a cation remains adsorbed on the electrode, even at potentials more positive than the pzc (Fig. 5.16).

The $DHPz^+$ cation is formed at potentials more negative than -1000 mV, in the hydrogen evolution region. However, as the scan is reversed to positive potential, some of the reduced pz compound is re-oxidized to pz (Fig. 5.12), but some apparently remains as $DHPz^+$ cation (Fig. 5.15), because pz reduction is an irreversible process. This positive ion is not expected to interact with the silver electrode at potentials more positive than the pzc. Hence, no $DHPz^+$ signal is expected in the range of potential between -450 mV to -700 mV. However, as observed in Figs. 5.15 and 5.16, the intensities for the $DHPz^+$ bands are very significant in this range. It is well known from SERS experiments on silver electrodes in halide-containing media that a halide layer exists in that potential range, and may partially remain on the electrode surface even at negative potentials. This kind of super-equivalent adsorption has been demonstrated for bromide adsorbed on silver single crystals [39, 40]. Consequently, the $DHPz^+$ cation can interact with the positively charged electrode through the halide layer. As the potential becomes negative, the halide leaves the electrode surface together with the $DHPz^+$ cation and the 1610 cm^{-1} band intensity decreases. The $DHPz^+$ signal can be observed again at potentials more negative than -900 mV, because at these potentials the electrode is negatively charged. This behaviour is also in accordance with the results presented by Thietke et al.. [8]. In their work, they claim that pz reduction is a reversible process. They reach that conclusion because no SERS bands due to the $DHPz^+$ were observed at potentials more positive than -900 mV. However, they were working in a SO_4^{2-} medium; this anion does not adsorb strongly to

the silver surface, and hence the $DHPz^+$ cation could not be observed on a positively charged electrode.

It is also important to point out the influence of the porous structure of the rough electrode on the electrochemical kinetics for the pz reduction. The surface morphology for a rough silver electrode prepared from a series of ORCs has been characterized [41]. Figure 5.18 shows the time dependence of the cathodic charge for the reduction of pz on both a rough and a smooth silver surface in bromide medium. The results presented in Fig. 5.18 were obtained by stepping the potential from -400 mV, where no faradaic process is occurring, to -1300 mV, where the reduction of pyrazine is the main contribution to the cathodic current. One can notice that the cathodic charge from a rough surface is at least 3 times larger than from a smooth surface. The increase in the cathodic charge due to the surface roughness can be explained by an overall increase in the surface area; however, it has been demonstrated that the surface morphology may affect both the diffusion and the transfer coefficient [42]. The cavities and irregularities present in a rough surface may also trap either pz or its decomposition product. Therefore, for a SERS study, the activation of the silver electrode in the absence of the organic molecule is generally preferable.

5.3.5. Part V: General discussion and comparison to the literature

The main features of the spectra presented in this work agree well with the literature. All works, except Dornhaus et al. [7] who worked in oxygen containing solution and recorded a transient spectrum (acquisition time of 25 ms), reported that the symmetrical modes yield the most enhanced bands. However, some works in the literature reported several forbidden bands that we have not observed. It is expected that more forbidden bands will be observed from pyrazine adsorbed on cold deposited silver [9] than

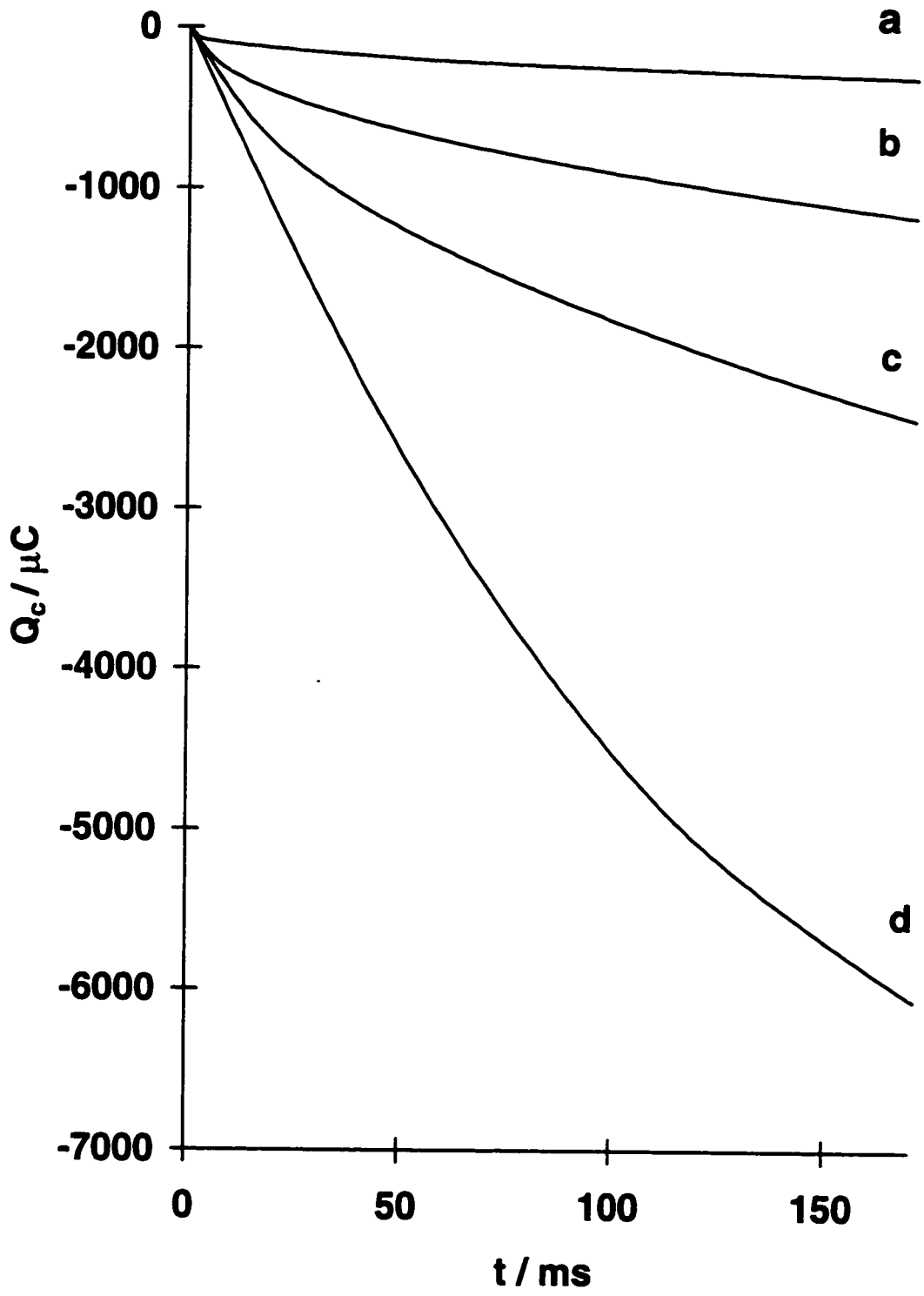

Figure 5.18: Chronocoulometric curves for Ag in 1 M KBr solution.
a) smooth Ag, [pz] = 0 M; b) smooth Ag, [pz] = 10 mM;
c) smooth Ag, [pz] = 50 mM; d) roughened Ag, [pz] = 50 mM.

for pz on the electrode surface; the geometry of the silver bumps from the cold deposited method favors the field gradient mechanism. This mechanism may be damped at the electrode surface due to the coadsorption of halides. On the other hand, from Tables 5.1 and 5.3, it is possible to discern that certain "forbidden bands" observed in some of the previous electrochemical SERS studies can be due to pz decomposition products, as suggested before by Muniz-Miranda et al. [11]. Since all previous works activated the electrode in the presence of pz, some trapped pz species could remain on the electrode surface.

Another point is the importance of the B_{1u} (12) ring mode at 1030 cm^{-1} for the determination of the orientation of pz at the electrode surface. Several authors have agreed that the presence of this band determines the molecular orientation on the electrode. Hallmark and Campion [43] studied the NRS of pz adsorbed on silver single crystal. They used a weak presence of this mode to draw the conclusion that pz changes its orientation from flat on Ag(111) to tilted on Ag(110). Based on Hallmark and Campion's results, Bhattacharjee [44] confirmed his theory for surface selection rules. Huang and Wu [12] and Zhong and Wu [13] stated that the absence of this band from a gold electrode can lead to the false conclusion that the molecule lies flat on the electrode surface. The ~ 1030 cm^{-1}-band is strong in the aqueous pzH^+ complex (Fig. 5.2, Region 3), but it always shows up as a very weak feature at the electrode, even in Huang and Wu's spectra. However, this band showed up with an appreciable intensity in the cold deposited silver experiment [9]. The NRS of pz adsorbed on a silver surface [43] had low signal-to-noise and the presence of this band is uncertain. Observing the description of this mode in ref. 17, one can qualitatively notice a significant contribution from polarizability components parallel to the electrode surface, when an end-on adsorption is inferred. Moreover, this mode is forbidden in the NRS of pz , and its presence on the electrode is possible due to the field gradient enhancement. This enhancement mechanism does not

yield a reliable set of selection rules necessary to infer the molecular orientation, as we demonstrate in this work. From the above arguments, we do not agree that the presence or absence of this mode is enough to draw conclusions about the orientation of pyrazine adsorbed on a metallic surface. The orientation of pz on the electrode surface must be inferred from the intensity of significant perpendicular modes, compared to the intensities of significant parallel modes.

In order to illustrate the discussion above, let us examine the spectra of pyrazine on a colloid, presented by Muniz-Miranda et al. [10, 11]. These spectra show several similarities to the aqueous pz spectrum, including the fact that the 1020 cm^{-1}-band is the strongest one, being ~ 8 times stronger than the 1595 cm^{-1}-band. They conclude that the 1590 cm^{-1}-band is 2 times enhanced and the out-of-plane CH bending (10a) at 920 cm^{-1} is 4 times enhanced. The most enhanced symmetric mode is the 1225 cm^{-1}-band. The 636 cm^{-1}-band is only 2 times enhanced, and it is still weaker than the 700 cm^{-1}-band. Muniz-Miranda et al. suggested end on adsorption based on the presence of a band at 220 cm^{-1}, assigned to the Ag-N mode. The presence of this band was suggested from an asymmetry of the Ag-Cl band. Despite the supposed presence of this Ag-N band, which points to an end on adsorption, all other evidence seems to support either tilted or flat pyrazine adsorption on the colloid. It is also important to point out that the asymmetry of bands in the metal-halide region, also observed in this work (Figure 5.3), may just reflect the existence of more than one type of SERS active site for halide [19, 20]. Moreover, the colloid spectrum is also similar to the one presented by Moskovits et al. [9] in the low pyrazine coverage experiment, except for the absence of the 1030 cm^{-1} mode. Hence, we conclude that the molecular orientation of species adsorbed on a metallic surface must be inferred from the analysis of a set of in-plane and out-of-plane vibrational modes. The presence or absence of weak bands is not sufficient; the entire spectrum should be considered.

5.4. Conclusion

Two activation procedures were used for the SERS study of pyrazine adsorbed on a silver electrode: one involved an ORC in the presence and the other in the absence of pyrazine. The band positions were not sensitive to the activation procedure, but the activation in the presence of pyrazine yielded better signal-to-noise. The pyrazine spectra obtained from an electrode activated in the presence of pyrazine may include additional bands from trapped species from the electrochemical reduction of pz; therefore, care must be taken in the activation procedure to avoid pyrazine reduction.

The SERS intensity and the potential profiles proved to be independent (within experimental error) of both the pz concentration and the excitation wavelength.

The electrochemical reduction of pyrazine in bromide medium is irreversible. The main electrochemical reduction product is 1,4-dihydropyrazine cation ($DHPz^+$). Bands due to $DHPz^+$ were observed at potentials more negative than -900 mV. The SERS intensities from pz bands decreased as the $DHPz^+$ cation was being formed at negative potentials. $DHPz^+$ was observed at potentials more positive than the pzc for silver in bromide medium (between -450 mV and -750 mV), even after the presence of an oxidation wave in the voltammogram. In spite of its positive charge, $DHPz^+$ (or one of its derivatives with similar structure) stays on the electrode surface at potentials more positive than the pzc; the cation interacts with the electrode via the halide layer. Its presence confirms that the electrochemical decomposition of pz is irreversible (It is apparently more difficult to extract protons from the product than to add them). The presence of $DHPz^+$ bands in the pz SERS spectrum can complicate the spectral analysis. The contamination of SERS spectra by electrochemically generated products can be avoided by activating the electrode in the absence of the organic molecule.

The pz molecule stands up and is bonded to the electrode by the N lone electron pair; however, a tilted configuration cannot be totally excluded. This conclusion was drawn from the observation of a greater enhancement from modes with polarizability components perpendicular to the electrode surface, when compared to the modes parallel to the surface. The main features presented here agree well with the literature; however, some previous misunderstandings have been clarified.

5.5. References

[1] L. Stolberg, J. Lipkowski and D. E. Irish, *J. Electroanal. Chem.*, **1991**, 300, 563.

[2] J. Lipkowski, L. Stolberg, S. Morin, D. E. Irish, P. Zelenay, M. Gamboa and W. Wieckowski, *J. Electroanal. Chem.*, **1993**, 355,147.

[3] D. E. Irish and G. Szymanski, *Proceedings of the XIII International Conference on Raman Spectroscopy*, Wurzburg, Germany, Wiley, Chichester, UK, **1992**, p.690.

[4] A. G. Brolo and D. E. Irish, *Z. Naturforsh. part A*, **1995**, 50a, 274.

[5] J. A. Creighton, *Advances in Spectroscopy Vol. 16 - Spectroscopy of Surfaces*, R. J. H. Clark and R. E. Hester, eds., Wiley, New York, **1988**, p. 37.

[6] G. R. Erdheim, R. L. Birke and J. R. Lombardi, *Chem. Phys. Lett.*, **1980**, 69, 495.

[7] R. Dornhaus, M. B. Long, R. E. Benner and R. K. Chang, *Surf. Sci.*, **1980**, 93, 240.

[8] J. Thietke, J. Billmann and A. Otto, *Dynamics on Surfaces - Proceedings of the XVII Jerusalem Symposium on Quantum Chemistry and Biochemistry*, Jerusalem, Israel, D. Reidel Publishing Company, **1984**, p. 345.

[9] M. Moskovits, D. P. DiLella and K. J. Maynard, *Langmuir*, **1988**, 4, 67.

[10] M. Muniz-Miranda, N. Neto and G. Sbrana, *J. Phys. Chem.*, **1988**, 92, 954.

[11] M. Muniz-Miranda, N. Neto and G. Sbrana, *J. Mol. Struct.*, **1986**, 143, 275.

[12] Y. Huang and G. Wu, *Spectrochim. Acta*, **1990**, 46A, 377.

[13] F. Zhong and G. Wu, *J. Mol. Struct.*, **1994**, 324, 233.

[14] A.G. Brolo and D. E. Irish, *J. Electroanal. Chem.*, **1996**, 414, 183.

[15] A. G. Brolo and D. E. Irish, *J. Chem. Soc. Faraday Trans.*, **1997**, 93, 419.

[16] A.G. Brolo, B. D. Smith and D. E. Irish, *J. Mol. Struct.*, **1997**, 405, 29.

[17] R. C. Lord, A.L. Marston and F. A. Miller, *Spectrochim. Acta*, **1957**, 9, 113.

[18] J. Zarembowitch and L. Bokobza-Sebagh, *Spectrochim. Acta A*, **1976**, 32, 605.

[19] D. J. Rogers, S. D. Luck, D. E. Irish, D. A. Guzonas and G. F. Atkinson, *J. Electroanal. Chem.*, **1984**, 167, 237.

[20] W. Kautek and J. G. Gordon II, *J. Electrochem. Soc.*, **1990**, 137, 3405.

[21] B. Pettinger, in *Adsorption of Molecules at Metal Electrodes*, J. Lipkowski and P. N. Ross, eds., VCH, New York, **1992**, Ch. 6, p. 285.

[22] R. Guidelli, in *Adsorption of Molecules at Metal Electrodes*, J. Lipkowski and P. N. Ross, eds., VCH, New York, **1992**, Ch. 1, p. 1.

[23] J. R. Lombardi, R. L. Birke, T. Lu and J. Xu, *J. Chem. Phys.*, **1986**, 84, 4174.

[24] D. A. Guzonas, D. E. Irish and G. F. Atkinson, *Langmuir*, **1990**, 6, 1102.

[25] A. Kudelski and J. Bukowska, *Chem. Phys. Lett.*, **1994**, 222, 555.

[26] A. Kudelski, J. Bukowska and K. Jackowska, *J. Raman Spectrosc.*, **1994**, 25, 153.

[27] T. E. Furtak and S. H. Macomber, *Chem. Phys. Lett.*, **1983**, 85, 329.

[28] J. K. Sass, H. Neff, M. Moskovits and S. Holloway, *J. Phys. Chem.*, **1981**, 85, 621.

[29] A. D. Buckingham, *Adv. Chem. Phys.*, **1967**, 12, 107.

[30] R. J. H. Clark and T. J. Dines, *Angew. Chem. Int. Ed. Engl.*, **1986**, 25, 131.

[31] I. Nenner and G. J. Schulz, *J. Chem. Phys.*, **1975**, 62, 1747.

[32] H-K. Hong and C. W. Jacobsen, *J. Chem. Phys.*, **1978**, 68, 1170.

[33] I. Suzuka, Y. Udagawa and M. Ito, *Chem. Phys. Lett.*, **1979**, 64, 333.

[34] L. N. Klatt and R. L. Rouseff, *J. Am. Chem. Soc.*, **1972**, 94, 7295.

[35] J. Swartz and F. C. Anson, *J. Electroanal. Chem.*, **1980**, 114, 117.

[36] D. Lin-Vien, N. B. Colthup, W. G. Fateley and J. G. Grasselli, *The Handbook of Infrared and Raman Characteristic Wavenumbers of Organic Molecules*, Academic, Toronto, **1991**.

[37] K. D. Beer, W. Tanner and R. L. Garrell, *J. Electroanal. Chem.*, **1989**, 258, 313.

[38] Z. Deng and D. E. Irish, *J. Phys. Chem.*, **1994**, 98, 9371.

[39] K. Bange, B. Straehler, J.K. Sass and R. Parsons, *J. Electroanal. Chem.*, **1987**, 229, 87.

[40] G. Valette and R. Parsons, *J. Electroanal. Chem.*, **1985**, 191, 377.

[41] J. E. Pemberton and M. M. Girand, *J. Electroanal. Chem.*, **1987**, 217, 79.

[42] R. de Levie, *J. Electroanal. Chem.*, **1990**, 281, 1.

[43] V. M. Hallmark and A. Campion, *J. Chem. Phys.*, **1986**, 84, 2933.

[44] R. Bhattacharjee, *J. Raman. Spec.*, **1990**, 21, 301.

Chapter 6

Adsorption of Monoprotonated Pyrazine (Pyrazinium Cation) onto Polycrystalline Silver Electrodes

6. Adsorption of Monoprotonated Pyrazine (Pyrazinium cation) on Polycrystalline Silver Electrodes

6.1. Introduction

Pyrazine is a centrosymmetric molecule which belongs to the D_{2h} point group. Protonation of one nitrogen will suppress the centre of inversion and reduce the symmetry to C_{2v}. This symmetry lowering will "activate" all the pyrazine vibrational modes in the Raman spectrum. However, pyrazine is a very weak base, and its low pK values (pK_{a1} = 0.65 and pK_{a2} = -5.8) [1] make protonation possible only in very acidic media.

A Raman spectral study of pyrazine and its protonated forms in aqueous solution has been performed (Chapter 2 and [2]). By observation of the shifts of the bands from the positions measured for neutral solutions, it has been possible to identify the unique characteristic bands of unprotonated pyrazine and its two protonated forms. The majority of the vibrational bands of the monoprotonated pyrazine (pzH^+) were identified and assigned [2]. The diprotonated pyrazine cation spectrum was only observed from very concentrated H_2SO_4 and $HClO_4$ solutions, and the presence of strong bands from these acids masked some of its bands [2]. The positions of these masked bands have been predicted theoretically in Chapter 4 of this thesis. The ab initio calculations for pyrazine and its two protonated forms provided useful confirmation of the assignments of the observed bands within 10% accuracy.

The identification and assignment of the vibrational bands from pyrazine and monoprotonated pyrazinium cation (pzH^+) in solution proved to be useful in the interpretation of the Raman spectrum of pyrazine adsorbed onto metallic surfaces [3].

New features have been observed in the SERS spectrum of pyrazine adsorbed on a silver electrode immersed in a 1.0 M KBr solution when the applied potential was more negative than -900 mV (Chapter 5 and [4]). These new bands were assigned to the main reduction product of pyrazine, the 1,4-dihydropyrazinium cation [5,6]. The 1,4-dihydropyrazinium cation, formed at negative potentials, can be adsorbed on the electrode surface even at potentials more positive than the pzc for silver in that medium. The presence of the 1,4-dihydropyrazinium cation on the silver electrode at positive potentials suggests that the monoprotonated pyrazine can also be adsorbed on a positively charged silver electrode by a similar mechanism. We have thus explored the adsorption of pzH^+ on a polycrystalline silver electrode in acidic media. The results presented in this chapter have been published elsewhere [7, 8].

6.2. Experimental

6.2.1. Reagent

The following chemicals were used without further purification: pyrazine 99+%, from Aldrich; KBr AnalR grade, from BDH; and concentrated $HClO_4$, from Baker. All solutions were prepared with Milli-Q-water.

6.2.2. Electrochemistry

The three electrode spectroelectrochemical cell has been described elsewhere [9]. A potentiostat PAR model 273 was used to control the potential applied to the working electrode. The counterelectrode was a 0.3 mm platinum wire (99.9%). A saturated calomel electrode (SCE) was used as reference. The working electrode was made from 99.9 % polycrystalline silver rod. A silver disk of ~ 2 mm radius was mounted in a Teflon holder. The working electrode was first polished with emery paper and then with progressively finer grades of alumina powder down to 0.3 μm. The electrode was rinsed with an abundant amount of Milli-Q-water, sonicated, rinsed again, and transferred to the spectroelectrochemical cell. The solution was degassed with Ar for half an hour prior to the experiment, and a gentle stream of Ar was maintained during the data acquisition.

6.2.3. Activation Procedure

The process of roughening the metal surface electrochemically, in order to create the necessary SERS active sites, is called the activation procedure. In this work we activated the electrode electrochemically by a sequence of Oxidation-Reduction Cycles (ORCs). ORCs were performed on the silver electrode from an aqueous solution containing 1.0 M KBr and 1.0 M $HClO_4$, by sweeping from -800 to -50 mV at 5 mV/s. The potentiostat was turned off, and pyrazine was added to the system. This sequence prevents decomposition, which might occur during the ORC; trapped decomposition products have been observed when the analyte was present during the ORC [4]. The pyrazine concentration used in all experiments was 0.1 M. After pyrazine was introduced

into the system, the potentiostat was switched on again, the ORC cycle was resumed and SERS of pyrazinium adsorbed on silver was recorded at the desired potential values.

6.2.4. Raman Spectra

Raman spectra were measured with a Dilor OMARS 89 spectrometer equipped with an Optical Multichannel analyzer (OMA). The intensified 512 diode array detector was thermoelectrically cooled to ca. -10 ^{o}C. The spectrometer was interfaced to an IBM computer. The data were transferred to an IBM 486 computer on which baseline correction, band-fitting, and plotting programs were available. The spectra were excited by using a 514.5 nm (100 mW at the head) line from a Coherent Innova 70 argon ion laser chopped at a 1 Hz. The chopping is a feature of the Dilor OMARS 89 spectrometer to improve signal-to-noise; it has the added advantage of diminishing photodegradation. The acquisition time was 1 second, and 10 accumulations were performed.

6.3. Results and Discussion

Figure 6.1 shows the spectrum obtained for pyrazine adsorbed from a 1.0 M KBr/1.0 M $HClO_4$/0.1M pyrazine solution onto the SERS-activated silver surface at open circuit potential (OCP) for several spectral regions. Band positions and assignments are presented in Table 6.1. Table 6.1 also shows the band positions of the pyrazine SERS spectrum obtained from a neutral solution [3] and the pyrazine and monoprotonated pyrazine bands from aqueous solution [2]. A comparison between the spectrum presented in Fig. 6.1 and the SERS spectrum of pyrazine adsorbed from a non acidic solution shows striking differences in the peak positions and intensities. It has been proposed that the

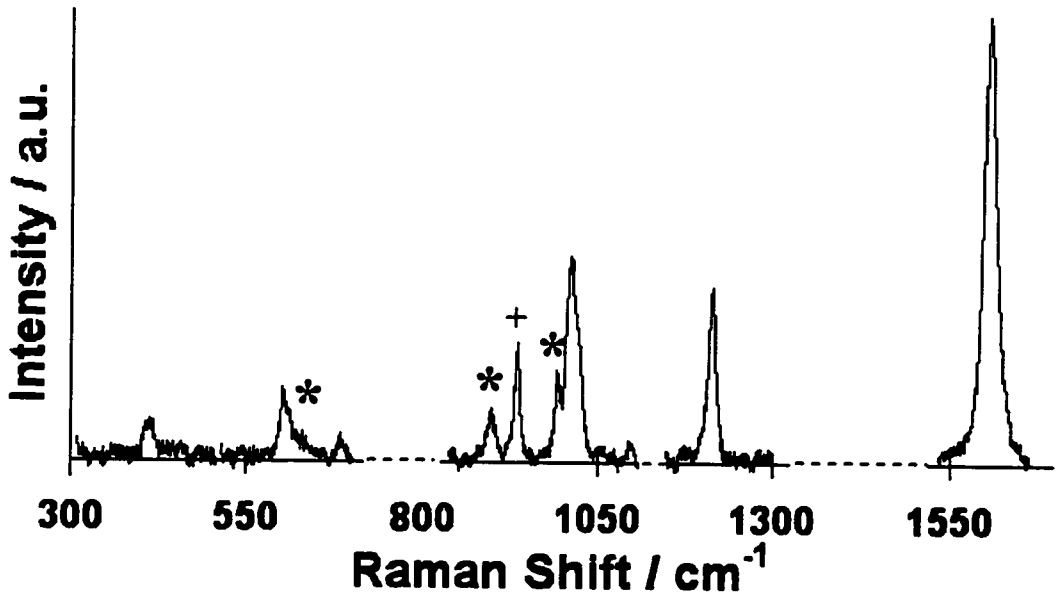

Figure 6.1: SERS spectrum of pyrazinium adsorbed on a silver electrode. Solution: KBr 0.1 M + $HClO_4$ + pz 0.1 M. (*) Bands which are not presented in the SERS spectrum of pz. (+) perchlorate stretch mode.

Table 6.1: Vibrational wavenumbers (cm^{-1}) of pyrazine (pz) adsorbed from acidic (Fig. 6.1) and non-acidic solutions onto silver electrodes and assignments

Adsorption from a 1.0 M KBr + 1.0 M $HClO_4$ + 0.1M pz solution			pzH^+ in solution (0.1M pz + 2.7 M HCl) (from ref. 2)	Adsorption from a 1.0 M KBr + 0.1M pz solution E=-700 mV (from ref. 3)	Pyrazine in solution (0.1 M pz) (from ref. 2)	Vibrational Assignments[a]. D_{2h} / C_{2v}
OCP	E ≈ -100 mV[b]	E ≈ -300 mV[c]				
411 (w)			(417) vvw	432 (w)		B_{2u} / B_2 (16b)
602 (m)			606 (w)			A_g /A_1 (6a)
611 (sh)				630 (m)	620 (w)	
710 (w)			688 (m)	697 (w)	702 (m)	B_{2g} / B_1 (6b)
898 (m)		898 (m)	898 (vw)		922 (w)	B_{1g} / A_2 (10a)
934 (s)	934 (s)	934 (s)				ClO_4^-
1002 (s)		1002 (s)				A_g / A_1 (1)
1018 (s)	1018 (s)		1020 (vs)	1019 (vs)	1020 (vs)	
1031 (sh)	1031 (sh)		1031 (s)			B_{1u} / A_1 (12)
1090 (w)			1112 (w)			B_{1u} / A_1 (18a)
1222 (s)	1222 (s)	1200 (m)	1223 (m)	1225 (m)	1218 (m)	A_g / A_1 (9a)
				1235 (m)	1238 (sh)	A_g / A_1 (11 +16b)
1616 (vs)	1616 (vs)		1618 (m)	1590 (vs)	1593 (m)	A_g / A_1 (8a)
1635 (sh)					1618 (vw)	A_g / A_1 (1+6a)

[a] The symmetry species are presented for both point groups D_{2h} (for pyrazine) and C_{2v} (for monoprotonated pyrazine). A correlation table was used (see ref. 2).
[b] perpendicular-adsorbed pzH^+
[c] flat-adsorbed pzH^+
v - very; s - strong; m - medium; w - weak; sh - shoulder

adsorption of neutral pyrazine onto a metallic surface would remove the molecular centre of symmetry [10]. Consequently, the molecular symmetry should be reduced from D_{2h} to C_{2v} due to the adsorption. In this case, it can be expected that the spectrum of adsorbed neutral pyrazine (under C_{2v} symmetry) should have some similarities with the spectrum of monoprotonated pyrazine cation (also C_{2v}) in solution. However, as observed in Table 6.1, the vibrational wavenumbers found for pyrazine adsorbed onto a silver electrode from acidic solution match more closely the wavenumbers of the monoprotonated pyrazine cation in solution, and the peak positions in the SERS spectrum of pyrazine adsorbed from neutral solution are more similar to those from the aqueous solution pyrazine spectrum. This is an indication that symmetry reduction, due to formation of a metal-organic molecule complex, is not a necessary consequence of adsorption; and that the interaction of pyrazine with the metal is not strong enough to induce a symmetry change.

The SERS spectra at potentials more positive than ca -100 mV were time dependent. The SERS signal decreased with time, and the rate of decrease became faster as the potential became more positive. A simple explanation is that a silver bromide film is formed during the silver oxidation step and this film quenches the SERS effect, which is a near-surface phenomenon. The time dependence of the SERS signals made the study of medium intensity and weak bands very difficult at these potentials. Hence, we focused our work on the 1000, 1200 and 1600 cm^{-1} regions where the strongest bands were found.

Figures 6.2, A to C, shows the SERS spectra of pyrazine adsorbed from acidic solution on a silver electrode at several potentials. The point of zero-charge for silver in

bromide medium is expected to be more negative than -900 mV [11] and, thus, the surface charge is positive. When the potential was swept to values more positive than -160 mV, the band intensity at 1002 cm^{-1} decreases, and one can just notice two bands near 1020 cm^{-1} at potentials close to the onset of the silver oxidation (around -100 mV). These two bands coalesce into a broad envelope that can be resolved using a bandfitting computer program. The experimental trace in this region and its bandfitted components are presented in Fig. 6.3. From the bandfitting analysis one can locate the positions of these two bands at ~ 1018 and at ~ 1031 cm^{-1}, respectively. Just one band is observed at 1222 (Fig. 6.2B) and 1616 cm^{-1} (Fig. 6.2C) at potentials more positive than -160 mV.

When the potential was swept to less positive values, the SERS intensity of pzH^+ was recovered, following the silver ion reduction around ca -200 mV. In this case, the 1002 cm^{-1}-band was present and it was more intense than the envelope at ~ 1000 cm^{-1}. The 1002 cm^{-1}-band is the only one left in the spectrum in the 1000 cm^{-1} region at potentials more negative than ca -280 mV (Fig. 6.2A). Two bands showed up in the 1200 cm^{-1} region after the silver ion reduction (Fig. 6.2B) - one band at 1222 cm^{-1} and another at ~ 1200 cm^{-1}. The 1616 cm^{-1} intensity decreased as the potential became negative (Fig. 6.2C), and its position remained unchanged. This band vanished completely near -300 mV.

The results presented above are consistent with adsorption of pyrazinium cation with different orientations at different potentials. One adsorption orientation is predominant during the silver oxidation (E > -170 mV), and the other dominates at potentials more negative than -300 mV. These two different orientations of adsorbed

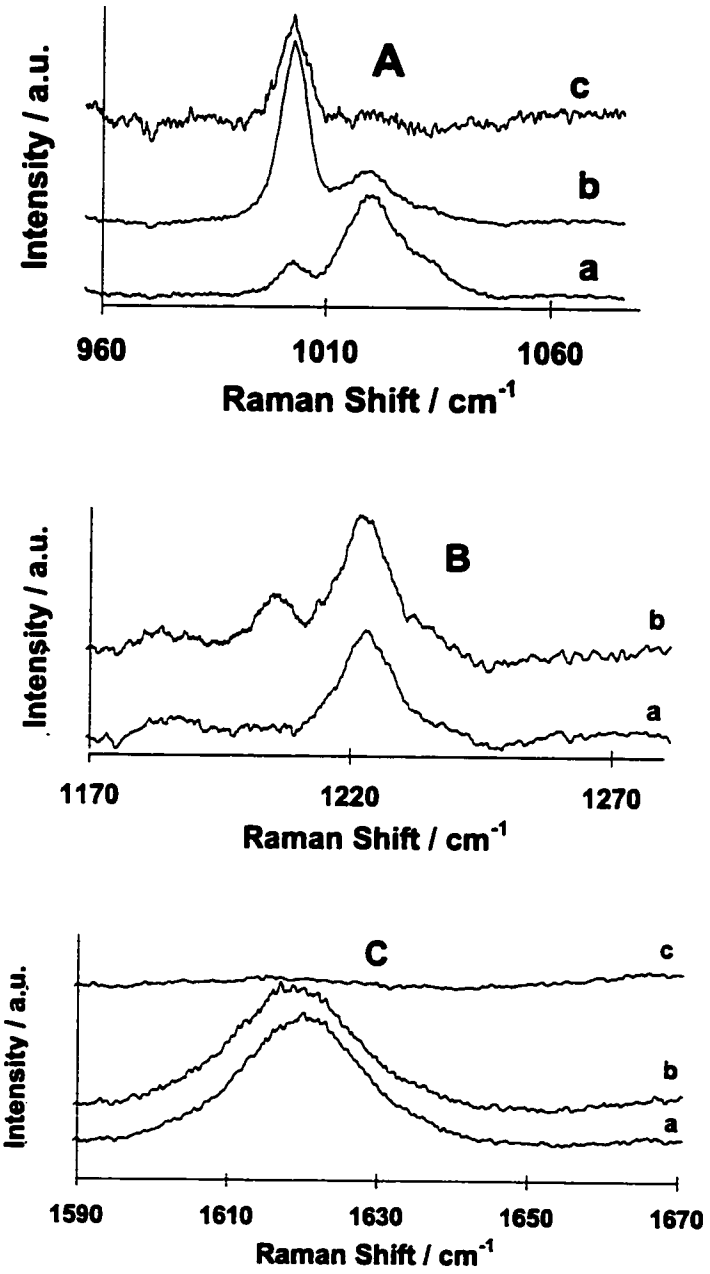

Figure 6.2: SERS spectrum of pyrazinium on a silver electrode adsorbed from a 1.0 M KBr + 1.0 M $HClO_4$ + 0.1 M pyrazine solution at several potentials. For region A: a) -160 mV; b) -250 mV; c) -340 mV. For region B: a) -170 mV; b) -240 mV. For region C: a) -170 mV; b) -250 mV; c) -310 mV.

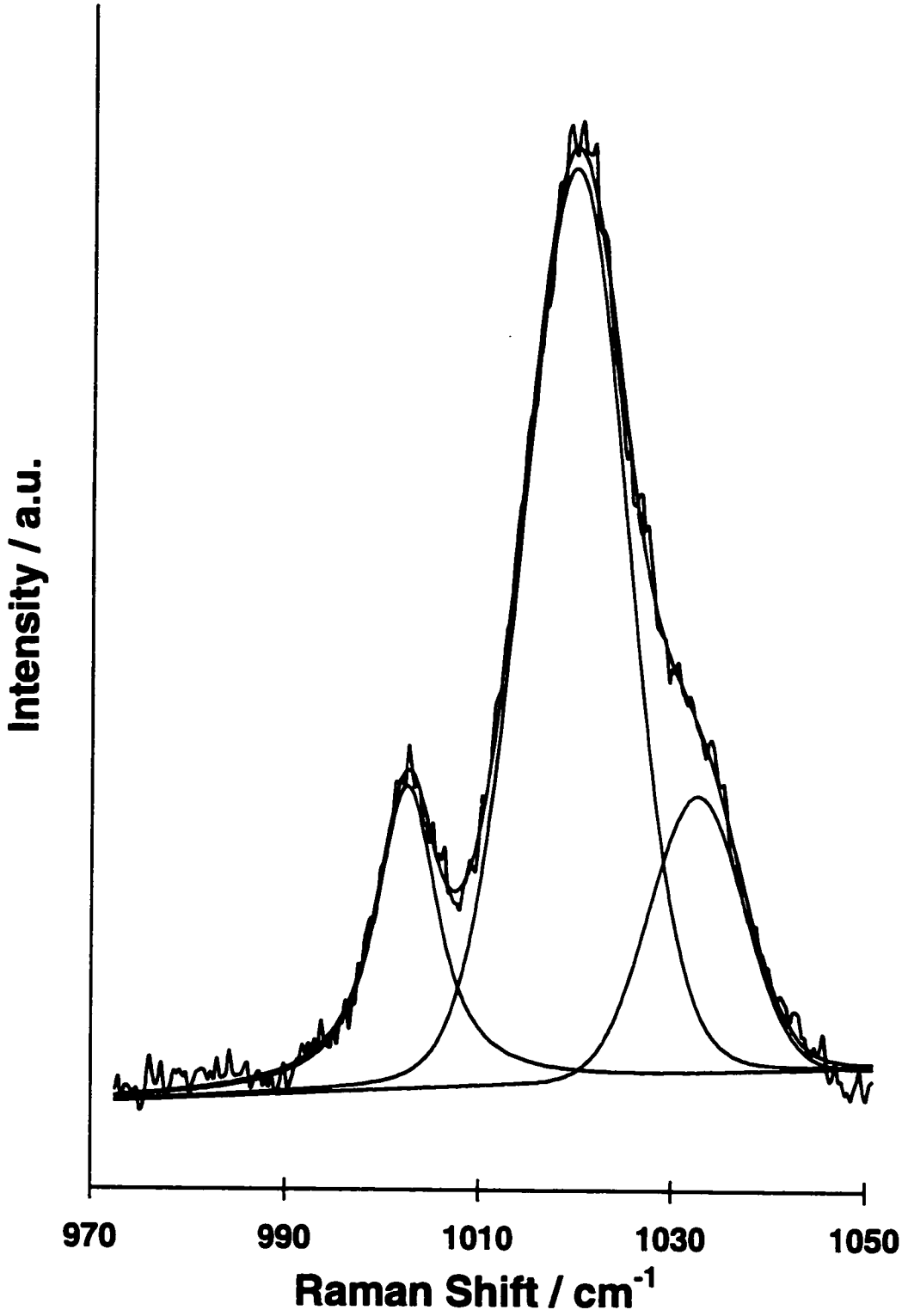

Figure 6.3: Observed SERS spectrum of pyrazinium on a silver electrode and its bandfitted components.Solution: 0.1 M KBr + 1.0 M $HClO_4$ + 0.1 M pz. E = -170 mV.

monoprotonated pyrazine can coexist on the metallic surfaces at intermediate potentials. Actually, the pyrazinium ion spectrum at OCP presented in Fig. 6.1 is an example of this. The two proposed different orientations for the monoprotonated pyrazine cation are illustrated in Fig. 6.4.

The surface selection rules for SERS predict that the vibrational modes with polarizability changes perpendicular to the electrode surface will be more enhanced than the parallel ones [12]. Pyrazine adsorbed from neutral solution is thought to bind to the metallic surface by means of one of its nitrogen atoms [3]. This end-on adsorption mode is confirmed by a SERS spectrum dominated mainly by the 630, 1019, 1225 and 1590 cm^{-1}-bands; for end-on adsorption these bands have components perpendicular to the surface.

The most predominant band in the pzH^+ spectrum at potentials more positive than -170 mV is the ring stretch mode 8a at 1616 cm^{-1} (Fig. 6.2C). This band is, at least, 3 times more intense than the ring breathing mode at ~ 1000 cm^{-1}. The 8a mode is more intense than the ring breathing mode in the SERS spectra of the perpendicular-adsorbed pyrazine [3]. Even considering that a CT contribution may be relevant for the large intensity of the band at 1616 cm^{-1} [13], the intensity ratio between this mode and the ring breathing mode (near 1000 cm^{-1}), observed in Fig. 6.2, suggests that pyrazinium is adsorbed end-on at those potentials where the silver oxidation occurs. The presence of the 1031 cm^{-1} δ - ring mode (number 12) also supports end-on adsorption. This mode is forbidden in the normal Raman spectrum of pyrazine, but becomes active (with very weak intensity) in the SERS spectrum of pyrazine [3]. It also appears with fair intensity in

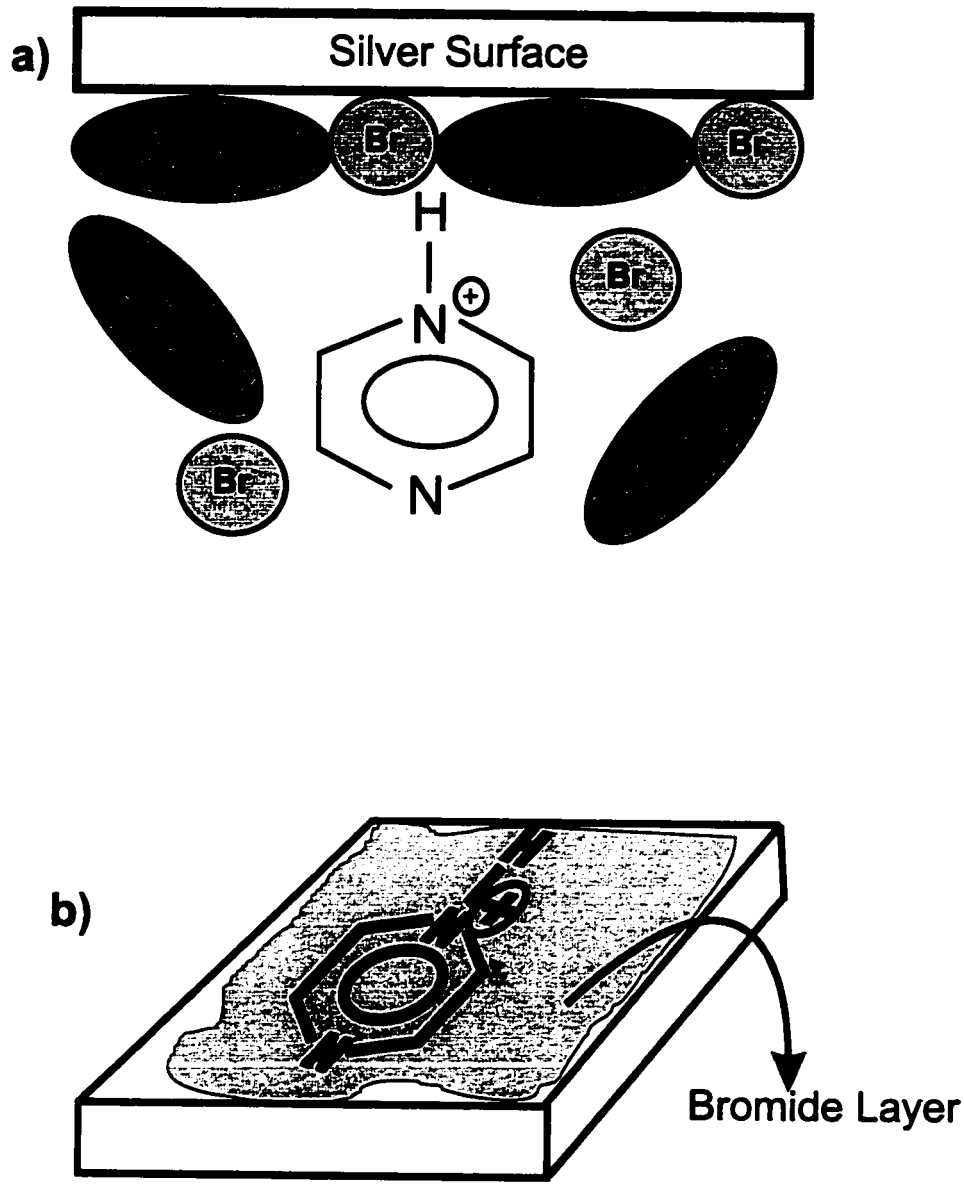

Figure 6.4: a) pyrazinium adsorbed end-on is the predominant species at potentials more positive than -170 mV. The cation may interact with either the halide or the soluble silver oxidation products which are adsorbed at the positively charged electrode. b) The positive charge can be delocalized throughout the entire pyrazine ring due to the protonation of pz, which enables the pyrazinium cation to adsorb flat through the halide layer. Flat adsorbed pyrazinium is the predominant species at potentials more negative than -300 mV.

the SERS spectrum of end-on adsorbed pyridine [5]. On the other hand, this mode is completely absent in the flat adsorbed benzene SERS spectrum [14].

Another point to be addressed is how a positive monoprotonated pyrazine can adsorb on a positively charged electrode (the pzc for silver in this bromide medium is expected to be more negative than -900 mV [11]). It is well known in the literature that positive species can use a halide layer as bridge to adsorb onto a positively charged surface [4, 15, 16]. During the silver oxidation, a AgBr film is expected to form. It is possible that film dissolution can occur in a highly concentrated halide medium, by formation of $[AgBr_x]^{-(x-1)}$ anions. We can conclude that the pyrazinium cation is bound to either a halide or to the $[AgBr_x]^{-(x-1)}$ and these anions are adsorbed to the positively charged electrode (see Fig. 6.4A). A low wavenumber band at 150 cm^{-1}, attributed to adsorbed Br^-, decreases in intensity as the electrode is made more negative; concomitantly the band of pzH^+ decreases in intensity. These observations are consistent with the potential dependent Br^- surface coverage determined electrochemically [11].

Different features in the pzH^+ spectrum were observed when the potential sweep was continued in the negative direction and the reduction of the silver oxidation products occurred. The Ag^+ ions reduced to Ag around -180 mV, forming the SERS-active sites, and the spectral lines became more intense. The intensity of the SERS bands decreased starting at ~ -300 mV. The main features of this pyrazinium spectrum in the 1000 cm^{-1} - region are the decrease in the intensities of the envelope that contains the 1018 and 1031

cm^{-1} bands and the appearance of a very strong band at 1002 cm^{-1} (Fig. 6.2A). In the 1200 cm^{-1} region (Fig. 6.2B) one can also notice the decrease in the 1222 cm^{-1} band and the appearance of a 1200 cm^{-1}-band. New bands are not formed in the 1600 cm^{-1} region (Fig. 6.2C). The 1616 cm^{-1} band intensity just decreases as the potential becomes negative and vanishes completely at -330 mV.

The spectral observations at potential values more negative than -200 mV suggest that the pyrazinium cation is either tilted or flat-adsorbed on the metallic surface. The bands at 1002 cm^{-1} and at 1200 cm^{-1} can be assigned to the ring modes, numbers 1 and 9a, respectively. The shifts of flat-adsorbed pyrazine ring modes to lower wavenumbers have been observed by Moskovits et al. [17]. Similar changes were also observed in the benzene SERS spectrum [14]. When aromatic molecules interact with the surface by π-electrons of the ring, they adsorb flat. This interaction is expected to shift the ring stretch wavenumbers down. The flat-adsorbed benzene SERS spectrum is also completely dominated by the ring breathing mode (number 1) [14]. For instance, this mode is several times more intense than the ring stretch mode number 8a which dominates the spectrum of the end-on adsorbed pyrazine. In Fig. 6.2, at a potential of ca -300 mV, the 8a mode is hardly observed, but the ring breathing mode is still intense. Another interesting band is at 898 cm^{-1}, marked with an asterisk (*) in Fig. 6.1. This band is assigned to the γ ring mode number 10a (out-of-plane), and it is completely absent in the SERS spectrum of pyrazine [3]. However, this band is fairly intense in the benzene spectrum [14] and, following the SERS selection rules, it is expected to be active only for a flat adsorbed molecule.

Similarly, the presence of the 1002 cm^{-1} band (also marked with an asterisk (*) in Fig. 6.1) is consistent with the flat orientation.

In the potential range where the monoprotonated pyrazine adsorbed flat, the silver oxidation products, AgBr or $[AgBr_2]^-$, have largely been reduced to metallic silver. This process increases the specific halide surface concentration very significantly. Hence, the flat adsorbed pyrazinium cation may be bound to the halide layer which is adsorbed to the positively charged silver surface, as shown in Fig. 6.4B.

6.4. Conclusions

The SERS spectrum of monoprotonated pyrazine was measured. The pyrazinium cation can adsorb onto the electrode surface by two different orientations. The end-on adsorbed monoprotonated pyrazine is predominant at potentials more positive than -170 mV. The flat-adsorbed pyrazinium cation is thought to be the only species on the surface at potentials more negative than -300 mV. The positively charged pyrazinium cation must use either the halide or the $[AgBr_x]^{-(x-1)}$ complex as a bridge to adsorb to a positive electrode surface.

6.5. References

[1] A. S-C. Chia and R. F. Trimble, Jr, *J. Phys. Chem.*, **1961**, 65, 863.

[2] A.G.Brolo and D.E.Irish, *Z. Naturforsch.*, **1995**, 50A, 274.

[3] A.G. Brolo and D. E. Irish, *J. Electroanal. Chem.*, **1996**, 414, 183.

[4] A.G. Brolo and D.E. Irish, *J. Chem. Soc. Faraday Trans.*, **1997**, 93, 419.

[5] L. N. Klatt and R. L. Rouseff, *J. Am. Chem. Soc.*, **1992**, 94, 7295.

[6] J. Swartz and F. C. Anson, *J. Electroanal. Chem.*, **1984**, 114, 117.

[7] A.G. Brolo and D.E. Irish, in *Solid-Liquid Electrochemical Interfaces*, G. Jerkiewicz, M.P. Soriaga, K. Uosaki and A. Wieckowski, eds., ACS Symposium Series No. 656, ACS Books, Washington DC, 1997, Ch. 22.

[8] A. G. Brolo and D. E. Irish, *Can. J. Chem.*, **1997**, 75, 1643.

[9] A. G. Brolo, B.D. Smith and D.E. Irish, *J. Mol. Struct.*, **1997**, 405, 29.

[10] G. R. Erdheim, R. L. Birke and J. R. Lombardi, *Chem. Phys. Lett.*, **1980**, 69, 495.

[11] G. Vallete and R. Parsons, *J. Electroanal. Chem.*, **1987**, 229, 87.

[12] J. A. Creighton, *Advances in Spectroscopy Vol. 16 - Spectroscopy of Surfaces*, R. H. Clark and R. E. Hester, eds., Wiley, NY, **1988**, p. 37.

[13] J. F. Arenas, M. S. Woolley, J. C. Otero and J. I. Marcos, *J. Phys. Chem.*, **1996**, 100, 3199.

[14] M. Moskovits and D. P. DiLella, *Chem. Phys.*, **1980**, 73, 6068.

[15] D. J. Rogers, S. D. Luck, D. E. Irish, D. A. Guzonas and G. F. Atkinson, *J. Electroanal. Chem.*, **1984**, 167, 237.

[16] Z. Deng and D. E. Irish, *Langmuir*, **1994**, 10, 586.

[17] M. Moskovitz, D. P. Dilella and K. J. Maynard, *Langmuir*, **1988**, 4, 67.

Chapter 7

SERS Studies of Pyrazine Adsorbed onto Polycrystalline Gold Electrodes

7. SERS Studies of Pyrazine Adsorbed on Polycrystalline Gold Electrodes

7.1. Introduction

The nature and the orientation of molecules adsorbed on certain rough electrode surfaces (mainly Ag, Au, and Cu) can be readily determined by electrochemical surface-enhanced Raman scattering (SERS) [1,2]. The million-fold enhancement of the Raman signal makes this technique sensitive even to sub-monolayer amounts of adsorbate. This surface-enhancement phenomenon, allied to basic characteristics of Raman scattering, such as the weak water activity, suggests that the SERS effect is potentially a very powerful tool for the investigation of electrochemical problems. However, the magnitude of the enhancement depends on several factors, such as applied potential, excitation wavelength, surface coverage, and morphology [1,2]. The dependence of the electrochemical SERS intensities on the applied potential and on the energy of the incident photon has been widely studied [3,4]. The relationships are well understood and can be interpreted based on the two most accepted surface-enhancement theories - the charge transfer (CT) [5] and the electromagnetic (EM) [6] mechanisms. However, no studies have dealt with the dependence of the SERS intensities on both surface coverage and morphology for molecules adsorbed on gold electrodes.

The relationship between SERS intensity and surface morphology has been addressed for species adsorbed on silver surfaces. Several authors [7,8,9] have shown

that, for silver electrodes, a maximum electrochemical SERS signal was obtained when the size of the surface roughness (determined by SEM) ranged from 80 to 100 nm. An apparatus for the simultaneous measurement of the silver electrode morphology (by scanning probe microscopy) and the SERS signal has been developed [10]. However, no attempt to systematically relate the surface features to the optical enhancement was made [10]. The size distribution of roughness features on silver electrodes has been analyzed from their inelastic Mie scattering [11]. Unfortunately, the distribution of large surface bumps (> 15 nm), which is supposed to yield strong SERS spectra, cannot be determined by this method, because their acoustic bands are merged into the Rayleigh line [11]. Two-dimensional SERS images of pyridine adsorbed on rough silver electrodes have been obtained and compared to the AFM data of the surface[12]. The results indicated that surface features from 50 to 400 nm were responsible for the enhancement of the Raman signal [12]. The differential reflectance spectrum of an electrochemically roughened silver electrode is also dependent on the surface morphology [13]. The enhancement factor of the Raman signal depends on the surface reflectivity. Silver electrodes with roughness bumps ranging between 100 to 300 nm presented a minimum reflectivity and a maximum SERS signal [13]. This range is in good agreement with the SERS intensities obtained from deposited silver in UHV procedures [14]. In this case, a maximum SERS signal was obtained for slowly-deposited silver, which produced silver bumps of 150 nm average size.

Various studies regarding the relationship between enhanced optical properties and the surface morphology, determined by scanning probe microscopy, for Ag films deposited over glass [15], silica [16], graphite [17], mica [18], Formvar [19] and suspended polymer

particles [20] have been reported. The metallic silver, deposited over different supports, yields distinct SERS-active substrates. The morphology (and the optical response) of these deposits depends on several factors, such as the nature of the substrate [21] and the conditions under which the metallic deposition is made [22]. The sizes of the silver bumps presented in these films are between 5 and 20 nm [15-22]. The SERS response depends also on the film thickness [22] and on the aggregation of the silver particles [23]. Silver films deposited on polymer nanoparticles have also been prepared [24]. SERS enhancement factors as high as 10^7 were obtained from these substrates. The silver-coated nanosphere of ~ 500 nm yielded the largest SERS signal [24].

A relationship between the SERS intensity and the fractal dimension has been proposed for molecules adsorbed on vacuum-deposited silver [25,26]. The silver films formed at low temperature (~ 100 K) possessed significant fractal characteristics and were SERS active. Films formed at high temperature (~ 300 K) possessed few fractal characteristics and gave no SERS activity.

Very few works deal with the relationship between SERS intensities and surface morphology for molecules adsorbed on gold surfaces (when compared to silver surfaces). SERS spectra from Rhodamine 6G were obtained for sputtered gold films on Au and Au/Si alloys [27]. The size of the roughness features on these surfaces was ~ 40 nm [27]. The dependence of the SERS response on the surface morphology was also investigated for a self-assembled monolayer of ferrocenylazobenzenes adsorbed on a Au thin film deposited on mica [28]. Enhancement factors of the order of 10^3 were observed from

these rough surfaces containing gold spheroidal particles with diameters in the 50-100 nm range [28]. Silver coated gold colloids have been used as SERS substrates [29,30]. A glass slide covered with these silver-modified gold colloid particles of various sizes was prepared using a combinatorial approach [31]. The two dimensional SERS spectra obtained from this substrate showed a maximum response from particles of ~ 20 nm size [31].

The relationship between electrochemical SERS intensities and surface coverage has been investigated for halides and pseudohalides adsorbed on silver electrodes [32,33]. A linear dependence between SERS intensity and surface concentration has been found for 2-amino-5-nitro-pyridine adsorbed on a rough silver electrode [34]. The study of the relationship between SERS intensity and surface coverage for molecules adsorbed on gold electrodes has been limited by the lack of independent electrochemical measurements of the surface concentration of the organic molecules. Recently, these electrochemical data are being produced in our Centre [35].

A previous study of the dependence of the SERS intensity of the pyridine (py) ring breathing mode on surface coverage, determined independently by electrochemical means, has been conducted in our laboratory [36]. For pyridine adsorbed on an "unroughened" gold electrode, the SERS intensities showed a direct proportionality to the surface concentration at low coverage ($\leq$ 2/3 monolayer). As the surface coverage value approached one monolayer, the SERS intensity decreased, and the relationship became inverse [36]. This deviation of the SERS intensities at high coverage was attributed to the

depolarising effects which the adsorbed molecules have on the local electromagnetic field [36]. The effect of the surface roughness was also investigated. Both the SERS intensities and their dependence on the applied potential were dependent on the degree of roughness of the surface. The SERS intensities obtained from such rough surfaces did not present any simple relationship with surface coverage [36].

The objective of this work is to extend our previous results to the study of the adsorption of pyrazine (pz) on polycrystalline gold electrodes. The surface concentration of pz at several potentials, measured recently [37], and the morphology of a gold electrode surface submitted to different numbers of oxidation-reduction cycles are compared to the SERS intensity from pz. Most of the results presented in this Chapter have been published elsewhere [38].

7.2. Experimental

7.2.1. Solutions

All solutions were prepared with Milli-Q water. All SERS experiments were performed in 0.1 M $KClO_4$ (BDH). The $KClO_4$ was purified by calcinating at 300 °C, recrystallizing twice from Milli-Q water, and then drying. 0.1 M KCl (BDH) was used for the preparation of the rough gold electrode. Pyrazine 99+% (Aldrich) was used without further purification. The solutions were purged with nitrogen for at least ½ hour before

taking measurements and a gentle N_2 stream was kept over the top of the solution during experiments.

7.2.2. Electrodes

The working electrode was a polycrystalline 4 mm diameter gold rod from Johnson Matthey (99.99% pure) mounted in a Teflon holder. The gold electrode was polished to a mirror finish with progressively finer grades of alumina, ending with the 0.3 μm grade. The electrode was then rinsed with copious amounts of Milli-Q water, and treated in an ultra-sonic bath to remove any excess of alumina. Finally, the electrode was cleaned by flaming and quenching with Milli-Q water [39], and transferred to an electrochemical cell for the activation procedure.

The counter electrode was a platinum wire, separated from the working electrode compartment by a porous glass frit. A saturated calomel electrode (SCE) was used as the reference electrode. Therefore, all potentials reported in this work are relative to the SCE. A Luggin capillary was used to minimize the IR drop.

7.2.3. Activation Procedures

7.2.3.1. Preparation of a rough gold electrode

The "activation procedure" is the process of creation of the necessary roughness, which allows the electrode surface to support the SERS effect. A clean gold electrode was

transferred to a typical electrochemical cell containing 0.1 M KCl solution for activation (roughening). The hanging electrode technique was used to make contact between the gold and the electrolyte solution [40]. Several methods for activating the gold electrode have been described in the literature [41,42,43]. The method developed by Gao et al. [41] yields a stable and reproducible surface, and was used in this work. One complete oxidation-reduction cycle (ORC) from this method is illustrated in Figure 7.1. The anion $[AuCl_4]^-$ is the main product from the electrochemical dissolution of metallic gold in chloride medium [44]. The formation of this anion is controlled by the diffusion of chloride to the gold surface. When the potential scan is reversed to the negative direction, the concentration of gold chloride species close to the surface is very high. The deposition of metallic gold is very fast (the scan rate was 500 mV/s), creating patches of gold clusters on the surface. As the number of ORCs increased, the size of these roughness features also increased. The cathodic and the anodic charge for each ORC were calculated by integrating the area under the voltammogram. Distinctly different rough surfaces were prepared by varying the number of ORCs performed. Figure 7.2 shows that the cathodic charge increases linearly with the number of ORCs, and the ratio between the cathodic and the anodic charge remains constant for different numbers of ORCs within 10%. Typically, 60% of the anodic charge is recovered in the reverse scan, indicating that some of the oxidation product diffused away from the electrode into the bulk solution. Following the last cycle, the activated electrode was rinsed with Milli-Q water and then transferred to the SERS cell, described in Chapter 2 and reference [1].

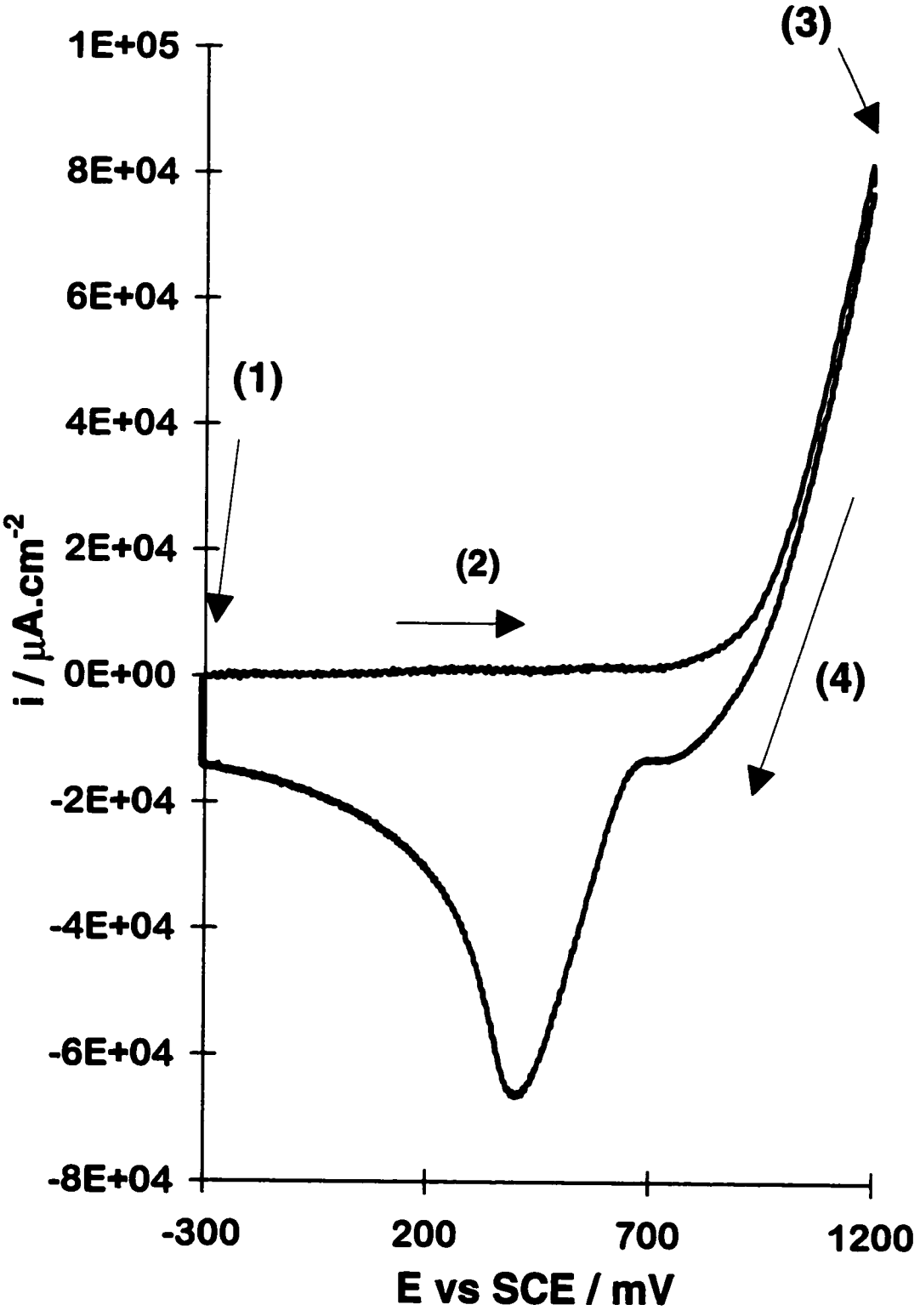

Figure 7.1: Cyclic voltammogram of a polycrystalline Au electrode in 0.1 M KCl.
(1) E = -300 mV for 30 sec.; (2) anodic scan at 1 V/s;
(3) E = +1.2 V for 1.2 sec.; (4) cathodic scan at 0.5 V/s.

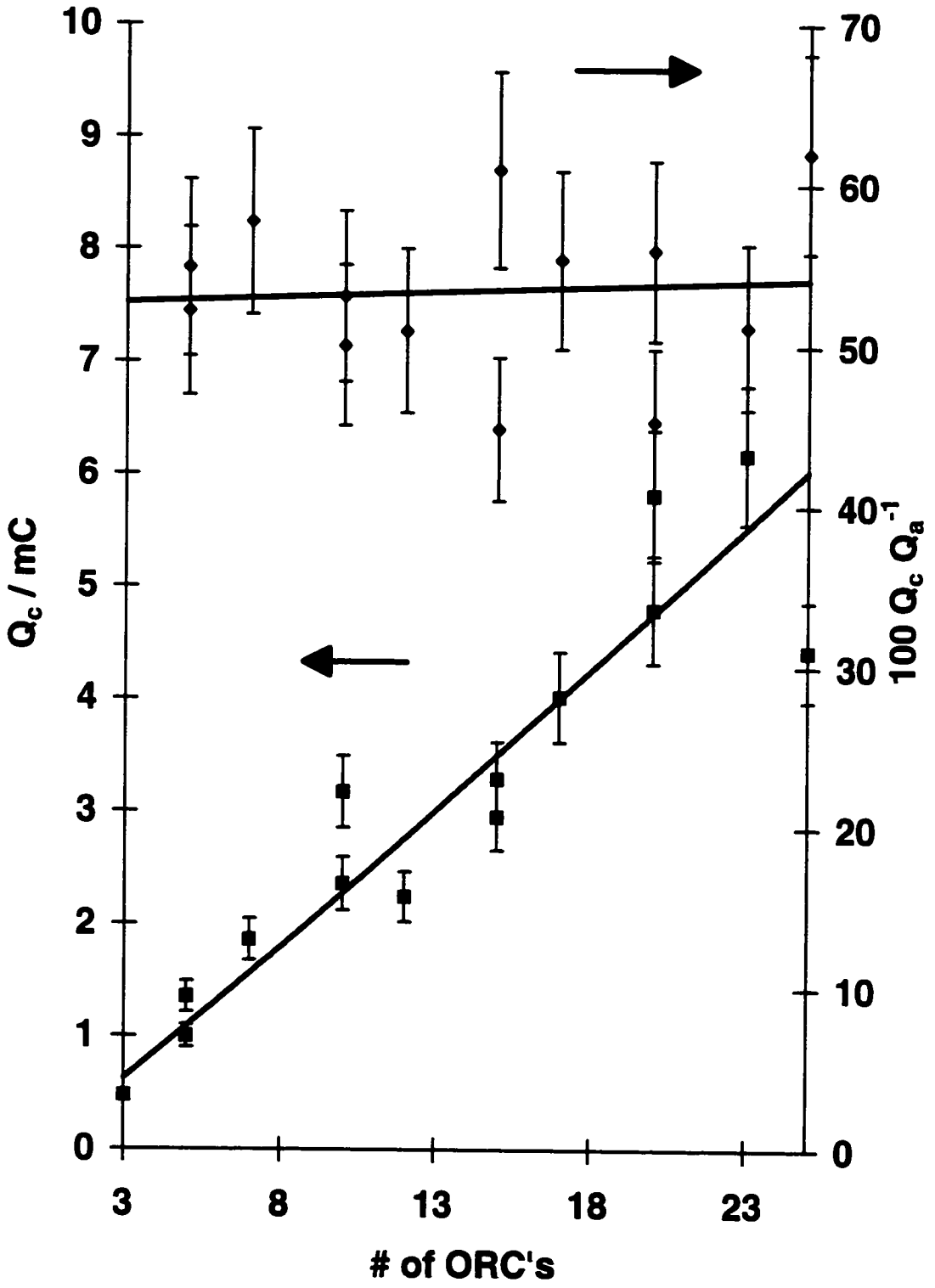

Figure 7.2: Dependence of both the cathodic charge (Q_c) and the ratio between cathodic and anodic charge (Q_a/Q_c) on the number of ORCs.

7.2.3.2. Preparation of an "unroughened" gold electrode

The SERS spectra of pz from an "unroughened" gold electrode were also obtained. The "unroughened" gold electrode was prepared using the technique developed in a previous work [36]. A cleaned gold electrode was placed in the SERS cell containing 0.1 M $KClO_4$ and the desired concentration of pz. The electrode was submitted to continuous cleaning cycles between the limits -0.8 V to 1.1 V at 20 mV/s. This cycling persisted until a cyclic voltammogram reproduced itself from one cycle to the next and displayed the features of a clean gold electrode.

7.2.4. Instrumentation

7.2.4.1. Spectroelectrochemical measurements

A Dilor OMARS-89 Spectrometer equipped with an OMA was used in the SERS experiments. The OMARS-89 was operated using the 1800 groove/mm gratings with two gratings operating in subtractive mode and a third grating dispersing the output onto the 512 diode array detector. The spectrometer was interfaced to an IBM AT computer. The spectra were transferred to a 486 computer where the programs for baseline correction and bandfitting were available. A potentiostat PAR model 273 was used in the electrochemical and SERS experiments. The cyclic voltammograms were recorded using a Kipp & Zonen XYY' plotter.

A Coherent 599 dye laser, pumped with a Coherent Innova 70 argon ion laser operating in all-lines mode, provided the laser excitation. The laser dye was DCM (Lambda Physik), and all spectra were excited by a 650 nm laser line.

For all SERS experiments the mechanical slit widths were 150 μm, which give a spectral slit of, approximately, 3 cm^{-1}. The laser power was set to 50 mW. An accumulation time of 1 second and 10 acquisitions were used to obtain the spectrum of pz adsorbed on a rough gold electrode. For "unroughened" gold electrodes, an accumulation time of 2 seconds and 100 accumulations were used.

7.2.4.2. Atomic force microscopy measurements

The microscope was a Nanoscope E (Digital Instruments). Standard silicon nitride tips were mounted on gold-plated 200 micrometer v-shaped cantilevers (spring constant 0.12 N/m) and a 15 micrometer piezo scanner was used. A schematic representation of an AFM apparatus is presented in Figure 7.3. Additional details about the working mechanism of scanning probe microscopies, including AFM, and their applications have been thoroughly reviewed [45, 46, 47].

The roughened gold substrate was activated (as described above) and dried before each measurement. All AFM images were obtained in air and in the contact mode (i.e., at constant force). Roughness factors (R) were calculated from each image (image

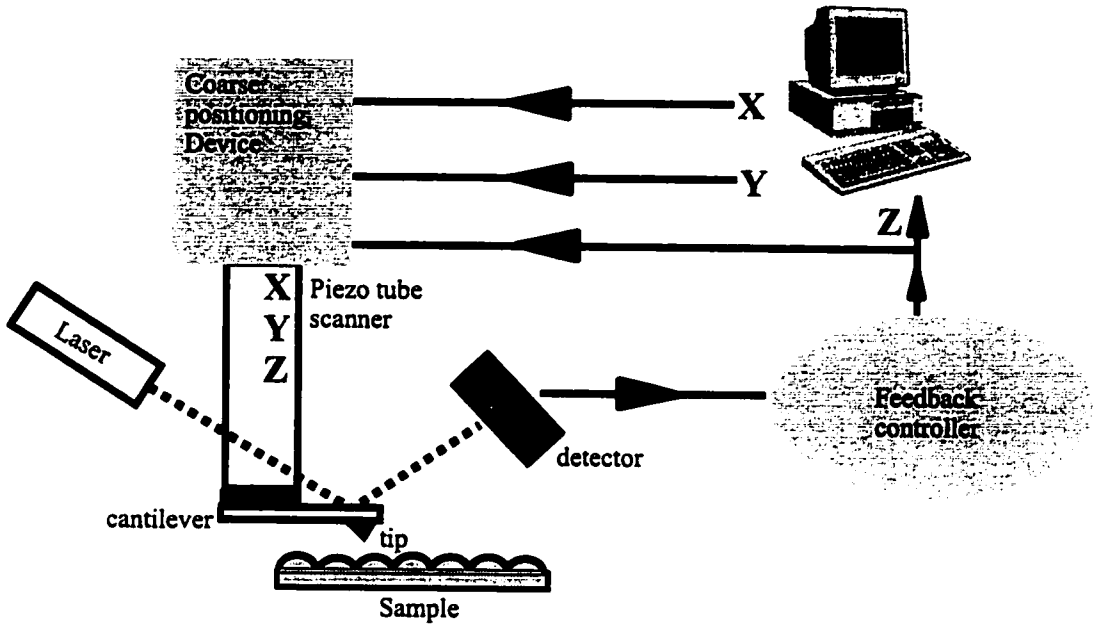

Figure 7.3: Schematic illustration of an AFM apparatus. The "coarse positioning device" is used to take the tip and move it a distance on the order of millimeters to micrometers from the surface. The fine positioning and scanning is accomplished using a piezoelectric tube. The forces exerted by the sample on the AFM tip bend the cantilever. A segmented photodiode (detector) is used to measured the deflection of the laser light reflected from the back of the cantilever (the laser beam deflection is provoked by the cantilever bending due to interaction with the surface). The signal from the detector is directed into a feedback system.

dimensions of 1 μm x 1 μm) obtained from different numbers of ORCs. The nanoscope software was used in these calculations. The roughness factors were directly proportional to the number of ORCs (R increases as the number of ORCs increases). Consequently, according to Fig. 7.2, the roughness factor is also linearly dependent on the cathodic charge.

7.3. Results and Discussion

7.3.1. The dependence of SERS intensities of pyrazine adsorbed on a polycrystalline gold electrode on the surface morphology

Figure 7.4 shows the SERS spectrum of pz adsorbed on a rough gold electrode (produced after 5 activation ORCs). The system is Au/$KClO_4$, 1 mM pz; no halide is present. The normal Raman spectra (NRS) of aqueous solutions of pyrazine (pz) and its protonated forms have been studied (Chapter 3 , [48]). The vibrational wavenumbers from the pz bands observed in Fig. 7.4 are in good agreement with the wavenumbers observed in the NRS of aqueous pz [48]. The small shifts of the pz bands on adsorption suggest a weak interaction between pz and the gold surface. An extensive study of pz adsorbed from aqueous halide solutions on a silver electrode (Chapter 5, [49,50]) showed that pz binds to the electrode surface via the N lone pair (end-on configuration). The relative intensities for the pz bands observed in the SERS spectrum presented in Fig. 7.4 are similar to those observed for pz adsorbed on silver electrodes; therefore, we can conclude that pz also adsorbs on gold with the same orientation as it adsorbs on silver.

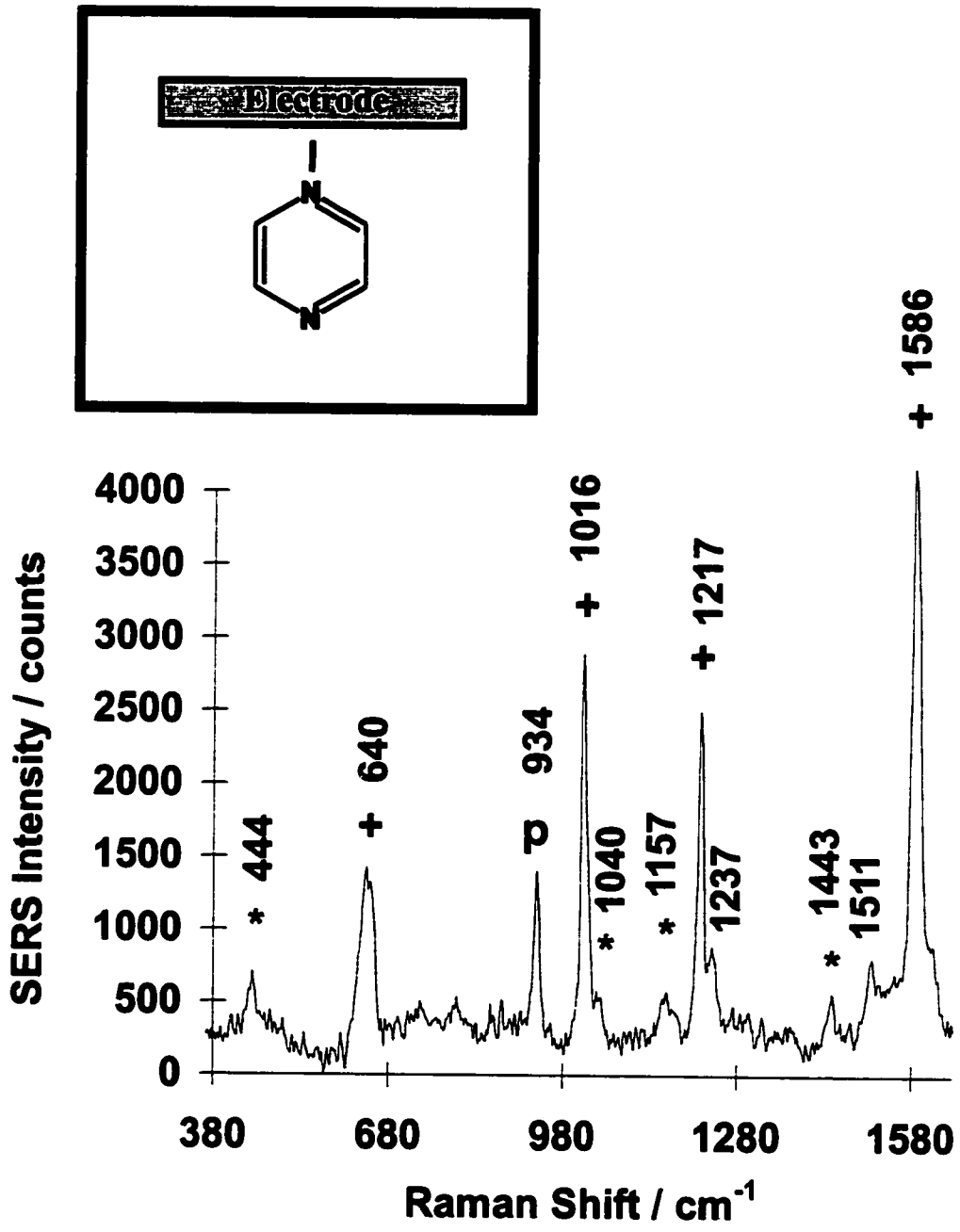

Figure 7.4: SERS spectrum of pyrazine adsorbed on a rough gold electrode (5 ORCs). E = -50 mV. (*) forbidden bands in the NRS of pz; (+) A_g modes (most enhanced); (p) perchlorate stretch band. The vibrational wavenumbers (cm^{-1}), are indicated. A 650 nm excitation line with laser power of 50 mW was used. The acquisition time was 1 second and 10 accumulations were made.

Figure 7.5 shows the dependence of the SERS intensity of the ring breathing mode of pyrazine, 1016 cm^{-1}, on the roughness factor (obtained for a rough gold electrode). The roughness factor was normalized by setting the value of a surface not subjected to any ORC to zero. The SERS intensities presented in Fig. 7.5 and subsequent figures have been normalized using the 934 cm^{-1} perchlorate stretch mode (from 0.1 M ClO_4^-) as an internal standard. This procedure avoids intensity changes due to laser power fluctuations. The SERS intensity increased with the roughness factor, reaching a maximum for a roughness factor value between 3 and 5 (which corresponds to a number of ORCs between 20 and 30), and decreased after the value of the normalized roughness factor reached ca. 4.5 (around 35 ORCs) (Fig. 7.5). A similar result was obtained by Gao et al. for the adsorption of benzonitrile and thiocyanate on gold electrodes [41]. The dependence of the SERS intensity on the roughness factor must be related to the morphology of the rough gold substrate.

Figure 7.6 (A - C) presents atomic force microscopy (AFM) images of the gold surface with different roughness factors. In this case, the gold electrode was roughened in 0.1 M KCl solution with the appropriate number of ORCs, and transferred to the AFM apparatus. The morphology of these surfaces (observed in the air) is considered to be similar to a rough electrode immersed in aqueous solution (used in the SERS experiments). Rough gold surfaces are very stable SERS substrates [41], which suggests high morphological stability. Therefore, we believe that it is valid to compare the SERS results (obtained using a rough gold electrode immersed in aqueous solution) to the AFM data (obtained *ex-situ*).

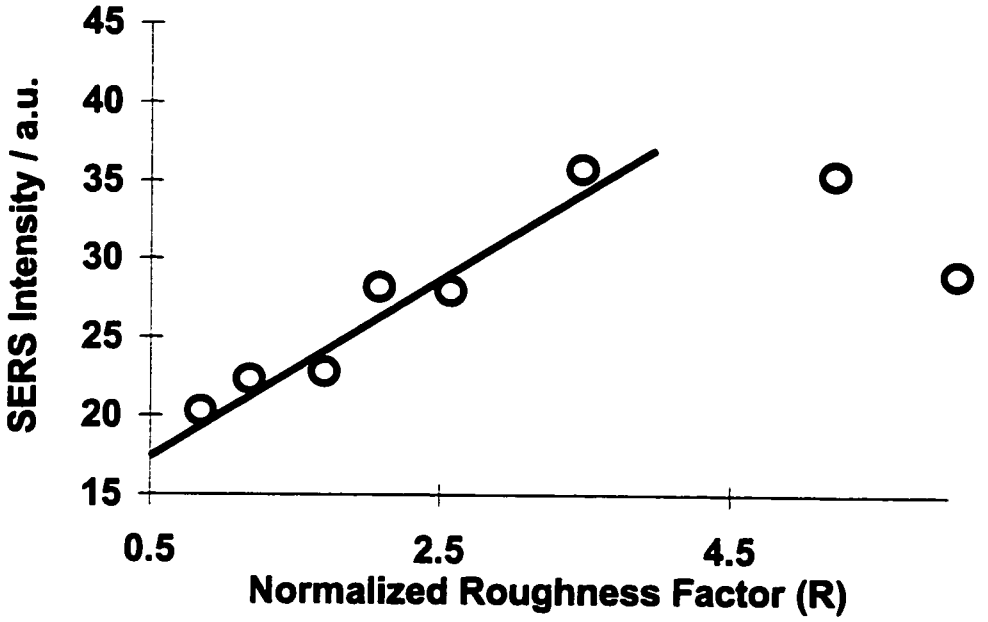

Figure 7.5: Dependence of the ring breathing mode SERS intensity of pz on the normalized roughness factor (R), obtained from the AFM images.

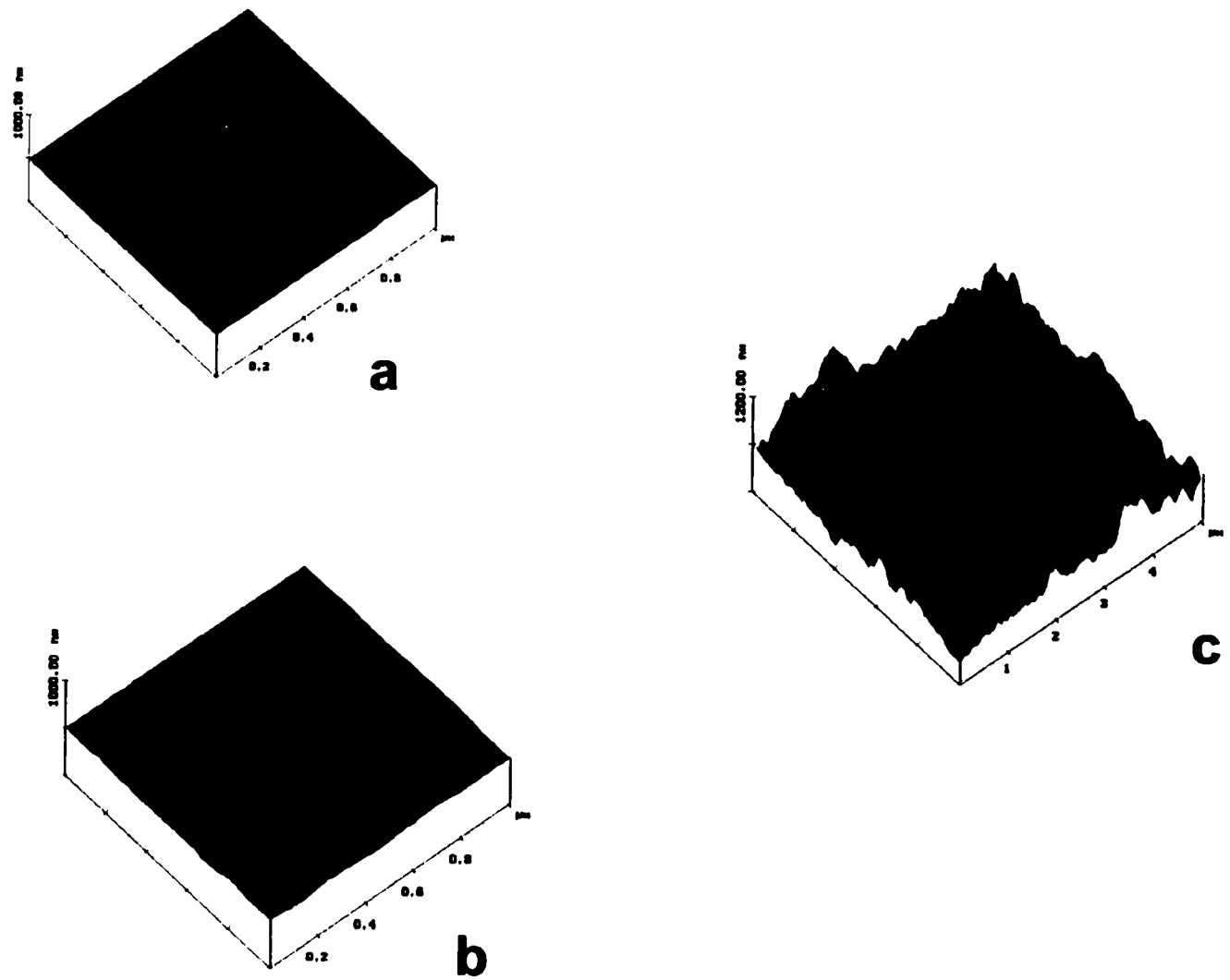

Figure 7.6: AFM images of rough gold electrodes: a) R=0.7 (5 ORCs); b) R=3.1 (20 ORCs); c) R=10.5 (60 ORCs)

The gold electrode with a normalized roughness factor equal to ca. 0.7 (subjected to only 5 ORCs) (Fig. 7.6A) presented roughness features of the order of 40 nm. As the number of ORCs increased, the small bumps seemed to coalesce to create bigger features. Fig. 7.6B shows the AFM image for a gold surface after 20 ORCs (normalized roughness factor of ~ 3). The sizes of the roughness features are now of the order of 100 nm. This surface yields a strong SERS signal. As the number of ORCs further increased, the average size of the roughness features increased. After 60 ORCs (normalized roughness factor of ~ 10), the average size of the roughness was ca. 400 nm, and the conical features were similar in size and shape. This kind of surface is not expected to be a good substrate for SERS. In fact, a very weak SERS spectrum was obtained from this substrate.

Two models are generally accepted to explain the SERS effect: the charge transfer (CT) [5] and the electromagnetic (EM) [6] mechanisms. The CT model attributes the enhancement to the formation of a molecule-metallic adatom complex. A charge transfer band, which has an energy similar to the photon energy of the incident light, between the molecule and the metal would increase the Raman cross-section as in the Resonance Raman effect [5]. The EM mechanism attributes the enhancement to the excitation of the metallic surface plasmons polaritons by the incident and the scattered photons [6]. The response of the rough metallic surface to an external electromagnetic field has been successfully described theoretically, and this EM mechanism can predict quantitatively several of the SERS features [6].

Several pieces of experimental evidence indicate that the contribution from the CT mechanism to the SERS of pz adsorbed on a silver electrode cannot be discarded [49,50,51,52,53]. However, it has been recently proposed, based on the calculation of the bond polarizabilities of adsorbed pz, that the CT is not as important for pz adsorbed on gold electrodes (under 1.06 μm excitation) as it is for pz adsorbed on silver electrodes [54]. The CT mechanism does not predict a dependence of the SERS intensity on the surface morphology; however, the variation of the SERS signal with the surface roughness can be interpreted as due to changes in the density of adatoms and, consequently, a variation in the number of adatom-molecule complexes. Unfortunately, it is very difficult to track the number density of adatoms in very rough surfaces such as the ones presented in Fig. 7.6. Therefore, it is not possible with these data to infer the real contribution of the CT to the SERS signal.

The dependence of SERS intensity on surface morphology is predicted by the electromagnetic enhancement mechanism [6]. The enhancement factor seems to be strongly dependent on the shape of the roughness features. In fact, theorists have calculated the enhancement factor for several metallic particle morphologies [6]. These calculations have been made using various formalisms, and considering both isolated and grouped spherical (or spheroidal) particles [55,56,57,58,59,60,61]. Several of the classical papers in SERS, including the earliest theoretical works, can be found elsewhere [62].

Accurate calculations have been recently performed using the discrete dipole approximation (DDA) method to determined Raman intensities from small metal particles

of arbitrary shape [63]. It also has been shown that the distance between the surface features is an important factor (together with their size and geometry), since contributions from surface plasmon modes localized between the particles is a major factor for the overall effect [64]. A million times enhancement in the Raman signal was calculated for the py ring breathing signal from a "small" (radius <<< wavelength of the incident light) silver sphere [55]. A peaked excitation profile (enhancement factor vs. excitation wavelength plot) was obtained for such a small particle (radius ≈ 5 nm) due to a dipolar response from the metallic sphere. The superposition of multipolar fields broadens the excitation profile as the radius of the metallic particle increases [55]. The contribution of these high order dipoles also decreases the magnitude of the maximum delocalized Raman enhancement factor by several orders of magnitude. The dependence of the enhancement factor on the radius of the spherical particle is not as large for gold as it is for silver [65]. The enhancement factor from a 1010 cm^{-1} vibration (close to the pz ring breathing frequency at ~ 1016 cm^{-1}) of a molecule adsorbed on a spherical gold particle is also dependent on the radius of the metallic particle [65]. Considering an excitation wavelength equal to 650 nm (the same excitation wavelength used in this work), the calculated enhancement factor would be approximately 100 for 5 nm radius gold spheres [65]. This enhancement factor increases to almost 1000 as the radius increases to 50 nm [65]. However, 500 nm gold spheres give an enhancement factor of only 10, approximately [65]. These calculated results agree well with the experimental data presented in Figs. 7.5 and 7.6. Hence, even these simple EM calculations, considering just the delocalized resonances, are enough to explain the qualitative trend of the dependence of the SERS intensity on surface morphology.

The complexity (roughness) of a surface can also be evaluated by a fractal analysis. One type of fractal analysis superimposes a three dimensional array of cubes on a three dimensional image, so that the cubes completely encompass the image. The size of the cubes is varied and the number of cubes intersected by the image is recorded for each cube size. For a given cube size, rougher samples intersect more cells than smooth samples. The fractal dimension (D) is defined as the slope of the line obtained by plotting the log of the cell size versus the log of the number of cells. The fractal dimension increases with the roughness of the sample. For a three dimensional image, the D value varies from a minimum of 2 for a flat surface to a maximum of 3 for an extremely rough surface.

Fractal analysis has been used to compare the SERS intensity to the surface morphology of cold deposited silver [25, 26]. However, there are no studies in the literature relating the SERS effect to fractal dimension obtained from electrochemically roughened surfaces. Figure 7.7 shows the plot of the fractal dimension (D) versus the normalized roughness factor for rough gold electrodes. The curves correspond to different image sizes (0.5 and 1 μm, respectively). No simple direct relationship has been found between SERS intensity and fractal dimension, but, from the analysis of Figs. 7.5 and 7.7, it is possible to observe that strong SERS signals are obtained when the D value is around 2.4 for 1 μm images. These results indicate that the electrode surfaces which yield strong SERS signals possess a strong fractal characteristic. Although fractality exists in SERS active substrates, it is not the only condition necessary for the enhancement to be

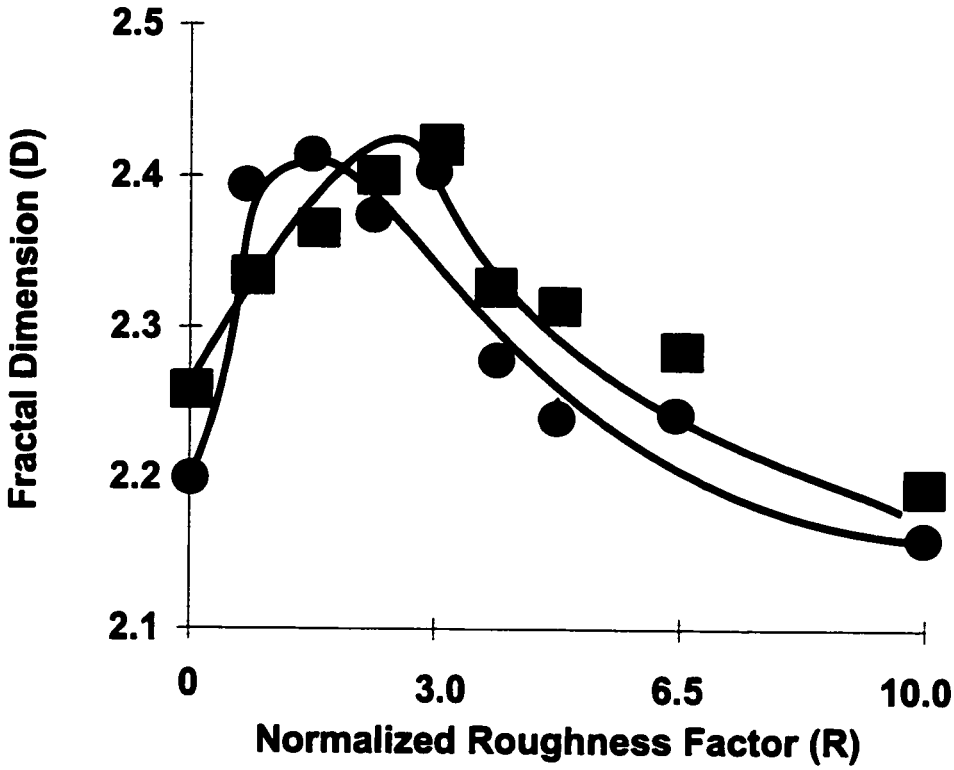

Figure 7.7: Dependence of the fractal dimension on the surface roughness. The SERS intensity is dependent on the surface roughness (Fig. 7.5). Circles: image size equals 0.5 micrometer; Squares: image size equals 1.0 micrometer.

observed. For instance, the fractal analysis cannot account to small scale active sites which may have significant importance on the overall effect.

7.3.2. The dependence of the SERS intensities of pz adsorbed to an "unroughened" polycrystalline gold electrode on surface coverage.

Figure 7.8 shows the relative integrated intensity of the ring breathing SERS band of pz, 1016 cm^{-1}, adsorbed on an "unroughened" gold electrode, as a function of the surface coverage (determined independently by electrochemical methods [37]), for several pz concentrations. A reasonably linear relationship between SERS intensity and surface coverage was obtained for the most dilute pz solution ([pz] = 5.50 x 10^{-5} M). The SERS intensities presented in Fig. 7.8 for other pyrazine concentrations (concentrations of pz equals to 1.23 x 10^{-4} M, 6.11 x 10^{-4} M, and 9.97 x 10^{-4} M) fail to track the surface coverage at surface concentrations higher than ~ 4 x 10^{-10} mol/cm^2 (inside the shadowed area in Fig. 7.8). The same behaviour has been observed for pyridine adsorbed on polycrystalline gold electrodes [36] and other systems such as cyanide adsorbed on silver island films [66]. The decrease of the SERS intensity as the adsorbed molecular dipoles approach each other (high surface coverage) can be explained using electromagnetic arguments [67, 68, 69]. As the surface coverage approaches the monolayer value, each adsorbed molecule is subjected to depolarising fields from its oscillating neighbours [70]. This depolarising effect decreases the magnitude of the local electromagnetic field responsible for the enhancement. Fig. 7.8 also shows that, despite the linearity between SERS intensity and surface coverage observed for all concentrations of pyrazine

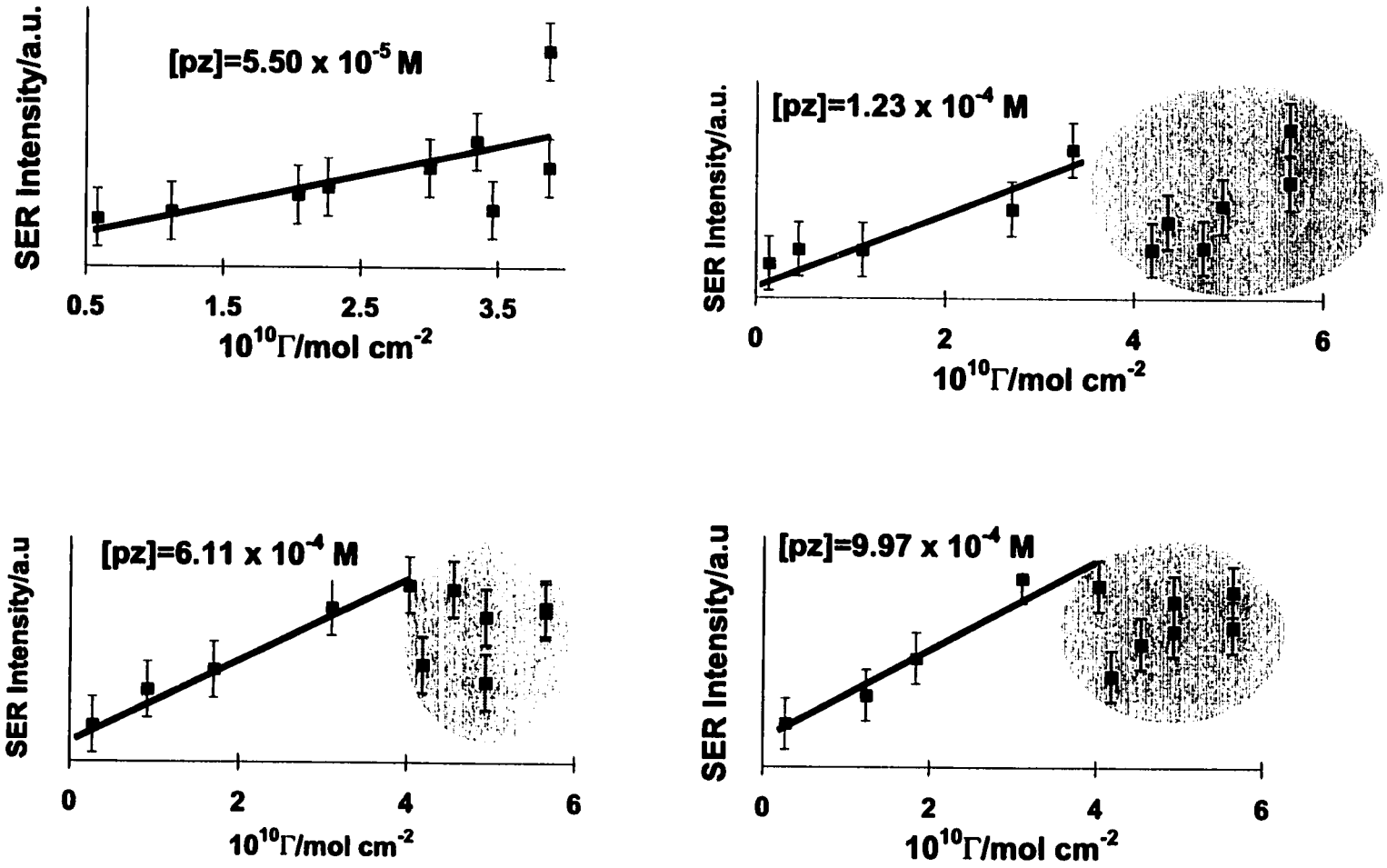

Figure 7.8: Dependence of the SERS intensity of pz adsorbed on an "unroughened" gold electrode on the surface concentration (Γ). The concentration of pz in solution is indicated on each plot. A fairly linear relationship between SERS intensity and surface coverage is observed for low surface concentration values. The shadowed areas indicate the region where the linearity breaks down and the points become scattered.

(up to 2/3 of a monolayer), the slopes of the SERS intensity vs. surface coverage plots increase marginally as the solution is made more concentrated in pz. The linearity between SERS intensity and surface coverage was also observed for pyridine adsorbed on polycrystalline gold [36], indicating that the SERS intensity increases with the increase of the number of molecules on the electrode surface, but the rate of this increase depends on both the pz concentration and the activation procedures.

It is possible to estimate the contribution from the chemical effects to the overall SERS intensities for pyrazine adsorbed on "unroughened" gold electrodes. The intensity of the SERS spectrum of molecules adsorbed on gold electrodes can be written as the product of various contributions:

$$I_{SERS} \propto Y_{(\nu,\nu_R)} X_{(\nu,\nu_R,E)} \theta_{(E)} \Lambda_{(E)} \Omega \qquad (1)$$

Here $Y_{(\nu,\ \nu_R)}$ is the electromagnetic contribution to the overall SERS intensity; it depends only on the energy of the incident (ν) and scattered photon (ν_R) for a given surface morphology. $X_{(\nu,\ \nu_R,\ E)}$ is the chemical contribution to SERS, which includes the charge-transfer mechanism. $\theta_{(E)}$ is the potential dependent surface coverage. $\Lambda_{(E)}$ includes the changes in line intensities due to geometrical rearrangement of the adsorbate. Ω is a constant that contains the instrumentation optical parameters (throughput, sensitivity and laser power).

The results presented in this thesis demonstrate that the molecular orientation of pyrazine does not change with the applied potential. This is supported by electrochemical data [37]. Hence, the term $\Lambda_{(E)}$ is also constant, and only $\theta_{(E)}$ and $X_{(\nu, \nu_R, E)}$ remain potential dependent in equation (1). Independent electrochemical measurements provided us with the amount of molecules adsorbed on the electrode surface for each potential [37]; therefore, $\theta_{(E)}$ is known. The relative enhancement ($\Im$) for each potential can then be evaluated:

$$\Im_{(\nu,\nu_R,E)} \propto \frac{I_{SERS}}{\theta_{(E)}} \propto Y_{(\nu,\nu_R)} X_{(\nu,\nu_R,E)} K \qquad (2)$$

Here K is a constant which contains Λ and Ω. Equation (2) shows that the chemical term (X) is the only one left which is potential dependent. For a SERS system with small or none chemical contribution this term would be irrelevant; therefore, for a electromagnetic-only surface-enhancement we have:

$$\left(\frac{\partial \Im}{\partial E}\right)_{(\nu,\nu_R)} = 0 \qquad (3)$$

The contribution from the chemical mechanism to the overall enhancement can be evaluated by studying the dependence of the enhancement on the applied potential. A

similar treatment has been applied to the SERS study of pyridine adsorbed on silver electrodes [71]. The total chemical enhancement factor was estimated for that system as being about 50.

Figure 7.9 shows the $\Im$ versus potential plot for pyrazine adsorbed on unroughened gold electrodes at several concentrations of pz in solution. All plots present basically the same features. The $\Im$ value decreases from -600 to -200 mV and remains fairly constant as the potential is made more positive. A better evaluation of the chemical contribution can be drawn from Figure 7.10, which presents the derivative of the enhancement over the potential ($\partial\Im/\partial E$) plotted against the potential (E). As shown in equation (3), the derivative should be zero at potentials where only the electromagnetic mechanism is operative. Figure 7.10 A - D show that, for all concentrations of pz in solution, the ($\partial\Im/\partial E$) is around zero in the range between -200 to +500 mV. This is a strong indication that the chemical contribution to the SERS intensity in this potential range is small (certainly less than an order of magnitude). The changes in the ($\partial\Im/\partial E$) observed for potentials more negative than -200 mV (Figs. 7.9 and 7.10) could be attributed to chemical contributions. However, a critical analysis of these results is necessary. Electrochemical methods cannot detect the presence of pz on the electrode at potentials more negative than -700 mV [37]. At potentials more negative than -300 mV, the surface concentration is very small, but the SERS signal can be clearly observed. Therefore, the changes of ($\partial\Im/\partial E$) for potentials more negative than -200 mV can be an artifact, created because we are using very small numbers as divisor, as the surface concentration approaches zero. Also, the maximum in the CT contributions for silver

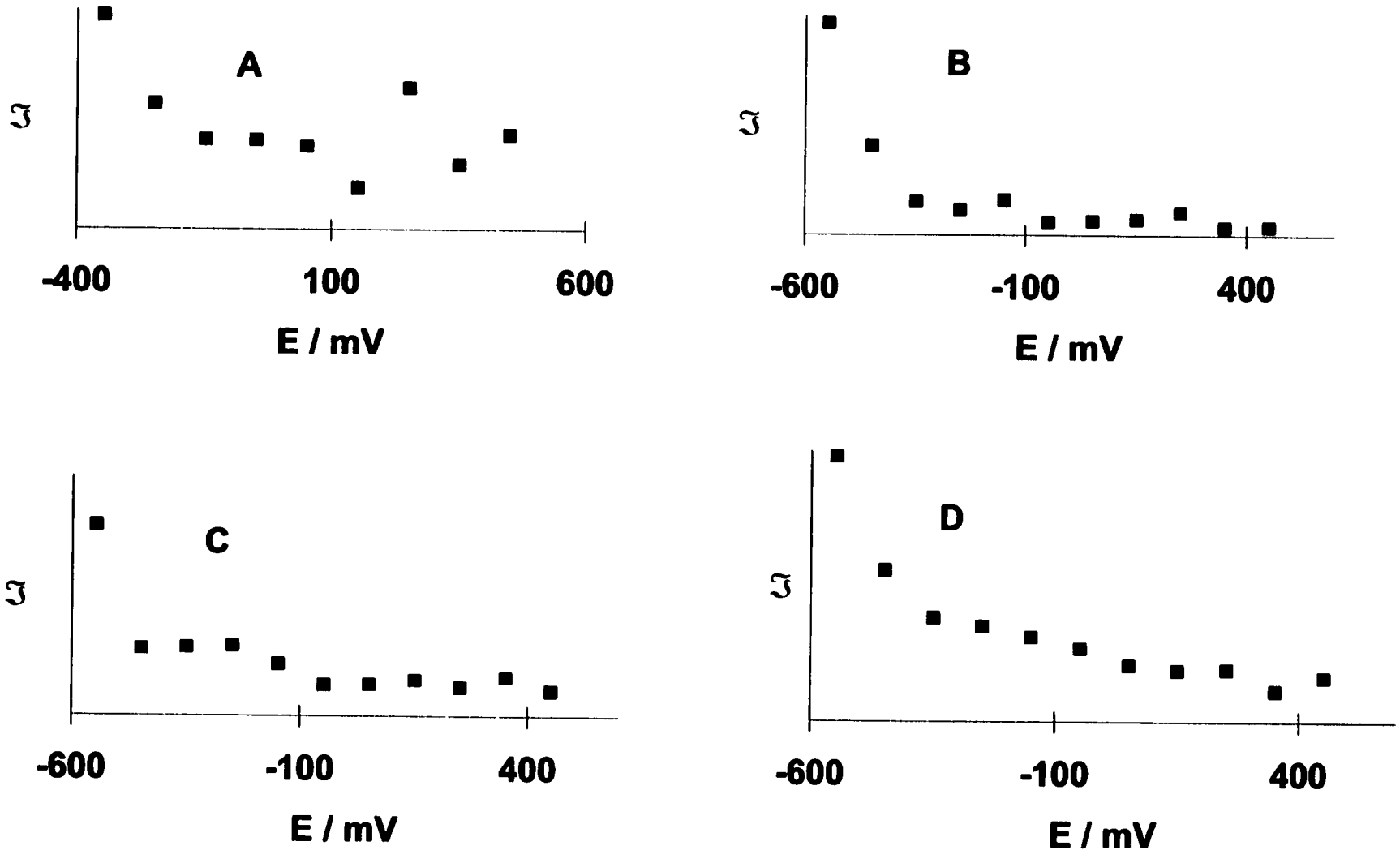

Figure 7.9: Relative enhancement versus potential for several pyrazine concentrations. A) 0.05 mM; B) 0.1 mM; C) 0.6 mM; D) 1.0 mM.

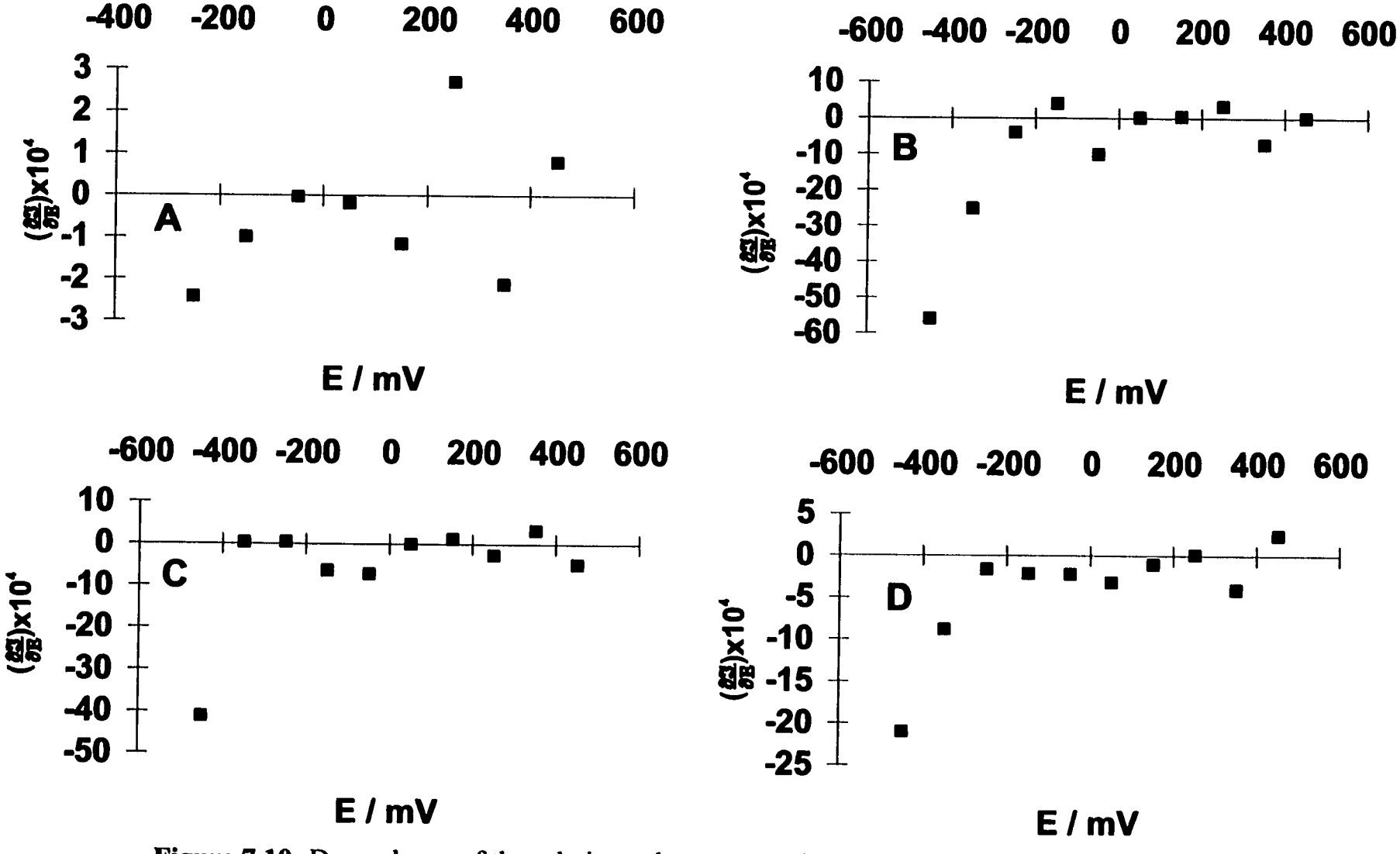

Figure 7.10: Dependence of the relative enhancement change with the potential versus the applied potential. A) [pz]= 0.05 mM; B) [pz]=0.1 mM; C) [pz]=0.6 mM; D) [pz]=1.0 mM.

electrodes is observed around the pzc for silver. We would expect a similar result for gold. The pzc for gold in perchlorate is around -50 mV, but no significant (order of magnitude) changes were observed in ($\partial\Im/\partial E$) for this potential (Figs. 7.9 and 7.10).

Figures 7.11 (A-C) show the dependence of both the SERS intensity of pz adsorbed on an "unroughened" polycrystalline gold electrode and the surface coverage (from ref. 37) on the concentration of pz in solution, for four selected potentials. The surface concentration (Γ) of pz adsorbed on gold becomes independent of the amount of pz in solution. On the other hand, the SERS intensities increase with the solution concentration of pz for all potentials (Figs. 7.11, A-D). The "cleaning" ORCs, used to prepare the "unroughened" gold electrode, are not expected to cause any drastic change in the surface morphology. In fact, only a few tenths of nanometers of the gold surface are removed during the positive sweep [72]. Therefore, the SERS intensity increases with the solution concentration (at these relatively high concentrations) when there is no change in the surface concentration for these "unroughened" surfaces.

For several systems, it has been observed that the SERS intensities obtained after activation ORCs performed in the presence of the organic adsorbate (or halides) is higher than when the electrode is activated in the absence of adsorbates [73]. However, the activation in the presence of the adsorbate may lead to erroneous results [73,74].

It has been proposed that strong adsorbates can stabilize atomic scale SERS active

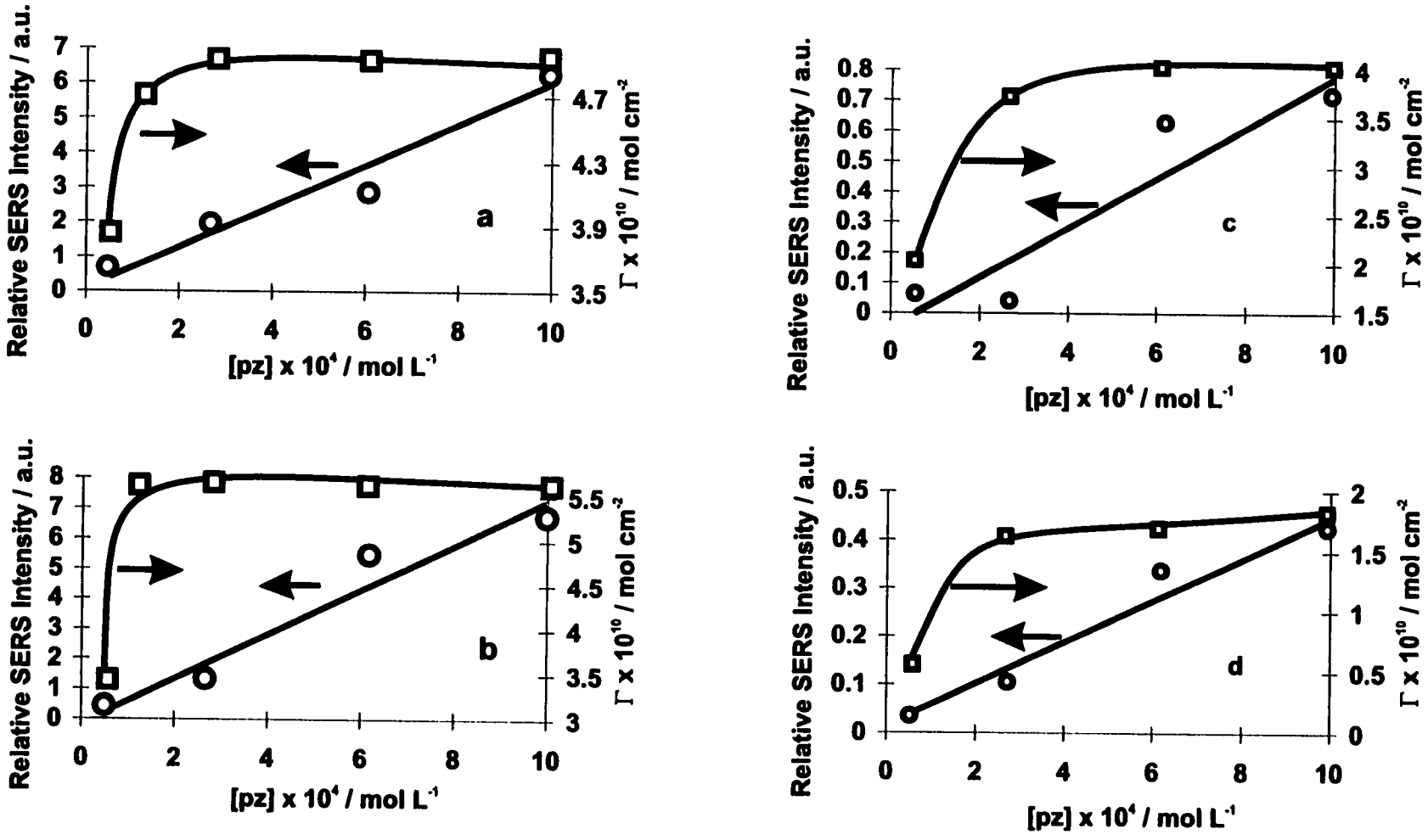

Figure 7.11: Dependence of both the SERS intensity (from an "unroughened" gold electrode) and the surface coverage on the solution concentration of pyrazine.
a) + 350 mV; b) +150 mV; c) -150 mV; d) -450 mV.

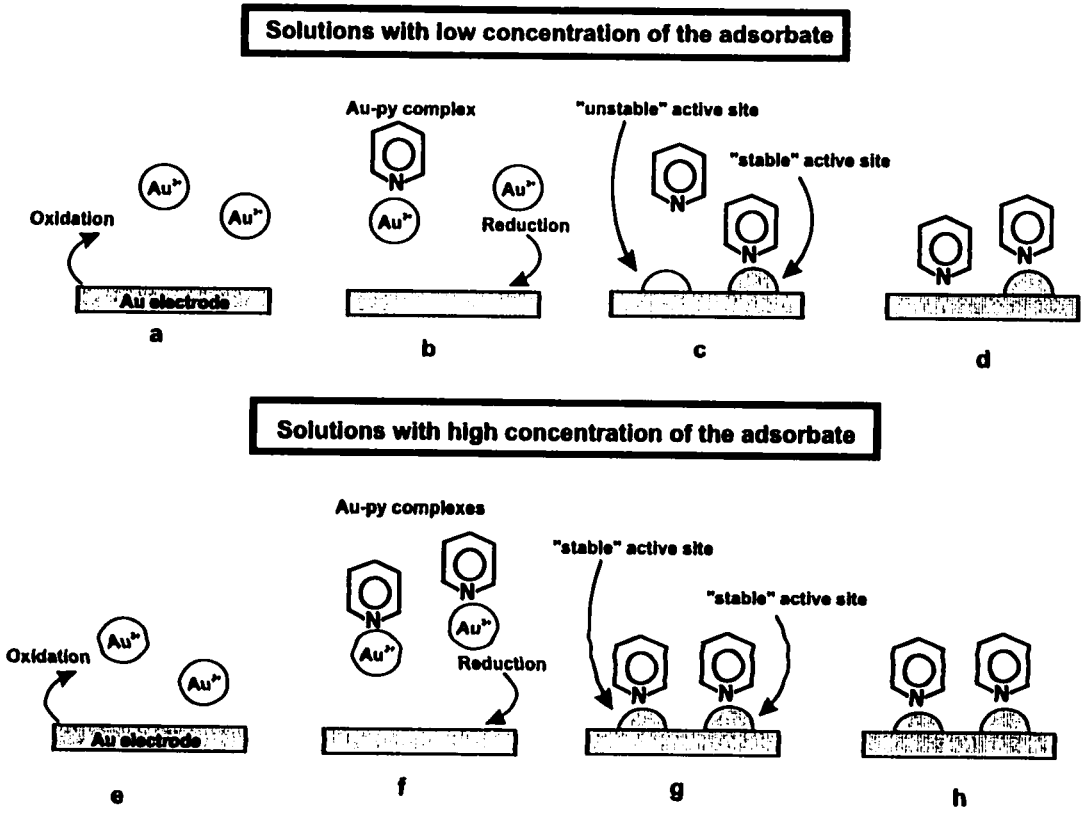

Figure 7.12: The effect of the solution concentration of the adsorbate (pyridine (py) is used as an example) on the SERS intensity. For solutions with low concentration of py: a) Au(III) ions are formed during the oxidation process; b) Au(III) forms a complex with py. However, the solution concentration of py is small and some gold remains "free"; c) Adatoms are formed on the reduction process. The small scale site formed from the complex is "stable" and has no mobility. The adatom formed from the "free" cation is "unstable" and can be incorporated into the lattice; d) Consequently, few molecules are adsorbed on the SERS acitve sites. For solutions with high concentration of py: e) The Au(III) ions are formed; f) Higher amounts of Au-py complexes are formed; g) The number of "stable" active sites formed during the reduction process is also higher; h) The same surface concentration as in (d) should yield a higher SERS signal, because more molecules are now adsorbed on "stable" active sites.

sites [75]. Based on this assumption, a possible explanation for the increase of the SERS intensity with the solution concentration for this "unroughened" substrate is given in Figure 7.12. During the cleaning ORCs positive sweep, in the presence of the organic compound, a complex may be formed between the oxidation products of the metal and the organic substrate (Figs. 7.12a and 7.12b). A higher number of these complexes will be formed in a solution more concentrated in the organic substrate (Figs. 7.12e and 7.12f). The complex (metal cation - organic molecule) may be reduced during the cathodic part of the sweep, together with the "free" cation (Fig. 7.12c and 7.12g). The metal - organic molecule system, formed on the surface during the electrochemical reduction process, decreases the mobility of the adatoms, creating "stable" small scale active sites. Thus the incorporation of the metallic adatoms into the metallic lattice is hindered [75]. The metallic deposit, which is not further stabilized by the organic molecule, is "unstable" and will be incorporated into the lattice. When the equilibrium between the amount of adsorbate in solution and on the metal is established, the same amount of adsorbate is present on the surface for both concentrations, because, as was demonstrated by Fig. 7.11, the surface concentration is independent of the solution concentration at all potentials, for the studied solutions. However, the most concentrated solution may have more organic molecules adsorbed on a group of stable active sites (Fig. 7.12h) than the diluted solution (Fig. 7.12d), and, therefore, the SERS spectrum obtained for molecules adsorbed from more concentrated solutions is expected to be more intense. This model implies a distinction between the group of small scale sites (i.e., SERS-active sites) and the total surface area available for electrochemical pz adsorption.

Attempts to obtain the SERS spectra by electrochemically cleaning the electrode in aqueous perchlorate solution and later adding pz (*ex situ* activation procedure) were unsuccessful. This fact indicates that the active sites formed by the mechanism presented in Fig. 7.12 are essential to produce the Raman scattering enhancement from an "unroughened" gold surface. Moreover, Figs. 7.9 and 7.10 indicates that the *chemical* mechanism does not play an important role in the SERS of pz adsorbed on gold electrodes. Therefore, we do not expect charge-transfer to occur on these "complexes" (active site + adsorbed pz). A group of the nanometric-sized bumps, formed during the preparation of these "unroughened" electrodes, may be enough to couple the incident radiation with the surface plasmons (The "unroughened" electrodes produce the electrochemical response (CVs) expected for "smooth" electrodes; therefore, the roughness features must be very small).

Finally, the results demonstrate that, for the "unroughened" gold surfaces, the SERS intensities are indeed proportional to both the surface coverage (up to 2/3 of a monolayer) (Figs. 7.8) and the solution concentration of the organic adsorbate (Figs. 7.11). These results suggest that SERS can be applied as an analytical tool to determine the concentration of organic compounds in dilute solution [76]; however, one must be aware that different results may be obtained for different preparations of the substrate [77].

7.3.3. The dependence of the SERS intensities of pz adsorbed on a "smooth" polycrystalline gold electrode on surface concentration

A poor relationship between SERS intensity and surface coverage was found in the work of Stolberg et al. [36] for py adsorbed on a rough polycrystalline gold surface (prepared by activating the gold in KCl solution - see experimental section). The potential profiles were dependent on the number of ORCs, and, consequently, on the surface morphology. We found, qualitatively, the same problems for the adsorption of pz on rough gold electrodes. Possibly, the lack of relationship occurs because we are comparing data obtained from a rough surface (SERS intensities) with data obtained from a smooth surface (surface coverage). In order to minimize this problem, we developed a procedure to calculate the SERS intensity of a "smooth" surface from the data obtained for a rough surface. The procedure consists of the following steps:

1) The SERS spectrum was obtained for different numbers of ORCs;
2) The area under the pyrazine ring-breathing mode (~ 1016 cm^{-1}) was calculated for different applied potentials and normalized using the 934 cm^{-1} band from the aqueous perchlorate as an internal standard;
3) As we observed in Fig. 7.5, there is a linear relationship between the SERS intensity and the roughness factor (or cathodic charge). Therefore, plots were made of the SERS intensity versus the cathodic charge (the cathodic charge is proportional to both the number of ORCs and the normalized roughness factor, (Fig. 7.2 and Fig. 7.5)) for different potentials (Figure 7.13);

4) The SERS intensity vs. roughness plots for each potential (Fig. 7.13) were extrapolated to zero roughness and thus the SERS intensity from a gold electrode not subjected to any ORC was graphically evaluated from the intercept.

Figure 7.14 shows the extrapolated SERS intensity plotted against the electrode potential. The surface coverage of pyrazine adsorbed on a gold electrode, obtained from ref. 37, is also shown in Fig. 7.14. The striking resemblance between the two curves presented in Fig. 7.14 is confirmed in Figure 7.15, where the extrapolated SERS intensity is plotted against the surface coverage for each potential. The extrapolated SERS intensity tracks the surface coverage over the whole range of potentials.

One may be surprised by the observation that the extrapolated SERS intensities (for a "smooth" surface) are only one order of magnitude lower than the optimal SERS signal obtained from a rough surface (Fig. 7.13). This result raises questions about the physical significance of our procedure and requires comments.

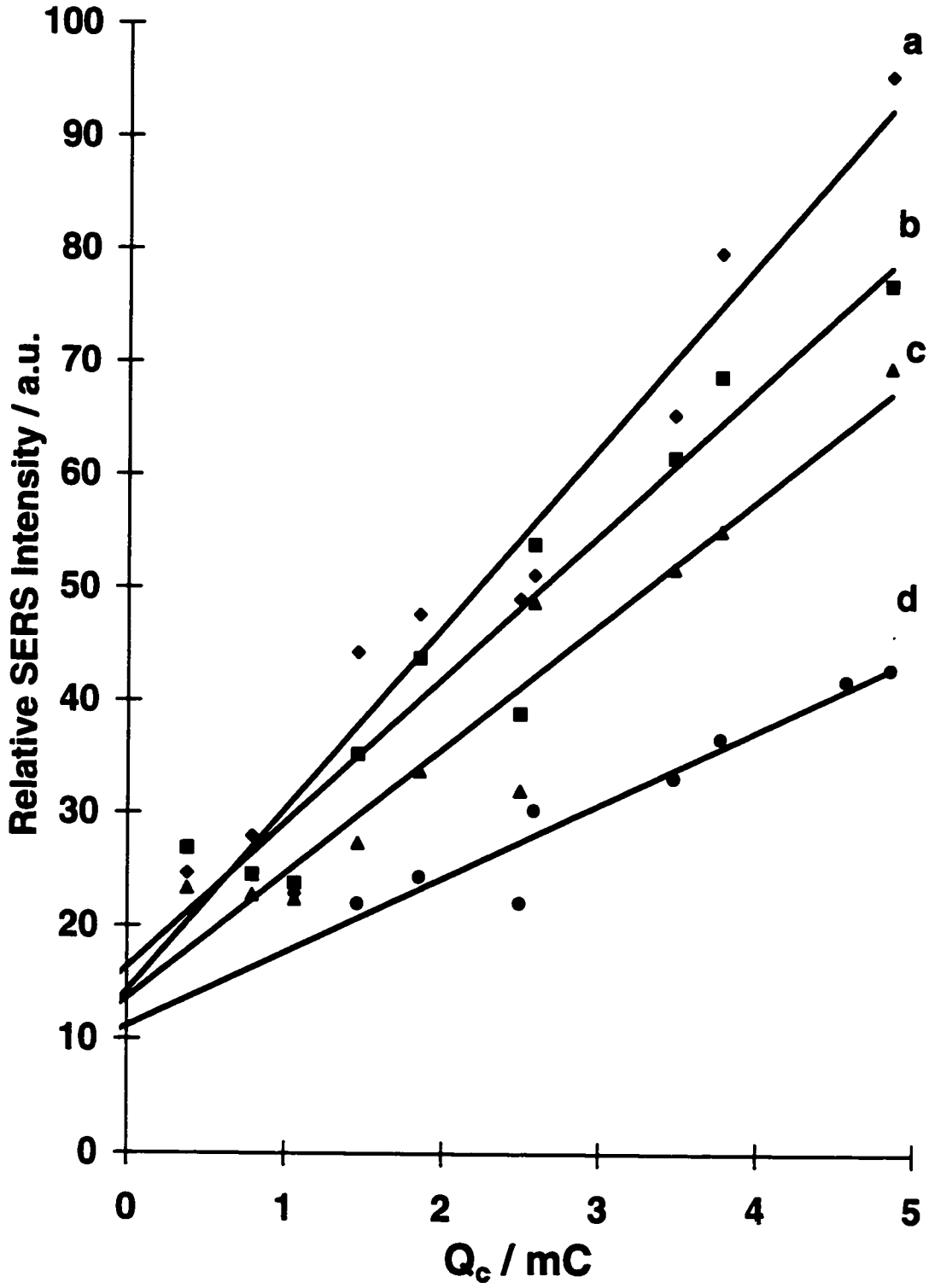

Figure 7.13: Dependence of the SERS intensity of pz on the cathodic charge.
a) +450 mV; b) +150 mV; c) -150 mV; d) -550 mV.

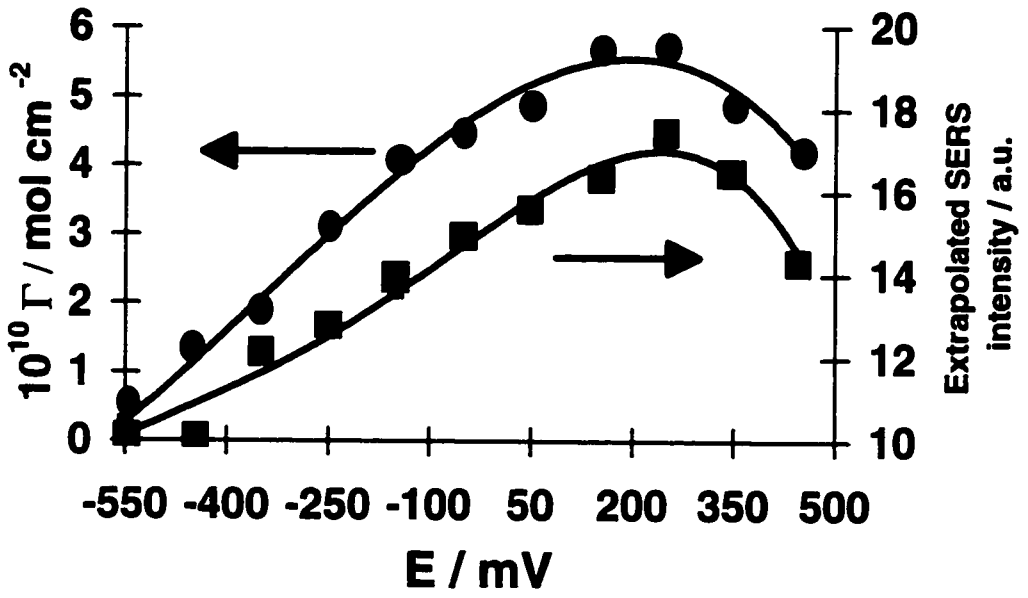

Figure 7.14: Surface concentration of pz vs. potential, and extrapolated SERS intensity of the ring breathing mode of pz (calculated from Fig. 7.13) vs. potential.

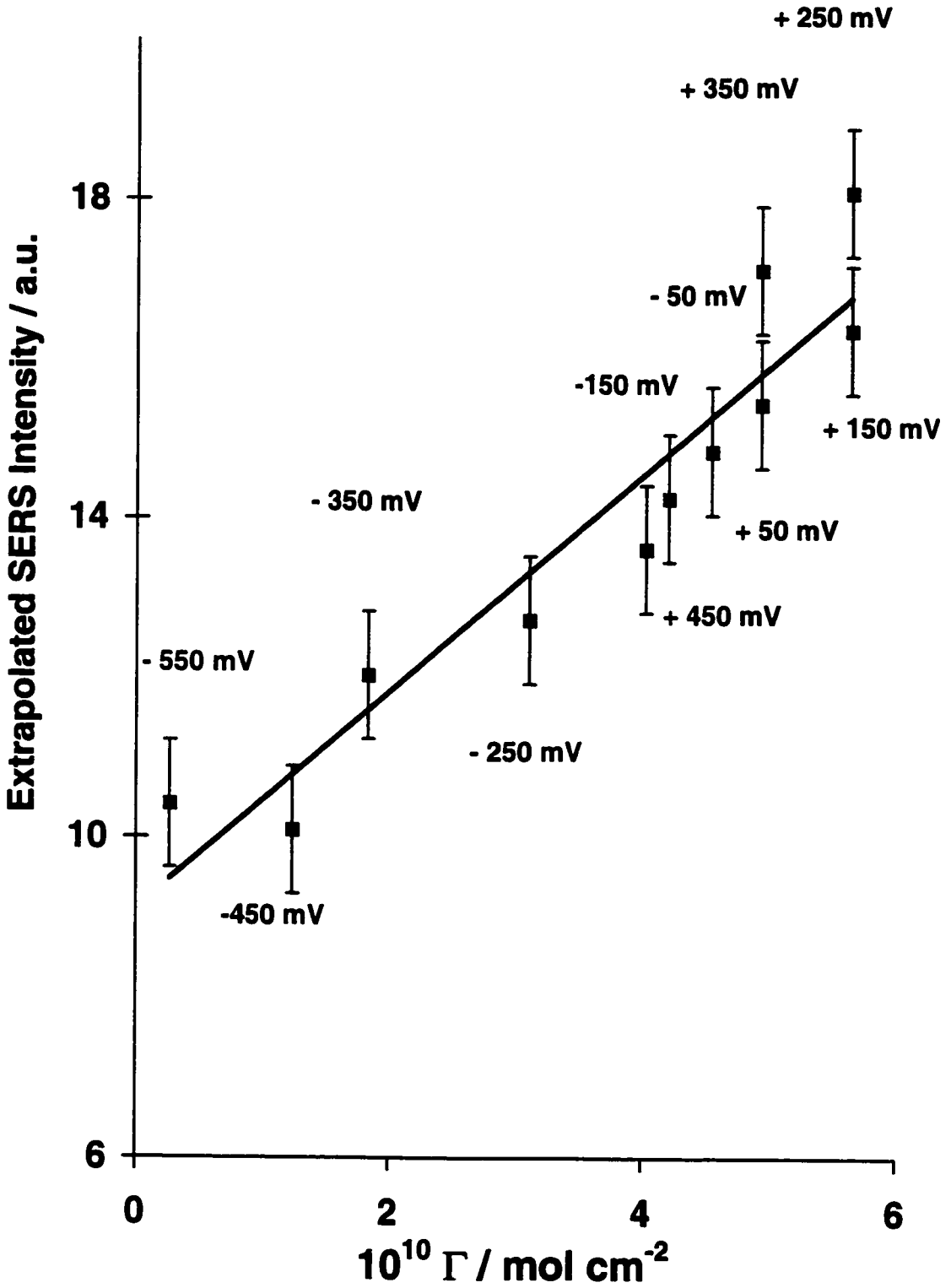

Figure 7.15: Dependence of the extrapolated SERS intensity of the ring breathing mode of pz on the surface coverage. The applied potential is indicated in the graph.

It is not possible to excite the surface plasmons directly from a smooth surface due to a momentum mismatch between the incident photon and the surface resonances [2]; therefore, a direct verification of the magnitude of these extrapolated SERS intensities can not be obtained. However, it has been demonstrated, from the observation of SERS spectra using silver-deposited films over polymer nanospheres [24], for instance, that the electromagnetic enhancement factor can be partitioned into different contributions from localized and delocalized surface plasmon excitations. Considering an overall enhancement of 10^7 from these silver-coated particles, it was proposed that a factor of ~ 10^2 was dependent on the size of the nanospheres [24]. The roles of these localized and delocalized surface plasmon contributions have been further confirmed recently [78]. The SERS spectra from single silver particles (~ 1 μm diameter) were observed [78]. Additional enhancement was obtained from a cluster of such particles, indicating that the interactions between the surface features are important factors for the overall enhancement. The dependence of the SERS intensities on the surface roughness (presented in Fig. 7.13) indicates that even a mild rough gold surface presents a large enhancement factor (only about 1 order of magnitude smaller than the "optimal" value). This enhancement may contain large contributions due to random substructure roughness which supports localized surface plasmon resonances. As the sizes of the surface roughness increase (and the SERS intensities also increase), the contribution from the delocalized surface plamons polaritons becomes more significant. This additional enhancement, due to delocalized resonances, is about 10^2 for silver [24]; hence it is not unreasonable to observe that its contribution in a rough gold electrode is of about 1 order of magnitude.

7.4. Conclusions

We have presented the dependence of the SERS intensities of pz adsorbed on a polycrystalline gold electrode on both the surface coverage and on the surface morphology.

The SERS intensities from rough gold electrodes increase with the surface roughness, reaching a maximum at ~ 25 ORCs. AFM pictures showed that the size of the surface roughness features increases with the number of ORCs, and surface features of ca. 100 nm yielded a strong SERS signal. A weak SERS response was observed from surfaces with roughness features of ~ 400 nm. These results are consistent with the expected enhancement factor calculated for gold spheres with different sizes. Strong SERS signals are observed from electrode surfaces with significant fractal characteristics.

The SERS technique proved to be useful for the determination of the amount of pz adsorbed on a low coverage surface (surface concentrations smaller than $4x10^{-10}$ mol cm^{-2}) of "unroughened" polycrystalline gold electrodes. As the surface concentration approaches one monolayer, the SERS signal decreases, due to the depolarising effects on the local electromagnetic field from neighbouring dipoles. The cleaning procedure (ORCs in the presence of the organic molecule), used in the preparation of the "unroughened" gold electrode, may increase the contribution from small-scale active sites to the overall enhancement. The amount of these active sites is dependent on the solution concentration

of the organic adsorbate. This effect can be useful in the determination of the amount of analyte in solution using SERS. Very small contributions from the chemical mechanism to the overall enhancement were observed in the potential range between -200 to + 600 mV. The chemical contribution in potentials more negative than -300 mV is unclear.

The dependence of the potential profile of the SERS intensities on the surface roughness has also been investigated. The extrapolated SERS intensity (for no ORCs), is directly proportional to the surface coverage for a wide range of potentials.

7.5. References

[1] A.G. Brolo, D.E. Irish and B. D. Smith, *J. Mol. Struct.*, **1997**, 405, 29.

[2] B. Pettinger, in *Adsorption of Molecules at Metals Electrodes*, J. Lipkowski and P.N. Ross, eds., VCH, New york, **1992**, Ch. 6, p. 285.

[3] D. Guzonas and D.E. Irish, *Langmuir*, **1990**, 6, 1102.

[4] R. L. Birke, T. Lu and J. R. Lombardi, in *Techniques for Characterization of Electrodes and Electrochemical Processes*, R. Varma and J. R. Selman, eds., Wiley, New York, **1991**, Ch. 5, p. 211.

[5] A. Otto, I. Mrozek, H. Grabhorn and W. Akemann, *J. Phys. Condens. Matter*, **1992**, 4, 1143.

[6] M. Moskovits, *Rev. Mod. Phys.*, **1985**, 57, 783.

[7] D. D. Tuschel, J. E. Pemberton and J. E. Cook, *Langmuir*, **1986**, 2, 380.

[8] N. A. Cross and J. E. Pemberton, *J. Electroanal. Chem.*, **1987**, 217, 93.

[9] S. Kruszewski, *Adsorpt. Sci. Technol.*, **1994**, 1, 217.

[10] Z. Q. Tian, W.H. Li, B. Ren, B. W. Mao, J.G. Chen, J. Q. Mu, X. D. Zhuo and D. Wang, *J. Electroanal. Chem.*, **1996**, 401, 247.

[11] N. Felidj, A. Aubard and G. Levi, *J. Chem. Phys.*, **1996**, 104, 9735.

[12] X. M. Yang, K. Ajito, D. A. Tryk, K. Hashimoto and A. Fujishima, *J. Phys. Chem.*, **1996**, 100, 7293.

[13] M. A. Bryant and J. E. Pemberton, *Langmuir*, **1990**, 6, 751.

[14] P. Dawson, J. W. Haas III, K. B. Alexander, J. Thompson and T. L. Ferrell, *Surf. Sci. Letters*, **1991**, 250, L383.

[15] S. E. Roak and K. L. Rowlen, *Chem. Phys. Letters*, **1993**, 212, 50.

[16] W. B. Lacy, J. M. Williams, L. A. Wenzier, T. P. Beebe and J. M. Harris, *Anal. Chem.*, **1996**, 68, 1003.

[17] J. V. Zoval, P. R. Biernacki and R. M. Penner, *Anal. Chem.*, **1996**, 68, 1585.

[18] D. J. Semin, A. Lo, S. E. Roak, R. T. Skodje and K. L. Rowlen, *J. Chem. Phys.*, **1996**, 105, 5542.

[19] S. E. Roark, D. J. Semin and K. L. Rowlen, *Anal. Chem.*, **1996**, 68, 473.

[20] P. A. Schueler, J. T. Ives, F. DeLaCroix, W. B. Lacy, P. A. Becker, J. Li, K. D. Caldwell, B. Drake and J. M. Harris, *Anal. Chem.*, **1993**, 65, 3177.

[21] S. E. Roark and K. L. Rowlen, *Anal. Chem.*, **1994**, 66, 261.

[22] D. J. Semin and K. L. Rowlen, *Anal. Chem.*, **1994**, 66, 4324.

[23] M. C. Chen, S. D. Tsai, M. R. Chen, S. Y. Ou, W-H., Li and K. C. Lee, *Phys. Rev. B*, **1995**, 51, 4507.

[24] R. P. Van Duyne, J. C. Hulteen and D. A. Treichel, *J. Chem. Phys.*, **1993**, 99, 2101.

[25] C. Douketis, T. L. Hasslett, Z. Wang, M. Moskovits and S. Ianotta, *Progres. Surf. Sci.*, **1995**, 50, 187.

[26] C. Douketis, Z. Wang, T. L. Hasslett and M. Moskovits, *Phys. Rev. B*, **1995**, 51, 11022.

[27] L. Maya. C. E. Vallet and Y. H. Lee, *J. Vac. Sci. Technol. A*, **1997**, 15, 238.

[28] W. B. Caldwell, K. Chen, B. R. Herr, C. A. Mirkin, J. C. Hulteen and R. P. Van Duyne, *Langmuir*, **1994**, 10, 4109.

[29] R. M. Bright, D. G. Walter, M. D. Musik, M. A. Jackson, K. J. Allison and M. J. Natan, *Langmuir*, **1996**, 12, 810.

[30] R. G. Freeman, M. B. Hommer, K. C. Grabar, M. A. Jackson and M. J. Natan, *J. Phys. Chem.*, **1996**, 100, 718.

[31] B. E. Baker, N. J. Kline, P. J. Treado and M. J. Natan, *J. Am. Chem. Soc.*, **1996**, 118, 8721.

[32] M. J. Weaver, J. T. Hupp, F. Barz, J.G. Gordon II and M. R. Philpott, *J. Electroanal. Chem.*, **1984**, 160, 321.

[33] H. Wetzel, H. Gerischer and B. Pettinger, *Chem. Phys. Lett.*, **1983**, 78, 5324.

[34] M. L. Foresti, A. M. Funtikov, R. Guidelli and M. Muniz-Miranda, *J. Electroanal. Chem.*, **1994**, 367, 223.

[35] J. Lipkowski and L. Stolberg, in *Adsorption of Molecules at Metal Electrodes*, J. Lipkowski and P.N. Ross, eds., VCH, New York, **1992**, Ch. 4, p. 171.

[36] L. Stolberg, J. Lipkowski and D. E. Irish, *J. Electroanal. Chem.*, **1991**, 300, 563.

[37] A. Iannelli, J. Richer and J. Lipkowski, *Langmuir*, **1989**, 5, 466.

[38] A. G. Brolo, D. E. Irish, G. Szymanski and J. Lipkowski, *Langmuir*, **1998**, 14, 517.

[39] J. Clavilier, *J. Electroanal. Chem.*, **1980**, 107, 211.

[40] D. Dickertmann, J. W. Schultze and F. D. Koppitz, *Electrochim. Acta*, **1976**, 21, 967.

[41] P. Gao, D. Gosztola, L.-W. H. Leung and M. J. Weaver, *J. Electroanal. Chem.*, **1987**, 233, 211.

[42] C.C. Busby and J. A. Creighton, *J. Electroanal. Chem.*, **1982**, 140, 379.

[43] H. Baltruschat, N. Staud and J. Heitbaum, *J. Electroanal. Chem.*, **1988**, 239, 361.

[44] G. M. Schimid and M. E. Curley-Fiorino, in *Encyclopedia of Electrochemistry of the Elements*, A. J. Bard, ed., Dekker, New York, **1975**, Vol IV, Ch. 3, p. 87.

[45] S. R. Cohen, *Heterog. Chem. Rev.*, **1994**, 1, 135.

[46] H. Rohrer, *Surf. Sci.*, **1994**, 299/300, 956.

[47] R. J. Hamers, *J. Phys. Chem.*, **1996**, 100, 13103.

[48] A. G. Brolo and D. E. Irish, *Z.Naturforsh.* Teil A, **1995**, 50, 274.

[49] A. G. Brolo and D. E. Irish, *J. Electroanal. Chem.*, **1996**, 414, 183.

[50] A. G. Brolo and D. E. Irish, in *Solid-Liquid Electrochemical Interfaces*, G. Jerkiewicz, M. P. Soriaga, K. Uosaki and A. Wieckowski, eds., *ACS Symposium Series N^0 656*, ACS, Washington DC, **1997**, *Ch. 22*, p. 310.

[51] J. F. Arenas, M. S. Woolley, J. C. Otero and J. I. Marcos, *J. Phys. Chem.*, **1996**, 100, 3199.

[52] Y. Huang and G. Wu, *Spectrochim. Acta*, **1990**, 46A, 377.

[53] J. Thietke, J. Billmann and A. Otto, in *Dynamics on Surfaces - Proceedings of the XVII Jerusalem Symposium on Quantum Chemistry and Biochemistry*, B. Pullman, J. Jortner, A. Nitzan and B. Gerber, eds., Reidel, Jerusalem, **1984**, Vol. 17, p. 345.

[54] F. Zhong and G. Wu, *J. Mol. Struct.*, **1994**, 324, 234.

[55] M. Kerker, D.-S. Wang and H. Chew, *Appl. Opt.*, **1980**, 19, 4159.

[56] T. Takemori, M. Inoue and K. Ohtaka, *J. Phys. Soc. Jpn.*, **1987**, 56, 1587.

[57] E. J. Zeman and G. Schatz, *J. Phys. Chem.*, **1987**, 91, 634.

[58] P. K. Aravind, A. Nitzan and H. Metiu, *Surf. Sci.*, **1981**, 110, 189.

[59] M. Xu and M. J. Dignam, *J. Chem. Phys.*, **1993**, 99, 2307.

[60] P. W. Barber, R. K. Chang and H. Massoudi, *Phys. Rev. B*, **1983**, 27, 7251.

[61] D.-S. Wang and M. Kerker, *Phys. Rev. B*, **1981**, 24, 1771.

[62] *Selected Papers on Surface-Enhanced Raman Scattering*, M. Kerker, ed., SPIE Milestone Series, Vol. MS10, **1990**.

[63] W-H. Yang, G. C. Schatz and R. P. Van Duyne, *J. Chem. Phys.*, **1995**, 103, 869.

[64] F. J. Garcia-Vidal and J. B. Pendry, *Phys. Rev. Lett.*, **1996**, 77, 1163.

[65] M. Kerker, *J. Opt. Soc. Am.B*, **1985**, 2, 1327.

[66] C. A. Murray and S. Bodoff, *Phys. Rev. B*, **1985**, 32, 671.

[67] H. Chew, D.-S. Wang and M. Kerker, *Phys. Rev. B*, **1983**, 28, 4169.

[68] H. A. Arunkumar and E. B. Bradley, *J. Chem. Phys.*, **1983**, 78, 2882.

[69] M. Xu and M. Dignam, *J. Chem. Phys.*, **1994**, 100, 197.

[70] C. A. Murray and S. Bodoff, *Phys. Rev. Lett.*, **1984**, 52, 2273.

[71] A. Kudelski, J. Bukowska and J. Jackowska, *J. Raman Spec.*, **1994**, 25, 153.

[72] D. Dickertmann, J. W. Schultze and K. W. Vetter, *J. Electroanal. Chem.*, **1974**, 55, 429.

[73] K. D. Beer, W. Tanner and R. L. Garrell, *J. Electroanal. Chem.*, **1989**, 258, 313.

[74] A.G. Brolo and D. E. Irish, *J. Chem. Soc. Faraday Trans.*, **1997**, 93, 419.

[75] R. L. Sobocinski and J. E. Pemberton, *Langmuir*, **1988**, 4, 836.

[76] S. Om-Apinyan, T. Rajmankina, C. De La Cruz, U. A. Jayasooriya, *Spectrochim. Acta A*, **1997**, 53, 877.

[77] G. Xue, Y. Lu and J. Gao, *Appl. Surf. Sci.*, **1994**, 78, 11.

[78] T. Xiao, Q. Ye and L. Sun, *J. Phys. Chem.*, **1997**, 101, 632.

Chapter 8

Adsorption of Pyridine and Pyrazine on a Au(210) Single-Crystal Electrode

8. Adsorption of Pyrazine and Pyridine on a Au(210) Single-Crystal Electrode.

8.1. Introduction

The identities and orientations of molecules adsorbed onto electrodes can be obtained by the "in situ" observation of their surface-enhanced Raman scattering (SERS) [1]. However, the necessity of creating a rough, and not well characterized, surface to activate SERS is a major impediment when seeking to correlate SERS intensity with surface coverage obtained from "unroughened" electrode surfaces [2].

Unenhanced Raman spectra from molecules adsorbed on single-crystal silver in a UHV situation have been reported, but the signal-to-noise ratio was low [3]. Relatively intense electrochemical SERS spectra from pyridine adsorbed on Ag(111) and Ag(100) have been reported [4, 5] showing, for each orientation, distinct spectral features as long as the oxidation-reduction cycles (ORCs) used to activated the electrodes were sufficiently weak. We believe, however, that these surfaces have changed even during these mild ORCs, performed in the presence of both halide and the organic molecule. Other techniques to obtain SERS spectra from molecules adsorbed on single-crystals have been used [6, 7]. For instance, the Raman signal can be improved either by under-potential deposition (UPD) of a monolayer of a SERS substrate onto the single-crystal face [6], or by the direct excitation of the surface plasmons from a flat surface, obtained using a hemispherical prism [7].

Recently, the signal-to-noise limitation is being overcome. Raman spectra from molecules adsorbed on "unroughened" surfaces can now be observed due to the advent of a new generation of high sensitivity Raman spectrometers equipped with CCD detectors. Consequently, both the enhanced and unenhanced Raman spectra from molecules adsorbed on "smooth" surfaces of polycrystalline [8] and single crystal electrodes [9] have been reported. Using these new systems, it is even possible to obtain Raman spectra from molecules adsorbed on unusual SERS substrates, such as platinum and nickel [10]. Thus the application of electrochemical Raman spectroscopy can now be extended to the "in-situ" investigation of a wide range of well structured interfaces. In fact, surface Raman spectroscopy is a common tool for the study of self-assembled monolayer (SAM) systems [11,12]. Although the SERS intensities may not accurately reflect the amount of adsorbed molecules [13], one cannot deny the importance of electrochemical SERS in the qualitative analysis of the solid-liquid interface (characterization of the structure, orientation and reactions of the adsorbed molecules). The comparison of the SERS intensities of pyridine [14] and pyrazine [15] adsorbed on an "unroughened" gold electrode to the electrochemically-determined surface coverage has been made. These results showed that the SERS intensities track the surface concentration of the adsorbed molecule up to about 2/3 of a monolayer. The possibilities brought by the new instruments suggest that these studies, involving the relationship between SERS intensities and surface concentrations, can be extended to single-crystal surfaces. The thermodynamic parameters of adsorption, including the surface coverage, for simple organic molecules adsorbed on

single-crystal gold electrodes, are being measured in our Centre [16]. These electrochemical data can be directly compared to our SERS results.

In this Chapter, the electrochemical SERS spectra of pyridine (py) and pyrazine (pz) adsorbed on an "unroughened" Au(210) electrode are presented. Au(210) was the chosen substrate, because this single-crystal surface is very stable, and, unlike other single-crystal faces, it does not undergo reconstruction during potential sweeps. Moreover, the "kinked" surface structure of Au(210), presented in Figure 8.1, provides a natural "roughness" which might increase the Raman signal. The potential-dependent SERS intensities of pyridine and pyrazine adsorbed on Au (210) were obtained. The SERS intensities were compared to the surface concentrations obtained electrochemically. Most of the results presented in this Chapter has been published elsewhere [17].

8.2. Experimental

8.2.1. Solutions

All solutions were prepared from Milli-Q water. All SERS experiments were performed in 0.1 M $KClO_4$ (BDH). The $KClO_4$ was purified by calcinating at 300 °C, recrystallizing twice from Milli-Q water, and then drying. Pyrazine (99+%) from Aldrich and pyridine (analytical grade) from BDH were used without further purification. The solutions were purged with nitrogen for at least ½ hour before taking measurements and a gentle N_2 stream was kept over the top of the solution during experiments.

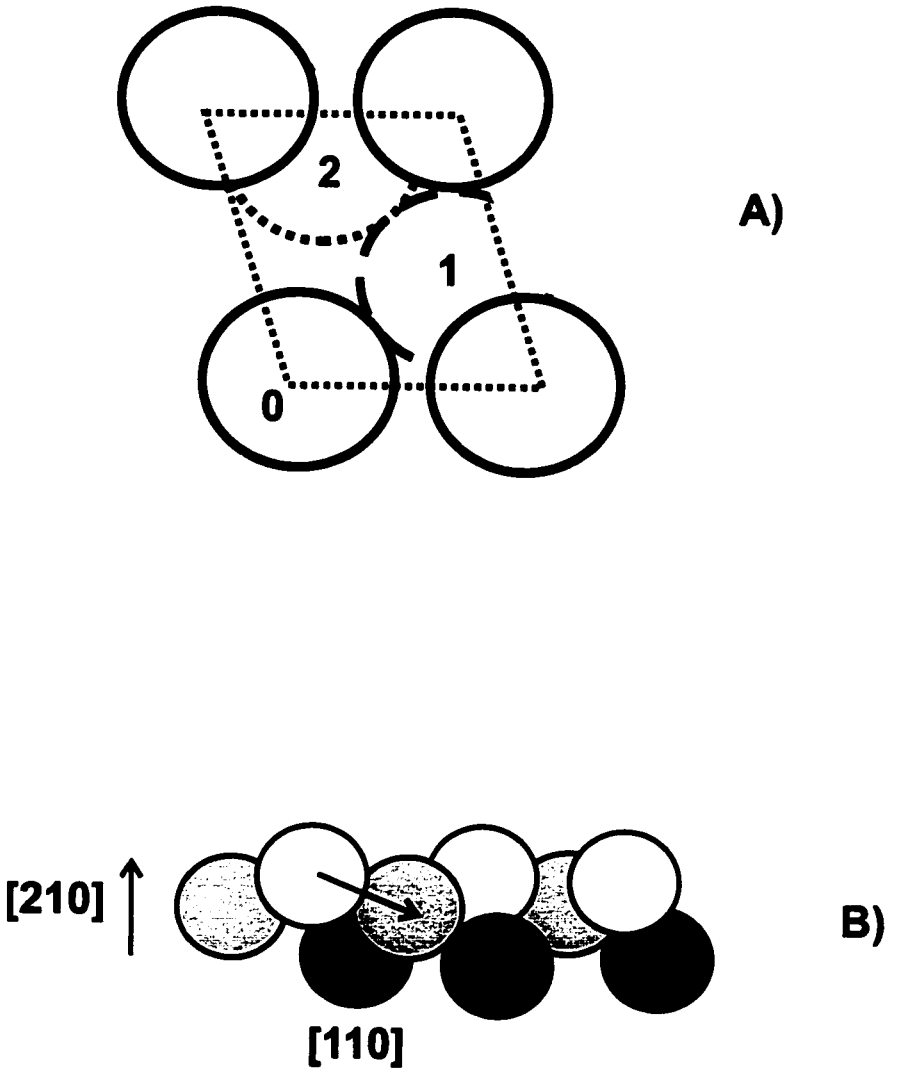

Figure 8.1: Structure of a Au(210) surface. Gold belongs to the face centered cubic system. A) top view; B) lateral view.

8.2.2. Electrodes

The Au(210) single crystal rod (Johnson Matthey 99.99% pure) was prepared according to the method described elsewhere [18, 19]. A Teflon holder was used. The gold electrode was polished to a mirror finish with progressively finer grades of alumina ending with the 0.3 μm grade. The electrode was cleaned by flaming and quenching with Milli-Q water, and transferred to the cell.

The counter electrode was a platinum wire, separated from the working electrode compartment by a porous glass frit. A saturated calomel electrode (SCE) was used as the reference electrode. Therefore, all potentials reported in this work are relative to the SCE. A Luggin capillary was used to minimize the IR drop.

8.2.3. Activation Procedure

8.2.3.1.Preparation of an "unroughened" Au(210) electrode

The "unroughened" gold electrode was prepared using the technique developed in a previous work [14]. A clean gold electrode was placed in the SERS cell containing 0.1 M $KClO_4$ and the desired concentration of adsorbate. The electrode was submitted to continuous cleaning cycles between the limits -0.8 V and +1.1 V at 20 mV/s. This cycling persisted until a cyclic voltammogram reproduced itself from one cycle to the next and displayed the features of a clean gold electrode. After the SERS experiments, the

electrode was rinsed with copious amounts of Milli-Q water, and flame annealed. The electrode was then transferred to a clean electrochemical cell containing 0.1 M $KClO_4$ solution. Cyclic voltammograms and differential capacitive curves, presented in Figure 8.2, were obtained in the region between -0.8 and +1.1 V at 20 mVs^{-1}. The voltammograms and the DC curves presented features uniquely characteristic of a Au(210) surface [20]. This surface characterization was carried out to confirm that the electrode surface was preserved during the SERS experiment.

8.2.4. Instrumentation

A Renishaw 1000 Raman microscope system equipped with a CCD was used in the SERS experiments. A macro point accessory, with 40 mm focal length, was used to redirect the laser light to the electrode surface in the spectroelectrochemical cell described elsewhere (Chapter 2 and [1]).

A PC computer, interfaced to the spectrometer, contained the data acquisition package with programs for baseline correction, smoothing, and bandfitting. A potentiostat PAR model 273 was used in the electrochemical and SERS experiments. The acquisition time was 10 seconds and 100 accumulations were performed.

A 35 mW Melles Griot He-Ne laser provided excitation at 632.8 nm. The laser power was ~ 6 mW at the sample. The diameter of the laser focus was ca. 5 μm.

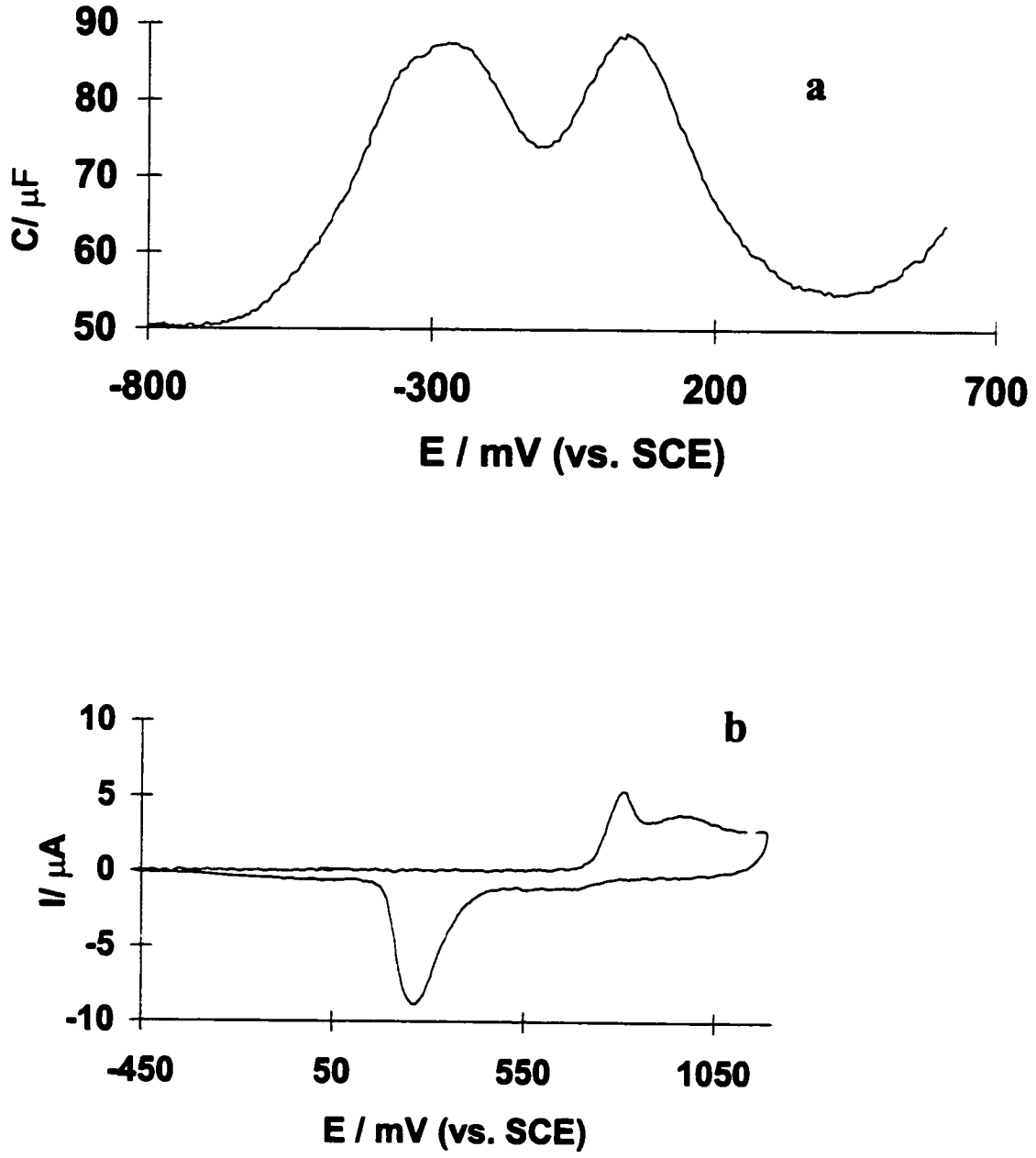

Figure 8.2: a) Differential Capacitance curve; b) Cyclic voltammogram at 10 mV/s. Au(210) in 0.1 M $KClO_4$.

8.3. Results and Discussion

Figure 8.3 shows the SERS spectra of pyridine adsorbed on Au(210) at several potentials. The band at ~ 1002 cm^{-1}, marked with an (*) in Fig. 8.3, is due to the ring breathing mode of the aqueous (1 mM) pyridine. The bands at ~ 1010 and ~ 1035 cm^{-1} correspond to the ring breathing mode (number 1) and the ring mode (number 12), respectively, for pyridine molecules adsorbed on the single-crystal face. The positions of these two peaks are in good agreement with the adsorption of neutral pyridine on electrode surfaces reported in previous SERS work [21].

The dependence of both the integrated SERS intensity of the ring breathing vibration and the surface coverage, for pyridine adsorbed on a Au(210) electrode, on the applied potential are compared in Figure 8.4. The SERS intensity presented in Fig. 8.4 was normalized, using the aqueous perchlorate stretch band (~ 934 cm^{-1} - not shown in Fig. 8.3) as an internal standard. The SERS potential profile (SERS intensities vs. applied potential plot) peaks at ca. -500 mV. This peak is considerably more negative than observed previously for the SERS of pyridine adsorbed on polycrystalline gold electrodes (-400 mV) [14]. The potential-of-zero-charge (pzc) for a Au(210) electrode in 0.1 M $KClO_4$ medium has been determined electrochemically [20]. Its value (ca. -100 mV) is more negative than the pzc determined for a polycrystalline gold electrode [22] (ca. -40 mV). Therefore, the shift in the maximum of the SERS potential profile is larger than the shift in the pzc value when these values, obtained for pyridine adsorbed on Au(210), are

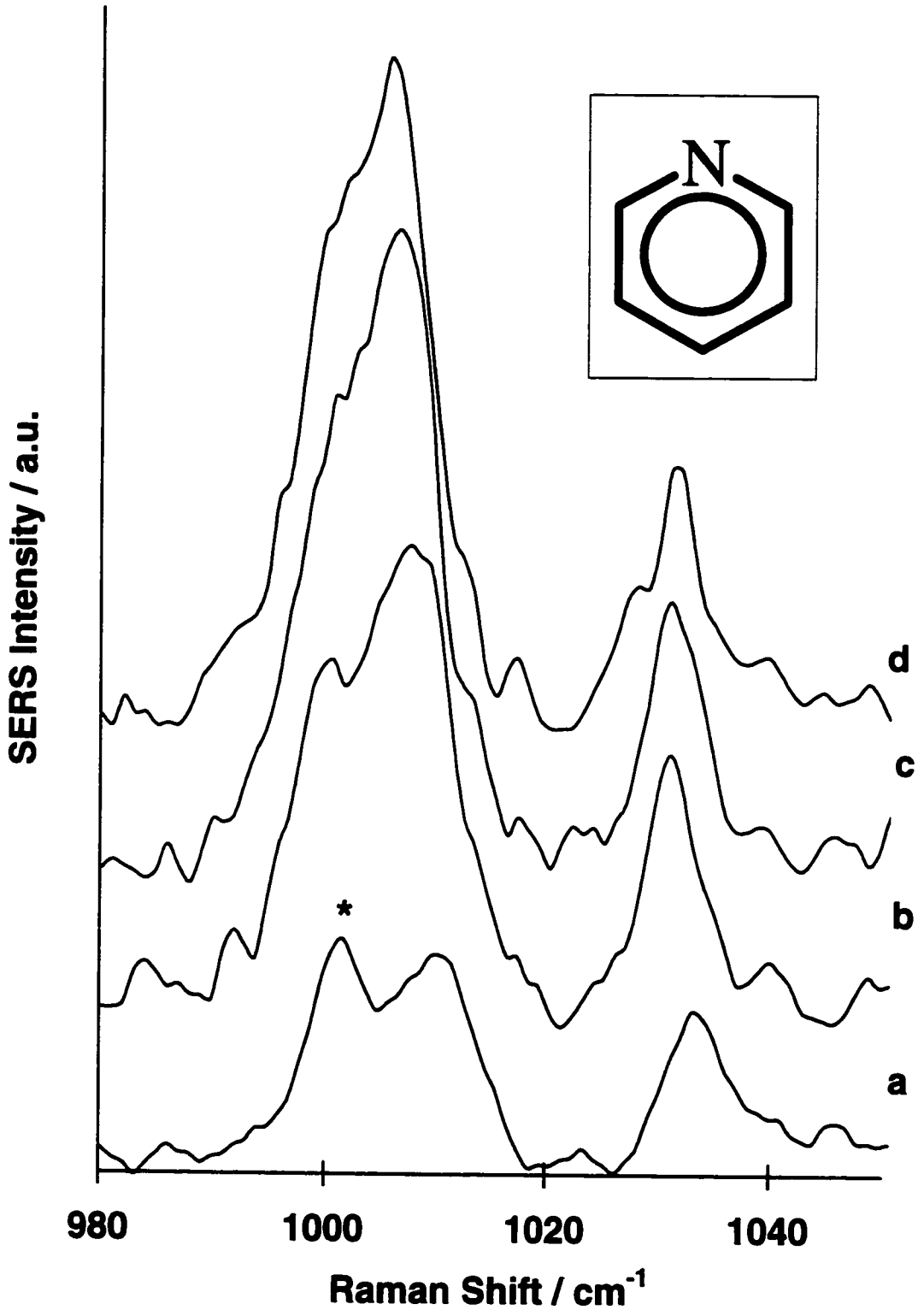

Figure 8.3: SERS spectra of pyridine adsorbed on a Au(210) electrode.
a) + 200 mV; b) -100 mV; c) -400 mV; d) - 600 mV.
(*) band from the aqueous pyridine.

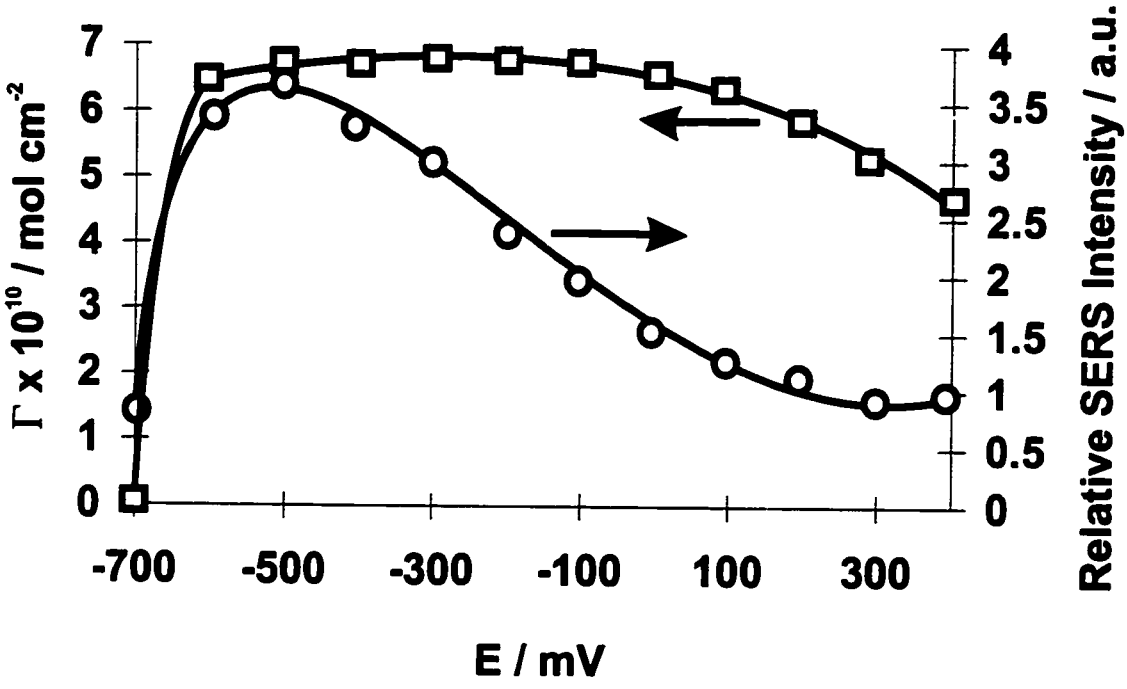

Figure 8.4: Dependence of both the integrated SERS intensity and the surface coverage on the applied potential for pyridine adsorbed on Au(210).

compared to the pyridine adsorption on Au(Poly). The surface concentration vs. applied potential plot (Fig. 8.4) shows that the Au(210) surface is heavily packed in the potential range between -600 and +400 mV. It has been demonstrated that the SERS intensity for molecules adsorbed on a polycrystalline gold electrode tracks the surface coverage only for low surface concentrations (up to 2/3 of a monolayer) [14]. Therefore, it is difficult to find some simple correlation between the SERS intensity and the surface coverage for pyridine adsorbed on Au(210). The surface concentration of a full monolayer of pyridine on this surface is about 6.7×10^{-10} mol.cm^{-2}. Hence, a relationship between the SERS intensity and the surface coverage is expected only for surface concentration values up to about 4.0×10^{-10} mol.cm^{-2}. This surface concentration value occurs, for this system, in a very limited potential range.

The surface concentration for one monolayer of pyridine, determined electrochemically, indicates that the molecule adsorbs on the electrode via its nitrogen lone pair (end-on orientation) [20]. The electrochemical data also show that the orientation is potential-independent. This result can be confirmed by the analysis of the spectra presented in Fig. 8.3 and SERS selection rules [23]. The procedure consists of determining the polarizability components of the most enhanced SERS bands. This procedure has been applied to several organic molecules adsorbed on electrode surfaces [23]. For a simple aromatic compound, such as py, the position of the ring breathing mode can give sufficient information to suggest the orientation. For instance, a flat-adsorbed pyridine would interact with the electrode surface using its π-electrons from the ring. This interaction is expected to decrease the frequency of the ring breathing mode when

compared to the spectrum of the "free" molecule in the liquid state. This behaviour is observed in the SERS spectra of flat-adsorbed benzene on silver [24]. The ring breathing mode of adsorbed benzene occurs at 982 cm^{-1}, compared to 992 cm^{-1} for liquid benzene. The data presented in Fig. 8.3 show no shift of the ring breathing to low wavenumbers due to the adsorption. In fact, it is clear from Fig. 8.3, that the frequency for the ring breathing mode of adsorbed py is higher than that observed for solution. This result strongly suggests that py is adsorbed on the Au(210) electrode in an end-on configuration. Moreover, the peak position does not change significantly with the potential. These SERS observations are in good agreement with the electrochemical results.

Figure 8.5 shows a portion of the SERS spectrum of pyrazine adsorbed on a Au(210) electrode at several potentials. The SERS spectrum of pyrazine adsorbed on a silver electrode has been extensively studied (Chapter 5, [25]). The peak at 1019 cm^{-1} corresponds to the ring breathing vibration of pz. The weak peak at ~ 1030 cm^{-1} is due to the ring mode number 12. This mode is forbidden in the normal Raman spectrum of pyrazine in solution; it has become active for adsorbed pyrazine due to a field gradient enhancement mechanism [25].

Figure 8.6 shows the comparison of the SERS potential profile and the surface coverage data [26, 27] for pz adsorbed on a Au(210) electrode. The maximum in the SERS intensity profile occurs at ca. + 100 mV. This maximum is shifted to negative values when compared to the adsorption of pyrazine on polycrystalline electrodes (ca. +450 mV [15]). This observation is similar to that previously described for the Au(210)-pyridine

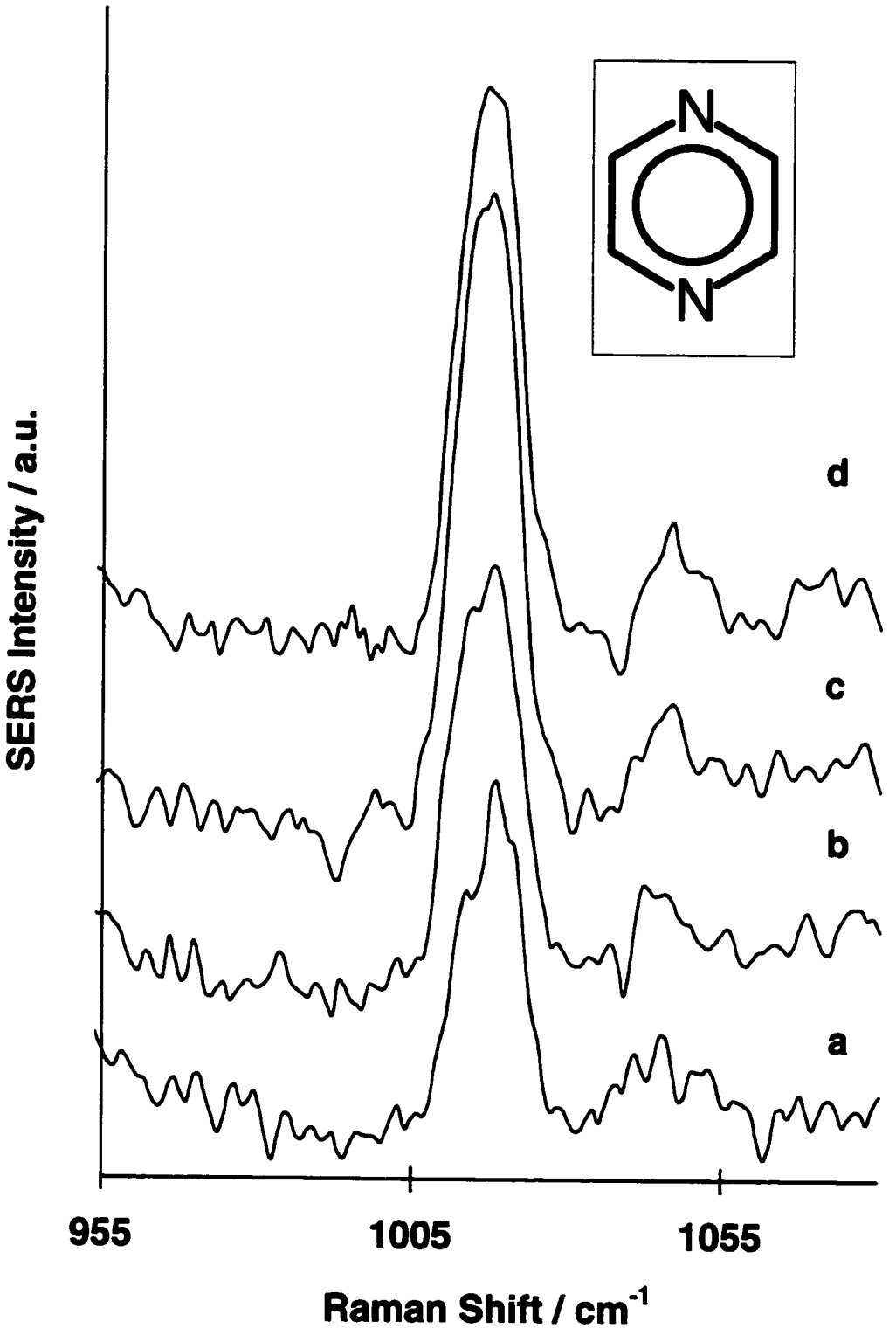

Figure 8.5: SERS spectra of pyrazine adsorbed on a Au(210) single-crystal electrode at several potentials. a) -450 mV; b) -150 mV; c) +200 mV; d) +300 mV.

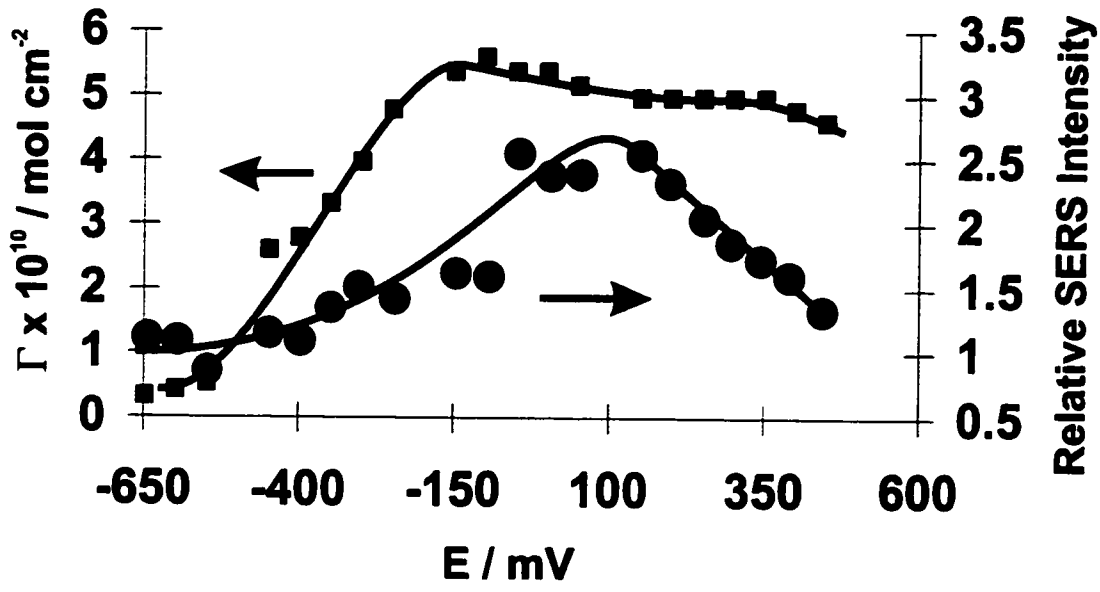

Figure 8.6: Dependence on both the integrated SERS intensity and the surface coverage on the applied potential for pyrazine adsorbed on Au(210) electrode.

system. The shift in the maximum of the potential profile may be induced by a change in the pzc. As we observed for the adsorption of pyridine, the surface coverage vs. potential curve (Fig. 8.6) indicates that the Au(210) surface seems to be saturated with pyrazine in a wide potential range. However, in this case, there is a more gentle rise in the surface coverage curve in the range between -650 to -150 mV. In this region, where the surface coverage value is a fraction of one monolayer, it seems that there is a correlation between the SERS intensity and the surface coverage; both surface coverage and SERS intensity increase as the potential becomes more positive.

The maximum in the surface concentration curve for pyrazine adsorbed on Au (210), determined electrochemically [26], is around 6.0×10^{-10} mol cm^{-2}. If one considers the area occupied by a vertically-oriented pyrazine molecule (~ 0.25 nm^2), this value is consistent with an end-on adsorbed pyrazine. The same argument used earlier to discuss the orientation of the pyridine molecule can be applied here. Raman spectra of aqueous pyrazine solutions [28] show the ring breathing mode at 1015 cm^{-1}. The position for adsorbed pz, 1019 cm^{-1}, is higher, consistent with an end-on orientation. Moreover, the general features of the SERS spectrum of pyrazine adsorbed on Au(210) resemble the spectra of pyrazine adsorbed on silver, which strongly suggested an end-on adsorption [25]. Therefore, the electrochemically-determined orientation of pyrazine on Au(210) is confirmed by our SERS results.

Finally, it is important to point out that the absolute signal for the spectra presented here is very low. In fact, the spectra from Fig. 8.5 are about 1000 times weaker

than for pyrazine adsorbed on a rough silver electrode in a halide medium, and, at least, 100 times weaker than the SERS spectrum of pyrazine adsorbed on a rough polycrystalline gold electrode. However, the spectra shown in Figs. 8.3 and 8.5 can be obtained with a reasonable signal-to-noise ratio. Therefore, the advent of the new generation of Raman instruments equipped with CCD detectors opens a new window of possibilities for the study of SERS spectra of molecules adsorbed on single-crystal electrodes.

8.4. Conclusions

Raman spectra from molecules adsorbed on "unroughened" single - crystal electrodes can now be obtained using the new generation of Raman spectrometers equipped with CCD detectors. SERS spectra of pyridine and pyrazine adsorbed on an "unroughened" Au(210) electrode have been obtained for the first time with a reasonable signal-to-noise ratio. From the analysis of the SERS spectrum, it is possible to infer that both pyridine and pyrazine adsorb on the electrode surface using the nitrogen lone pair, in an end-on configuration. This result is in good agreement with previous electrochemical data. The SERS intensities have been compared to electrochemically-determined surface concentrations for both species adsorbed on Au(210). No simple relationship between the SERS intensity and the surface coverage has been found for surface concentrations close to one monolayer. However, the SERS intensity seems to follow the surface coverage for low surface concentrations.

8.5. References

[1] A. G. Brolo, B. D. Smith and D. E. Irish, *J. Mol. Struct.*, **1997**, 405, 29.

[2] B. Pettinger in *Adsorption of Molecules at Metal Electrodes*, **1992**, J. Lipkowski and P. N. Ross, eds., VCH, New York, Ch. 1, p. 285.

[3] V. Hallmark and A. Campion, *J. Chem. Phys.*, **1986**, 84, 2933.

[4] B. Pettinger and U. Wenning, *Chem. Phys. Lett.*, **1978**, 56, 253.

[5] B. Pettinger, U. Wenning and D. M. Kolb, *Ber. Bunsenges. Phys. Chem.*, **1978**, 82, 1326.

[6] M. Takahashi and M. Ito, *J. Electon Spect. and Relat. Phenon.*, **1990**, 54, 913.

[7] S. P. Byahut and T. E. Furtak, *Electrochim. Acta*, **1991**, 36, 1879.

[8] N. Matsuda, T. Sawaguchi, M. Osawa and I. Uchida, *Chem.Lett.*, **1995**, 145.

[9] T. Sueoka, J. Inukai and M. Ito, *J. Electron Spectrosc. and Relat. Phenom.*, **1993**, 64/65, 363.

[10] B. Ren, Q. J. Huang, W. B. Cai, B. W. Mao, F. M. Liu and Z. Q. Tian, *J. Electroanal. Chem.*, **1996**, 415, 175.

[11] W. B. Caldwell, K. Chen, B. R. Herr, C. A. Mirkin, J. C. Hulteen and R. P. Van Duyne, *Langmuir*, **1994**, 10, 4109.

[12] W. B. Caldwell, D. J. Campbell, K. Chen, B. R. Herr, C. A. Mirkin, A. Malik, M. K. Durbin, P. Dutta and K. G. Huang, *J. Am. Chem. Soc.*, **1995**, 117, 6071.

[13] J. Lipkowski, L. Stolberg, S. Morin, D. E. Irish, P. Zelenay, M. Gamboa and W. Wieckowski, *J. Electroanal. Chem.*, **1993**, 355, 147.

[14] L . Stolberg, J. Lipkowski and D. E. Irish, *J. Electroanal. Chem.*, **1991**, 300, 563.

[15] A. G. Brolo and D. E. Irish, *Langmuir*, **1998**, 14, 517.

[16] J. Lipkowski and L. Stolberg, in *Adsorption of Molecules at Metal Electrodes*, **1992**, J. Lipkowski and P. N. Ross, eds., VCH, New York, Ch. 4, p. 171.

[17] A. G. Brolo and D.E. Irish, *J. Phys. Chem. B*, **1997**, 101, 3906.

[18] A. Hamelin, *J. Electroanal. Chem.*, **1982**, 138, 395.

[19] L. Stolberg, Ph.D. Thesis, University of Guelph, June **1990**.

[20] D. F. Yang, L. Stolberg, J. Lipkowski and D.E. Irish, *J. Electroanal. Chem.*, **1992**, 329, 259.

[21] D. J. Rogers, S. D. Luck, D. E. Irish, D. A. Guzonas and G. F. Atkinson, *J. Electroanal. Chem.*, **1984**, 167, 237.

[22] A. Iannelli, J. Richer and J. Lipkowski, *Langmuir*, **1989**, 5, 466.

[23] J. A. Craighton, in *Advances is Spectroscopy, Vol 16, Spectroscopy of Surfaces*, **1988**, R. J. H. Clark and R. E. Hester, eds., Willey, New York, Ch. 2, p. 37.

[24] M. Moskovits and D. P. DiLella, *J. Chem. Phys.*, **1980**, 73, 6068.

[25] A. G. Brolo and D. E. Irish, *J. Electroanal. Chem.*, **1996**, 414, 183.

[26] A. Iannelli, M.Sc. Thesis, University of Guelph, September **1990**.

[27] A. Iannelli, A. G. Brolo, J. Lipkowski and D. E. Irish, *Can. J. Chem.*, **1997**, 75, 1694.

[28] A. G. Brolo and D. E. Irish, *Z. Naturforsh. A*, **1995**, 50a, 274.

Chapter 9

General Summary

9. General Summary

The surface-enhancement Raman scattering (SERS) technique is one of the most powerful tools for the *in situ* investigation of electrochemical problems. However, the dependence of the enhancement factor on several variables, such as electrode potential, laser wavelength, surface coverage, and morphology, severely limits its applications. In this thesis we expand the knowledge of the influence of these factors on the overall SERS effect.

Pyrazine (pz) was chosen as the probe molecule. Pz has a molecular centre of inversion which makes this molecule a good model for molecular orientation studies.

A Raman spectral study of pyrazine and its protonated forms in aqueous solution has been performed. By observation of the shifts of the bands from the positions measured for neutral solutions, it has been possible to identify the unique characteristic bands of unprotonated pyrazine and its two protonated forms. The majority of the vibrational bands of the monoprotonated pyrazine (pzH^+) were identified and assigned. The diprotonated pyrazine cation spectrum was only observed from very concentrated H_2SO_4 and $HClO_4$ solutions, and the presence of strong bands from these acids masked some of its bands. The positions of these masked bands have been predicted theoretically. The ab initio calculations for pyrazine and its two protonated forms provided useful confirmation of the assignments of the observed bands within 10% accuracy.

The identification and assignment of the vibrational bands from pyrazine and monoprotonated pyrazinium cation (pzH^+) in solution proved to be useful in the interpretation of the Raman spectrum of pyrazine adsorbed onto metallic surfaces. The positions of the vibrational bands in the surface-enhanced Raman scattering (SERS) spectrum of pyrazine adsorbed on a polycrystalline silver electrode are more similar to those of aqueous pyrazine than those of its monoprotonated derivative. However, several "forbidden" pyrazine modes were activated by the electrode surface. The presence of Raman forbidden bands in the SERS spectrum of pyrazine can be explained either by the "chemical" (charge transfer - CT) or by the "electromagnetic" enhancement mechanisms. The intensities of all bands in the SERS spectrum of pyrazine are potential dependent, and their maxima depend on the electrolyte and on the activation procedure. The spectrum is mainly dominated by the ring stretch (number 8a) mode at ~ 1590 cm^{-1}. The ring breathing (number 1) mode at ~ 1019 cm^{-1} is the second most intense band, followed by the other A_g modes at 630 and 1235 cm^{-1}. Vibrational bands at ca. 360, 432, 700, 1225, and 1520 cm^{-1} were also observed.

New features have been observed in the SERS spectrum of pyrazine adsorbed on a silver electrode immersed in a 1.0 M KBr solution when the applied potential was more negative than -900 mV. These new bands were assigned to the main reduction product of pyrazine, the 1,4-dihydropyrazinium cation. The 1,4-dihydropyrazinium cation, formed at negative potentials, can be adsorbed on the electrode surface even at potentials more positive than the pzc for silver in that medium. In this case, the reduced pyrazine cation

binds to the halide layer. The halide, which is adsorbed on the positively charged metal surface, acts like a bridge. The same mechanism is operative in the adsorption of monoprotonated pyrazine (pzH^+) on positively charged polycrystalline silver electrodes. The features in the SERS spectrum of the adsorbed pyrazinium cation were dependent on the applied potential. This potential dependence suggested that the cation was adsorbed in two distinct orientations. The end-on adsorbed pyrazinium is predominant at potentials more positive than -170 mV. The flat adsorbed monoprotonated pyrazine cation is the only species on the surface at potentials more negative than -300 mV.

SERS spectra of pyrazine adsorbed on "smooth" and rough polycrystalline gold electrodes were also obtained. The roughness factors of a number of gold surfaces, prepared by varying the number of oxidation-reduction cycles (ORCs) applied, were monitored by atomic-force microscopy (AFM). The surface-enhancement was correlated to the surface morphology. The results indicated that an optimum SERS signal was generated from a surface containing features of, approximately, 100 nm-size. The SERS intensity was also correlated to surface concentration data, obtained independently by electrochemical methods. The SERS intensities track the surface concentration up to approximately 2/3 of a monolayer. However, the SERS intensity correlates linearly to the solution concentration of the adsorbate. The dependence of the relative enhancement factor on the applied potential indicated that the CT contribution to the overall enhancement mechanism is very small for pz adsorbed on "unroughened" gold electrodes. A novel procedure to determine the SERS intensity from a "smooth" surface was developed. The procedure consisted of obtaining the SERS intensity for the ring breathing

band of pz for different degrees of roughness. The SERS intensity from a "smooth" surface was obtained graphically from the plot between SERS intensity and roughness factor. A linear relationship between the extrapolated SERS intensities ("smooth" surface) and the surface concentration data was observed.

The SERS spectra from pz and pyridine adsorbed on a Au(210) single-crystal electrode were obtained; this is the first report of a SERS spectrum from this "unroughened" surface. The correlation between the SERS intensities and the surface coverage was also investigated for Au(210). A direct relationship was observed between SERS intensities and the surface coverage of organic molecules on the single-crystal face only for a fraction of a monolayer.

Appendices

Appendix 1: SERS Intensity and Surface Coverage Data for Pyrazine Adsorbed on a "Unroughened" Polycrystalline Gold Electrode (data used Chapter 7)

	E / mV	Γ x 10^{10} / mol cm^{-2}	SERS Intensity / a.u.
[pz] = 5.50 x 10^{-5} M			
	450	3.34	0.88
	350	3.87	0.69
	250	3.87	1.51
	150	3.46	0.40
	50	3	0.69
	-50	2.26	0.56
	-150	2.04	0.50
	-250	1.12	0.39
	-350	0.58	0.34
[pz] = 1.23 x 10^{-4} M			
	450	4.18	1.82
	350	4.73	1.90
	250	5.64	2.25
	150	5.64	3.30
	50	4.93	3.42
	-50	4.35	4.85
	-150	3.34	5.47
	-250	2.7	3.31
	-350	1.12	1.79
	-450	0.443	1.82
	-550	0.132	1.28
[pz] = 6.11 x 10^{-4} M			
	450	4.18	2.47
	350	4.93	2.86
	250	5.64	5.51
	150	5.64	5.40
	50	4.93	5.19
	-50	4.54	6.17
	-150	4.02	6.32
	-250	3.1	5.52
	-350	1.7	3.29
	-450	0.915	2.57
	-550	0.264	1.29
[pz] = 9.97 x 10^{-4} M			
	450	4.18	3.56
	350	4.93	4.48
	250	5.64	5.48
	150	5.64	6.87
	50	4.93	5.33
	-50	4.54	4.84
	-150	4.02	7.08
	-250	3.1	7.39
	-350	1.83	4.25
	-450	1.23	2.79
	-550	0.264	1.68

Appendix 2: SERS Intensity and Surface Coverage Data for Pyridine and Pyrazine Adsorbed on a "Unroughened" Single-Crystal Au(210) Electrode (data used Chapter 8)

Pyridine (1mM py solution in 0.1 M $KClO_4$)

E / mV	Γ x 10^{10} / mol cm^{-2}	SERS Intensity / a.u.
400	4.6	0.92
300	5.25	0.91
200	5.8	1.08
100	6.25	1.25
0	6.55	1.50
-100	6.7	1.96
-200	6.7	2.34
-300	6.7	2.93
-400	6.7	3.29
-500	6.7	3.63
-600	6.46	3.36
-700	0	0.81

Pyrazine (1mM pz solution in 0.1 M $KClO_4$)

E / mV	Γ x 10^{10} / mol cm^{-2}	SERS Intensity / a.u.
450	4.61	1.31
400	4.79	1.58
350	4.98	1.70
300	4.98	1.84
250	4.98	2.04
200	4.98	2.31
150	4.98	2.54
50	5.18	2.39
0	5.39	2.37
-100	5.61	1.58
-150	5.39	1.62
-250	4.79	1.39
-300	3.98	1.51
-400	2.8	1.07
-450	2.61	1.14
-550	0.55	0.84

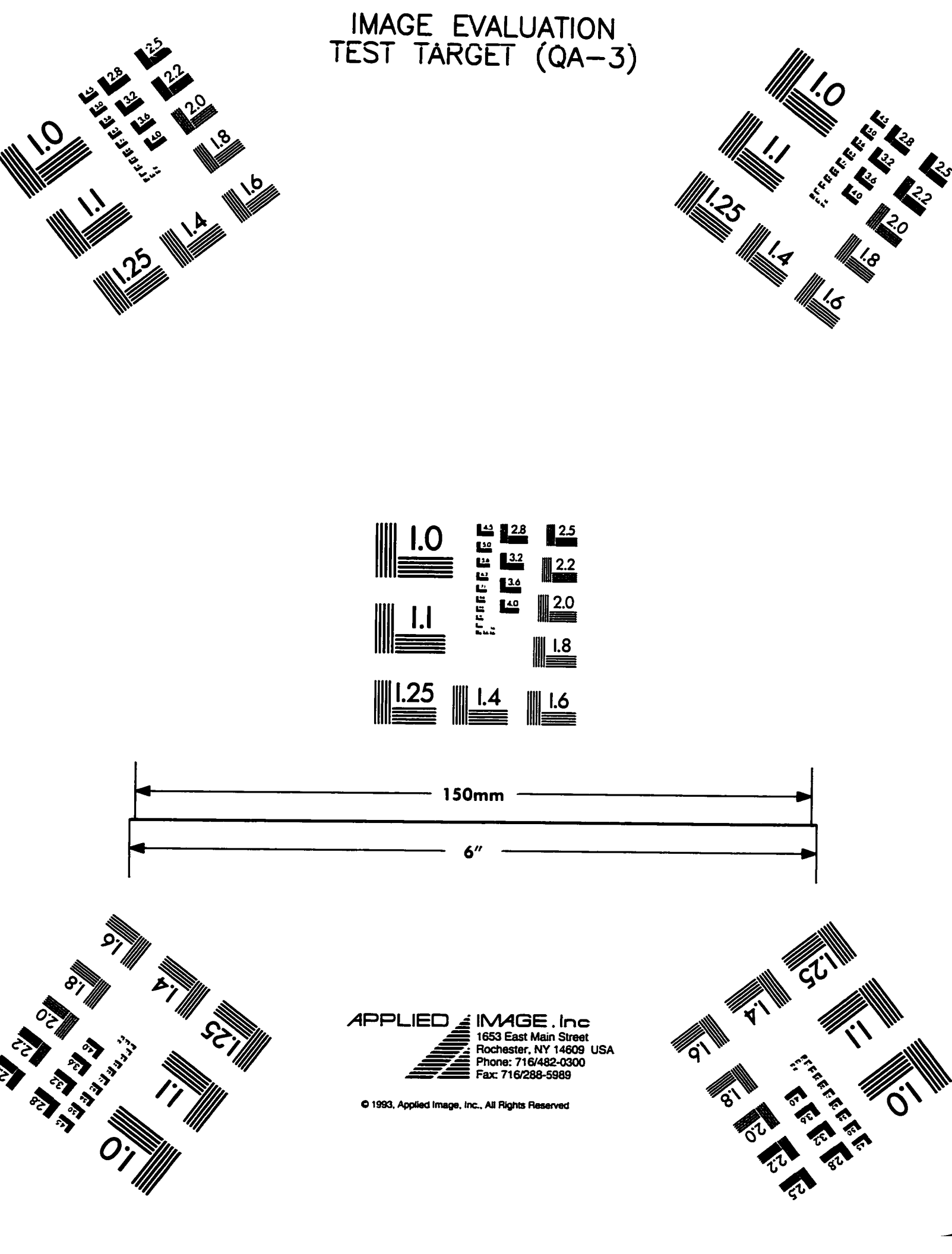
IMAGE EVALUATION
TEST TARGET (QA-3)
1.0
1.1
1.25
1.4
1.6
1.8
2.0
2.2
2.5
2.8
3.2
3.6
4.0
150mm
6"
APPLIED IMAGE, Inc
1653 East Main Street
Rochester, NY 14609 USA
Phone: 716/482-0300
Fax: 716/288-5989
© 1993, Applied Image, Inc., All Rights Reserved